Post-2000 nonlinear optical materials and measurements: data tables and best practices

Journal of Physics: Photonics

PAPER

Post-2000 nonlinear optical materials and measurements: data tables and best practices

Nathalie Vermeulen[1,17,*], Daniel Espinosa[2], Adam Ball[3], John Ballato[4,17], Philippe Boucaud[5], Georges Boudebs[6], Cecília L A V Campos[7], Peter Dragic[8], Anderson S L Gomes[7,17], Mikko J Huttunen[9,17], Nathaniel Kinsey[3,17], Rich Mildren[10], Dragomir Neshev[11], Lázaro A Padilha[12], Minhao Pu[13,17], Ray Secondo[3], Eiji Tokunaga[14], Dmitry Turchinovich[15,17], Jingshi Yan[11], Kresten Yvind[13], Ksenia Dolgaleva[2] and Eric W Van Stryland[16,17]

[1] Brussels Photonics (B-PHOT), Department of Applied Physics and Photonics (IR-TONA), Vrije Universiteit Brussel, Pleinlaan 2, 1050 Brussel, Belgium
[2] School of Electrical Engineering and Computer Science, University of Ottawa, Ottawa, ON K1N 6N5, Canada
[3] Department of Electrical & Computer Engineering, Virginia Commonwealth University, Richmond, VA 23284, United States of America
[4] Department of Materials Science and Engineering, Clemson University, Clemson, SC 29634, United States of America
[5] Université Côte d'Azur, CNRS, CRHEA, Rue Bernard Grégory, 06905 Sophia-Antipolis, France
[6] Univ Angers, LPHIA, SFR MATRIX, F-49000 Angers, France
[7] Departamento de Física, Universidade Federal de Pernambuco, 50670-901 Recife, PE, Brazil
[8] Department of Electrical & Computer Engineering, University of Illinois at Urbana-Champaign, Urbana, IL 61801, United States of America
[9] Photonics Laboratory, Physics Unit, Tampere University, Tampere FI-33014, Finland
[10] MQ Photonics Research Centre, Macquarie University, Sydney, 2109 NSW, Australia
[11] ARC Centre of Excellence for Transformative Meta-Optical Systems (TMOS), Department of Electronic Materials Engineering, Research School of Physics, Australian National University, Canberra ACT, 2601, Australia
[12] Instituto de Fisica 'Gleb Wataghin', Universidade Estadual de Campinas, Campinas, Sao Paulo 13083-970, Brazil
[13] Department of Electrical and Photonics engineering, Technical University of Denmark, DK-2800 Kgs. Lyngby, Denmark
[14] Department of Physics, Faculty of Science, Tokyo University of Science, 1-3 Kagurazaka, Shinjuku-ku, Tokyo 162-8601, Japan
[15] Fakultät für Physik, Universität Bielefeld, Universitätsstr. 25, 33615 Bielefeld, Germany
[16] CREOL, The College of Optics and Photonics, University of Central Florida, Orlando, FL, United States of America
[17] Team leaders for the material categories considered in the article.
[*] Author to whom any correspondence should be addressed.

E-mail: Nathalie.Vermeulen@vub.be

Keywords: nonlinear optics, bulk materials, metamaterials, low-dimensional materials, fibers, on-chip waveguides, THz nonlinear optics

OPEN ACCESS

RECEIVED
4 May 2022

REVISED
15 September 2022

ACCEPTED FOR PUBLICATION
27 October 2022

PUBLISHED
17 May 2023

Abstract

In its 60 years of existence, the field of nonlinear optics has gained momentum especially over the past two decades thanks to major breakthroughs in material science and technology. In this article, we present a new set of data tables listing nonlinear-optical properties for different material categories as reported in the literature since 2000. The papers included in the data tables are representative experimental works on bulk materials, solvents, 0D–1D–2D materials, metamaterials, fiber waveguiding materials, on-chip waveguiding materials, hybrid waveguiding systems, and materials suitable for nonlinear optics at THz frequencies. In addition to the data tables, we also provide best practices for performing and reporting nonlinear-optical experiments. These best practices underpin the selection process that was used for including papers in the tables. While the tables indeed show strong advancements in the field over the past two decades, we encourage the nonlinear-optics community to implement the identified best practices in future works. This will allow a more adequate comparison, interpretation and use of the published parameters, and as such further stimulate the overall progress in nonlinear-optical science and applications.

Contents

List of symbols

$d_{(\mathrm{eff})}$	effective second-order nonlinear coefficient
$\mathrm{d}k/\mathrm{d}t$	change in wave-number with temperature
$\mathrm{d}n/\mathrm{d}t$	change in linear refractive index with temperature
$g_{\mathrm{Brillouin}}$	Brillouin gain coefficient
g_{Raman}	Raman gain coefficient
$I_{\mathrm{sat(eff)}}$	(effective) saturation irradiance
n_0	linear refractive index
$n_{2(\mathrm{eff})}$	(effective) nonlinear index
α_0	linear loss coefficient
α_2	two-photon absorption coefficient
α_3	three-photon absorption coefficient
$\gamma_{(\mathrm{eff})}$	effective nonlinear coefficient
$\gamma_{\mathrm{Brillouin}}$	Brillouin gain factor
γ_{Raman}	Raman gain factor
$\Delta\alpha$	change in absorption
Δn	change in refractive index
Δn_{g}	change in group index
$\Delta\mathrm{OD}$	change in optical density
ΔT	change in pulse duration
ε	dielectric permittivity
η	conversion efficiency
λ	wavelength
λ_{pump}	pump/excitation wavelength
λ_{probe}	probe/signal wavelength
σ	nonlinear conductivity
τ_{pump}	pump/excitation pulse duration
τ_{probe}	probe/signal pulse duration
$\chi^{(2)}$	second-order susceptibility
$\chi^{(3)}$	third-order susceptibility
ω	frequency

List of abbreviations

0D	zero-dimensional
1D	one-dimensional
2D	two-dimensional
2FBS	two-frequency beat signal
2PA	two-photon absorption
3PA	three-photon absorption
3WM	three-wave mixing
BD	beam deflection
BIC	bound states in the continuum
CAIBE	chemically assisted ion-beam etching
CDQW	coupled double quantum well
ChG	chalcogenide glass
CVD	chemical vapor deposition
CVT	chemical vapor transport
CW	continuous-wave
dB	decibels
DB	diffusion bonded
DFG	difference-frequency generation
DUV	deep ultraviolet
EFISH	electric-field-induced second-harmonic generation
ENZ	epsilon near zero
EO	electro-optic
ER	ellipse rotation
FCA	free-carrier absorption
FEL	free-electron laser
FEOS	free-space electrooptic sampling
FIB	focused ion beam
FSR	free spectral range
FWHM	full width at half maximum
FWM	four-wave mixing
GO	graphene oxide

GVD	group velocity dispersion
GVM	group velocity mismatch
HHG	high-harmonics generation
HPHT	high pressure high temperature
HRS	hyper-Rayleigh scattering
HVPE	hydride vapor phase epitaxy
HW1/e^2M	half width at 1/e^2 maximum
IGA	induced-grating autocorrelation
IR	infrared
IRS	inverse Raman scattering
ISBT	intersubband transitions
ITO	indium tin oxide
LED	light emitting diode
LIDAR	light detection and ranging
LN	lithium niobate
LO	longitudinal optical mode
LPCVD	low-pressure chemical vapor deposition
LSPR	localized surface plasmon resonance
MBE	molecular-beam epitaxy
MFD	mode field diameter
MOCVD	metal-organic chemical vapor deposition
MOVPE	metal-organic vapor-phase epitaxy
MPAPS	multiphoton absorption photoluminescence saturation
MQWs	multiple quantum wells
NA	numerical aperture
NLA	nonlinear absorption
NLO	nonlinear optics/nonlinear-optical
NLR	nonlinear refraction
NSM	nanostructured material
NZI	near-zero index
OC	optically contacted
OP	orientation patterned
OPA	optical parametric amplification
OPG	optical parametric generation
OPO	optical parametric oscillation
PAMBE	plasma-assisted molecular beam epitaxy
PCF	photonic-crystal fiber
PDI	periodic domain inversion
PECVD	plasma-enhanced chemical vapor deposition
PhC	photonic crystal
PI	periodically inverted
PIC	photonic integrated circuit
PVT	physical vapor transport
PLD	pulse laser deposition
QCSE	quantum-confined Stark effect
QD	quantum dot
QPM	quasi-phase-matching
QW	quantum well
rGO	reduced graphene oxide
RIE	reactive ion etching
SA	saturable absorption
SBS	stimulated Brillouin scattering
SCG	supercontinuum generation
SEED	self-electro-optic effect device
SEM	scanning electron microscope
SESAM	semiconductor saturable absorber mirror
SFG	sum-frequency generation
SHG	second-harmonic generation
SLR	surface lattice resonance
SOI	silicon-on-insulator
SpBS	spontaneous Brillouin scattering
SPDC	spontaneous parametric down-conversion
SPM	self-phase modulation
SpRS	spontaneous Raman scattering
SRR	split-ring resonator

SRS	stimulated Raman scattering
SRTBC	spectrally resolved two-beam coupling
SWCNT	single-wall carbon nanotube
TDS	time-domain spectroscopy
TE	transverse-electric
THG	third-harmonic generation
TM	transverse-magnetic
TMD	transition metal dichalcogenide
TO	transverse optical mode
TPFP	tilted pulse front pumping
TRI	time-resolved interferometry
WZ	wurtzite
XPM	cross-phase modulation
ZB	zinc blende

1. General introduction

The idea of composing a new set of data tables for NLO materials emerged in 2020 on the occasion of 60 years of NLO research [Franken1961, Kaiser1961]. In those 60 years, the field has witnessed tremendous growth, and several NLO data tables were published before the turn of the century [Robinson1967, Chase1994, Van Stryland1994, Sutherland1996, Dmitriev1999]. After the year 2000, additional data tables were introduced for specific material types (see, for example, [Nikogosyan2005, Smith2018]), but a data table that focuses on the post-2000 NLO research developments for a wide range of materials has not yet been presented. Nevertheless, there have been major advances in materials science and technology since 2000, and these have also accelerated the overall progress in NLO research. Whereas the idea of creating a new set of NLO data tables was originally introduced by John Dudley, we further elaborated on it along the following approach: the data tables presented here have been composed based on a representative set of experimental works published since 2000. In other words, the list of publications included in the table is not comprehensive. We mostly focused on experimental papers that not only provided NLO coefficients, but also reported experimental parameters that give the context and limits of validity for using the quoted coefficient values. In this regard, we also listed best practices for performing and reporting NLO experiments. Some of these best practices are appropriate for any NLO measurement, while others are specific for the chosen NLO characterization technique, e.g., SHG, Z-scan, FWM, etc. In turn, many of these NLO techniques are appropriate only for specific categories of NLO materials: bulk materials, 0D–1D–2D materials, metamaterials, fiber waveguiding materials, on-chip waveguiding materials, and/or hybrid waveguiding systems. Both the NLO techniques and the material categories are defined in more detail in the specific separate sections. With this work, besides providing a set of NLO data tables focused on the progress since 2000, we also aim at stimulating the use of the listed best practices in future NLO publications to allow a better comparison, interpretation and use of the published parameters. The long-term goal of this article is to help advance the development of innovative NLO materials, devices and systems for real-life applications in optical data communication, signal processing, metrology, medical imaging, sensing, laser and quantum light generation, and many other areas.

Most of the NLO materials listed in the data tables are solids, but we also included some solvents as they are often used as reference materials in NLO measurements or for preparing solutions or dispersions. However, we did not consider organic/polymeric NLO materials since these are so numerous that tabulating them is outside the scope of this work. Gases are not included either, except for a few examples in the hybrid waveguiding systems category. More specifics of what is and is not included are given in the respective material category sections. We point out that these will be 'living' data tables that can be updated, so the materials that are currently absent might be added in the future.

To build the data tables presented here, we started by identifying the different material categories while also listing the different NLO techniques and their associated best practices. We then performed a literature search for experimental NLO papers published since 2000 and made a selection based on the listed best practices. Note that we did not limit our search to optical-wavelength-based experiments only but also included works on THz NLO. Finally, we filled out the data in dedicated table templates per material category. To minimize errors, the data filled out by each co-author were also cross-checked by another co-author. Hence, the parameter values listed in the tables should match with those provided in the selected papers.

The main NLO coefficients that we considered for composing the data tables are: the second-order nonlinear susceptibility $\chi^{(2)}$, the effective second-order nonlinear coefficient d_{eff}, the third-order nonlinear susceptibility $\chi^{(3)}$, the effective nonlinear index $n_{2,\text{eff}}$, the effective third-order nonlinear coefficient γ_{eff}, the two- and three-photon absorption coefficients α_2, α_3, the saturation irradiance I_{sat} specified for saturation of

the linear absorption, and the Raman and Brillouin gain coefficients g_{Raman}, $g_{\text{Brillouin}}$. Further information about the underlying physics for each of these coefficients can be found, for example, in [Sutherland1996, Bloembergen1996, Shen2002, Stegeman2012, Boyd2020]. We have not tabulated hyperpolarizabilities, photorefractive effects, electro-optic effects, stimulated polariton scattering, nor cascaded NLO processes. Note that the meaning of 'effective' is different for d_{eff} than for $n_{2,\text{eff}}$ and $\text{Re}(\gamma_{\text{eff}})$. For d_{eff} the subscript 'effective' implies that the coefficient comprises all contributions from the different tensor components being studied during the experiment. In contrast, $n_{2,\text{eff}}$ and $\text{Re}(\gamma_{\text{eff}})$ are effective coefficients in the sense that they might not be solely due to bound-electronic nonlinear transitions as one would expect for a 'pure' n_2 and $\text{Re}(\gamma)$, but instead could also contain contributions from, e.g., nuclear and/or thermal effects (see also section 2.1). Finally, we point out that some works in the data tables do not only report a NLO coefficient but also provide NLO conversion efficiencies η and bandwidths in case techniques such as SHG, THG, Raman, Brillouin and FWM are used. These parameters are then also tabulated for those works since they are important to assess the practical use of the material in wavelength conversion applications.

The outline of the manuscript is as follows: in section 2 we list various NLO measurement techniques and describe some best practices for performing and reporting NLO experiments. Here we make a distinction between best practices that can be applied in general and those that are technique-specific. In section 3 we present the actual data tables per material category, together with background information of the status prior to 2000, a brief discussion of the advancements since 2000 and of the remaining challenges, and some recommendations for future works. Finally, we summarize and conclude in section 4.

As an intermezzo before the main body of the manuscript, we want to visit what is arguably the single most studied material in NLO, namely fused silica. We think this digression is instructive on the difficulties inherent in making NLO measurements as well as in obtaining a complete theoretical understanding. It is also of significant importance because fused silica has been used as a reference in many studies of other materials, i.e., if the reference value is in error, so is the reported value of the measured material. This history of NLO measurements in fused silica is also illustrative of how NLO materials properties are not as well understood as one often assumes.

1.1. Fused silica nonlinearity

To illustrate the difficulties in reporting accurate values of nonlinear parameters, let us look at n_2 of fused silica (see table 1 below). Fused silica is often used as a reference for determining the n_2, or $n_{2,\text{eff}}$ of other materials. We use $n_{2,\text{eff}}$ since while the bound-electronic nonlinearity is essentially instantaneous, other nonlinearities, including those involving nuclei, depend on the pulsewidth used. The values found in the literature for fused silica do not always agree, and, of course, there is dispersion. [Milam1998] attempted to determine the best experimental values at various wavelengths by taking a weighted average, determined by experimental error bars, of the published values up to 1998. This approach gave a value of $\sim 2.7 \times 10^{-20}$ m^2 W^{-1} in the IR with little dispersion from 1–1.6 μm, with values increasing toward the UV. As summarized in [Agrawal2013] the nuclear (Raman) contribution to the nonlinear refractive index of fused silica may be of the order of ∼20% as first discussed by the seminal work of [Hellwarth1975, Hellwarth1977]. Under this assumption, the bound-electronic nonlinearity is $n_2 \cong 2.2 \times 10^{-20}$ m^2 W^{-1}. However, the nuclear contribution estimated in other publications varies from 13% [Smolorz1999] to 26% [Heiman1979]. Following [Agrawal2013], for pulses much longer than ∼1 ps, the nuclear contribution should be fully established. However, [Santran2004] calculates a response function, from which they determine a pulsewidth dependence curve indicating that the nuclear contribution would not be fully developed until >10 ps. It appears that [Stolen1992] was the first to predict the pulsewidth dependence of $n_{2,\text{eff}}$ for fused silica, showing the effective Raman contribution decreasing for pulsewidths ⩽100 fs, going to zero for a pulsewidth of ∼30 fs, and then predicting that it actually turns negative for even shorter pulses. These two publications are the only ones we find that present the projected pulsewidth dependence for $n_{2,\text{eff}}$. Note that when using femtosecond experiments, the finite duration/finite bandwidth of the pulses results in spectral-filtering effects on the intrinsic material response that can result in difficulties in interpreting the experimental data [McMorrow1990]. For much longer pulses (>1 ns) electrostriction can become important and can further significantly increase the measured $n_{2,\text{eff}}$. This is particularly important in fibers [Buckland1996]. Additionally, more recent measurements tend to use shorter pulses and yield smaller values of $n_{2,\text{eff}}$ (see table 1). [Buckland1996] also calculates that $n_{2,\text{eff}}$ is reduced by a factor of 8/9 due to the polarization randomization in fibers as indicated in table 1. We also note that measurements of $n_{2,\text{eff}}$ reported for fibers have rarely been corrected for any modal overlap with the cladding. In principle, there could be a small systematic difference between fiber measurements and bulk measurements, but given the spread of data it is challenging to discern.

Among the several publications where attempts were made to measure the temporal response function, e.g., [Kang1996a, Aber2000, Santran2004, Patwardhan2021], the only one to see a temporal dependence is

Table 1. Nonlinear refractive index of fused silica giving some historical references to early works as well as a representative group of more recent publications (not inclusive)—listed in order of year published. *Note:* Fused silica is high purity synthetic glass (amorphous SiO_2) and different from naturally occurring or synthetic quartz (crystalline α-SiO_2). All measurements listed use linearly polarized inputs except where noted. Legend for superscripts: see below the table. The following abbreviations have been used: de-pol = de-polarized; pol-maint = polarization maintaining; ER = ellipse rotation; SF-Pcr = self-focusing using the critical power for self-focusing, Pcr; Freq Mix = frequency mixing; TRI = time-resolved interferometry; SPM = self-phase modulation; 3WM = three-wave mixing; XPM = cross-phase modulation; 2FBS = two frequency beat signal; Multiple = multiple techniques were used in this compilation of publication data; SRTBC = spectrally resolved two-beam coupling; IGA = induced-grating autocorrelation-based upon time-delayed four-beam coupling in a photorefractive crystal.

Method	$n_{2,\mathrm{eff}}$ ($\times 10^{-20}$ m^2 W^{-1})	λ (nm)	Fiber/Bulk	Pulse Width	Notes	Reference
ER	3.2	694	Bulk	13 ns	Fused quartz	[Owyoung1972, Owyoung1973]
SF Pcr	3.94	1064	Bulk	30 ps		[Smith1975]
Freq Mix	5.2	∼525	Bulk	3 ns		[Levenson1974]
TRI	2.73	1064	Bulk	125 ps		[Milam1976]
TRI	2.73	1064	Bulk	100–150 ps		[Weber1978]
SPM	2.7; 3.3	515	100 m fiber	90 ps	2nd entry ×9/8	[Stolen1978]
3WM	2.4	1064	Bulk	3 ns	CS_2 used as ref	[Adair1992]
SPM	2.36; 2.66	1319	250 m fiber	110 ps	2nd entry ×9/8	[Kim1994]
XPM	2.48; 2.79	1550	Fiber	CW	1% F doping	[Kato1995b]
2FBS	2.2; 2.5[a]	1550	Fiber	CW	2nd entry ×9/8	[Boskovic1996]
XPM	2.47	1550	Fiber	CW	de-pol input not ×9/8	[Wada1996]
Z-scan	2.14	1064	Bulk	30 ps		[DeSalvo1996]
Z-scan	2.24	532	Bulk	22 ps		[DeSalvo1996]
Z-scan	2.41	355	Bulk	17 ps		[DeSalvo1996]
Z-scan	7.8	266	Bulk	15 ps		[DeSalvo1996]
Multiple	2.56	800–1550	Bulk	ps to ns	Compilation of ref. data	[Milam1998]
SRTBC	2.3	∼800	Bulk	18 fs		[Smolorz1999, Riggs2000]
IGA	2.44	1064	24 m fiber pol-maint	53 ps	not ×9/8	[Garcia2003]
IGA	2.2; 2.5	1064	23 m fiber	50–70 ps	2nd entry ×9/8	[Oguama2005a]
IGA	1.81; 2.04	1064	∼100 m fiber	56 ps	2nd entry ×9/8	[Oguama2005b]
IGA	2.22	1064	Short fiber pol-maint	50–70 ps	not ×9/8	[Oguama2005]
ER	2.5	775	Bulk	150 fs		[Miguez2015]
Z-scan	2.23	1030	Bulk	140 fs		[Flom2015]
SPM	2.1; 2.4	1550	Fiber	Telecom	Vascade fiber	[Makovejs2016]
SRTBC	1.94	2300	Bulk	>65 fs		[Patwardhan2021]
SRTBC	2.0	3500	Bulk	>65 fs		[Patwardhan2021]

[a] Values should be reduced by 16% [Smolorz1999] due to electrostrictive contribution estimated by [Buckland1996].

[Smolorz1999], which used 'spectrally-resolved two-beam coupling' with 18 fs, 800 nm pulses. They observed a small oscillatory signal in fused silica lasting for 100s of femtoseconds after excitation indicating a ∼13% nuclear contribution to $n_{2,\mathrm{eff}}$.

In all the papers of which we are aware where fused silica is used as a reference, its $n_{2,\mathrm{eff}}$ is assumed constant. For all the materials reported in the tables in this publication that have been referenced to fused silica, this adds to the uncertainly of the reported $n_{2,\mathrm{eff}}$ values. For very short pulses, ∼10 fs, the nonlinear response could be reduced by as much as the above quoted fractions of the Raman contribution, the highest estimate being 26%.

We are not aware of any direct measurement of the variation of $n_{2,\mathrm{eff}}$ with pulsewidth in the picosecond to femtosecond regime to determine its time dependence. Future measurements of the temporal dependence of the nonlinear response of fused silica and other materials would be quite useful, as has been done for solvents (see section 3.2).

2. NLO characterization techniques and their best practices

2.1. General best practices to obtain and report high-quality NLO measurement data

Before addressing the existing NLO characterization techniques, we provide some general 'best practices' that apply to most of them, i.e., some general rules for obtaining and reporting high-quality, useful NLO measurement data regardless of the technique employed:

- First, the material's composition, dimensions, method of fabrication and linear optical properties as well as temperature need to be known. Particularly, the linear loss/absorption at the wavelengths used in the NLO measurements is an essential parameter, but also other linear optical characteristics such as dispersion coefficients and the properties of optically excited free carriers can be relevant.
- Second, a careful quantification of the NLO pump/excitation parameters *inside* the material and, if relevant for the technique used, also of the signal/probe parameters is required. These parameters, relevant for both pulsed and CW operation, include (but are not limited to):

  * Wavelength
  * Peak power, irradiance (or in some cases electric field amplitude), and/or pulse energy
  * Beam size (specified as, e.g., FWHM, HW1/e^2M) and beam shape
  * Pulse width (specified as, e.g., FWHM, HW1/e^2M) and pulse shape
  * Pulse repetition rate (for pulsed operation)
  * Beam polarization and orientation with respect to crystal axes if appropriate and relative polarization for two-beam experiments

- Last, the generated NLO response needs to be carefully measured, and the measurement results should be appropriately analyzed to extract the NLO coefficient(s). This can be done by means of a model for the technique used, by means of a benchmark measurement on a sample with well-known characteristics, etc. Models should also account for other effects that may interfere with the NLO measurements, and additional supporting information for the conclusions drawn (e.g., investigation of the dependence on pump power/irradiance/energy, the wavelength dependence, or the temporal dependence of the NLO response) is often required (see previous section 1.1). In addition, special attention should be paid to the influence of the sample substrate (if any) and to the possible occurrence of sample damage when performing high-irradiance NLO experiments. When specifying conversion efficiencies and bandwidths, it should be clear which formulas were used for determining them. Finally, the inclusion of error bars on the data sets is very valuable to understand the limitations of the measurements and the extracted parameters.

We consider these general best practices to be an appropriate set of rules for carrying out, analyzing and reporting NLO measurements, independently from the type of technique used. It is also important to keep in mind the following general insights valid for any kind of NLO measurement: whenever long pulse durations and/or high pulse repetition rates are employed in NLO experiments, thermal effects can occur. They can build up collectively over many pulses or arise within the pulse duration, depending upon the material absorption and pulse width. These irradiance-dependent thermal effects can mask the NLO effect one aims to study. More generally speaking, it is unusual for a single nonlinearity to fully determine the overall NLO response. Hence, one should try to unravel the various contributions, e.g., by studying the power/irradiance/energy dependence, the wavelength dependence, the temporal dependence, etc, or at least consider the measured nonlinearity as an 'effective' coefficient for the input parameters quoted. We note that long and short pulses can trigger very different NLO processes (see, e.g., section 3.2 on the NLO response of solvents) and could also exhibit different damage thresholds for the material under study. Also, measuring the wavelength dependence of the NLO response provides crucial information, since knowing the spectrum of the NLA and the dispersion curve of the NLR of a material is extremely helpful for understanding the fundamental physical interactions leading to the observed NLO effects. In some cases, the nonlinear absorption spectra/dispersion curves are necessary information for a proper interpretation of the experimental results. A more detailed discussion of the underlying physics can be found in [Christodoulides2010, Van Stryland2009a, Van Stryland2009b, Boyd2020, Stegeman2012, Sutherland2003, Shen2002, Bloembergen1996].

2.2. Technique-specific best practices

Besides the general best practices identified above, one should also consider additional best practices that are specific for the NLO technique used. In what follows, we list the most common technique families[18], the NLO coefficients they yield and the technique-specific best practices we have identified for each of them.

[18] There exist very specialized techniques that are not addressed in this section as they are only employed in very specific or rather uncommon experiments. Some of these specialized techniques are used in a few papers included in the tables of this work. The reader is directed to those papers for further information on these techniques.

2.2.1. Best practices for second-order NLO techniques

2.2.1.1. Second-order wave mixing

Second-order wave mixing processes, mainly SHG, SFG and DFG [Shen1989, Shen2002, Sutherland2003, Wang2009, Liang2017, Prylepa2018], are often utilized in characterization of bulk materials, 0D–1D–2D materials, metamaterials, fiber waveguiding materials, on-chip waveguiding materials, and hybrid waveguiding systems. The developed techniques allow one to extract the material's $\chi^{(2)}$ and d_{eff} coefficients, and the conversion efficiency of the associated process. In some cases, the techniques also allow characterization of the relevant components of the $\chi^{(2)}$ tensor, or the conversion bandwidth of the process. Second-order wave mixing is also at the heart of OPO, OPG, and OPA [Shen2002, Sutherland2003]. We note that EFISH is in fact a third-order wave mixing process that in the presence of an external static electric field gives rise to SHG.

Besides the general best practices in section 2.1, it is important to verify successful phase matching of the NLO interaction in the material and to determine the parameters on which the considered phase matching approach relies (e.g., dispersion, poling parameters in some cases of QPM, etc). Furthermore, when reporting the conversion efficiency and conversion bandwidth of the material, the used parameter definitions should be clearly stated. Finally, when performing SHG experiments, it is important to verify that the SHG response is not masked by two-photon-excited fluorescence effects.

2.2.1.2. Second-order nonlinear imaging

Second-order nonlinear imaging techniques, most notably SHG imaging [Gannaway1978, Kumar2013, Yin2014, Woodward2016], can be meaningfully applied to material categories exhibiting spatially varying second-order nonlinear parameters (0D–1D–2D materials, metamaterials, on-chip waveguiding materials, and hybrid waveguiding systems). Second-order nonlinear imaging allows one to characterize the magnitude of $\chi^{(2)}$ along with the conversion efficiency associated with the material and the performed experiments.

While the general best practices listed in section 2.1 also apply for second-order nonlinear imaging, we further stress the importance of carefully characterizing the NLO excitation parameters (the peak power/irradiance/energy, beam size, pulse width and polarization) inside the material. This is particularly important, because optical components such as microscope objective lenses may considerably modify the properties of incident pulses. Furthermore, when using SHG imaging, the occurrence of two-photon-excited fluorescence effects should be avoided.

2.2.2. Best practices for third-order NLO techniques

2.2.2.1. Third-order parametric wave mixing

Third-order parametric wave mixing refers to techniques such as FWM [Jain1979, Friberg1987, Agrawal2001], THG [Ward1969, Soon2005], and SPM/XPM [Alfano1986, Agrawal2001], and can be applied to all material categories considered in this work. Third-order parametric wave mixing allows measuring the magnitude of $\text{Re}(\chi^{(3)})$, $n_{2,\text{eff}}$ (which is usually assumed to be real), and $\text{Re}(\gamma_{\text{eff}})$. Specifically in the case of SPM/XPM one can also extract the sign of these nonlinearities [Vermeulen2016a]. When using THG one most often quantifies a $\text{Re}(\chi^{(3)})$ value that is specifically associated with bound-electronic nonlinear transitions. Note also that FWM may be more complex than THG and SPM/XPM as often the imaginary part of the third-order nonlinearity cannot be neglected. To separate the real and imaginary parts of the nonlinearity in a FWM signal, special experimental modifications and careful analysis involving also 2PA and Raman contributions, which will be described in the following sections, are generally required [Burris1985].

In FWM and THG experiments one most often measures the power/energy of the new signal generated by these wave mixing interactions, whereas SPM/XPM experiments are focused on measuring the phase modulation effects (e.g., spectral broadening, SCG [Dudley2010], …) that these processes induce. Besides the general best practices listed in section 2.1, FWM and THG also require that their phase matching conditions are addressed. When the conversion efficiency of FWM or THG is measured, attention needs to be paid as to how the conversion efficiency and bandwidth are defined. For SPM experiments the spectral shape and phase information, i.e., chirp, of the input pulses also need to be known to allow for a correct measurement of the NLO coefficients [Vermeulen2016a]. However, in the case of wideband SCG, the input chirp typically has a negligible impact on the output spectrum and hence does not necessarily have to be known to allow for a correct extraction of the NLO coefficients. Finally, it is important to keep in mind that, besides the material's bound-electronic (Kerr) nonlinearity, other effects can also contribute to its third-order parametric wave mixing response (e.g., free-carrier effects contributing to SPM- and XPM-induced spectral broadening [Vermeulen2018, Zhang2016]).

2.2.2.2. Raman/Brillouin gain measurement techniques

The material intrinsic NLO parameter that most often characterizes stimulated scattering for the Raman/Brillouin processes is the gain coefficient $g_{\text{Raman/Brillouin}}$ (m W^{-1}). In the context of waveguides, the parameter can be expressed as a gain factor $\gamma_{\text{Raman/Brillouin}}$ (m^{-1} W^{-1}). Two classes of measurement methods are distinguishable: (a) direct methods—which rely on the amplification of a Stokes field, and (b) indirect methods—which rely on the determination of the spontaneous scattering cross-section and the dephasing time. Both methods can in principle be applied to all material categories considered in this work. Although most of the literature has focused on the Raman gain coefficient, the considerations often apply analogously to Brillouin scattering. Besides the general best practices listed in section 2.1, we have identified the following best practices specifically for Raman and Brillouin gain measurements:

- Direct methods are based on measuring the threshold for SRS/SBS [Ippen1972, Zverev1999], the threshold of laser action [McQuillan1970] and probing gain in an amplifier [Stappaerts1980, Niklès1997]. In the tables presented further on, these are indicated as 'SRS/SBS threshold', 'Raman/Brillouin laser threshold', and 'SRS/SBS pump-probe', respectively. Major contributors to the measurement uncertainty include the precision of beam sizes and shapes, and the specification of the relative polarization of pump and Stokes (in relation to crystal axes in the case of crystals) and the pulse shape. In cases where the Rayleigh range of the beams are comparable to or shorter than the material length, the variation in beam waist upon propagation through the medium should be factored-in [Boyd1969]. The gain is a function of the pump and Stokes linewidths, decreasing markedly as the widths approach that of the phonon resonance [Georges1991, Agrawal2001, Bonner2014] or, equivalently, as pulse durations approach the T_2 phonon relaxation time [Basiev1999b]. For methods involving co-propagating multi-longitudinal mode beams, correlations between the pump and Stokes irradiances also need to be considered [Stappaerts1980, Sabella2015]. Benchmarking against better known values of other materials [Basiev1999b], or the Kerr nonlinearity [Sabella2015], are valuable ways to increase confidence in the obtained values. For measurements at frequencies approaching the bandgap, a model is needed that includes a description of other nonlinearities occurring in the material (2PA, multiphoton absorption, FCA, …). It should be noted that measurements of the stimulated scattering threshold often use a chosen exponential gain value G in the vicinity of $G = 20$, i.e., it is assumed that for typical spontaneous seeding, an irradiance growth of e^G with $G \sim 20$ leads to a readily observable stimulated scattering signal [Grasyuk1998, Ippen1972]. However, there is no universally accepted value for G which may lead to some variability between reported values. In waveguides, two-color pump-probe techniques have been used to better separate the gain signal from background noise and other complications [Yang2020, Renninger2016].
- The gain coefficient may be determined indirectly by measuring the total cross-section for spontaneous scattering and its peak linewidth (T_2 dephasing time) [Basiev1999a], which are indicated in the tables, by the terms 'SpRS/SpBS cross-section' and 'SpRS, SpBS linewidth'. Absolute measurements of the cross section are rare due to the increased practical difficulties associated with precise photometric measurements; a problem often mitigated by benchmarking against better known materials. It has also been shown that IRS of a probe beam at the anti-Stokes frequency also gives access to absolute values without benchmarking [Schneebeli2013]. For Brillouin scattering, the cross-section may be determined from the photoelastic tensor [Ippen1972]. Determination of the linewidth may be readily achieved using a spectrometer provided that the instrument width is sufficiently small or is adequately deconvolved. The linewidth may also be determined from direct measurements of T_2 by using fast pump–probe optical pulses [Waldermann2008].

2.2.2.3. Third-order polarization rotation

Third-order polarization rotation refers to techniques where the change of polarization of an intense pump beam, or of a probe beam, is monitored to determine the real (or imaginary) part of the nonlinear susceptibility $\chi^{(3)}$, which may also yield the nonlinear refractive index $n_{2,\text{eff}}$ or a nonlinear absorption coefficient, e.g., α_2. Examples are ER measurements [Maker1964, Owyoung1972, Miguez2014], specifically for linearly isotropic materials such as liquids (see section 3.2 on solvents), or Optical Kerr Gating [Duguay1969, McMorrow1988]. If the polarization is changed solely by refractive index changes, this refers to the quadratic Kerr effect. These techniques are most often used for bulk materials, such as isotropic liquids or linearly isotropic or cubic symmetry solids, but can also be applied to other material categories such as fiber materials and on-chip waveguiding materials.

Besides the general best practices listed in section 2.1, third-order polarization rotation measurements also require special attention to precisely knowing the polarization of the source, or sources in the case of pump-probe experiments where knowledge of the relative polarization is also needed. The example of ER is illustrative. In that method for isotropic materials, due to symmetry, there are three unknown susceptibility

elements. The key in an ER experiment is to create an elliptically polarized beam of well-known orientation. This can be done, e.g., by starting with a linearly polarized beam and introducing a quarter-wave plate, and then carefully measuring the transmission of the beam through a polarizer as a function of orientation, both before and after propagation through the NLO medium.

For pump-probe experiments, the optical Kerr gate is a good example. Starting with linearly polarized pump and probe beams with a relative polarization at 45 degrees, the pump induces a birefringence in the nonlinear sample that rotates the transmitted polarization. Monitoring the transmittance of the probe through a polarizer crossed to give zero transmittance without the pump gives a sensitive method for measuring the induced refractive index or absorption changes [Stegeman2012, Duguay1969, McMorrow1988]. Again, careful attention to the polarization is needed in these experiments.

2.2.2.4. Beam distortion/absorption

In beam distortion measurements, one quantifies the spatial variation of the beam due to a NLO process by measuring the power that passes through a fixed reference (e.g., pin-hole) or using a spatially resolved detector (e.g., quad-cell). For beam absorption measurements, one seeks to measure the nonlinearity-dependent power reflected/transmitted (also referred to as 'nonlinear R/T') from the material, with the transmission dependent on both nonlinear absorption and scattering. In either case, it is possible to utilize single-beam or pump-probe style measurements. While more complex, the latter case provides more versatility to explore the temporal, polarization, and angular dependences of the nonlinearity as well as degenerate and non-degenerate spectral dependences.

Beam distortion and absorption refer to techniques such as Z-scan [Sheik-Bahae1989, Sheik-Bahae1990b, Balu2004, de Araújo2016], I-scan [Taheri1996], nonlinear reflection/transmission (loss) [Bloembergen1962, Clays1991, Sutherland2003, Cheng2018, Dong2018, DaSilva-Neto2020], BD [Ferdinandus2013, Ferdinandus2017], and power limiting [Siegman1962, Smirl1975, Soileau1983, Gu2006, Maas2008, Liaros2013, Riggs2000]. Note that the I-scan technique had previously been used before being named as such (see, for example, [Bechtel1976, Van Stryland1985]). As these techniques involve spatial distortion/pointing and/or loss of the beam, they are generally used for the extraction of nonlinear parameters in free space. As a result, bulk materials, 0D–1D–2D materials, and metamaterials are commonly evaluated using these techniques. However, nonlinear loss measurements can also be used in waveguides and fibers, and is common for characterizing, e.g., 2PA and saturable absorption [Sorin1984, Colin1996, Set2004, Jiang2018a].

In addition to the general best practices listed in section 2.1, beam distortion techniques are the simplest to analyze using clean Gaussian beam profiles as this is currently an assumption of many subsequent analysis techniques [Sheik-Bahae1990b, Gu2005] to extract the NLO coefficients; however, by using reference samples of known nonlinearity, such techniques can be calibrated for non-Gaussian beams [Bridges1995]. Furthermore, for thick samples and/or short pulses, it is useful to characterize the pulse chirp to correct for modifications in the temporal response of the nonlinearity due to varying group velocities. We also note that nonlinear beam distortion and loss, when used together, provide a complete methodology for characterizing lossy and/or lossless materials, enabling accurate evaluation of the magnitude, sign, and dispersion of the nonlinear refractive index n_2, $n_{2,\mathrm{eff}}$, α_2, $\alpha_{2,\mathrm{eff}}$, thermal index ($\mathrm{d}n/\mathrm{d}T$ and $\mathrm{d}k/\mathrm{d}T$), etc through the fitting of experimental quantities. With subsequent analysis [DelCoso2004, Christodoulides2010], the complex value and sign of, e.g., a pure $\chi^{(3)}$ can be determined as well. When only one of the techniques is used, the information is often restricted. Beam distortion alone is sometimes sufficient to discern the sign and magnitude of the complex nonlinear index and susceptibility in the case of lossless (or low-loss) materials. However, in the case of very lossy materials ($\mathrm{Im}(\varepsilon) \sim \mathrm{Re}(\varepsilon)$), the terms of the complex susceptibility are inextricably coupled in measurements of both nonlinear losses and NLR. The use of beam distortion (Z-scan or other methods) alone results in an effective coefficient which combines contributions from both nonlinear absorption and refraction [Del Coso2004].

In general, it can be difficult to separate the different contributions using a single methodology (e.g., Z-scan requires both open and closed aperture experiments), although information on the sign of the respective nonlinearities can often be obtained. Beam absorption alone is typically sufficient to discern the sign and magnitude of nonlinear absorption but does not give information on the NLR, although in some cases the sign of the NLR can be predicted [Smith1999] (here negative absorption would correspond to either absorption saturation or gain depending on circumstances). Since both components cannot be individually interpreted, absorption alone also cannot provide complete information on the $\chi^{(3)}$ although it may be possible to discern the sign of the terms. Pump-probe experiments such as BD [Ferdinandus2013] again require simultaneous transmittance and deflection signals to determine both absorptive and refractive components [Ferdinandus2017]. These restrictions can be easily understood by comparing the number of unknowns (NLR and absorption coefficients) for a given material with the constraints (distortion and absorption measurements) imposed by the experimental information. In the case of an under-constrained

problem such as when attempting to extract two coefficients with a single measurement, the sign can be argued based on Kramers–Kronig causality if one knows the underlying mechanism(s) and/or the spectral response of one of the nonlinear terms. Lastly, we reiterate that although in some cases a singular technique is sufficient to obtain information on the nonlinearity of a material, if one assumes a pure $\boldsymbol{\chi}^{(3)}$ process, it is rare for this assumption to be absolutely accurate (e.g., higher-order processes may provide non-negligible contributions). In this scenario, a single measurement will return only an effective nonlinear response, comprising multiple underlying physical mechanisms. Thus, the use of several analysis techniques is highly encouraged. This will provide more data to constrain analysis and elucidate the response of various contributing effects.

2.2.2.5. Nonlinear interferometry

The purpose of NLO interferometry is usually to measure the real part of the nonlinear susceptibility $\chi^{(2,3)}$, but this technique can also be used to measure both the real and imaginary parts by suitable experimental modifications [Chang1965, Sutherland2003]. When using a wavelength of operation at which the NLO material is transparent, the most important part is the non-resonant $\mathrm{Re}(\chi^{(n)})$. In contrast, if we are interested in the enhancement of $\chi^{(n)}$ by resonance effects, information on both $\mathrm{Re}(\chi^{(n)})$ and $\mathrm{Im}(\chi^{(n)})$ spectra is needed. Although dispersion relations similar to the Kramers–Kronig relations hold for NLO coefficients [Sheik-Bahae1990a, Bassani1991, Sheik-Bahae1991, Hutchings1992], it is practically impossible to strictly apply the Kramers–Kronig relations and there are restrictive conditions under which the Kramers–Kronig relations hold in time-resolved spectroscopy [Tokunaga1995]. Thus, direct measurement of the real and imaginary parts is often required. NLO interferometry is most often used for bulk materials, but can be applied to other material categories as well. Although interferometric methods are also modified as heterodyne detection to be employed in SFG [Ostroverkhov2005, Nihonyanagi2013, Wang2017] (otherwise only $|\chi^{(2)}|$ is obtained), most of the targeted nonlinearities measured by NLO interferometry are third-order nonlinearities in a pump-probe setup. In this case, a NLO interferometer is often based on pump, probe (signal), and reference beams. There are multiple interferometric configurations possible. They can be categorized in two-arm types (Michelson, Mach–Zehnder, Sagnac, etc, or two-beam interference) and resonator types (Fabry-Perot, or multiple-beam interference), and hybrids of them, e.g., Laser Interferometer Gravitational-Wave Observatory combining Michelson and Fabry-Perot [Abbott2016]. There are also other classifications such as common path (Sagnac) and non-common path (Michelson) for the two arms, and also beam division methods are specified (space, time, direction, polarization, etc).

In addition to the general best practices outlined in section 2.1, it is important to evaluate the measurement sensitivity of the NLO interferometric method used and to account for a possible surface reflectance change due to changes in both the $\mathrm{Re}(\chi^{(3)})$ and $\mathrm{Im}(\chi^{(3)})$ parts. The bulk NLR can also change the propagation time of pulses. With pulsed lasers, it is convenient to use time division (i.e., in the same sample path, reference, pump, and probe pulses arrive at the sample in that order) and spectral interference [Tokunaga1995, Chen2007]. In addition to time division, common path interferometry such as division by direction [Misawa1995] or by polarization [van Dijk2007] (where the reference and probe share a common optical path) is advantageous for obtaining stable interference, but otherwise active control to stabilize the optical path length is often required [Cotter1989]. In order to cancel instabilities of the laser irradiance, balanced detection can also be employed by dividing the probe beam in two to be detected with an identical detector for subtractive detection [Waclawek2019]. Resonance cavity effects with Fabry-Perot interferometers are also useful for enhancing the NLO effects by increasing the light-matter interaction [Birnbaum2005, Fryett2018, Wang2021].

2.2.2.6. Third-order nonlinear imaging

Third-order nonlinear imaging techniques, most notably THG imaging [Squier1999, Woodward2016, Karvonen2017], can be meaningfully applied to material categories exhibiting spatially varying third-order nonlinear parameters (0D–1D–2D materials, metamaterials, on-chip waveguiding materials, and hybrid waveguiding systems). Third-order nonlinear imaging allows one to characterize the magnitude of $\chi^{(3)}$ along with the conversion efficiency associated with the material and the performed experiments.

While the general best practices listed in section 2.1 also apply for third-order nonlinear imaging, we further stress the importance of carefully characterizing the NLO excitation parameters (the peak power/irradiance/energy, beam size, pulse width and polarization) inside the material. This is particularly important, because optical components such as microscope objective lenses may considerably modify the properties of incident pulses.

2.2.3. Remarks on choice of NLO technique

The technique-specific best practices listed above combined with the general best practices in section 2.1 should form a solid basis to obtain high-quality NLO measurement data and appropriate analysis results.

When selecting a technique for characterizing a given NLO coefficient, it should be noted that for single-wavelength experiments only a specific frequency component of this nonlinearity will be revealed. For example, when applying both THG and SPM with pump frequency ω to characterize the $\chi^{(3)}$ of a given material, THG will yield $\chi^{(3)}$ ($3\,\omega$: ω, ω, ω) whereas SPM will provide information about $\chi^{(3)}$ (ω: $-\omega$, ω, ω) plus permutations [Bloembergen1996, Shen2002, Sutherland2003, Stegeman2012, Boyd2020]. This underlines the importance of including the technique used in each entry of the data tables presented below. And, as we have previously stated, it is highly desirable to use multiple techniques and/or multiple wavelengths and/or multiple pulse widths etc, as this both helps to distinguish different nonlinearities (with perhaps multiple being present simultaneously) and yields more physical insight into the NLO response(s) of the material under study.

3. Data tables and discussion

After having listed the most common NLO technique families and their best practices, we present here the actual data tables for bulk materials, 0D–1D–2D materials, metamaterials, fiber waveguiding materials, on-chip waveguiding materials, and hybrid waveguiding systems. The tables contain NLO data of representative experimental papers published since 2000 that we selected after verifying both the general best practices and the best practices specifically for the NLO techniques used in these works. In some cases, publications missing just one important parameter as specified in the best practices could not be included, although they seemed technically sound. The NLO coefficients that we searched for in the literature since 2000 are: $\chi^{(2)}$, d_{eff}, $\chi^{(3)}$, $n_{2,\text{eff}}$, γ_{eff}, α_2, α_3, I_{sat}, g_{Raman}, and $g_{\text{Brillouin}}$. We particularly looked for works that provide the most extensive NLO information, such as the dependence of the NLO coefficients on wavelength, on pulse duration, on doping level, on material composition, etc. For some recently developed materials in the data tables such extensive studies are yet to be performed; in those cases we selected papers that provide at least some quantitative NLO information, e.g., a single NLO coefficient and/or conversion efficiency, while complying with all (or almost all) the best practices. Note that no hyperpolarizabilities have been listed in the tables as these are typically only characterized at the molecular level, and that all the considered nonlinearities are of the second or third order, except for the 3PA coefficient α_3. However, nonlinearities from, e.g., 2PA-induced free carriers, appear as effective fifth-order nonlinearities and may possibly contribute to some values reported in the literature. Note also that we have not included photorefractive effects, electro-optic effects, stimulated polariton scattering, nor cascaded second-order nonlinearities. The latter can very closely mimic bound-electronic nonlinearities but require propagation [DeSalvo1992, Torruellas1995, Stegeman1996]. These can sometimes be difficult to separate from other NLO responses. It is also important to keep in mind that some nonlinearities cannot properly be classified as either second or third order. As an example, we cite absorption saturation which in principle contains all orders of nonlinearities; however, it is often discussed as third order since at the lowest inputs it behaves that way. Furthermore, for several NLO coefficients the 'effective' values are often reported in the literature. When taking the example of the nonlinear index n_2, strictly speaking it originates only from the Kerr-nonlinear response of bound electrons in the material, but in practice the measured value can also comprise the nonlinear response from free electrons, electrostriction, thermal effects, etc so that the terminology of an 'effective' nonlinear index $n_{2,\text{eff}}$ is more appropriate [Christodoulides2010, Buckland1996]. Also, some $\chi^{(3)}$ values in the literature are in fact 'effective' $\chi^{(3)}$ values containing multiple nonlinearity contributions rather than just the bound-electronic contribution. Finally, we point out that, besides tabulating NLO coefficients, the tables also contain NLO conversion efficiencies and bandwidths specified in works based on, e.g., SHG, THG or FWM. This way we also pay attention to those materials for which the NLO coefficients were reported before 2000 but that witnessed strong progress after 2000 in terms of attainable conversion efficiencies and bandwidths.

The general approach used for filling out the data tables has been to have a single entry per paper. For example, for a paper where the wavelength dependence of a given material nonlinearity is reported, there is typically only a single table entry, specifying a prominent nonlinearity value (in many cases the highest value) and the corresponding wavelength, but with a special annotation in this entry that shows the paper also contains information on the wavelength dependence. Note that a paper reporting on multiple materials is documented in the table with multiple entries, i.e., one entry per material. Another general policy has been to include only those parameter values that are explicitly specified in the paper. In other words, conversions from one physical quantity to another have been avoided to rule out calculation errors from our side. As such, when for a given entry in the tables there is no value for, e.g., pump peak power or irradiance, the paper under consideration might have specified the pump excitation in terms of fluence or average power rather than peak power or irradiance.

The data tables in the following subsections (sections 3.1–3.8) are presented per material category (bulk materials, solvents, 0D–1D–2D materials, metamaterials, fiber waveguiding materials, on-chip waveguiding

materials, and hybrid waveguiding systems) and include those parameters that are most important for the material category under consideration. The entries in these tables present NLO data at optical excitation wavelengths, and some of the tabulated works report on THz generation through, e.g., DFG of two optical excitation beams. However, for those papers where THz radiation was used as the excitation source, we added a dedicated THz table[19] at the end of the manuscript (see section 3.8). The different data tables are accompanied by an introductory text addressing relevant background information prior to 2000, followed by a discussion of the general trends seen in the data tables (e.g., how the new post-2000 data represent an advancement) and some recommendations for future NLO research. Each of the subsections (sections 3.1–3.8) starts with the names of the contributing co-authors in alphabetical order ('team') and the team leader.

We would like to emphasize again that it has not been our goal to include a comprehensive overview of papers but rather a representative set of works in these data tables. The current version of the tables contains papers with a publication date up to May 2021. Also, we point out that the existing literature already provides very valuable review papers that give an overview of NLO works for a specific material or material category, with a detailed discussion of the underlying physics. We refer to several of these recent review papers in the introductory texts and discussions below.

3.1. Bulk materials: data table and discussion

Team: *Adam Ball, Philippe Boucaud, Georges Boudebs, Ksenia Dolgaleva, Daniel Espinosa, Anderson Gomes,* ***Nathaniel Kinsey (team leader)****, Rich Mildren, Ray Secondo, Eiji Tokunaga, Eric Van Stryland*

3.1.1. Introduction

3.1.1.1. Bulk materials and their NLO applications

The bulk materials category is a highly diverse segment that presents NLO data on macroscopic 3D-material samples (ranging from thin films of ∼100 nm thickness to crystalline material samples on the scale of cm's), where material structuring (see metamaterials category in section 3.4) and quantum size effects (see 0D–1D–2D materials category in section 3.3) are not important. The properties of bulk materials are typically measured using free-space diffracting beams (usually one or two-beam experiments). Most experiments are performed with sample lengths less than the diffraction length (Rayleigh range) to allow for simple analysis.

Many bulk materials themselves are key for applications including frequency synthesis, stimulated scattering, ultrafast pulse characterization, and lasers. In addition, bulk materials generally serve as a starting point for the investigation of new materials before they are integrated into devices for applications across fields such as optoelectronics and fiber optics including uses in sensing, optical communications, and fiber lasers, as well as other types of active fibers and integrated photonics technology.

The listed materials, which include high-purity as well as impurity-doped materials, have been grouped into three sub-categories of insulators, semiconductors, and conductors. Within these groups, we focus our efforts on the development of inorganic materials only. Solvents are included in a separate section of this article (see section 3.2), and we also draw attention to section 3.8 on the characterization of material nonlinearities in the THz regime, many of which are bulk materials. These works have been separated to account for their unique considerations and in view of the rising area of THz NLO. However, works which utilize optical beams to generate THz waves remain in this section.

In keeping with this article's focus on post-2000 developments, the listed NLO materials emphasize those featured in research since 2000 but is not all-inclusive, giving priority to those publications that contain the most experimental information (see best practices in section 2).

3.1.1.2. Background prior to 2000

3.1.1.2.1. Background for insulators/dielectrics

When the laser was invented in 1960 EO crystals were already in use. Nevertheless, the terminology of 'nonlinear optics' was not typically employed in this context. The first use of dielectrics for NLO is considered to be the wavelength conversion experiment in the seminal work of [Franken1961]. Some of the most important NLO materials are insulating crystals such as lithium niobate [Midwinter1968, Schaufele1966, Smith1965], beta-barium borate [Chen1987], and potassium titanyl phosphate [Bierlein1989], to name a few. Works from the earliest days of NLO have demonstrated efficient nonlinear

[19] The focus of the THz table is on the intrinsic THz NLO properties of various materials. It is useful to note that active electronic devices, such as Schottky diodes, high electron mobility transistors, resonant tunneling diodes, etc can also generate (sub-)THz radiation when paired with appropriate in- and out-coupling structures. However, due to the fundamentally different nonlinear mechanisms of these devices, they are not included in this manuscript.

actions accompanied by well-developed theories of nonlinear light-matter interaction and crystal optics [Boyd2020, Stegeman2012, Sutherland2003]. Thus, these nonlinear crystals have been key enablers for many past and current technologies including harmonic generators, OPO/OPG/OPA, optical modulators and switches making use of numerous second- and third-order nonlinear phenomena such as the Pockels effect, parametric mixing, and Raman scattering. In addition, efforts worked to improve the efficiency limits of phase matching by introducing periodically poled crystals with QPM [Lim1989, Myers1997, Wang1999]. In this regard lithium niobate is by far the most developed. Of course, much work went into the study of glasses as well. For example, the laser fusion program developed low nonlinear index glasses to prevent optical damage from catastrophic self-focusing in laser host glasses as well as other glass optical elements [Agrawal2013, Tollefson2021]. Another interesting development was the measurement of third-order effects in popular second-order NLO crystals [Sheik-Bahae1997a] using Kerr lens autocorrelation [Sheik-Bahae1997b]. While third-order nonlinearities are generally masked by second-order processes, and thus might be neglected, certain applications can be limited by third-order effects such as self-focusing within the nonlinear crystal. Thus, understanding and correcting for these higher-order nonlinearities is a key feature for high-power applications or scenarios requiring especially large crystals.

Another key advance occurred during the late 1960s to 1970s with the invention of the laser diode, and the development of optical fibers. Together these opened new avenues to pursue all-optical devices aimed at applications in communications [Willner2019], and motivated studies of the nonlinearities in fused silica and other optical glasses [Agrawal2013]. Despite the small nonlinearity of silica-based glasses, the low propagation loss in fused silica fibers provided a platform to explore various nonlinear phenomena with appreciable efficiency including pulse compression [Dietel1983, Palfrey1985], temporal soliton propagation [Agrawal2013, Boyd2020, Stegeman2012], and all-optical switching [Agrawal2013, Boyd2020, Mollenauer1980, Stegeman2012] that have led to applications in fiber lasers [Ter-Mikirtychev2014] and communication systems [Willner2019] (see fiber waveguiding materials category in section 3.5 for more information). Similarly, efforts also focused on increasing the typically weak nonlinearity of glasses by employing doped glasses [Alekseev1980, Ekimov1988, Kityk2002], photorefractive glasses [Hall1985] (not included in the table), and more recently ChGs [Asobe1997]. Models to describe the nonlinearities in these dielectrics also evolved alongside experimental studies [Agrawal2013, Boyd2020, Stegeman2012]. The linear dispersion can be used in a semi-empirical way to predict nonlinear index changes in low-loss optical glasses. This so-called 'BGO' model, named after Boling, Glass and Owyoung [Boling1978] was found to be valid to estimate n_2 of many glasses. This includes ChGs [Fedus2010] despite the presence of NLA. It was also noted that for dielectrics, the bandgap determines the NLA spectrum as well as the dispersion of the NLR [DeSalvo1996, Sheik-Bahae1990a, Sheik-Bahae1991]. Thus, the BGO model and bandgap scaling are complementary.

3.1.1.2.2. Background for semiconductors

Bulk semiconductors from groups II–VI, III–V, or IV, like ZnSe, GaAs, or Si, respectively, have been a mainstay in NLO since the invention of the laser. While the study of such materials in their bulk form has been a key starting point for the study of new semiconductors, structuring and combining semiconductors in novel ways has continually ignited many unique and important technologies such as detectors, lasers, and amplifiers. Much of this research excitement in semiconductors originated from the near-gap resonant nonlinearities which produced large NLO responses, with potential application in all-optical switching, all-optical computing, etc, albeit with limited bandwidth and recovery times [Hardy2007, Miller2010]. Applications involving resonant nonlinearities have included semiconductor optical amplifiers [Olsson1989, Urquhart2011], laser diodes [Bhattacharya1997], and more recently the generation of broadband infrared and THz waves [Krotkus2010, Shan2004]. Additionally, the introduction of quantum well structures provided large second-order nonlinearities, able to be engineered by altering the layer stack [Schmitt-Rink1989] (see the 0D–1D–2D materials category in section 3.3 for more information). Such approaches have led to several useful technologies including SESAMs [Jung1997, Keller1996, Kim1989], which have directly enabled ultrashort mode locked laser technologies, and SEEDs [Miller1989]. Theoretical descriptions for the response of resonant nonlinearities in semiconductors evolved similarly, encompassing effects such as band-filling, saturation, bandgap renormalization, and exciton resonance [Garmire1998].

Similarly, below-gap non-resonant nonlinearities including harmonic generation, and wave mixing were also studied [Boyd2020, Stegeman2012], and while they provide nearly an instantaneous response, these were noted as being weaker than their resonant counterparts and challenging to phase match due to the limited anisotropy of many semiconductors. Through fabrication advances, these challenges were addressed via the use of QPM approaches [Armstrong1962, Gordon1993, Thompson1976, Hum2007]. Another key advance in semiconductor nonlinearities came from a unified model of the nonlinear refractive index. In the case of direct bandgap semiconductors in their transparency range, they were understood in terms of

nonlinear Kramers–Kronig relations [Hutchings1992, Sheik-Bahae1991] as a consequence of the NLA mechanisms of 2PA, Raman, and AC-Stark effects. Through this, it was noted that as the incident photon energy moves from resonant linear absorption saturation near the bottom of the conduction band to a non-resonant transition, the nonlinearity smoothly transitions from real saturation to 'virtual' saturation otherwise known as the AC-Stark effect. Scaling rules and nonlinear dispersion relations based on the material bandgap were subsequently developed which supplied theoretical models to predict NLO coefficients, and to analyze the variety of reported NLO data [Hutchings1992, Sheik-Bahae1990a, Sheik-Bahae1991, Wherrett1984]. Since 2000, Dinu's [Dinu2003a] and Garcia's [Garcia2012] models have been widely used for similar descriptions of indirect bandgap semiconductors.

3.1.1.2.3. Background for conductors

Nonlinearities in metals and conducting materials have been studied for nearly as long as NLO with early works examining harmonic generation in thin films [Bloembergen1968, Bloembergen1969, Sipe1980] as well as in percolated or random films [Shalaev1998]. The majority of research focused on elemental metals such as Au [Sun1994], Ag [Bloembergen1968], Cu [Elsayed-Ali1987], etc, and was closely tied with the fields of transient thermoreflectance to measure the thermal properties of metals [Brorson1990, Hohlfeld2000]. While bulk metals have exhibited large nonlinearities, they have not led to many applications in large part due to their high loss and propensity to be damaged under the high irradiances needed for NLO. One key exception to this has been surface enhanced nonlinearities, useful for achieving large improvement in processes such as Raman scattering [Wang2020b]. Yet due to their limitations, the study of bulk metals was largely relegated to fundamental measurements and understanding of various light-induced effects such as so-called 'Fermi-smearing', interband transitions, and free-electron photoionization [Allen1987, Anisimov1974]. More recently, metals are finding great interest in areas including plasmonics [Maier2007, Maradudin2014], metamaterials and nanoparticles embedded in dielectrics [Cai2009] (see metamaterials category in section 3.4), as well as in the closely related area of ENZ effects [Liberal2017, Reshef2019] (see section 3.1.2.1.2).

3.1.1.3. Considerations for bulk materials when performing NLO measurements

For solid materials, attention should be paid to thermal effects when using high-repetition-rate lasers or with materials showing linear absorption. Thermal effects may build up collectively over many pulses or arise within the pulse width depending upon the loss of the material. As a result, one must clearly identify the different roles of thermal and non-thermal nonlinearities [Bautista2021, Falconieri1999]. Also, the role of the pulse duration is very important in determining the origin of the nonlinearity being exploited [Christodoulides2010, De Araújo2016] and should be considered accordingly. Additionally, in many cases, bulk materials are explored as thin films grown on substrates. In this scenario, researchers should carefully characterize and remove the response of the substrate. Works should contain a detailed description of how the substrate contribution was removed as well as a report of the substrate-only response for comparison. In addition to these specific considerations for bulk materials, also the best practices described in section 2 should be taken into account when performing NLO measurements.

3.1.1.4. Description of general table outline

Tables 2A and B show a representative list of, respectively, the second- and third-order NLO properties reported since 2000 for our range of bulk materials, across our three subcategories. The works included in tables 2A and B were selected based upon the best practices in section 2 and the considerations outlined above. Table 2B lists, besides third-order nonlinearities, also 3PA coefficients. Each entry in the tables contains information about the material and its properties, linear optical properties, NLO technique used, the excitation parameters, and the resulting NLO parameter(s).

The entries are arranged in alphabetical order, and within each material, entries are ordered by NLO technique (referred to as 'Method' in the tables). The works that report dispersive datasets or dependences of the NLO parameter on multiple parameters (e.g., thickness, doping, composition, etc) are denoted by '[a b]' respectively, in the Tables. The papers included in the Tables nominally report data obtained at room temperature, unless denoted otherwise by '[c]'. The works reporting different compositions or material variations are split into different entries where applicable. For papers with multiple thicknesses of the same material, the thickest material is reported. The data is sub-divided into 'Material properties', 'Measurement details', and 'Nonlinear properties'. Measurements using two beams have the properties of the pump and probe beam listed separately, where provided, while single beam measurements are contained within the pump column. Units are contained within the table unless noted in the header. Within each column the information is given in the order of the header description. If dispersive values for the NLO parameter were

provided, the cited value represents the peak value for the material within the stated measurement range. For works that report tensor components, the component is shown as a leading number followed by a colon and the value (e.g., $\chi^{(2)}{}_{15} = 1 \times 10^{-12}$ (m V^{-1}) → 15: 1×10^{-12} (m V^{-1})). Indices are shown as listed in the original paper. Lastly, some papers relied on non-standard NLO measurement techniques (e.g., method listed as 'Other') or have notes associated with their measurement/analysis (e.g., identifying the definition used for the conversion efficiency η). These values and information are listed within the 'Comments' column with the value and unit identified.

3.1.2. Discussion

3.1.2.1. Advancement since 2000 and remaining challenges

3.1.2.1.1. Advancement and challenges for insulators/dielectrics

Dielectrics are one of the most well-developed and well-understood NLO material platforms. While several works have continued to refine the understanding of nonlinearities in dielectrics such as fused silica (see section 1.1) and sapphire [Nikolakakos2004] due to their use as reference materials, after 2000 most of the advancement has been focused on applications, providing new devices and enhancing performance of existing methods, including pushing the efficiency of cascaded NLO processes (not included in tables). While new material research is still ongoing, it has been more focused. In particular, advance in IR NLO materials such as ChGs, pnictide, and oxides has been realized, driven by emerging lasers, spectroscopy, sensing, and imaging applications in the mid- to far-IR. Among them, ChGs have received attention due to their ability to be integrated with optical fiber [Dudley2009, Knight2003]. When doped with rare earth elements such as Er, Nd, Pr, etc or undoped, many applications of active and passive optical devices have been proposed [Mairaj2002, Sanghera2009, Ta'eed2005, Yan2016]. The high optical nonlinearities of these glasses have been studied over a wide range of wavelengths to optimize their compositions for applications related to all-optical switching or optical limiting [Chen2020, Cherukulappurath2004, Ensley2019, Fedus2010, Petit2009]. Furthermore, experiments have been made on mid-IR SCG by pumping bulk or fiber ChG with fs pulses [Gattass2012, Granzow2011, Marandi2012, Møller2015, Petersen2018, Yu2013, Yu2014]. Similar advances in bulk form have been realized for cm-scale materials such as $CdSiP_2$ and lead oxyhalides, wherein lead oxides demonstrate both high transparency and strong SHG [Abudurusuli2021].

We also note the continued expansion of organic and organic-crystal materials for NLO applications from the mid-1990s and well into the 2000s [Bosshard2020, Nalwa1997]. While our effort here focuses on the development of inorganic materials, advances in organic nonlinearities have nonetheless constituted a major effort since 2000. For more information we direct the reader to reviews on organic NLO [Wang2012, Yesodha2004].

3.1.2.1.2. Advancement and challenges for semiconductors

Major advancements in semiconductor nonlinearities have been made largely due to improved fabrication and characterization methods. New measurements were completed on many semiconductors, such as Si, diamond, GaN, AlN, GaAs, GaP, InN, and InSb over a wide range of wavelengths, and compared to existing models of the NLR and NLA coefficients, leading to better understanding of the 3rd-order NLO coefficient's spectral behavior [Almeida2019, Bristow2007, Chen2017b, Fishman2011, Hurlbut2007, Lin2007, Oishi2018a, Oishi2018b, Olszak2010, Wang2013]. A unifying theory of 3PA has also been reported and compared to Wherrett's scaling model for most binary II–VI and III–V semiconductors [Wherrett1984, Benis2020].

Due to these advances in fabrication and characterization, new potential applications of semiconductors have begun to emerge. For example, QPM techniques in OP GaAs and GaP have surpassed the strict constraint of birefringent phase-matching to produce efficient SHG, DFG, OPO, and OPG. As a result, a wide range of IR (wavelengths from 2500 nm to 14 200 nm) [Feaver2013, Kuo2006, O'Donnell2019, Smolski2018, Vodopyanov2014] and THz (from 0.4 THz to 4.5 THz) frequencies [Kiessling2013, Schaar2008] can be generated.

Spurred by parallel advancements in plasmonics and metamaterials, in the last 5 years, another key area of advancement has been in the study of semiconductors that exhibit ENZ or NZI properties [Kinsey2019, Liberal2017, Reshef2019] occurring from either free-electrons or phononic resonances (see also the metamaterials category in section 3.4). Although optically lossy, which must be carefully considered for its impact upon applications, homogeneous ENZ materials have demonstrated extraordinarily large index modification ($\Delta n \sim 0.5$–1) [Alam2016, Benis2019, Caspani2016, Clerici2017, Kinsey2015a], enhanced harmonic generation [Capretti2015a, Capretti2015], negative refraction [Bruno2020], optically defined

surfaces [Saha2020], and recently temporal interfaces and interactions such as frequency shifting [Khurgin2020, Shaltout2016, Zhou2020b]. While initial works demonstrated effects through experimental efforts, more recently theory has followed to provide a deterministic and predictive explanation of nonlinearities in popular ENZ materials [Khurgin2021, Secondo2020, Solís2021]. Currently, efforts have focused on the exploration of doped oxides such as Dy:CdO, Al:ZnO, and Sn:InO in the near-IR (∼1300–1600 nm) but undoubtedly other materials will be explored in the future expanding into the mid- and far-IR spectral ranges.

3.1.2.1.3. Advancement and challenges for conductors

Since 2000, the growth of NLO research in plasmonics, metamaterials, metal nanoparticles, and nanophotonics [Maier2007, Maradudin2014] has brought a renewed interest in the study of nonlinearities in bulk metals and conducting materials [Kauranen2012]. The ability to nanostructure metals with ultra-tight light confinement has led to studies that make use of the inherent metal nonlinearity [MacDonald2009, Mayer2011, Mesch2016] as well as for enhancing the NLO response of an external material [Lee2014]. One key application has been in the enhancement of Raman interactions for sensing and material study [Jiang2010]. This has been the primary advance in the study, application, and understanding of metals in NLO since 2000 (see metamaterials category in section 3.4 for more information). Ignited by materials exploration within the field of plasmonics, another advancement in conductors was the expansion of studied materials for optical applications, with many heavily doped semiconductors, conducting ceramics, and alloys being investigated [Saha2020]. These compound metallic materials provided additional benefits such as robustness, tunability of the NLO response, and new potential applications in sensing [Golubev2018, Robert2016] while exhibiting similar NLO responses to previously explored materials.

Similarly, the rise of topological materials and topological photonics has also affected NLO in the 21st century. While the area is closely linked to low dimensional materials (see 0D–1D–2D materials category in section 3.3), some multilayer or bulk variants have also been studied. In particular, large second-order NLO effects have been reported in Weyl semimetals such as TaAs, TaP, and NbAs [Osterhoudt2019, Patankar2018, Wu2017, Yan2017], as well as enhanced surface nonlinearities in Dirac nodal-line ZrSiS semi-metals [Chi2020].

While the losses that occur in conducting materials and their propensity for damage remain a primary concern for the broad adoption of bulk conductors in NLO applications, the expansion of available materials combined with new physical understanding and physics may provide the ingredients for metals to make a contribution to the NLO field. Regardless, they remain key supporting materials for various fields of photonics, and understanding their inherent nonlinearities remains an important task for the field of NLO.

3.1.2.2. Recommendations for future works on bulk materials

As lasers and various methods of measurement continue to advance, our ability to characterize materials evolves in parallel. Systems with several tunable excitation beams, supercontinuum probes, variable repetition rates, etc are expanding characterization capabilities and allowing more flexibility, which before 2000 was difficult to put into practice. We encourage future NLO works to embrace these new capabilities, exploring characterization and datasets which include more than just single wavelengths and pulse widths. Among various parameters, temporal and spectral information are perhaps the most useful information to be added for bulk materials, although this depends upon the application area of the material. In addition, the more thorough characterization will support an improved understanding of the NLO interactions at play, helping to delineate the roles of unwanted effects such as thermal nonlinearities and nonlinear scattering, and improving the reliability of results.

Another area of recommendation for the community is in the reporting of key experimental metrics. In many cases, papers are missing certain parameters of the experiment (peak/average power, beam waist, repetition rate, pulse width, etc, see tables) or do not report the method for calculation (flat top, Gaussian, full-width-half-max, etc). This can lead to difficulty when interpreting the results as well as invoke questions as to the experimental rigor. By meticulously reporting the metrics of experiments, we can improve the trust in the results, aid in reproducibility, and help to avoid errors.

Lastly, the new millennium has seen an explosion in new materials available for study. In many cases, it can be observed that works jump directly to the demonstration of example applications without performing rigorous characterization of the material's NLO response. While such studies are useful, we remind the community that carefully conducted experiments and reporting of inherent NLO coefficients ($\chi^{(2,3)}$, n_2, g_{Raman}, etc) is of key importance to the field as new materials and applications continue to be explored.

3.1.3. Data table for bulk materials

Table 2A. Second-order NLO properties of bulk materials from representative works since 2000. Legend for superscripts: see below the table.

Second-Order Nonlinearities										
		Material Properties			Measurement Details		Nonlinear Properties			
					Pump	**Probe**				
Material	Method	Thickness Fabrication Substrate	Index Abs. coeff. Wavelength	Crystallinity Bandgap Doping level	Wavelength Peak power or irradiance Pulse width Rep. rate	Wavelength Peak power or irradiance Pulse width	$\chi^{(2)}$ (m V^{-1})[d]	d (m V^{-1})[d]	η (%)[d, e]	Comments Reference
Conductors										
NbAs[a]	SHG	— Vapor transport — —	— 5 μm^{-1} 800 nm	Monocrys. — —	800 nm — 100 fs —	— — —	—	33: 2.7 ± 10^{-9}	—	— [Wu2017]
TaAs[a]	SHG	— Vapor transport — —	— 5 μm^{-1} —	Monocrys. — —	800–2500 nm — 50 fs —	— — —	—	—	—	Nonlinear conductivity $\sigma = 5 \pm 10^{-3}$ (Ω-V)$^{-1}$ [Patankar2018]
TaAs[a, c]	SHG	— Vapor transport — —	— 5 μm^{-1} 800 nm	Monocrys. — —	800 nm — 100 fs —	— — —	—	33: 3.6 ± 10^{-9}	—	— [Wu2017]
TaAs	Other (see comments)	— Chemical vapor transport —	— — —	Monocrys. — $N_e = 8.08 \pm 10^{+23}$ $N_h = 9.35 \pm 10^{+23}$ m^{-3}	10 600 nm — CW —	— — —	—	—	—	Method: Bulk Photovoltaic Effect Nonlinear conductivity $\sigma_{aac} = 154 \sim 17$ μA V^{-2} [Osterhoudt2019]

(Continued.)

Table 2A. (Continued.)

Second-Order Nonlinearities											
		Material Properties			Measurement Details		Nonlinear Properties				
Material	Method	Thickness Fabrication Substrate	Index Abs. coeff. Wavelength	Crystallinity Bandgap Doping level	**Pump** Wavelength Peak power or irradiance Pulse width Rep. rate	**Probe** Wavelength Peak power or irradiance Pulse width	$\chi^{(2)}$ (m V^{-1})[d]	d (m V^{-1})[d]	η (%)[d, e]	Comments Reference
TaP[a]	SHG	— Vapor transport — —	— 5 μm^{-1} 800 nm	Monocrys. — —	800 nm — 100 fs —	— — —		33: 3.2 ± 10^{-9}	—	— [Wu2017]
ZrSiS	SHG	— Chemical vapor transport —	— — —	Monocrys. — —	1300 nm 7.6 MW m^{-2} 120 fs 1 kHz	— — —	4.78 ± 10^{-9}	—	0.011	— [Chi2020]
Semiconductors											
$Al_{0.08}Ga_{0.92}N$ [b]	SHG	980 nm MOCVD (0001) c-Sapphire	— — —	Monocrys. — —	1064 nm — 5 ns 14 Hz	— — —	—	31: 1.45 ± 10^{-12} 15: 1.45 ± 10^{-12} 33: 2.9 ± 10^{-12}	—	— [Passeri2004]
$Al_{0.5}Ga_{0.5}N$	SHG	63 nm MOCVD (0001) c-Sapphire	— — —	Monocrys. — —	1064 nm — 5 ns 13 Hz	— — —	—	33: 1.20 ± 10^{-12}	—	— [Larciprete2006]
$Al_xGa_{1-x}N$ [b]	SHG	2.13 μm MOCVD and HVPE (0001) c-Sapphire	— — —	Monocrys. — —	1064 nm — — 82 MHz	— — —	31: 5.3 ± 10^{-12} 33: 7.4 ± 10^{-12}	—	—	— [Sanford2005]

AlN	SHG	340 nm MBE Sapphire	— — —	Monocrys. — —	800 nm 360 kW 7 fs 80 MHz	— — —	—	3.22 ± 10^{-12}	—	— [Kobayashi2007]
AlN [b]	SHG	620 μm PVT —	— 60 m^{-1} 1030 nm	Monocrys. — —	1030 nm 2.2 TW m^{-2} 10 ns 1 kHz	— — —	—	31: 9.55 ± 10^{-14} — 33: 4.3 ± 10^{-12}	—	— [Majkić2017]
DB-GaAs[a]	DFG	5.05 mm — —	— — —	— — —	2100–2130 nm — 6 ps 50 MHz	2130–2160 nm — —	—	—	0.012 1.2	Optical-to-THz Conversion Eff. Quantum Eff. DFG was also performed in OC-GaAs and OP-GaAs samples. [Schaar2008]
PI-GaAs	DFG	653 μm — —	— — —	— — —	2119.6 nm — 4.6 ns 24 kHz	2138.4 nm — 4.6 ns	—	—	4.31 ± 10^{-5} 0.0103	DFG Conversion Eff. Quantum Eff. [Mei2016]
OP-GaAs	DFG	1.8 mm — —	— — —	— — —	1053 nm — 17 ns 2 kHz	— — —	—	—	0.6 4.2	DFG Energy/Pump Energy Quantum Conversion Eff. [Boyko2018]
GaAs [b]	SHG	— — —	— — —	Monocrys. 1.42 eV —	852 nm — 14 ps —	— — —	7.50 ± 10^{-10}	—	—	— [Bergfeld2003]

(Continued.)

Table 2A. (Continued.)

Second-Order Nonlinearities										
		Material Properties			Measurement Details		Nonlinear Properties			
Material	Method	Thickness Fabrication Substrate	Index Abs. coeff. Wavelength	Crystallinity Bandgap Doping level	**Pump** Wavelength Peak power or irradiance Pulse width Rep. rate	**Probe** Wavelength Peak power or irradiance Pulse width	$\chi^{(2)}$ (m V^{-1})[d]	d (m V^{-1})[d]	η (%)[d, e]	Comments Reference
OP-GaAs	SHG	500 μm MBE and HVPE —	— 8 m^{-1} 4135 nm	— — —	4135 nm — 63 ns 25 Hz	— — —	—	1.09 ± 10^{-10}	33	— [Skauli2002]
OP-GaAs [b]	Other (see comments)	1 mm — —	— — —	— — —	1952 nm — 46 ps 1 MHz	— — —	—	—	22.5	Method: Optical parametric generation OPA Power Conversion Eff. [Fu2018]
OP-GaAs [b]	Other (see comments)	1 mm — —	— — —	— — —	1992 nm 150 GW m^{-2} 95 ps 100 MHz	— — —	—	—	32.6	Method: Optical Parametric Oscillation [Fu2020b]
DB-GaAs [b]	Other (see comments)	— MBE and HVPE —	3.33 — 4400 nm	— — —	4400 nm 100 TW m^{-2} 100 fs 1 kHz	— — —	—	—	0.087 3.3	Method: Optical Rectification Internal Optical-to-THz Conversion Eff. Internal Photon Conversion Eff. [Vodopyanov2006]

OP-GaAs	Other (see comments)	500 μm MBE and HVPE —	— — —	— — —	3250 nm — 1 ps —	— — —	—	—	51 15	Method: Optical parametric generation Slope Eff. External Conversion Eff. [Kuo2006]
OP-GaAs	Other (see comments)	400 μm MBE and HVPE —	— — —	— — —	1980 nm — 120 fs 100 MHz	— — —	—	—	1.60 ± 10^{-4} 4.70 ± 10^{-4}	Method: Parametric down conversion Optical-to-THz Conversion Eff. Internal Optical-to-THz Conversion Eff. [Imeshev2006]
OP-GaAs	Other (see comments)	250 μm — —	3.01 — 4200 nm	— — —	1000 nm — 70 fs 250 MHz	— — —	—	—	25	Method: Half-Harmonic Generation Slope Conversion Eff. [Sorokin2018]
GaN [b]	SHG	229.67 μm MOCVD and HVPE Free-standing	— — —	Monocrys. — —	1064 nm — — 82 MHz	— — —	31: 5.7 ± 10^{-12} 33: 9.2 ± 10^{-12}	—	—	— [Sanford2005]
GaN [b]	SHG	4.2 μm — Sapphire	2.2978 — 1064 nm	Monocrys. — —	1064 nm — 10 ns 10 Hz	— — —	zxx: 15.3 ± 10^{-12} xzx: 14.8 ± 10^{-12} zzz: 30.3 ± 10^{-12}	—	—	— [Fujita2000]
GaN	SHG	3.5 μm MBE (0001) c-Sapphire	— — —	— — —	1980 nm — 6 ns 30 Hz	— — —	2.80 ± 10^{-11}	—	—	— [Nevou2006]

(Continued.)

Table 2A. (Continued.)

Second-Order Nonlinearities											
		Material Properties			Measurement Details		Nonlinear Properties				
Material	Method	Thickness Fabrication Substrate	Index Abs. coeff. Wavelength	Crystallinity Bandgap Doping level	**Pump** Wavelength Peak power or irradiance Pulse width Rep. rate	**Probe** Wavelength Peak power or irradiance Pulse width	$\chi^{(2)}$ (m V^{-1})[d]	d (m V^{-1})[d]	η (%)[d, e]	Comments Reference
GaN	SHG	2 μm MOCVD (0001) c-Sapphire	— — —	Monocrys. 3.42 eV —	1064 nm — 5 ns 14 Hz	— — —	—	31: 2.4 ± 10^{-12} 15: 1.8 ± 10^{-12} 33: 3.7 ± 10^{-12}	—	— [Passeri2004]
GaN	SHG	302 nm MOCVD (0001) c-Sapphire	— — —	Monocrys. 3.42 eV —	1064 nm — 5 ns 13 Hz	— — —	—	33: 4.82 ± 10^{-12}	—	— [Larciprete2006]
GaN	SHG	340 nm MBE Sapphire	— — —	Monocrys. — —	800 nm 360 kW 7 fs 80 MHz	— — —	—	1.59 ± 10^{-11}	—	— [Kobayashi2007]
GaN	SHG	1 μm MOCVD (0001) c-Sapphire	2.29 — 1064 nm	Monocrys. 3.4 eV —	1064 nm — 7 ns 10 Hz	— — —	—	31: 5.45 ± 10^{-12} 33: 1.107 ± 10^{-11} 15: 5.48 ± 10^{-12}	—	— [Kravetsky2000]
GaN	SHG Imaging	2.5 μm — —	— — —	— — —	1230 nm — 150 fs 125 MHz	— — —	3.00 ± 10^{-12}	—	—	— [Sun2000]
ITO[a]	SHG	37 nm Sputtering Silicon	— — —	— — —	1100 nm 420 GW m^{-2} 150 fs 81 MHz	— — —	xzx: 5 ± 10^{-14} zzz: 1.8 ± 10^{-13}	—	3.00 ± 10^{-13}	Photon Conversion Eff. [Capretti2015a]

(110)-GaP [b]	DFG	663 μm — —	— — —	— — —	1074 nm 1.3 TW m^{-2} 5 ns 10 Hz	1064 nm 1.5 MW 10 ns	—	—	0.182 39.6	THz/Input Photon Conversion Eff. [Jiang2011]
(110)-GaP	DFG	663 μm — —	3.217 220 m^{-1} 120 000 nm	— — —	1064 nm — 10 ns —	— 1.2 TW m^{-2} 5 ns	—	—	0.22 25	Internal Eff. Photon Conversion Eff. [Jiang2010]
OP-GaP[a]	DFG	1 mm — —	— — —	— — —	1550 nm — 110 fs 93.4 MHz	1800–1960 nm — 60 fs	—	—	19	Photon Conversion Eff. [Lee2017]
OP-GaP [b]	DFG	1.7 mm — —	— 32 m^{-1} 1064 nm	— — —	1064 nm — 23 ns 80 kHz	1748 nm — —	—	—	1 2.5	Pump-to-DFG Eff. Photon Conversion Eff. [Wei2018]
OP-GaP	DFG	1.7 mm — —	— — —	— — —	1064 nm — 23 ns 80 kHz	1748 nm — 16 ns	—	1.30 ± 10^{-11}	1.2	— [Wei2017]
OP-GaP	Other (see comments)	1 mm — —	— — —	— 2.27 eV —	1048 nm — 140 fs 80 MHz	— — —	—	—	8.6 28.9	Method: Optical Parametric Oscillation Idler Slope Conversion Eff. Quantum Eff. [O'Donnell2019]
OP-GaP	Other (see comments)	500 μm — —	3.3 — 4200 nm	— 2.26 eV —	1000 nm — 70 fs 250 MHz	— — —	—	—	59	Method: Half-Harmonic Generation Slope Conversion Eff. [Sorokin2018]

(Continued.)

Table 2A. (Continued.)

Second-Order Nonlinearities											
		Material Properties			**Measurement Details**		**Nonlinear Properties**				
Material	Method	Thickness Fabrication Substrate	Index Abs. coeff. Wavelength	Crystallinity Bandgap Doping level	**Pump** Wavelength Peak power or irradiance Pulse width Rep. rate	**Probe** Wavelength Peak power or irradiance Pulse width	$\chi^{(2)}$ (m V^{-1})[d]	d (m V^{-1})[d]	η (%)[d, e]	Comments Reference
4H SiC	SHG	— — SiC	2.54 — 1064 nm	Monocrys. — —	1064 nm 3.71 GW m^{-2} 100 ns 5 kHz	— — —	—	31: 6.5 ± 10^{-12} 15: 6.7 ± 10^{-12} 33: 11.7 ± 10^{-12}	—	— [Sato2009]
6H SiC	SHG	— — SiC	2.54 — 1064 nm	Monocrys. — —	1064 nm 3.71 GW m^{-2} 100 ns 5 kHz	— — —	—	31: 6.7 ± 10^{-12} 15: 6.5 ± 10^{-12} 33: 12.5 ± 10^{-12}	—	— [Sato2009]

[a] Multiple wavelengths reported.
[b] Multiple parameters (e.g., thickness, crystal orientation) reported.
[c] Measurement taken at a temperature other than room temperature.
[d] Units as illustrated unless otherwise indicated in table.
[e] See Comments for a description of conversion efficiencies.

Table 2B. Third-order NLO properties of bulk materials from representative works since 2000. In addition, 3PA coefficients are provided at the end of the table. Legend for superscripts: see below the table.

Third-Order Nonlinearities									
		Material Properties			Measurement Details		Nonlinear Properties		
					Pump	**Probe**			
Material	Method	Thickness Fabrication Substrate	Index Abs. coeff. Wavelength	Crystallinity Bandgap Doping level	Wavelength Peak power or irradiance Pulse width Rep. rate	Wavelength Peak power or irradiance Pulse width	$\chi^{(3)}$ (m^2 V^{-2})[d]	n_2 (m^2 W^{-1}) α_2 (m W^{-1})[e] α_3 (m^3 W^{-2})	Comments Reference
Conductors									
TiN	Z-scan	52 nm Sputtering Fused Silica	2.66 35 μm^{-1} 1550 nm	Polycrys. — —	1550 nm 14.1 TW m^{-2} 150 fs 1 kHz	— — —	5.9 ± 10^{-17} i1.7 ± 10^{-16}	3.70 ± 10^{-15} 6.60 ± 10^{-9}[e] —	— [Kinsey2015b]
TiN	Beam Defl.	30 nm Sputtering Fused Silica	— 54.8 μm^{-1} 650 nm	Polycrys. 5 eV —	800 nm — 55 fs 1 kHz	650 nm — 110 fs	—	4.70 ± 10^{-13} 2.15 ± 10^{-7} —	— [George2019]
Insulators									
Al_2O_3[a]	Z-scan	1 mm — —	— — —	Monocrys. 7.3 eV —	550 nm — 1ps 1 kHz	— — —	—	3.30 ± 10^{-20} — —	— [Major2004]
As_2S_3	Z-scan	— Amorphous Mat. Inc. —	— — — —	— — — —	2000 nm 20 TW m^{-2} 90 fs 26 Hz	— — — —	—	2.50 ± 10^{-18} — — —	— [Ensley2019]
AsSe	Z-scan	— Amorphous Mat. Inc. —	— — — —	— — — —	2000 nm 20 TW m^{-2} 90 fs 26 Hz	— — — —	—	6.20 ± 10^{-18} — — —	— [Ensley2019]

(Continued.)

Table 2B. (Continued.)

Third-Order Nonlinearities									
		Material Properties			**Measurement Details**		**Nonlinear Properties**		
Material	Method	Thickness Fabrication Substrate	Index Abs. coeff. Wavelength	Crystallinity Bandgap Doping level	**Pump** Wavelength Peak power or irradiance Pulse width Rep. rate	**Probe** Wavelength Peak power or irradiance Pulse width	$\chi^{(3)}$ ($m^2\ V^{-2}$)[d]	n_2 ($m^2\ W^{-1}$) α_2 ($m\ W^{-1}$)[e] α_3 ($m^3\ W^{-2}$)	Comments Reference
$(Bi_2O_3)_{0.25}$ $(ZnO)_{0.375}(B_2O_3)_{0.375}$	Z-scan	— Melt Quench —	— — —	— — —	532 nm — 80 ps 10 Hz	— — —	—	3.00 ± 10^{-18} 5.50 ± 10^{-11} —	— [Gomes2007]
$Ga_{10}Sn_{20}Se_{70}$	Z-scan	— Melt Quench —	2.65 1000 m^{-1} 1064 nm	— 1.58 eV —	1064 nm 10 TW m^{-2} 17 ps 10 Hz	— — —	—	6.50 ± 10^{-17} 1.14 ± 10^{-10} —	— [Chen2020]
$Ge_{0.18}Ga_{0.05}$ $Sb_{0.07}S_{0.3}Se_{0.4}$	Z-scan	— Melt Quench —	— — —	— 1.66 eV —	1064 nm 20 TW m^{-2} 15 ps 10 Hz	— — —	—	4.60 ± 10^{-18} 9.00 ± 10^{-12} —	— [Petit2006]
$Ge_{0.1}As_{0.1}Se_{0.6}$ $Te_{0.2}$	Z-scan	— Melt Quench —	2.9 317 m^{-1} 1064 nm	— 1.23 eV —	1064 nm 14 TW m^{-2} 15 ps 10 Hz	— — —	—	2.00 ± 10^{-17} 8.00 ± 10^{-11} —	— [Cherukulappurath2004]
$Ge_{0.115}As_{0.24}$ $Se_{0.645}$	Z-scan	— Melt Quench —	2.265 — 1550 nm	— 1.75 eV —	1550 nm 10 TW m^{-2} 260 fs 1 kHz	— — —	—	7.90 ± 10^{-18} $<1.00 \pm 10^{-13}$ —	— [Wang2014a]
$Ge_{0.15}Sb_{0.1}Se_{0.75}$	Z-scan	— Melt Quench —	2.598 — 1550 nm	— 1.72 eV —	1550 nm 10 TW m^{-2} 260 fs 1 kHz	— — —	—	7.50 ± 10^{-18} $<1.00 \pm 10^{-13}$ —	— [Wang2014a]

$Ge_{0.16}Sb_{0.14}S_{0.7}$	Z-scan	— Melt Quench —	2.31 — 1064 nm	— 2.1 eV —	1064 nm 20 TW m^{-2} 15 ps 10 Hz	— — —	—	2.10 ± 10^{-18} $<1.00 \pm 10^{-12}$ —	— [Petit2009]
$Ge_{0.23}Sb_{0.07}Se_{0.7}$	Z-scan	— Melt Quench —	2.58 — 1064 nm	— 1.66 eV —	1064 nm 5 TW m^{-2} 15 ps 10 Hz	— — —	—	1.03 ± 10^{-17} 2.40 ± 10^{-11} —	— [Petit2007]
$Ge_{0.33}As_{0.12}Se_{0.55}$	Z-scan	— Amorphous Mat. Inc. —	— — — —	— — — —	2000 nm 20 TW m^{-2} 90 fs 26 Hz	— — —	—	3.80 ± 10^{-18} — —	— [Ensley2019]
$Ge_{0.33}As_{0.12}Se_{0.55}$	Z-scan	— Amorphous Mat. Inc. —	— — — —	— — — —	3900 nm 20 TW m^{-2} 240 fs 10 Hz	— — —	—	7.50 ± 10^{-18} — —	— [Ensley2019]
$(GeS_2)_{0.1}(Sb_2S_3)_{0.75}$ $(CsI)_{0.15}$	Z-scan	— Melt Quench —	2.8 — 1064 nm	— — —	1064 nm 20 TW m^{-2} 17 ps 0.1 Hz	— — —	—	8.10 ± 10^{-18} 1.20 ± 10^{-11} —	— [Fedus2010]
$(NaPO_3)_{0.4}(BaF_2)_{0.1}$ $(WO_3)_{0.5}$	Z-scan	— Melt Quench —	— — —	— — —	532 nm — 80 ps 10 Hz	— — —	—	6.00 ± 10^{-19} 5.00 ± 10^{-12} —	— [Falcão-Filho2004]
$(Pb(PO_3)_2)_{0.4}$ $(WO_3)_{0.6}$	Z-scan	— Melt Quench —	1.93 116 m^{-1} 1064 nm	— — —	1064 nm 50 TW m^{-2} 17 ps 10 Hz	— — —	—	4.50 ± 10^{-19} $<2.00 \pm 10^{-13}$ —	— [Oliveira2010]
$(PbO)_{0.46}(Ga_2O_3)_{0.1}$ $(Bi_2O_3)_{0.426}$ $(BaO)_{0.014}$	Z-scan	— Melt Quench —	2.3 — 1064 nm	— — —	1064 nm 30 TW m^{-2} 15 ps 10 Hz	— — —	—	1.60 ± 10^{-18} $<1.00 \pm 10^{-12}$ —	— [De Araújo2005]

(Continued.)

Table 2B. (Continued.)

Third-Order Nonlinearities									
		Material Properties			Measurement Details		Nonlinear Properties		
Material	Method	Thickness Fabrication Substrate	Index Abs. coeff. Wavelength	Crystallinity Bandgap Doping level	**Pump** Wavelength Peak power or irradiance Pulse width Rep. rate	**Probe** Wavelength Peak power or irradiance Pulse width	$\chi^{(3)}$ ($m^2\ V^{-2}$)[d]	n_2 ($m^2\ W^{-1}$) α_2 ($m\ W^{-1}$)[e] α_3 ($m^3\ W^{-2}$)	Comments Reference
$(TeO_2)_{0.7}(GeO_2)_{0.15}$ $(K_2O)_{0.05}(Bi_2O_3)_{0.1}$	Z-scan	— Melt Quench —	2.1 11 m^{-1} 1064 nm	— 3.08 eV —	1064 nm 50 TW m^{-2} 17 ps 10 Hz	— — —	—	7.50 ± 10^{-20} $<2.00 \pm 10^{-13}$ —	— [Oliveira2014]
Semiconductors									
Al:ZnO	Nonlin. R/T	900 nm PLD —	— — —	— — —	785 nm 13 000 TW m^{-2} 100 fs 100 Hz	1258 nm — 100 fs	8 ± 10^{-20} $+ i2 \pm 10^{-20}$	3.50 ± 10^{-17} 2.50 ± 10^{-10}[e] —	— [Caspani2016]
Al:ZnO[b]	Nonlin. R/T	900 nm PLD —	— — —	— — —	787 nm 900 TW m^{-2} 100 fs 100 Hz	1120–1550 nm — —	3.5 ± 10^{-19} $i2 \pm 10^{-19}$	5.20 ± 10^{-16} 7.10 ± 10^{-9}[e] —	— [Carnemolla2018]
Diamond	Brillouin laser threshold	5 mm CVD —	— — —	Monocrys. — 40 ppb	532 nm — CW —	— — —	—	— — —	$g_{Brillouin} = 6.0 \pm 10^{-10}$ m W^{-1} Brillouin Shift = 167 GHz [Bai2020]
Diamond	I-scan	100 μm Natural —	— — —	Monocrys. — —	250 nm 500 TW m^{-2} 100 fs —	— — —	—	— 2.20 ± 10^{-11} —	— [Gagarskiĭ2008]
Diamond	Nonlin. R/T	100 μm Type IIa —	— — —	Monocrys. — —	273 nm 90 TW m^{-2} 150 fs 1 kHz	410 nm — —	—	— 2.40 ± 10^{-11} —	— [Roth2001]

Diamond	Nonlin. R/T	300 μm CVD —	— — —	Monocrys. — —	800 nm — 40 fs 100 kHz	— — —	—	7.30 ± 10^{-21} 9.00 ± 10^{-13} —	— [Motojima2019]
Diamond	Nonlin. R/T	300 μm CVD —	— — —	Monocrys. — $N_{ion\ flux} = 2 \pm 10^{+11}$ cm^{-2}	800 nm — 40 fs 100 kHz	— — —	—	1.20 ± 10^{-20} 1.75 ± 10^{-12} —	— [Motojima2019]
Diamond	Nonlin. R/T	300 μm CVD —	— — —	Monocrys. — $N_{ion\ flux} = 1 \pm 10^{+12}$ cm^{-2}	800 nm — 40 fs 100 kHz	— — —	—	2.42 ± 10^{-19} 1.01 ± 10^{-12} —	— [Motojima2019]
Diamond	SRS pump-probe	8 mm CVD —	— — —	Monocrys. — —	1864 nm 100 kW 4 ns —	2480 nm 3.75 kW 4 ns	—	— — —	$g_{Raman} = 3.8 \pm 10^{-11}$ m W^{-1} Raman Shift $= 1.33 \pm 10^{+5}$ m^{-1} [Sabella2015]
Diamond	THG	1 μm CVD Si	— — —	Nanocrystalline — —	1055 nm 150 GW m^{-2} 90 fs 1 kHz	— — —	5.00 ± 10^{-22}	— — —	Conversion Eff. $= 5.6 \pm 10^{-6}$ % [Trojánek2010]
Diamond	Z-scan	300 μm CVD —	— — —	Monocrys. — —	800 nm — 40 fs 100 kHz	— — —	—	4.16 ± 10^{-20} 9.93 ± 10^{-14} —	— [Motojima2019]
Diamond	Z-scan	300 μm CVD —	— — —	Monocrys. — $N_{ion\ flux} = 1 \pm 10^{+12}$ cm^{-2}	800 nm — 40 fs 100 kHz	— — —	—	5.50 ± 10^{-20} 1.61 ± 10^{-13} —	— [Motojima2019]
Diamond	Z-scan	1 μm CVD Si	— — —	Nanocrystalline — —	580 nm 2500 TW m^{-2} 90 fs 1 kHz	— — —	4.00 ± 10^{-19}	2.00 ± 10^{-17} — —	— [Trojánek2010]

(Continued.)

Table 2B. (Continued.)

Third-Order Nonlinearities									
		Material Properties			**Measurement Details**		**Nonlinear Properties**		
Material	Method	Thickness Fabrication Substrate	Index Abs. coeff. Wavelength	Crystallinity Bandgap Doping level	**Pump** Wavelength Peak power or irradiance Pulse width Rep. rate	**Probe** Wavelength Peak power or irradiance Pulse width	$\chi^{(3)}$ ($m^2\ V^{-2}$)[d]	n_2 ($m^2\ W^{-1}$) α_2 ($m\ W^{-1}$)[e] α_3 ($m^3\ W^{-2}$)	Comments Reference
Diamond	Z-scan	— CVD —	— — —	Monocrys. — —	310 nm 700 TW m^{-2} 100 fs 1 kHz	— — —	—	— 9.00 ± 10^{-12} —	— [Kozák2012]
Diamond	Z-scan	— CVD —	— — —	Monocrys. — —	350 nm — 100 fs 1 kHz	— — —	—	9.00 ± 10^{-20} — —	— [Kozák2012]
Diamond	Z-scan	530 μm CVD —	— — —	Monocrys. — —	260 nm 400 TW m^{-2} 120 fs 1 kHz	— — —	—	— 2.30 ± 10^{-12} —	— [Almeida2017]
Diamond	Z-scan	530 μm CVD —	— — —	Monocrys. — —	427.5 nm 400 TW m^{-2} 120 fs 1 kHz	— — —	—	1.70 ± 10^{-19} — —	— [Almeida2017]
Diamond	Other (see comments)	700 μm CVD —	— — —	Polycrys. — —	351 nm — 200 fs —	515 nm — 200 fs	2.70 ± 10^{-21}	1.40 ± 10^{-19} — —	Method: Phase Object Pump-Probe [Zhang2017b]
Diamond	Raman linewidth (TCUPS [f])	500 μm CVD —	— — —	Monocrys. — <1 ppm N_2	808 nm — 80 fs 78 MHz	— — —	—	— — —	Raman Linewidth = 150 m^{-1} [Lee2010]

Diamond	Raman linewidth (TCUPS [f])	250 μm Natural —	— — —	Monocrys. — <1 ppm N_2	808 nm — 80 fs 78 MHz	— — —	—	— — —	Raman Linewidth = 190 m^{-1} [Lee2010]
Diamond	Raman linewidth (TCUPS [f])	420 μm HPHT —	— — —	Monocrys. — 10–100 ppm N_2	808 nm — 80 fs 78 MHz	— — —	—	—	Raman Linewidth = 190 m^{-1} [Lee2010]
Diamond	SRS pump-probe	6.5 mm CVD —	— — —	Monocrys. — —	532 nm — 8 ns —	573 nm — 8 ns	—	— — —	$g_{Raman} = 4.2 \pm 10^{-10}$ m W^{-1} Raman Shift = $1.33 \pm 10^{+5}$ m^{-1} [Savitski2013]
GaAs	Nonlin. R/T	— — —	— — —	— 1.42 eV —	8700 nm — 10 ps 10 Hz	900 nm — 10 ps	—	— 5.00 ± 10^{-9} —	— [Fishman2011]
(001)-GaAs	Nonlin. R/T	425 μm — —	— — —	Monocrys. — —	1305 nm 1.09 TW m^{-2} 68.1 fs 1 kHz	0.5, 1, 2 THz — —	—	— 4.25 ± 10^{-10} —	— [Tiedje2007]
GaAs	SPM/XPM	1 mm — —	— — —	— — —	1064 nm — 53 ps 100 MHz	— — —	—	2.83 ± 10^{-10} esu — —	— [Garcia2000]
GaAs	Z-scan	350 μm — —	— — —	Monocrys. 1.42 eV —	1680 nm 29 TW m^{-2} 111 fs 1 kHz	— — —	—	3.00 ± 10^{-17} 2.50 ± 10^{-11} —	— [Hurlbut2007]
GaAs	Other (see comments)	700 μm — —	— 1.33 μm^{-1} 800 nm	Monocrys. — —	810 nm — 55 fs 1 kHz	— — —	—	— (110): 2.2 ± 10^{-9} (100): 1.8 ± 10^{-9} —	Method: Optical-Pump THz-Probe [Kadlec2004]

(Continued.)

Table 2B. (Continued.)

Third-Order Nonlinearities									
		Material Properties			**Measurement Details**		**Nonlinear Properties**		
Material	Method	Thickness Fabrication Substrate	Index Abs. coeff. Wavelength	Crystallinity Bandgap Doping level	**Pump** Wavelength Peak power or irradiance Pulse width Rep. rate	**Probe** Wavelength Peak power or irradiance Pulse width	$\chi^{(3)}$ ($m^2\ V^{-2}$)[d]	n_2 ($m^2\ W^{-1}$) α_2 ($m\ W^{-1}$)[e] α_3 ($m^3\ W^{-2}$)	Comments Reference
GaN[b]	THG Imaging	2.5 μm — —	— — —	— — —	1230 nm — 150 fs 125 MHz	— — —	1.00 ± 10^{-20}	— — —	— [Sun2000]
GaN	Z-scan	10 μm MOVPE Sapphire	— — —	— 3.39 eV $1 \pm 10^{+23}\ m^{-3}$	800 nm — 120 fs —	— — —	—	2.80 ± 10^{-18} — —	— [Almeida2019]
GaN	Z-scan	10 μm MOVPE Sapphire	— — —	— 3.39 eV $1 \pm 10^{+23}\ m^{-3}$	550 nm — 120 fs —	— — —	—	— 2.90 ± 10^{-11} —	— [Almeida2019]
GaN	Z-scan	500 μm HVPE GaN	— — —	Monocrys. — $1 \pm 10^{+23}\ m^{-3}$	724 nm 90 TW m^{-2} —	— — — —	—	2.50 ± 10^{-18} 9.00 ± 10^{-12} —	— [Chen2017b]
GaN	Z-scan	1 mm HVPE GaN	— — —	Monocrys. 3.39 eV —	760 nm 200 TW m^{-2} 190 fs 20 Hz	— — —	—	1.55 ± 10^{-18} — —	— [Fang2015]
(100)-GaP[a]	Nonlin. R/T	350 μm — —	— — 610–745; 760–980 nm	— 2.26 eV —	650; 800 nm — 7 fs —	650; 800 nm — 7 fs	—	2 ± 10^{-18}; 4 ± 10^{-18} 3 ± 10^{-11}; 8 ± 10^{-11} —	— [Grinblat2019]

(100)-GaP[a]	Z-scan	350 μm — —	— — —	— 2.26 eV —	800 nm 14 TW m^{-2} 7 fs —	— — —	—	1.60 ± 10^{-17} 8.00 ± 10^{-11} —	—	[Grinblat2019]
(100)-GaP[a,b]	Z-scan	500 μm — —	3.1 — 1040 nm	— 2.27 eV —	1040 nm — 61 fs 52 MHz	— — —	—	7.00 ± 10^{-18} — —	—	[Liu2010]
(100)-GaP[a,b]	Z-scan	500 μm — —	— 2.2 mm^{-1} 800 nm	— 2.27 eV —	800 nm — 37 fs 100 MHz	— — —	—	— 4.16 ± 10^{-11} —	—	[Liu2010]
InN[a,b]	FWM	680 nm PAMBE GaN-on-sapphire	2.78 1.2 μm^{-1} 1400 nm	— 0.82 eV —	1400 nm 35 TW m^{-2} 100 fs 1 kHz	— — —	4.20 ± 10^{-10} esu	— — —	—	[Naranjo2007]
InN[b]	FWM	1 μm PAMBE GaN-on-Si	2.95 870 mm^{-1} 1500 nm	Monocrys. 0.75 eV $1 \pm 10^{+25}$ m^{-3}	1500 nm — 100 fs 1 kHz	— — —	8.00 ± 10^{-10} esu	— 3.40 ± 10^{-10} —	—	[Naranjo2009]
InN	Nonlin. R/T	750 nm Sputtering GaN-on-Sapphire	— — —	Polycrys. 1.74 eV $1 \pm 10^{+26}$ m^{-3}	1550 nm 153 TW m^{-2} 100 fs 100 MHz	1550 nm 15.3 TW m^{-2} 100 fs	—	— 1.67 ± 10^{-9} —	—	[Valdueza-Felip2012]
InN	Z-scan	250 nm MBE AlN on c-Sapphire	2.45 8.7 μm^{-1} 790 nm	— 0.8 eV $5.5 \pm 10^{+24}$ m^{-3}	790 nm 26 TW m^{-2} 200 fs 80 MHz	— — —	—	— — —	Nonlinear Absorption Cross Section: 4 ± 10^{-21} m^2	[Tsai2009]
InN	Z-scan	1.4 μm PAMBE AlN/GaN on R-sapphire	— — —	Monocrys. 0.65 eV $1.4 \pm 10^{+25}$ m^{-3}	1500 nm 20 TW m^{-2} 120 fs —	— — —	—	1.90 ± 10^{-14} 4.75 ± 10^{-8} —	—	[Ahn2014]

(Continued.)

Table 2B. (Continued.)

Third-Order Nonlinearities									
		Material Properties			**Measurement Details**		**Nonlinear Properties**		
Material	Method	Thickness Fabrication Substrate	Index Abs. coeff. Wavelength	Crystallinity Bandgap Doping level	**Pump** Wavelength Peak power or irradiance Pulse width Rep. rate	**Probe** Wavelength Peak power or irradiance Pulse width	$\chi^{(3)}$ ($m^2\ V^{-2}$)[d]	n_2 ($m^2\ W^{-1}$) α_2 ($m\ W^{-1}$)[e] α_3 ($m^3\ W^{-2}$)	Comments Reference
InP[a,b]	I-scan	2 mm — —	— — —	— — —	1064 nm 6 TW m^{-2} 10 ps —	— — —	—	— 2.55 ± 10^{-10} —	— [Gonzalez2009]
(001)-InP:Fe	Nonlin. R/T	350 μm — —	3.1 — 1640 nm	— — —	1640 nm 5 TW m^{-2} 250 fs 50 MHz	— — —	xxxx: 2.066 ± 10^{-18} xxyy: 3.11 ± 10^{-19} xyyx: 1.231 ± 10^{-18}	— 3.70 ± 10^{-10} —	— [Matsusue2011]
(001)-InP:Fe	Nonlin. R/T	365 μm — —	— — —	Monocrys. — —	1305 nm 1.42 TW m^{-2} 68.1 fs 1 kHz	0.5, 1, 2 THz — —	—	— 7.03 ± 10^{-10} —	— [Tiedje2007]
(001)-InP:Fe	Nonlin. R/T	310 μm — —	— 2 m^{-1} 1600 nm	Monocrys. — —	1600 nm 1.1 TW m^{-2} 160 fs	1600 nm — 160 fs —	—	— 3.30 ± 10^{-10} —	— [Vignaud2004]
(001)-InP:S	Nonlin. R/T	310 μm — —	— 490 m^{-1} 1600 nm	Monocrys. — $7 \pm 10^{+24}$ m^{-3}	1600 nm 1.1 TW m^{-2} 160 fs	1600 nm — 160 fs —	—	— 2.60 ± 10^{-10} —	— [Vignaud2004]

(001)-InP:Zn	Nonlin. R/T	310 μm — —	— 2.83 mm^{-1} 1600 nm	Monocrys. — $1.5 \pm 10^{+24}$ m^{-3}	1600 nm 1.1 TW m^{-2} 160 fs	1600 nm — 160 fs —	—	— 3.10 ± 10^{-10} —	— [Vignaud2004]
(001)-InP:Fe	Z-scan	579 μm — —	3.147 — 1640 nm	— — —	1640 nm — 194.7 fs 47.8 MHz	— — —	xxxx: 2.619 ± 10^{-18} xxyy: 4.92 ± 10^{-19} xyyx: 1.531 ± 10^{-18}	— 2.20 ± 10^{-10} —	— [Oishi2018b]
(001)-InP:Fe	Z-scan	581 μm — —	3.147 — 1640 nm	— — —	1640 nm — 194.7 fs 47.8 MHz	— — —	2.65 ± 10^{-18}	— 2.30 ± 10^{-10} —	— [Oishi2018a]
InSb	Nonlin. R/T	1 mm — —	— — 10 600 nm	— 0.18 eV —	10 600 nm — — —	— — —	—	— —	Nonlinear Free Carrier Refraction Cross Section: 4.5 ± 10^{-19} m^2 [Dubikovskiy2008]
InSb	Z-scan	540 μm — —	— — —	Monocrys. 0.18 eV $9.00 \pm 10^{+19}$ m^{-3}	9000 nm — 370 fs 1 kHz	— — —	—	— 2.90 ± 10^{-8} —	— [Olszak2010]
InSn:O	Beam Defl.	310 nm — Float Glass	— — —	— — —	1242 nm — 100 fs 1 kHz	1050 nm — —	—	5.50 ± 10^{-17} — —	— [Benis2017]
InSn:O	THG	37 nm Sputtering Silicon	— — 1550 nm	— — —	— 400 GW m^{-2} 150 fs 81 MHz	— — —	3.50 ± 10^{-18}	— — —	— [Capretti2015a]

(Continued.)

Table 2B. (Continued.)

Third-Order Nonlinearities									
		Material Properties			**Measurement Details**		**Nonlinear Properties**		
Material	Method	Thickness Fabrication Substrate	Index Abs. coeff. Wavelength	Crystallinity Bandgap Doping level	**Pump** Wavelength Peak power or irradiance Pulse width Rep. rate	**Probe** Wavelength Peak power or irradiance Pulse width	$\chi^{(3)}$ ($m^2\ V^{-2}$)[d]	n_2 ($m^2\ W^{-1}$) α_2 ($m\ W^{-1}$)[e] α_3 ($m^3\ W^{-2}$)	Comments Reference
Silicon[a,b]	Z-scan	675 μm — —	— — —	Monocrys. — $1 \pm 10^{+21}$ m^{-3}	2600 nm 570 TW m^{-2} 150 fs 1 kHz	— — —	—	2.50 ± 10^{-18} — 2.00 ± 10^{-27}	— [Wang2013]
Silicon	Z-scan	125 μm — —	— — —	Monocrys. 1.12 eV Intrinsic	1220 nm 78 TW m^{-2} 200 fs 1 kHz	— — —	—	4.70 ± 10^{-18} 2.10 ± 10^{-11} —	— [Bristow2007]
Silicon	Z-scan	480 μm — —	— — —	Monocrys. — 10 (Ω-cm)	1540 nm 7 TW m^{-2} 130 fs 76 MHz	— — —	—	4.50 ± 10^{-18} 7.90 ± 10^{-12} —	— [Dinu2003b]
Silicon	Z-scan	500 μm — —	— — —	Monocrys. — Intrinsic	1550 nm — 190 fs 1 kHz	— — —	—	5.00 ± 10^{-18} 1.03 ± 10^{-11} —	— [Gai2013]
Silicon	Z-scan	500 μm — —	— — —	Monocrys. — 20 (Ω-cm)	1501 nm — — 500 Hz	— — —	—	2.20 ± 10^{-18} 4.80 ± 10^{-12} —	— [Lin2007]
4H SiC[a]	Z-scan	498 μm — —	— — —	Monocrys. 3.25 eV —	530 nm — 123 fs 50 kHz	— — —	—	3.19 ± 10^{-19} 2.00 ± 10^{-12} —	— [Guo2021]

6H SiC[a]	Z-scan	258 μm — —	— — —	Monocrys. 2.99 eV —	800 nm — 176 fs 50 kHz	— — —	—	3.88 ± 10^{-19} 3.95 ± 10^{-13} —	— [Guo2021]
6H SiC[b]	Z-scan	340 μm — —		Monocrys. 3.10 eV 1.00 ± 10^{21} m^{-3}	780 nm — 160 fs 41 Hz	— — —	—	4.75 ± 10^{-19} 6.40 ± 10^{-13} —	— [DesAutels2008]
6H SiC[b]	Z-scan	220 μm — —		Monocrys. 3.10 eV 2.5 ± 10^{23} m^{-3}	780 nm — 160 fs 41 Hz	— — —	—	4.00 ± 10^{-19} 5.20 ± 10^{-13} —	— [DesAutels2008]
Three photon absorption									
$Al_2Se_{1.5}S_{1.5}$	Z-scan	— — —	2.7 — 1550 nm	— 1.74 eV —	1550 nm — 150 fs 1 kHz	— — —	—	— — 5.50 ± 10^{-26}	— [Shabahang2014]
CdS	Nonlin. R/T	— — —	2.34 — 1064 nm	— 2.42 eV —	1064 nm — 30 ps —	— — —	—	— — 1.50 ± 10^{-26}	— [Benis2020]
CdS	Z-scan	— — —	2.34 — 1200 nm	— 2.42 eV —	1200 nm — 150 fs 1 kHz	— — —	—	— — 1.10 ± 10^{-26}	— [Benis2020]
CdSe	Z-scan	— — —	2.5 — 1500 nm	— 1.9 eV —	1500 nm — 150 fs 1 kHz	— — —	—	— — 2.40 ± 10^{-25}	— [Benis2020]
CdTe	Z-scan	— — —	2.7 — 1750 nm	— 1.44 eV —	1750 nm — 150 fs 1 kHz	— — —	—	— — 1.20 ± 10^{-24}	— [Benis2020]

(Continued.)

Table 2B. (Continued.)

Third-Order Nonlinearities										
		Material Properties			Measurement Details		Nonlinear Properties			
Material	Method	Thickness Fabrication Substrate	Index Abs. coeff. Wavelength	Crystallinity Bandgap Doping level	**Pump** Wavelength Peak power or irradiance Pulse width Rep. rate	**Probe** Wavelength Peak power or irradiance Pulse width	$\chi^{(3)}$ ($m^2\ V^{-2}$)[d]	n_2 ($m^2\ W^{-1}$) α_2 ($m\ W^{-1}$)[e] α_3 ($m^3\ W^{-2}$)	Comments Reference
GaAs[a]	Z-scan	— — —	3.4 — 2300 nm	— 1.42 eV —	2600 nm — 15 ps 1 kHz	— — —	—	— — 9.00 ± 10^{-25}	— [Benis2020]
GaAs[a]	Z-scan	— — —	3.4 — 2300 nm	— 1.42 eV —	2600 nm — 150 fs 1 kHz	— — —	—	— — 7.50 ± 10^{-25}	— [Benis2020]
GaAs	Z-scan	— — —	3.4 — 2300 nm	— 1.42 eV —	2300 nm — 100 fs 1 kHz	— — —	—	— — 3.50 ± 10^{-25}	— [Hurlbut2007]
InSb [c]	Z-scan	— — —	3.95 — 12 000 nm	— 0.228 eV —	12 000 nm — 10 ps 1 kHz	— — —	—	— — 2.50 ± 10^{-20}	— [Benis2020]
4H SiC	Z-scan	498 μm — —	— — —	Monocrys. — —	990 nm — 177 fs 50 kHz	— — —	—	— — 1.90 ± 10^{-27}	— [Guo2021]
6H SiC	Z-scan	258 μm — —	— — —	Monocrys. — —	990 nm — 177 fs 50 kHz	— — —	—	— — 4.00 ± 10^{-28}	— [Guo2021]

ZnO	Nonlin. R/T	— — —	1.94 — 1064 nm	— 3.27 eV —	1064 nm — 30 ps —	— — —	—	— — 2.20 ± 10^{-26}	— [Benis2020]
ZnO	Z-scan	— — —	1.95 — 900 nm	— 3.27 eV —	900 nm — 100 fs 1 kHz	— — —	—	— — 5.40 ± 10^{-27}	— [He2005]
ZnS[a]	Z-scan	— — —	2.3 — 800 nm	— 3.54 eV —	960 nm — 30 ps 1 kHz	— — —	—	— — 1.60 ± 10^{-27}	— [Benis2020]
ZnS	Z-scan	— — —	2.3 — 800 nm	— 3.54 eV —	800 nm — 100 fs 1 kHz	— — —	—	— — 1.70 ± 10^{-27}	— [He2005]
ZnSe[a]	Nonlin. R/T	— — —	2.48 — 1064 nm	— 2.67 eV —	1064 nm — 30 ps —	— — —	—	— — 1.50 ± 10^{-26}	— [Benis2020]
ZnSe	Nonlin. R/T	— — —	2.48 — 1064 nm	— 2.67 eV —	1350 nm — 30 ps —	— — —	—	— — 9.10 ± 10^{-27}	— [Cirloganu2008]
ZnTe	Z-scan	— — —	2.8 — 1200 nm	— 2.28 eV —	1200 nm — 150 fs 1 kHz	— — —	—	— — 2.00 ± 10^{-26}	— [Benis2020]

[a] Multiple wavelengths reported.
[b] Multiple parameters (e.g., thickness, crystal orientation) reported.
[c] Measurement taken at a temperature other than room temperature.
[d] Units as illustrated unless otherwise indicated in table.
[e] A negative value of α_2 represents saturable absorption.
[f] TCUPS: transient coherent ultrafast phonon spectroscopy.

3.2. Solvents: data table and discussion

***Team: Eric Van Stryland (team leader)**, Eiji Tokunaga*

As mentioned in section 3.1 on bulk materials, we include here a separate section dedicated specifically to solvents. In table 3, we show a list of the 3rd-order nonlinearities of a variety of liquids, mainly organic solvents at room temperature, taken from representative experimental works in the literature. These are included primarily because our understanding of their NLO responses has advanced and one of them, carbon disulfide (CS_2) is often used as a reference. Besides reporting the values of the effective nonlinear refractive indices, $n_{2,\text{eff}}$, where listed in the original works, we report the 2PA coefficient, α_2, and the 3PA coefficient, α_3. However, in most of the publications the 2PA is not listed since the wavelengths used are with photon energies where such absorption is not energetically possible and 3PA is also extremely small or not energetically allowed.

These solvent nonlinearities are important not only because CS_2 is used as a reference material, but also because of the many measurements of organic dye nonlinearities in the literature (not included in the current data tables) as well as for measurements of particle suspensions, as they are usually performed for these materials dissolved or dispersed in various solvents. A lack of knowledge of the nonlinearities of the solvents can potentially confuse interpretation of such measurements. We also refer the reader to section 3.7 on hybrid waveguiding systems that includes, amongst others, hollow fibers filled with solvents.

The primary difficulty in reporting the solvent nonlinearities in table 3, is that it is now known that there are four separate physical processes leading to the reported NLR, i.e., the bound-electronic nonlinearity, which can be considered instantaneous for any pulse widths reported in this publication, and three nuclear contributions whose temporal characteristics depend on the solvent but are on the order of femtoseconds to picoseconds. These nonlinearities are reorientational, librational, and collisional [McMorrow1988, Reichert2014]. For nanosecond and longer pulses, other nonlinearities of electrostriction and thermal origin also become important. We restrict ourselves here to the subnanosecond range. Using single-beam measurements, it is problematic to separate the various nonlinearities. Excite-probe experiments are needed for this. The bound-electronic and collisional nonlinearities can be separated from the rotational and librational nonlinearities by their symmetries given the signals using different relative polarizations of the excitation and probe beams. The nuclear nonlinearities have both rise and fall times and each has an associated response function given, e.g., in [Reichert2014]. Thus, the response is quite complicated. In rare cases the NLR response is dominated by a single nonlinearity. In fact, this only occurs in the case of extremely short pulses (usually a few femtoseconds) where only the bound-electronic response is activated. Even in 3D symmetrical molecules, the nuclear collisional nonlinearity is still present for pulses longer than a few femtoseconds. Thus, the overall NLO response depends on the pulsewidth used for the experiment. This has led to difficulties in reported nonlinearities of multiple materials since CS_2, included in this table, has often been used as a reference standard for measurements of other materials. In this regard, we point out [Miguez2017, Zhao2018, Reichert2014] where measurements of CS_2 include the nuclear components. The effective nonlinearity can be calculated from the values of the four nonlinear responses along with their temporal responses as in [Zhao2018, Reichert2014]. We show results for CS_2 in figure 1 taken from [Reichert2014] because of its wide use as a reference material. [Ganeev2004] shows a dependence consistent with that of [Reichert2014] for several pulsewidths from 110 fs to 75 ns. The fast and slow nonlinearities referred to in [Miguez2017] are combinations of the four nonlinearities; thus, attempts to combine information from [Miguez2017, Zhao2018, Reichert2014] which are the only ones in table 3, reporting the separate nuclear nonlinear responses, into a single table are problematic. Therefore, the reader will have to consult the original papers to get the full details of the NLR [Miguez2017, Zhao2018, Reichert2014]. The two values of n_2 reported in table 3 for [Zhao2018, Reichert2014] are the predicted bound-electronic n_2 that would be measured using few femtosecond pulses along with an estimate of the effective nonlinear refractive index, $n_{2,\text{eff}}$, that would be measured in a single beam experiment such as Z-scan using pulses of $>$100 ps, i.e. long compared to the rise and fall times of the nuclear nonlinearities but short compared to times where electrostriction and thermal effects become important. These values are estimated from the temporal dependence plots given in those works [Zhao2018, Reichert2014]. These values can be compared to the predictions from [Miguez2017] where pulses from 60 fs to 2 ps were used to measure the nonlinearities and separate slow and fast responses. In table 3 we report the 2 values for the slow and fast components. The sum of these components should give the same long pulse limit as the 2nd value given in the table for [Zhao2018, Reichert2014].

There is one final set of data that does not fit on this table, and that is the dispersion of the NLO response. The data in the table only covers wavelengths from 532 nm to 1064 nm so little dispersion information is shown. However, the dispersion of the three nuclear contributions to the NLR should be small [Reichert2014, Alms1975, Zahedpour2015]. On the other hand, the bound-electronic nonlinearity should follow similar dispersion to other materials having UV resonances [Hutchings1992]. For CS_2, the short pulse limit values

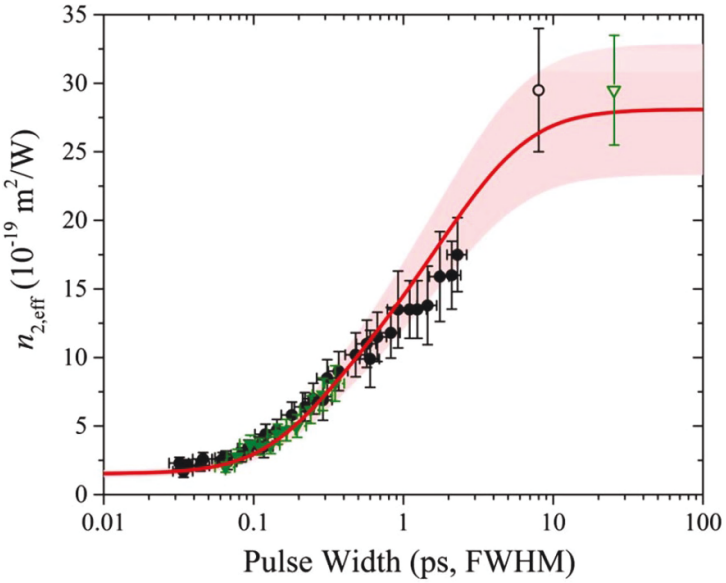

Figure 1. Results of BD experiments for CS_2 yielding the four nonlinearities with their response functions to calculate the predicted $n_{2,\mathrm{eff}}$ in a Z-scan experiment (solid red line), along with Z-scan measurements at various pulse widths and two wavelengths namely 700 nm (black circles) and 1064 nm (green triangles). Reprinted with permission from [Reichert2014] © 2014 Optica Publishing Group.

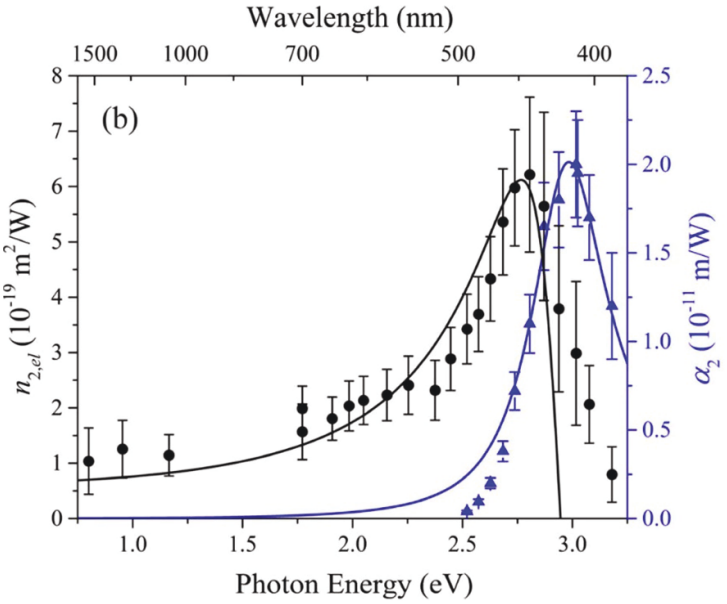

Figure 2. Z-scan measurements of bound-electronic n_2 (black circles—labeled as $n_{2,\mathrm{el}}$) for femtosecond pulses with non-instantaneous components subtracted, and α_2 (blue triangles) for CS_2. Curves represent model fits as described in [Reichert2014]. Reprinted with permission from [Reichert2014] erratum © 2016 Optica Publishing Group.

for $n_{2,\mathrm{eff}}$ show essentially no dispersion between 1064 nm and 700 nm (see figure 1). However, [Reichert2014] performed both open and closed aperture Z-scans over a much larger wavelength range from 390 nm to 1550 nm using the shortest pulsewidths available which resulted in signals dominated by bound-electronic n_2 and/or 2PA. Furthermore, the values of the nuclear contributions at these pulsewidths could be confidently subtracted resulting in the plot of n_2 along with α_2 as a function of wavelength as shown in figure 2.

Future work on solvents could include measurements of the 2PA spectra along with the dispersion of the bound-electronic n_2 to test theory as done in figure 2, as well as measurements verifying the lack of dispersion of the nuclear contributions, and the inclusion of more solvents. Additionally, there are few measurements of solvents in spectral regions where there is significant linear loss [Marble2018, Bautista2021]. Determination of the influence of polar versus nonpolar solvents on the second-order hyperpolarizabilities could also be of interest to spur theoretical calculations for some of these molecules. This could also test local field effects as was done for CS_2 in [Reichert2014].

Table 3. NLO measurement results for solvents. The methods used are Z-scan, BD, ER, and THG. All liquid samples reported in this table were held in either 1 or 2 mm internal thickness cuvettes and were at room temperature. The $\chi^{(3)}$ values specified in the table are in fact $\chi^{(3)}{}_{\text{eff}}$ values containing multiple nonlinearity contributions rather than just the bound-electronic contribution. Legend for superscripts: see below the table. The following abbreviations have been used: DMSO = dimethyl sulfoxide; ODCB = o-dichlorobenzene; DCM = dichloromethane; BS = butyl salicylate; ACN = acetonitrile; NB = nitrobenzene; CB = chlorobenzene; THF = tetrahydrofuran; CH = cyclohexane; CCl_4 = carbon tetrachloride; CS_2 = carbon disulfide; D_2O = deuterated water; lin = linear polarization; cir = circular polarization.

Material	Method	$\chi^{(3)} \times 10^{-14}$ (esu)	$\chi^{(3)} \times 10^{-22}$ ($m^2\,W^{-1}$)	$n_{2,\text{eff}} \times 10^{-20}$ ($m^2\,W^{-1}$)	2:α_2 ($m\,W^{-1}$) 3:α_3 ($m^3\,W^{-2}$)	λ_{pump} (nm)	τ_{pump} Rep-rate	λ_{probe} (nm)	τ_{probe} (fs)[a]	Reference
CCl_4	Z-scan		20.8	28		1064	16 ps 10 Hz			[Rau2008]
	THG		11.1	15		1064	16 ps 10 Hz			
Chloroform	Z-scan		27.8	38		1064	16 ps 10 Hz			[Rau2008]
	THG		9.77	13.3		1064	16 ps 10 Hz			
DCM	Z-scan		26.8	37		1064	16 ps 10 Hz			[Rau2008]
	THG		8.56	11.8		1064	16 ps 10 Hz			
CH	Z-scan		14	19		1064	16 ps 10 Hz			[Rau2008]
	THG		9.03	12.2		1064	16 ps 10 Hz			
n-Hexane	Z-scan		11.2	17		1064	16 ps 10 Hz			[Rau2008]
	THG		6.17	9.35		1064	16 ps 10 Hz			
Acetone	Z-scan		14.9	23		1064	16 ps 10 Hz			[Rau2008]
	THG		6.55	10.1		1064	16 ps 10 Hz			
Methanol	Z-scan		11.1	18		1064	16 ps 10 Hz			[Rau2008]
	THG		4.16	6.74		1064	16 ps 10 Hz			
Ethanol	Z-scan		11.5	18		1064	16 ps 10 Hz			[Rau2008]
	THG		4.82	7.57		1064	16 ps 10 Hz			
DMF	Z-scan		29.8	42		1064	16 ps 10 Hz			[Rau2008]
	THG		7.78	11		1064	16 ps 10 Hz			
Water	Z-scan		8.7	14		1064	16 ps 10 Hz			[Rau2008]
	THG		3.91	6.28		1064	16 ps 10 Hz			
CB	Z-scan		95.9	117		1064	16 ps 10 Hz			[Rau2008]
	THG		14.8	18.1		1064	16 ps 10 Hz			
Toluene	Z-scan		73.4	93		1064	16 ps 10 Hz			[Rau2008]
	THG		13.7	17.4		1064	16 ps 10 Hz			
CS_2	Z-scan		289	310		1064	16 ps 10 Hz			[Rau2008]
	THG		32.1	34.5		1064	16 ps 10 Hz			
Toluene	Z-scan			lin 5.7		800	125 fs			[Yan2012a]
				cir 3.3			1 kHz			
ODCB	Z-scan			lin 4.8		800	125 fs			[Yan2012a]
				cir 2.8			1 kHz			
DMF	Z-scan			lin 4.0		800	125 fs			[Yan2012a]
				cir 2.2			1 kHz			
Acetone	Z-scan	20.5		43.7	2: 6.0×10^{-13}	532	30 ps 10 Hz			[BalaMuraliKrishna2013]
	Z-scan	4.37		9.34	3: 7.8×10^{-23}	800	100 fs 1 kHz			
Chloroform	Z-scan	27.6		51.9	2: 1.25×10^{-12}	532	30 ps 10 Hz			[BalaMuraliKrishna2013]
	Z-scan	4.96		9.37	3: 5.2×10^{-23}	800	100 fs 1 kHz			
DMF	Z-scan	24.5		47	2: 1.22×10^{-12}	532	30 ps 10 Hz			[BalaMuraliKrishna2013]
	Z-scan	5.37		10.4	3: 9.7×10^{-23}	800	100 fs 1 kHz			
THF	Z-scan	20.1		40.1	2: 5.70×10^{-13}	532	30 ps 10 Hz			[BalaMuraliKrishna2013]
	Z-scan	6.46		12.9	3: 150×10^{-23}	800	100 fs 1 kHz			
Toluene	Z-scan	25.4		42.7	2: 3.20×10^{-12}	532	30 ps 10 Hz			[BalaMuraliKrishna2013]
	Z-scan	7.95		14	3: 20.5×10^{-23}	800	100 fs 1 kHz			
CS_2	Z-scan	762		1130	2: 2.00×10^{-11}	532	30 ps 10 Hz			[BalaMuraliKrishna2013]
	Z-scan	12		17.8	3: 74.7×10^{-23}	800	100 fs 1 kHz			
Ethanol	Z-scan	5.11		10.9	3: 21.0×10^{-23}	800	100 fs 1 kHz			[BalaMuraliKrishna2013]
CCl_4	Z-scan	6.31		11.7	3: 18.2×10^{-23}	800	100 fs 1 kHz			[BalaMuraliKrishna2013]
CS_2	Z-scan	87.1	122	519		532	35 ps 10 Hz			[Iliopoulos2015]
	Z-scan	0.668	0.932	3.97		800	40 fs 10 Hz			
NB	Z-scan	23.3	32.6	153		532	35 ps 10 Hz			[Iliopoulos2015]
	Z-scan	0.151	0.21	0.988		800	40 fs 10 Hz			
DB	Z-scan	18.6	26	122		532	35 ps 10 Hz			[Iliopoulos2015]
	Z-scan	0.158	0.22	1.03		800	40 fs 10 Hz			
Aniline	Z-scan	17.8	24.9	112		532	35 ps 10 Hz			[Iliopoulos2015]
	Z-scan	0.165	0.23	1.03		800	40 fs 10 Hz			
Toluene	Z-scan	15.3	21.4	108		532	35 ps 10 Hz			[Iliopoulos2015]
	Z-scan	0.143	0.2	1.01		800	40 fs 10 Hz			
Benzene	Z-scan	12.6	17.5	88		532	35 ps 10 Hz			[Iliopoulos2015]
	Z-scan	0.246	0.343	1.72		800	40 fs 10 Hz			
Chloroform	Z-scan	4.4	6.1	33		532	35 ps 10 Hz			[Iliopoulos2015]
	Z-scan	0.11	0.153	0.827		800	40 fs 10 Hz			

(Continued.)

Table 3. (Continued.)

Material	Method	$\chi^{(3)} \times 10^{-14}$ (esu)	$\chi^{(3)} \times 10^{-22}$ (m^2 W^{-1})	$n_{2,\text{eff}} \times 10^{-20}$ (m^2 W^{-1})	2:α_2 (m W^{-1}) 3:α_3 (m^3 W^{-2})	λ_{pump} (nm)	τ_{pump} Rep-rate	λ_{probe} (nm)	τ_{probe} (fs)[a]	Reference
DMF	Z-scan	4.3	6	33		532	35 ps 10 Hz			[Iliopoulos2015]
	Z-scan	0.101	0.141	0.781		800	40 fs 10 Hz			
DCM	Z-scan	4.1	5.7	32		532	35 ps 10 Hz			[Iliopoulos2015]
	Z-scan	0.1	0.14	0.781		800	40 fs 10 Hz			
DMSO	Z-scan	3.9	5.4	28		532	35 ps 10 Hz			[Iliopoulos2015]
	Z-scan	0.102	0.142	0.735		800	40 fs 10 Hz			
Acetone	Z-scan	2.6	3.6	22		532	35 ps 10 Hz			[Iliopoulos2015]
	Z-scan	0.075	0.105	0.528		800	40 fs 10 Hz			
ACN	Z-scan	2.3	3.2	20		532	35 ps 10 Hz			[Iliopoulos2015]
	Z-scan	0.0474	0.0661	0.413		800	40 fs 10 Hz			
n-Hexane	Z-scan	2	2.8	17		532	35 ps 10 Hz			[Iliopoulos2015]
	Z-scan	0.0496	0.0692	0.413		800	40 fs 10 Hz			
THF	Z-scan	1.4	1.9	11		532	35 ps 10 Hz			[Iliopoulos2015]
	Z-scan	0.0721	0.101	0.574		800	40 fs 10 Hz			
CS_2	BD			15.0; 275[c]		800	50 fs 1 kHz	650	158	[Reichert2014]
CS_2	Z-scan			15.0; 300[d]		1064	65 fs-25 ps 1 kHz			[Reichert2014]
CS_2	Z-scan			15.0; 300[d]		700	32 fs-8 ps 1 kHz			[Reichert2014]
CS_2	Z-scan			$BEn_2 = 30$	2: 2.0×10^{-11}	420[e]	1 KHz			
				$BEn_2 = 60$	2: 0.7×10^{-11}	545[e]	1 kHz			[Reichert2014]
Toluene	BD			6.0; 49[c]		800	150 fs 1 kHz	700	150	[Zhao2018]
NB	BD			6.0; 77[c]		800	150 fs 1 kHz	700	150	[Zhao2018]
Benzene	BD			6.0; 44[c]		800	150 fs 1 kHz	700	150	[Zhao2018]
p-Xylene	BD			6.2; 52[c]		800	150 fs 1 kHz	700	150	[Zhao2018]
Pyridine	BD			6.0; 53[c]		800	150 fs 1 kHz	700	150	[Zhao2018]
ODCB	BD			6.0; 51[c]		800	150 fs 1 kHz	700	150	[Zhao2018]
DCM	BD			3.0; 15[c]		800	150 fs 1 kHz	700	150	[Zhao2018]
Chloroform	BD			4.1; 16[c]		800	150 fs 1 kHz	700	150	[Zhao2018]
CCl_4	BD			4.8; 6.8[c]		800	150 fs 1 kHz	700	150	[Zhao2018]
Acetone	BD			4.0; 12[c]		800	150 fs 1 kHz	700	150	[Zhao2018]
ACN	BD			3.5; 11[c]		800	150 fs 1 kHz	700	150	[Zhao2018]
DMF	BD			4.0; 21[c]		800	150 fs 1 kHz	700	150	[Zhao2018]
BS	BD			3.8; 26[c]		800	150 fs 1 kHz	700	150	[Zhao2018]
THF	BD			3.2; 6.2[c]		800	150 fs 1 kHz	700	150	[Zhao2018]
Hexane	BD			3.2; 7.0[c]		800	150 fs 1 kHz	700	150	[Zhao2018]
CH	BD			3.5; 5.9[c]		800	150 fs 1 kHz	700	150	[Zhao2018]
Methanol	BD			3.0; 4.4[c]		800	150 fs 1 kHz	700	150	[Zhao2018]
1-Octanol	BD			4.0; 4.9[c]		800	150 fs 1 kHz	700	150	[Zhao2018]
1-Butanol	BD			3.3; 4.4[c]		800	150 fs 1 kHz	700	150	[Zhao2018]
Ethanol	BD			3.2; 4.2 [c]		800	150 fs 1 kHz	700	150	[Zhao2018]
CS_2	BD			15.0; 275[c]		800	150 fs 1 kHz	700	150	[Zhao2018]
DMSO	BD			4.5; 8.2[c]		800	150 fs 1 kHz	700	150	[Zhao2018]
D_2O	BD			2.8; 3.7[c]		800	150 fs 1 kHz	700	150	[Zhao2018]
H_2O	BD			2.5; 3.2[c]		800	150 fs 1 kHz	700	150	[Zhao2018]
CS_2	ER			23.9; 260[b]		790	Fast ∼fs Slow ∼ps			[Miguez2017]
Toluene	ER			11.5; 45.2[b]		790	Fast ∼fs Slow ∼ps			[Miguez2017]
DMSO	ER			9.15; 5.23[b]		790	Fast ∼fs Slow ∼ps			[Miguez2017]
Chloroform	ER			5.45; 9.1[b]		790	Fast ∼fs Slow ∼ps			[Miguez2017]
Acetone	ER			5.66; 9.6[b]		790	Fast ∼fs Slow ∼ps			[Miguez2017]
Methanol	ER			4.62; 1.44[b]		790	Fast ∼fs Slow ∼ps			[Miguez2017]
Ethanol	ER			4.43; 1.02[b]		790	Fast ∼fs Slow ∼ps			[Miguez2017]
H_2O	ER			3.35; 1.06[b]		790	Fast ∼fs Slow ∼ps			[Miguez2017]

[a] Repetition Rate for the probe is the same as for the pump.

[b] The 1st entry is the sum of the fast components, and the 2nd entry, which is the sum of the slow entries, is also the predicted $n_{2,\text{eff}}$ for pulses >100 ps as described in [Miguez2017].

[c] The two entries are the predicted bound-electronic n_2, and the predicted $n_{2,\text{eff}}$ for pulses >100 ps.

[d] The 1st entry is the predicted bound-electronic n_2, while the 2nd is from measured Z-scan data for the longest ps pulses. See figure 1.

[e] The peak 2PA is at 420 nm, and the peak bound-electronic n_2 is at 545 nm. Depending on the wavelength, the minimum pulse width varies from 32 to 165 fs.

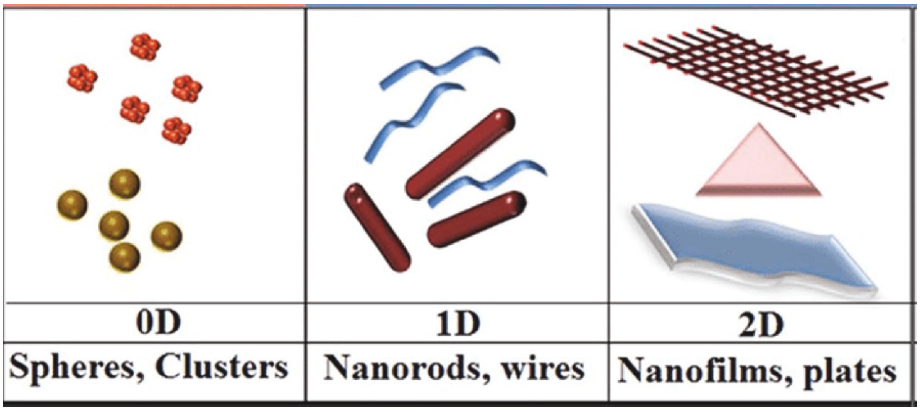

Figure 3. A typical representative diagram of 0D–1D–2D NSM, as used in this text. Reprinted under CC BY license from [Sajanlal2011].

3.3. 0D–1D–2D materials: data table and discussion

Team: *Cecília Campos, Ksenia Dolgaleva, Daniel Espinosa,* ***Anderson Gomes (team leader)****, Mikko Huttunen, Dragomir Neshev, Lázaro Padilha, Jingshi Yan, Nathalie Vermeulen*

3.3.1. Introduction

3.3.1.1. 0D–1D–2D materials and their NLO applications

Among the ways to categorize nanomaterials or NSMs, at least two approaches can be followed [Ngo2014]. In one case, the bulk material is the starting point, and one employs the general definition that a nanomaterial contains at least one dimension of 100 nm or less. Thus, a thin film whose thickness is 100 nm or less is a nanomaterial, such as a nanofilm or a nanoplate. If two dimensions are under 100 nm, then they are named nanowires, nanofibers or nanorods. Finally, under the above definition, if all three dimensions are smaller than 100 nm, it is a nanoparticle. An alternative way becomes relevant if one looks at the material nanostructure. In this case, the dimensionality of the nanoscale component leads to the definition. When the nanostructure has a length larger than 100 nm in one direction only, it is 1D (wire, fiber or rod, for instance). If no dimension is larger than 100 nm, it is 0D (nanoparticle), and a thin film, with two dimensions larger than 100 nm, is a 2D nanostructure (this holds as well for plates and multilayers). A typical representative diagram of the subcategories 0D–1D–2D for NSMs, as used in this text, is shown in figure 3 (adapted from [Sajanlal2011]). Besides these general definitions, we note that the dimension shorter than 100 nm might confine the movement of free charge carriers and produce a quantum confinement effect [Fox2001]. In this case, the optical properties of the material would become size-dependent. 0D, 1D and 2D materials presenting quantum confinement effects are called QDs, quantum wires, and QWs, respectively.

There is a myriad of NLO and other applications for 0D–1D–2D NSMs, which can be revisited in [Liu2017, Zhang2017a, Xu2017, Autere2018a, Jasim2019, Eggleton2019, Liu2019a, Wang2020, Ahmed2021]. Based upon the already known and well-established fundamental understanding, and upon the NLO applications in bulk materials, researchers have demonstrated that most NLO effects could also occur at the nanoscale or can be engineered in different ways [Zhang2021] when they take place in nanoscale dimensions. Although the practical applicability of 0D–1D–2D NSMs is at times limited by e.g. fabrication quality issues and/or losses, the NLO properties of 0D–1D–2D NSMs have already been exploited in LEDs, nanolasers, nanobiosensors, imaging, as well as in nonlinear microscopy, photoacoustics, photocatalysis, energy harvesting, optical limiting, and saturable-absorber-based mode-locked lasing. Nonlinear nanoplasmonics is another field where NLO in 0D–1D–2D materials has been gaining much attention. The field of nanoplasmonics deals with the study of optical phenomena and applications in the nanoscale neighborhood of dielectric–metal interfaces [Stockman2011]. It goes 'beyond' plasmonics—with decreasing interaction dimension—aiming at focusing light below the diffraction limit, determined by the Abbe diffraction formula, which can be roughly approximated by $\lambda/2$, where λ is the wavelength of light being used in the light – matter interaction. Physically, it is performed by converting photons into localized charge-density oscillations—so-called surface plasmons—on metallic nanostructures. Further reviews on nanoplasmonics and applications can be found at [Barbillon2017, Panoiu2018, Krasavin2019]. Finally, it should be noted that 0D–1D–2D NSM can also feature unusual NLO properties in the THz domain. Whereas this section focuses on the nonlinearities of 0D–1D–2D NSMs at optical wavelengths, further details on the THz nonlinearities are provided in section 3.8.

3.3.1.2. Background prior to 2000

The history of NSMs has been traced back to the 9th century and several other examples of ancient artifacts using nanocomposites emerged throughout the centuries, which of course were only explained after the 19th century with the availability of electron microscopes capable of measuring in the nanoworld [Heiligtag2013]. But the general nanoscience and nanotechnology scientific history and first publication date back to 1857 with Michael Faraday's work [Faraday1857]. Then came Feynman's lecture (1959), Taniguchi's 'nanotechnology' (1974) and Drexler (1981), as reviewed in [Heiligtag2013]. Thereafter, the broad field of nanoscience and nanotechnology flourished. Nowadays the material subcategories described here have become a reality, and the study of their NLO properties is a continuously growing research field.

3.3.1.2.1. Background for 0D materials

The first studies about the optical properties of so-called semiconductor microspheres date back from the early 1980s after the works from Efros and Efros [Efros1982] and Brus [Brus1984]. Those nanomaterials were nano-sized semiconducting spheres embedded in a glass matrix. However, they exhibited poor optical quality, mostly due to the difficulties in controlling the particle size distribution and in eliminating surface trap sites. Later, in the early 1990s, colloidal semiconductor QDs were first synthesized, narrowing the size distribution and improving the optical properties after surface treatment with organic ligands [Murray1993]. Major breakthroughs were achieved after the control over the optical properties in II–VI QDs and the field grew rapidly in the late 1990s and early 2000s. During this period, the scientific interest moved from simple core-only nanospheres to more complex nanostructures, including nanorods, nanoplatelets, tetrapods, and core-shell heterostructures, reaching an unprecedented level of control over the optical and electronic properties of those semiconductors by manipulating their sizes, compositions, and shapes. At this stage, the NLO properties of those nanomaterials came to the spotlight as they emerged as promising candidates for a number of applications including bio-labeling, all-optical signal processing, light detectors, and lighting technologies [Kairdolf2013, García de Arquer2021].

3.3.1.2.2. Background for 1D materials

Unidimensional structures of different materials were fabricated before 2000. Single-crystalline nanowires made of semiconductors such as GaN, SnO_2, ZnO, and Si, as well as carbon nanotubes were particularly attractive for photonics applications. The confinement of light and the cavity-like resonances in the nanowires are interesting features to realize nanolasers, LEDs, frequency converters, solar cells, photodetectors, and sensors [Pauzauskie2006]. Some linear optical characterizations of the 1D structures were performed before 2000, but there were no extensive experimental measurements of the optical nonlinearities, although some specific works started exploring NLO responses in unidimensional materials in 2000 [Kishida2000, Ogasawara2000]. In 2002, the first measurement of the NLO properties of a single semiconductor nanowire was reported [Johnson2002]. In the same year, the saturable absorption nonlinearity of SWCNTs was demonstrated for the first time [Chen2002]. Generally speaking, prior to 2002, if the information on the NLO coefficient of a particular 1D material was needed, one usually had to rely on the bulk value.

3.3.1.2.3. Background for 2D materials

The potential of semiconductor QW structures for efficient third-order NLO processes has been explored since the early 1980s, especially GaAs-AlGaAs multiple quantum wells (MQWs). Resonant excitonic effects near the band edge region provide the mechanism for NLA and NLR in these materials [Chemla1985]. By 2000, the importance of semiconductor QWs had already been established, with various applications in optoelectronics, such as laser diodes, LEDs, solar cells, modulators, and detectors [Fox1996].

Single-layer 2D materials, as we know today, have had very little or almost no scientific impact before 2000. As pointed out in [Miró2014], according to classical physics, at any finite temperature they would be thermodynamically unstable due to thermal lattice fluctuations (see [Miró2014] and references therein). The major experimental breakthrough came only in the post-2000 years, after the 2004 publication by Novoselov *et al* [Novoselov2004] who first isolated a single-layer 2D material, namely graphene, through the Scotch tape exfoliation of graphite. After 2004, the field of single-layer 2D materials grew rapidly, with many novel materials beyond graphene [Lv2015, Zhang2015a], and among the several review articles that have been published, we highlight those related to NLO in 2D materials published in recent years [Liu2017, Autere2018a, You2018, Eggleton2019, Yamashita2019, Zhou2020a, Ahmed2021, Vermeulen2022]. Several other excellent review articles on different aspects of 2D materials can be found in the literature and have not been indicated here.

3.3.1.3. Considerations for 0D–1D–2D materials when performing NLO measurements

Assessing NLO properties in photonic materials, regardless of their dimensions, requires a great amount of scientific care and proper planning regarding the optical source to be employed, the chosen technique, and whether the technique will adequately address the desired information. From the optical material point of view, preferably all the morphological and optical information should be known in order to perform a proper analysis of the results. Regarding 0D–1D–2D materials, further considerations must be taken into account. For 0D materials, size and shape must be properly characterized, and the same holds for the environment in which the 0D material is embedded, e.g., a solvent, in the case of suspensions, a matrix, or a substrate. It is very important to characterize the NLO properties of the solvent, matrix or substrate. This is also valid for 1D and 2D materials. Another aspect to be considered, in the case of 0D–1D–2D materials in suspension, is the scattering, both linear and nonlinear. Therefore, when measuring the linear absorption, the researcher should also insure the knowledge of the extinction coefficient and, in turn, the scattering coefficient of the sample. During the NLO measurement, the influence of nonlinear scattering can contribute to the NLO properties in an undesirable manner. We also point out that for some materials such as graphene, the level of doping strongly influences the NLO response [Jiang2018b] and as such needs to be specified in order to correctly interpret the measurement data. When working with 0D–1D–2D materials in a free-space excitation setup, it is often preferred to use ultrashort excitation pulses (picosecond, femtosecond) to avoid damage to the sample. We point out that the short propagation distance of the excitation beam through nanometer-thick 0D–1D–2D materials typically rules out the need for phase matching in NLO experiments. It is also worth noting that some works on 2D materials report $\chi^{(2)}/\chi^{(3)}$ values either considering sheet susceptibilities or bulk-like susceptibilities, as differentiated in the tables below. The units are different for both cases, as the bulk-like susceptibility is typically assumed to be the sheet susceptibility divided by the monolayer thickness [Autere2018a]. Finally, we point out that the nonlinearities can also be expressed in terms of conductivities $\sigma^{(2)}/\sigma^{(3)}$ rather than susceptibilities [Cheng2014]. In addition to these specific considerations for 0D–1D–2D materials, also the best practices described in section 2 should be taken into account when performing NLO measurements.

3.3.1.4. Description of general table outline

Tables 4A and B show a representative list of, respectively, second-order and third-order NLO properties of 0D, 1D and 2D materials taken from the literature since 2000, with the entries arranged in alphabetical order. Based upon the best practices in section 2, tables 4A and B were put together using inclusion criteria for publications that clearly state the required technical information for an unambiguous and clear identification of the NLO properties being evaluated. In some cases, publications missing only one important parameter could unfortunately not be considered, although they were technically sound. The tables are subdivided into 'Material properties', 'Measurement details' and 'Nonlinear properties'. The same set of columns was used for 0D, 1D and 2D materials. Within each column the information is given in the order of the header description. The NLO technique used is provided in the 'Method' column. Some papers relied on non-standard NLO measurement techniques (e.g., method listed as 'Other') or have notes associated with their measurement/analysis. These values and information are listed within the 'Comments' column. The works included in the tables nominally report data obtained at room temperature, unless denoted otherwise in the 'Comments' column. For works that report dependences of the nonlinearity on parameters such as wavelength/energy, polarization, sample size, input fluence, doping level, pulse length/peak power, and concentration, these dependencies are denoted by '$^{1\,2\,3\,4\,5\,6\,7}$' respectively, in the 'Comments' column. If dispersive values for the NLO parameter were provided, the cited value represents the peak value for the material within the measurement range. The tables are restricted to optical nonlinearities up to the third order, and although higher orders have become of interest [Reyna2017], they are not covered here.

3.3.2. Discussion

3.3.2.1. Advancement since 2000 and remaining challenges

3.3.2.1.1. Advancement and challenges for 0D materials

Since 2000, as the field of 0D semiconductor nanomaterials was growing, stable, monodisperse nanoparticles were becoming available, and the interest in investigating their NLO response has increased. This was mainly due to the initial excitement created by the predictions that the NLO response in 0D materials would be highly enhanced as compared to bulk semiconductors [Brunhes2000a] since the quantum confinement should enhance the oscillator strength as the nanomaterial size was reduced. Thus, several groups started to experimentally study distinct optical properties regarding QDs, including the second-order susceptibility [Brunhes2000b, Sauvage2001], third-order susceptibility [Valdueza-Felip2008], NLR [Wang2019], and NLA [Pu2006, Wang2019, Alo2020]. The first reports on the magnitude of the 2PA cross-section indicated that, for spherical nanomaterials, the magnitude of this process was linearly dependent on the nanoparticle

volume [Pu2006, Padilha2007, Makarov2014]. Strategies to better control the NLO response in 0D materials have involved band-structure optimization, obtained with PbS QDs [Padilha2011], and shape control [Scott2015]. In the last decade, a fair amount of effort has been put into gaining further control over the electronic and optical properties of these nanostructures by developing sophisticated heterostructures, and by shape control. Strong enhancement of 2PA cross-sections has been reported in CdSe nanoplatelets, with superlinear dependence on the volume [Scott2015]. On the other hand, sublinear volume dependence has been recently reported for core/shell heterostructures [Alo2020]. By shape controlling and heterostructuring these nanomaterials, it is expected that one can obtain further control over the nanomaterials' NLO response towards the development of tailored nanostructures for on-demand NLO.

3.3.2.1.2. Advancement and challenges for 1D materials

Since the year 2000, NLO characterizations of 1D structures in various arrangements and shapes were reported. We give several examples in the following. While many studies focused on experiments involving many nanowires with a distribution of dimensions, a few involve only single nanowires. SHG and SRS measurements were performed on individual GaP nanowires [Wu2009, Sanatinia2014]. SHG was also evaluated in a single GaAs nanoneedle [Chen2010] or even in areas within a single GaAs nanowire with different crystal phases [Timofeeva2016]. Often, the NLO technique is applied to a collection of 1D structures, either random or spatially ordered. For example, SHG was measured in an array of GaP nanowires embedded in a polydimethylsiloxane matrix [Fedorov2020] or grown on a GaP substrate [Sanatinia2012]. Also, Z-scan experiments were performed in single-walled carbon nanotubes (SWCNTs) deposited on a glass substrate as a thin-film [Seo2006] or dispersed in a colloidal suspension [Shi2019a]. In the latter case, the authors reported that a semiconductor-SWCNTs colloid exhibits a lower saturation irradiance and a lower 2PA coefficient as compared to a mixture of metallic-SWCNTs and semiconducting-SWCNTs [Shi2019a].

One exciting feature of 1D materials is the optical nonlinearity dependence on the structure dimensions due to resonances or surface effects. For example, in GaP nanowires (with a diameter of 210 nm), the SHG efficiency increases with increasing equivalent thickness (total volume of nanowires per unit area) [Fedorov2020], while the SRS irradiance decreases with increasing length [Wu2009]. Furthermore, the SHG irradiance in GaP nanopillars (with diameters from 100 nm to 250 nm) presents a strong dependence on the pillar diameter [Sanatinia2012]. Moreover, polarization-dependent measurements can be used to distinguish between the second-harmonic light generated in bulk or on the surface [Johnson2002, Sanatinia2012, Sanatinia2014, Sanatinia2015]. Indeed, by using polarization-dependent measurements, the nonlinear coefficient at the surface of a GaP nanopillar was observed to be approximately 15 times higher than that from the bulk [Sanatinia2015]. Conversely, the SHG light from a wurtzite (WZ) GaAs single nanoneedle was shown to be primarily originating from the bulk [Chen2010].

Advances in SHG polarimetry also allow studying the crystal structure of a nonlinear material because the SHG is sensitive to crystallographic symmetry. A per-pixel analysis of SHG images was used to distinguish between GaAs nanowires in the pure WZ, pure zinc blende (ZB), WZ-ZB mixed phases, or with ZB rotational twins [Timofeeva2016].

Despite the advancements reported on SHG measurements, this material category is far from being thoroughly characterized. There is still room to use other second- and third-order NLO techniques to exploit the large surface-to-volume ratio and strong Mie and Fabry-Perot resonances of the 1D structures.

3.3.2.1.3. Advancement and challenges for 2D materials

The study of NLO in quantum-well structures post-2000 emphasizes the effects of ISBTs rather than excitonic effects. GaN-AlN and GaN-AlGaN MQW structures have been shown to be particularly suitable for both second-order and third-order processes resonant at the ISBT frequency [Rapaport2003, Nevou2006].

The advancements in single-layer 2D materials, which can be considered a novel field of research with less than two decades of R&D, have been outstanding both from the point of view of scientific understanding and applications. Both refractive and absorptive nonlinearities have been investigated. Particularly, graphene has been shown to exhibit extremely strong third-order nonlinearities and a low saturable absorption threshold [Chen2015, Miao2015, Dremetsika2017, Jiang2018b, Soavi2018. Thakur2019], and there are several other 2D materials and particularly TMDs such as MoS_2 that feature a pronounced second-order NLO response as well (see, e.g., [Woodward2016, Autere2018b]). Nevertheless, in view of the large family of 2D materials, further characterization will be required to get the full picture of their NLO behavior, including the contributions from exciton resonances, free carriers, etc, in order to fully exploit their application potential in, e.g., optoelectronics [Sundaram2018]. The progress made so far has been promoted by advances in the 2D materials synthesis and proper morphological characterization. Also, the tunability of the NLO response using electrical gating [Jiang2018b, Soavi2018] is an important advantage for the practical use of both the refractive and absorptive nonlinearities in, e.g., wavelength converters and saturable-absorption-based

modelocked lasers, respectively [Vermeulen2022]. Nevertheless, further fabrication improvement is necessary to achieve large-area films on a wide range of substrates, easy placement of contact points, proper etching, and advanced metrology control. The NLO characterization might also provide metrology methods to control parameters of interest for practical NLO applications of 2D materials.

3.3.2.2. Recommendations for future works on 0D–1D–2D materials

The future of NLO in 0D–1D–2D materials relies on a more in-depth NLO characterization of the already existing materials and on the development of novel materials. A multidisciplinary approach will also be required to further exploit their optical nonlinearities. Among the novel 0D–1D–2D materials, we highlight nanodiamonds, nanoporous materials, core–shell nanoparticles, perovskite nanostructures, silicene, antimonene, MXenes, 2D metal-organic framework nanosheets, boron nitride nanosheets, and metal-based nanomaterials [Baig2021]. Metal-based nanomaterials are at the basis of nanoplasmonics, and the field of nonlinear nanoplasmonics is also a flourishing and promising area, opening new avenues for future works [Panoiu2018, Krasavin2019]. Further NLO research on 0D materials could benefit, amongst others, biosensing applications [Wang2020]. Regarding 1D materials, assemblies of 1D nanomaterials have been recently introduced, and their NLO properties need to be further understood [Chen2019a]. 2D materials also have significant potential for future study and applications. For instance, 2D rare-earth based materials are opening new avenues [Chen2021], since rare-earth materials are quite well studied and have already found a great deal of applications. Also, various methods to enhance the NLO response, including plasmonics, gating, and functionalization [Wei2019] can be further explored. That said, to enable further progress in the overall understanding of 0D–1D–2D materials, it will be important that future works report in detail both the fabrication aspects, the material properties and the NLO experiments carried out with the materials. Parameters such as the linear absorption loss (which is typically quite high in 0D–1D–2D materials) and the doping level are often overlooked, yet essential to properly evaluate the observed NLO behavior [Vermeulen2022]. In addition, great care is needed to adequately extract and describe the actual NLO coefficients that underpin the measurement data, especially when the dependence of the NLO coefficients on, e.g., wavelength is also being studied. Only such a systematic approach allows building up an extensive and in-depth understanding of the NLO physics of this promising category of materials and the potential they hold for NLO applications.

3.3.3. Data table for 0D–1D–2D materials

Table 4A. Second-order NLO properties of 0D–1D–2D materials from representative works since 2000. Legend for superscripts: see below the table.

Second-Order Nonlinearities							
		Material Properties			Measurement Details	Nonlinear Properties	
Material	Method	Fabrication Substrate	Width Number of layers	Crystallinity Bandgap Doping level	Pump Wavelength Peak power Peak irradiance Beam spot size Pulse width Rep. rate	$\chi(2)$ d_{eff}	Reference Additional parameters and comments
0D materials							
InAs/GaAs QD	SHG	MBE GaAs	— 40	— — —	7381 nm — $2.00 \pm 10^{+12}$ W m^{-2} — — —	1.20 ± 10^{-9} m V^{-1} —	[Brunhes2000b] Nonlinearity dependence[1, 2] shown in figure 2 of reference paper. InAs QD height/diameter = 0.2 (diameter = 2.3 ± 10^{-8} m) $\chi^{(2)}$: 1.2 ± 10^{-9} m V^{-1} (sample) 2 ± 10^{-7} m V^{-1} (1 QD layer) Pump polarization: TE (in the layer plane)
InAs/GaAs QD	SHG	MBE (001)-GaAs	— 30	— — —	20 000 nm — $1.00 \pm 10^{+12}$ W m^{-2} 1.50 ± 10^{-4} m — —	2.50 ± 10^{-6} m V^{-1} —	[Sauvage2001] $\chi^{(2)}$ for 1 QD layer 1 layer: InAs QD height of 3 ± 10^{-9} m InAs QD base length 1.5 ± 10^{-8} m GaAs barrier thickness of 5 ± 10^{-8} m Pump polarization: 50% in the layer plane along [110] direction, 50% along z-growth axis Temperature: 10 K

(Continued.)

Table 4A. (Continued.)

Second-Order Nonlinearities							
		Material Properties			Measurement Details	Nonlinear Properties	
Material	Method	Fabrication Substrate	Width Number of layers	Crystallinity Bandgap Doping level	Pump Wavelength Peak power Peak irradiance Beam spot size Pulse width Rep. rate	$\chi(2)$ d_{eff}	Reference Additional parameters and comments
1D materials							
GaP nanopillars	SHG	Nanosphere litho-graphy/ RIE/ CAIBE GaP (100)	1.50 ± 10^{-7} m —	Monocrystalline 2.26 eV —	840 nm — — 1.00 ± 10^{-6} m 1.00 ± 10^{-13} s $8.20 \pm 10^{+7}$ Hz	— —	[Sanatinia2012] Nonlinearity dependence[3] shown in figure 2(b) of reference paper $\eta = 2.00 \pm 10^{-7}$ % The efficiency is for the SHG light generated by the array of nanopillars. The authors did not take into account the light collection efficiency of the microscope objective
GaP nanowires	SHG	MBE/ G-coating Silicon (111)	1.50 ± 10^{-7} m —	Monocrystalline — —	1048 nm — — 5.00 ± 10^{-6} m 1.50 ± 10^{-13} s $8.00 \pm 10^{+7}$ Hz	— —	[Fedorov2020] $\eta = 1.00 \pm 10^{-2}$ % Nonlinearity dependence[1] shown in figure 2(c) of the reference paper
WZ-GaAs nanoneedle	SHG	MOCVD Silicon (111) sapphire	1.50 ± 10^{-6} m —	Monocrystalline — —	806 nm — — 5.00 ± 10^{-7} m 1.20 ± 10^{-13} s $7.60 \pm 10^{+7}$ Hz	5.30 ± 10^{-11} m V^{-1} —	[Chen2010] Diameter: 1.5 ± 10^{-6} m (base) 2 ± 10^{-9} m to 4 ± 10^{-9} m (tip) $\chi^{(2)}$: aca: 5.3 ± 10^{-11} m V^{-1} ccc: 1.15 ± 10^{-10} m V^{-1} caa: 2.6 ± 10^{-11} m V^{-1}

WZ-GaAs nanowires	SHG imaging	MBE Silicon (111)/ Si_3N_4 thin film	1 ± 10^{-7} m —	Monocrystalline — —	820 nm — — 2.50 ± 10^{-6} m 1.00 ± 10^{-13} s $8.00 \pm 10^{+7}$ Hz	— $d_{15} = d_{24} = 4.2 \pm 10^{-11}$ m V^{-1} $d_{31} = d_{32} = 2.1 \pm 10^{-11}$ m V^{-1} $d_{33} = 1.15 \pm 10^{-10}$ m V^{-1}	[Timofeeva2016] Nonlinearity dependence[2] shown in figure 5 of the reference paper While they did not extract the tensor elements' values from the data, the values were used in the theoretical model that fitted well the experimental data The deposition substrate was silicon (111), but the nanowire was transferred to the Si_3N_4 thin film substrate to perform the SHG measurement
2D Materials							
$Al_{0.08}Ga_{0.92}N$/ GaN QW	SHG	MOCVD GaN-on-(0001)-c-sapphire	— 10	Monocrystalline — —	1064 nm — — — 5.00 ± 10^{-9} s $1.40 \pm 10^{+1}$ Hz	— $d_{31} = 2.2 \pm 10^{-12}$ m V^{-1} $d_{33} = 4.80 \pm 10^{-12}$ m V^{-1}	[Passeri2004] Thickness for 1 layer $Al_{0.08}Ga_{0.92}N$/GaN: 1.4 ± 10^{-8} m/2.4 ± 10^{-9} m The authors also provided information for $Al_{0.15}Ga_{0.85}N$/GaN QW and $Al_{0.08}Ga_{0.92}N$/GaN with different thickness Pump: p and s-polarization
GaN-AlN QW	SHG	MBE AlN-on-c-sapphire	— 200	— — —	1980 nm $2.50 \pm 10^{+3}$ W — 1.50 ± 10^{-4} m 6.00 ± 10^{-9} s $3.00 \pm 10^{+1}$ Hz	1.14 ± 10^{-10} m V^{-1} —	[Nevou2006] Thickness for 1 layer GaN-AlN: 2.593 ± 10^{-9} m/3 ± 10^{-9} m Nonlinearity dependence[1] shown in figure 3 of reference paper The nonlinear conversion efficiency in MQW sample was 16 times higher compared to that in a reference bulk GaN sample Pump: p-polarization

(Continued.)

Table 4A. (Continued.)

Second-Order Nonlinearities							
		Material Properties			**Measurement Details**	**Nonlinear Properties**	
					Pump		
Material	Method	Fabrication	Width	Crystallinity	Wavelength Peak power	$\chi(2)$	Reference
		Substrate	Number of layers	Bandgap	Peak irradiance Beam spot size	d_{eff}	Additional parameters and comments
				Doping level	Pulse width Rep. rate		
Graphene	DFG	CVD	—	—	547 nm —	3.00 ± 10^{-7} m V^{-1}	[Constant2016]
		Quartz	Monolayer	—	— 3.00 ± 10^{-4} m	—	DFG enhanced through plasmonic excitation Probe parameters:
				0.3 eV	1.00 ± 10^{-13} s $1.00 \pm 10^{+3}$ Hz		$\lambda = 615$ nm Pulse duration: 1.00 ± 10^{-13} s Polarization: p-polarization Pump: p-polarization
Graphene	SHG	CVD	—	Monocrystalline	1035 nm —	3.00 ± 10^{-11} m V^{-1}	[Zhang2019a]
		Fused silica	Monolayer	—	— —	—	Electric-quadrupole SHG Pump: p and s-polarization
				0.9 eV	2.00 ± 10^{-13} s $8.00 \pm 10^{+7}$ Hz		Nonlinearity dependence[5] in figure 4 of the reference paper
MoS_2	SHG	Micromechanical exfoliation	0.65 ± 10^{-9} m	—	1560 nm $2.70 \pm 10^{+3}$ W	5.40 ± 10^{-12} m V^{-1}	[Autere2018b]
		Si/SiO_2 (285 nm)	Monolayer	—	— —	—	Nonlinearity dependence[2] in figure 5 of the reference paper
				—	1.50 ± 10^{-13} s $5.00 \pm 10^{+7}$ Hz		
MoS_2	SHG	Mechanical exfoliation	—	—	870 nm —	8 ± 10^{-20} m^2 V^{-1}	[Malard2013]
		Si/SiO_2	Monolayer	—	— 6.00 ± 10^{-7} m	—	Nonlinearity dependence[1] shown in figure 3(e) of reference paper. Specified second-order nonlinearity is the sheet susceptibility
				—	1.40 ± 10^{-13} s $8.00 \pm 10^{+7}$ Hz		

MoS_2	SHG	Micromechanical cleavage Si/SiO_2	— Monolayer	— — —	1560 nm $8.00 \pm 10^{+3}$ W — 9.30 ± 10^{-7} m 1.50 ± 10^{-13} s $5.00 \pm 10^{+7}$ Hz	2.20 ± 10^{-12} m V^{-1} —	[Säynätjoki2017] Nonlinearity dependence[2, 3, 6] in figures 3(c), 4 and 5 of the reference paper The authors also provided information for 2 and 5 layers at 1560 nm $\eta_{conv} = 6.47 \pm 10^{-9}$%
MoS_2	SHG imaging	CVD SiO_2/Si (300 nm)	7.00 ± 10^{-10} m Monolayer	— — —	1560 nm — $1.00 \pm 10^{+15}$ W m^{-2} 1.80 ± 10^{-6} m 1.50 ± 10^{-13} s $8.90 \pm 10^{+5}$ Hz	2.90 ± 10^{-11} m V^{-1} —	[Woodward2016] Nonlinearity dependence[1] shown in figures 3(a) and (b) of the reference paper
$MoSe_2$	SHG	Micromechanical exfoliation Si/SiO_2 (285 nm)	0.65 ± 10^{-9} m Monolayer	— — —	1560 nm $2.70 \pm 10^{+3}$ W — — 1.50 ± 10^{-13} s $5.00 \pm 10^{+7}$ Hz	3.70 ± 10^{-11} m V^{-1} —	[Autere2018b] Nonlinearity dependence[2] in figure 5 of the reference paper
WS_2	SHG	Micromechanical exfoliation Si/SiO_2 (285 nm)	0.65 ± 10^{-9} m Monolayer	— — —	1560 nm $2.70 \pm 10^{+3}$ W — — 1.50 ± 10^{-13} s $5.00 \pm 10^{+7}$ Hz	1.62 ± 10^{-11} m V^{-1} —	[Autere2018b] Nonlinearity dependence[2] in figure 5 of the reference paper
WS_2	SHG	CVD SiO_2/Si	6.50 ± 10^{-10} m Monolayer	— — —	832 nm — — 1.80 ± 10^{-6} m 1.06 ± 10^{-13} s $8.80 \pm 10^{+7}$ Hz	— 4.50 ± 10^{-9} m V^{-1}	[Janisch2014] —
WS_2–MS	SHG	CVD Sapphire	— Monolayer	— — —	804 nm — — 4.00 ± 10^{-6} m 8.00 ± 10^{-15} s $8.00 \pm 10^{+7}$ Hz	— —	[Li2019] The authors reported a 20-fold enhancement of the optical SHG from WS_2 monolayers by cooperating with SiO_2 dielectric microspheres (MSs)

(Continued.)

Table 4A. (Continued.)

Second-Order Nonlinearities							
		Material Properties			Measurement Details	Nonlinear Properties	
Material	Method	Fabrication Substrate	Width Number of layers	Crystallinity Bandgap Doping level	**Pump** Wavelength Peak power Peak irradiance Beam spot size Pulse width Rep. rate	$\chi(2)$ d_{eff}	Reference Additional parameters and comments
WSe_2	SHG	Micromechanical exfoliation Si/SiO_2 (285 nm)	0.65 ± 10^{-9} m Monolayer	— — —	1560 nm $2.70 \pm 10^{+3}$ W — — 1.50 ± 10^{-13} s $5.00 \pm 10^{+7}$ Hz	1.65 ± 10^{-11} m V^{-1} —	[Autere2018b] Nonlinearity dependence[2] in figure 5 of the reference paper
WSe_2	SHG	CVT SiO_2/Si (300 nm)	7.00 ± 10^{-10} m Monolayer	— — —	816 nm — — — 1.07 ± 10^{-13} s $8.80 \pm 10^{+7}$ Hz	— 5.00 ± 10^{-9} m V^{-1}	[Ribeiro-Soares2015] Nonlinearity dependence[2] in figure 3 of the reference paper
WSe_2	SHG	Micromechanical exfoliation Fused silica	1.17 ± 10^{-9} m Monolayer	— 1.65 eV —	1546 nm — — $(0.8 \sim 0.1) \pm 10^{-6}$ m 2.00 ± 10^{-13} s $8.00 \pm 10^{+7}$ Hz	$(0.7 \sim 0.09) \pm 10^{-19}$ m^2 V^{-1} —	[Rosa2018] Nonlinearity dependence[2, 3] in figures 2 and 4 of the reference paper The authors also provided information for 4, 5, 6 and 9 layers at 1546 nm Specified second-order nonlinearity is the sheet susceptibility

Superscripts indicate the work reports the nonlinearity dependence on [1]wavelength/energy, [2]polarization, [3]sample size (width, diameter, thickness, number of layers), [4]input fluence, [5]doping level, [6]pulse length/peak power, [7]concentration.

Table 4B. Third-order NLO properties of 0D–1D–2D materials from representative works since 2000. The $\chi^{(3)}$ values specified in the table might in some cases be $\chi^{(3)}{}_{\text{eff}}$ values containing multiple nonlinearity contributions rather than just the bound-electronic contribution. Legend for superscripts: see below the table.

Third-Order Nonlinearities								
		Material Properties				Measurement Details	Nonlinear Properties	
Material	Method	Fabrication Solvent/ Substrate	Width Number of layers	Index Abs. coeff. Wavelength	Crystallinity Bandgap Doping Level	**Pump** Wavelength Peak power Peak irradiance Beam spot size Pulse width Rep. rate	$\chi(3)$ $n_{2,\text{eff}}$ α_2	Reference Additional parameters and comments
0D materials								
CdSe QDs	Other (add in comments)	Organic Chemical Route Toluene	6.00 ± 10^{-9} m —	— — —	— — 1.96 eV	800 nm — — — 8.00 ± 10^{-14} s $1.00 \pm 10^{+3}$ Hz	— — $2.00 \pm 10^{+4}$ GM	[Alo2020] 2PA cross-section in GM (10^{-50} cm^4 . s . photon^{-1}) The authors also provided NLO parameters for different diameters (3 ± 10^{-9} m, 4 ± 10^{-9} m and 5 ± 10^{-9} m) and doping levels The technique is called MPAPS. The bandgap is defined as the excitonic peak position in figure S1 of reference paper
CdSe QDs	Other (add in comments)	Organic Chemical Route Toluene	4.80 ± 10^{-9} m —	— — —	— — 2.04 eV	800 nm — — — 1.00 ± 10^{-13} s $8.20 \pm 10^{+7}$ Hz	— — $1.03 \pm 10^{+4}$ GM	[Pu2006] 2PA cross-section in GM (10^{-50} cm^4 . s . photon^{-1}) The authors also provided NLO parameters for different diameters (2.4 ± 10^{-9} m to 4.6 ± 10^{-9} m) Nonlinearity dependence[3] shown in figure 1 of the reference paper Two-photon excited photoluminescence

(Continued.)

Table 4B. (Continued.)

Third-Order Nonlinearities								
		Material Properties				**Measurement Details**	**Nonlinear Properties**	
Material	Method	Fabrication Solvent/ Substrate	Width Number of layers	Index Abs. coeff. Wavelength	Crystallinity Bandgap Doping Level	**Pump** Wavelength Peak power Peak irradiance Beam spot size Pulse width Rep. rate	$\chi(3)$ $n_{2,\text{eff}}$ α_2	Reference Additional parameters and comments
CdSe/CdZnS QDs	Other (add in comments)	Organic Chemical Route Toluene	1.24 ± 10^{-8} m —	— — —	— — 2.03 eV	800 nm — — — 8.00 ± 10^{-14} s $1.00 \pm 10^{+3}$ Hz	— — $2.70 \pm 10^{+4}$ GM	[Alo2020] 2PA cross-section in GM (10^{-50} cm^4 . s . photon^{-1}) Nuclei diameter: 4.0 nm Shell thickness: 4.2 nm The authors also provided NLO parameters for shell thicknesses of 1.2 nm, 2.5 nm, and 3.0 nm Nonlinearity dependence[1] shown in figure 4 of the reference paper The technique is called MPAPS. The bandgap defined as the excitonic peak position is shown in figure S1 of the reference paper
CdTe QDs	Other (add in comments)	Organic Chemical Route Toluene	5.40 ± 10^{-9} m —	— — —	— — 1.8 eV	840 nm — — — 1.00 ± 10^{-13} s $8.20 \pm 10^{+7}$ Hz	— — $7.96 \pm 10^{+3}$ GM	[Pu2006] 2PA cross-section in GM (10^{-50} cm^4 . s . photon^{-1}) The authors also provided NLO parameters for different diameters (4.4 ± 10^{-9} m to 5.2 ± 10^{-9} m) and doping levels Nonlinearity dependence[3] shown in figure 1 of the reference paper Two-photon excited photoluminescence

GaN-AlN QD	FWM	MBE	—	—	—	1500 nm	1.3 ± 10^{-6} esu	[Valdueza-Felip2008]
						—		
		AlN-on-sapphire	20	—	—	—	—	The authors also provided NLO parameter for 200 layers GaN-AlN QD
						—		
				—	—	1.00 ± 10^{-13} s	—	For 1 layer: GaN QD height is 1.1 ± 10^{-9} m and AlN barrier thickness is 3 ± 10^{-9} m
						$1.00 \pm 10^{+3}$ Hz		
Graphene QDs	Z-scan	—	$< 5 \pm 10^{-9}$ m	—	—	355 nm	—	[Wang2019]
						—		
		Water	—	$2.53 \pm 10^{+3}$ m^{-1}	—	$2.6 \pm 10^{+14}$ W m^{-2}	$(5.7 \sim 1.2) \pm 10^{-19}$ m^2 W^{-1}	Details regarding fabrication: www.strem.com/catalog/v/06-0334/44/nanomaterials_1034343-98-0
				—	—	$2.30 \pm 10^{+1}$ m		
						1.00 ± 10^{-11} s	1.40 ± 10^{-11} m W^{-1}	Peak irradiance: $2.5 \pm 10^{+13}$ W m^{-2} to $26 \pm 10^{+13}$ W m^{-2}
						$1.00 \pm 10^{+1}$ Hz		No NLO response is presented at 532 nm and infrared regions. At 355 nm, authors have brought out a clear saturable absorption effect
1D materials								
GaP nanowires	SRS Threshold	Pulsed Laser Vaporization (PLV)	2.10 ± 10^{-7} m	—	Monocrystalline	514.5 nm	—	[Wu2009]
			—	—	—	—	—	Authors studied stimulated Raman scattering from GaP NWs as a function of their length
		Silicon		—	—	4.00 ± 10^{-7} m	—	Raman shift (m^{-1}): $3.62 \pm 10^{+4}$ (TO)/$3.98 \pm 10^{+4}$ (LO)
						CW		
						—		The quality factor for the nanowire segment was measured as Q 18 000 by assuming $g_{\text{Raman}} = 10$ cm/GW (the gain coefficient for GaP bulk material from Rhee *et al* [Rhee1984])

(Continued.)

Table 4B. (Continued.)

Third-Order Nonlinearities								
		Material Properties				Measurement Details	Nonlinear Properties	
Material	Method	Fabrication Solvent/ Substrate	Width Number of layers	Index Abs. coeff. Wavelength	Crystallinity Bandgap Doping Level	Pump Wavelength Peak power Peak irradiance Beam spot size Pulse width Rep. rate	$\chi(3)$ $n_{2,\text{eff}}$ α_2	Reference Additional parameters and comments
s-SWCNT	Z-scan	CoMoCAT catalytic CVD process (SigmaAldrich) Petroleum ether	0.6 ± 10^{-9} m to 1.1 ± 10^{-9} m —	— 22.6 % 1064 nm	— — —	1064 nm — $3.20 \pm 10^{+12}$ W m^{-2} — 4.00 ± 10^{-9} s $1.00 \pm 10^{+1}$ Hz	— — 2.90 ± 10^{-12} m W^{-1}	[Shi2019a] Saturation irradiance: $2.13 \pm 10^{+12}$ W m^{-2} 14% non-saturable absorption
SWCNT	Z-scan	HIPCO SWNT Glass	1.00 ± 10^{-9} m —	— $8.40 \pm 10^{+4}$ m^{-1} 532 nm	— — —	532 nm — $1.60 \pm 10^{+10}$ W m^{-2} 1.20 ± 10^{-5} m 8.00 ± 10^{-9} s $1.00 \pm 10^{+1}$ Hz	(1.4 ± 10^{-15} + i4.3 ± 10^{-16}) m^2 V^{-2} — 7.10 ± 10^{-7} m W^{-1}	[Seo2006] —
SWCNT	Z-scan	CoMoCAT catalytic CVD process (SigmaAldrich) Petroleum ether	—	— 17.2 % 1064 nm	— — —	1064 nm — $3.20 \pm 10^{+12}$ W m^{-2} — 4.00 ± 10^{-9} s $1.00 \pm 10^{+1}$ Hz	— — 5.20 ± 10^{-12} m W^{-1}	[Shi2019a] Saturation irradiance: $2.95 \pm 10^{+12}$ W m^{-2} 12% non-saturable absorption

2D materials								
AlGaN-GaN QW	Nonlinear transm./refl.	MBE c-Sapphire	— 100	— — —	— — —	1500 nm — $7.00 \pm 10^{+10}$ W m^{-2} — 1.00 ± 10^{-13} s $1.00 \pm 10^{+3}$ Hz	5.00 ± 10^{-19} m^2 V^{-2} 2 ± 10^{-17} m^2 W^{-1} 4.00 ± 10^{-10} m W^{-1}	[Rapaport2003] NLO parameters are for GaN/$Al_{0.65}Ga_{0.35}$N/GaN The technique used to measure n_2 was cross-phase modulation. α_2 is due to SA The saturation irradiance was measured using many different pump wavelengths (see figure 3 of the reference paper) Beam radius of 8.5 ± 10^{-5} m for the saturation irradiance measurement Pump and probe polarization: p-polarized Thickness for 1 layer of GaN/$Al_{0.65}Ga_{0.35}$N/GaN 1.2 ± 10^{-9} m/1.5 ± 10^{-9} m/7.8 ± 10^{-10} m [(±3 periods) barrier] Information also for GaN/$Al_{0.15}Ga_{0.85}$N/GaN
Black phosphorus	THG	Exfoliated Glass + AlOx encapsulation	9.50 ± 10^{-9} m 20	— $7.00 \pm 10^{+7}$ m^{-1} 520 nm	— — —	1560 nm — $5.58 \pm 10^{+15}$ W m^{-2} 2.00 ± 10^{-6} m 1.00 ± 10^{-13} s $8.00 \pm 10^{+6}$ Hz	1.64 ± 10^{-19} m^2 V^{-2} — —	[Autere2017] Nonlinearity dependence[3] in figure 4(b) of the reference paper
Black phosphorus	Z-scan	Solvent exfoliation + gradient centrifugation NMP	— 13 to 15	— $3.86 \pm 10^{+2}$ m^{-1} 800 nm	— — —	800 nm — $3.54 \pm 10^{+15}$ W m^{-2} — 1.00 ± 10^{-13} s $1.00 \pm 10^{+3}$ Hz	3.01 ± 10^{-14} esu 2.07 ± 10^{-20} m^2 W^{-1} —	[Xu2017b] Saturation irradiance: $6 \pm 10^{+13}$ W m^{-2} Nonlinearity dependence[3] in table 1 of the reference paper Real part of $\chi^{(3)}$ 28.5% non-saturable absorption

(Continued.)

Table 4B. (Continued.)

Third-Order Nonlinearities								
		Material Properties				**Measurement Details**	**Nonlinear Properties**	
Material	Method	Fabrication Solvent/ Substrate	Width Number of layers	Index Abs. coeff. Wavelength	Crystallinity Bandgap Doping Level	**Pump** Wavelength Peak power Peak irradiance Beam spot size Pulse width Rep. rate	$\chi(3)$ $n_{2,\text{eff}}$ α_2	Reference Additional parameters and comments
Black phosphorus	Z-scan	Nanoplatelets obtained by grinding bulk material and then dispersed NMP/PVA	30 ± 10^{-9} m to 60 ± 10^{-9} m 50 to 100	— around 7% 500 nm to 2000 nm	— — —	800 nm — $1.30 \pm 10^{+16}$ W m^{-2} 4.00 ± 10^{-5} m 1.00 ± 10^{-13} s $1.00 \pm 10^{+3}$ Hz	— 1.20 ± 10^{-13} m^2 W^{-1} 4.50 ± 10^{-10} m W^{-1}	[Zheng2015a] —
Electrochemical graphene oxide (GO)	Z-scan	Electrochemical method/ Vacuum filtration —	3.00 ± 10^{-7} m Thin film	>2.0 above 350 nm — 300 nm to 1800 nm	— 0.88 eV —	800 nm — — 1.00 ± 10^{-5} m 8.50 ± 10^{-14} s $1.00 \pm 10^{+4}$ Hz	— 3.63 ± 10^{-13} m^2 W^{-1} 7.00 ± 10^{-11} m W^{-1}	[Ren2016] Nonlinearity dependence[4] in figures 3 and 4 of the reference paper n_2 is 3.63 ± 10^{-13} m^2 W^{-1} at $8 \pm 10^{+2}$ J m^{-2} n_2 is 2.82 ± 10^{-13} m^2 W^{-1} at $1 \pm 10^{+3}$ J m^{-2} n_2 is 1.91 ± 10^{-13} m^2 W^{-1} at $2 \pm 10^{+3}$ J m^{-2} n_2 is 0.57 ± 10^{-13} m^2 W^{-1} at $4 \pm 10^{+3}$ J m^{-2} Nonlinear absorption coefficient is 7 ± 10^{-11} m W^{-1} at $4 \pm 10^{+3}$ J m^{-2}
GaN-AlN QW	Nonlinear transm./refl.	MBE AlN-on-(0001)sapphire	— 292	— — —	— — —	1550 nm — $1.10 \pm 10^{+13}$ W m^{-2} — 1.00 ± 10^{-13} s $1.00 \pm 10^{+5}$ Hz	5.50 ± 10^{-18} m^2 V^{-2} — —	[Hamazaki2004] Saturation irradiance: $2.7 \pm 10^{+14}$ W m^{-2} Thickness for 1 layer of GaN-AlN: 1.1 ± 10^{-9} m/2.8 ± 10^{-9} m Probe parameters: $\lambda = 1550$ nm Irradiance $= 1.1 \pm 10^{+12}$ W m^{-2} Pulse width $= 1 \pm 10^{-13}$ s Polarization: p-polarized Pump polarization: p-polarized

GaN-AlN QW	FWM	MBE	—	—	—	1500 nm	2.40 ± 10^{-7} esu	[Valdueza-Felip2008]
		AlN-on-sapphire	100	—	—	—	—	Thickness for 1 layer of GaN-AlN QW: 1.5 ± 10^{-9} m/1.5 ± 10^{-9} m
				—	—	—	—	Pump polarization: p-polarized
						1.00 ± 10^{-13} s		
						$1.00 \pm 10^{+3}$ Hz		
Graphene	Z-scan	CVD	—	—	—	435 nm to 1100 nm	—	[Chen2015]
		Quartz	Monolayer	$7.1 \pm 10^{+7}$ m^{-1} to $10.5 \pm 10^{+7}$ m^{-1}	—	—	—	Saturation irradiance: $2.3 \pm 10^{+13}$ W m^{-2} to $2.15 \pm 10^{+14}$ W m^{-2}
				435 nm to 1100 nm	0.2 eV	$2.00 \pm 10^{+14}$ W m^{-2}	3.6 ± 10^{-9} m W^{-1} to 8.6 ± 10^{-9} m W^{-1}	Nonlinearity dependence[1] in figure 3 and in table S1 of the reference paper
						2.5 ± 10^{-5} m to 3.5 ± 10^{-5} m		Authors confirmed via email that α_0 equals $7.1 \pm 10^{+7}$ m^{-1} to $10.5 \pm 10^{+7}$ m^{-1} (typo in the exponent in suppl. info)
						1.50 ± 10^{-13} s		
						$1.00 \pm 10^{+3}$ Hz		
Graphene	Other (add in comments)	CVD	—	—	—	1600 nm	$(\ 6\ \ i\ 9.6) \pm 10^{-16}$ m^2 V^{-2}	[Dremetsika2017]
		Glass	Monolayer	—	—	—	$(\ 1\ \ i\ 1.6) \pm 10^{-13}$ m^2 W^{-1}	Technique: optically-heterodyne-detected optical Kerr effect
				—	0.3 eV to 0.2 eV	$5.00 \pm 10^{+12}$ W m^{-2}	—	Probe parameters: $\lambda = 1600$ nm Irradiance $= 3 \pm 10^{+11}$ W m^{-2} Pulse width $= 1.8 \pm 10^{-13}$ s Beam radius $= 1.5 \pm 10^{-5}$ m
						2.00 ± 10^{-5} m		
						1.80 ± 10^{-13} s		
						$8.20 \pm 10^{+7}$ Hz		Specified $\chi^{(3)}$ values are for $\chi_{xyxy} + \chi_{xyyx}$
Graphene	FWM	CVD	—	—	—	1040 nm	3.00 ± 10^{-17} m^2 V^{-2}	[Jiang2018b]
		Fused silica	Monolayer	—	—	—	—	Nonlinearity dependence[5] in figure 5(d) of the reference paper
				—	0 eV	—	—	Probe parameters:
						2.00 ± 10^{-13} s		$\lambda = 1300$ nm
						$8.00 \pm 10^{+7}$ Hz		Pulse width $= 2.00 \pm 10^{-13}$ s

(Continued.)

Table 4B. (Continued.)

Third-Order Nonlinearities								
		Material Properties				**Measurement Details**	**Nonlinear Properties**	
Material	Method	Fabrication	Width	Index	Crystallinity	**Pump** Wavelength Peak power Peak irradiance Beam spot size Pulse width Rep. rate	$\chi(3)$	Reference
		Solvent/ Substrate	Number of layers	Abs. coeff.	Bandgap		$n_{2,\text{eff}}$	Additional parameters and comments
				Wavelength	Doping Level		α_2	
Graphene	Z-scan	CVD	—	—	—	1930 nm —	—	[Miao2015]
		Quartz	6 to 8	14.9 %	—	$5.75 \pm 10^{+11}$ W m^{-2}	4.58 ± 10^{-11} m^2 W^{-1}	Saturation irradiance: $1 \pm 10^{+10}$ W m^{-2}
				1000 nm to 2500 nm	0 eV	3.50 ± 10^{-5} m 2.80 ± 10^{-12} s $3.23 \pm 10^{+7}$ Hz	—	Nonlinearity also at 1562 nm specified in the reference paper
Graphene	THG	CVD	—	—	—	3100 nm —	8.00 ± 10^{-17} m^2 V^{-2}	[Soavi2018]
		Sapphire	Monolayer	2.3 %	—	$2.40 \pm 10^{+12}$ W m^{-2}	—	Nonlinearity dependence[1, 5] in figures 3(b) and (d) of reference paper
				1250 nm	0.25 eV	4.70 ± 10^{-6} m 3.00 ± 10^{-13} s $8.00 \pm 10^{+7}$ Hz	— η: 1 ± 10^{-11}%	
Graphene	Z-scan	CVD	—	—	—	900 nm —	—	[Thakur2019]
		Quartz	Monolayer	—	—	$4.59 \pm 10^{+13}$ W m^{-2}	1.08 ± 10^{-12} m^2 W^{-1}	Nonlinearity dependence[1, 6] in figures 2(b) and 5(b) of the reference paper
				—	0 eV	— 1.00 ± 10^{-13} s $8.00 \pm 10^{+7}$ Hz	—	

Graphene oxide (GO)	Z-scan	Modified Hummers method/ Self-assembly/ Vacuum filtration process H_2SO_4/ H_2O_2/deionized water/methanol mixture	1.00 ± 10^{-6} m Thin film	— — —	— — —	1560 nm — $3.80 \pm 10^{+12}$ W m^{-2} — 6.70 ± 10^{-14} s $2.00 \pm 10^{+7}$ Hz	— 4.50 ± 10^{-14} m^2 W^{-1} —	[Xu2017a] Nonlinearity dependence[6] in figure 4(a) of the reference paper
Graphene oxide (GO)	Z-scan	Self-assembly H_2SO_4/ H_2O_2/deionized water/methanol mixture	8 ± 10^{-7} m to 2 ± 10^{-6} m Thin film	— — —	— — —	800 nm — — 2.50 ± 10^{-6} m 1.00 ± 10^{-13} s —	— — 4.00 ± 10^{-7} m W^{-1}	[Zheng2014] α_2 is 4.00 ± 10^{-7} m W^{-1} at 32 μJ cm^{-2} Nonlinearity dependence[4] in figure 4(a) of reference paper Information also for reduced Graphene Oxide (rGO)
Graphene oxide (GO) with gold nanoparticles	Z-scan	Vacuum filtration process Water	1.00 ± 10^{-6} m Thin film	— <20% 800 nm	— — —	800 nm — — — — —	— 2.40 ± 10^{-16} m^2 W^{-1} 1.00 ± 10^{-9} m W^{-1}	[Fraser2015] Nonlinearity dependence[7] in figure 4 of the reference paper n_2 of reference GO film is 4 ± 10^{-17} m^2 W^{-1} α_2 of reference GO film is 1.7 ± 10^{-10} m W^{-1} Input fluence is $1.4 \pm 10^{+2}$ J m^{-2}
$Mo_{0.5}W_{0.5}S_2$	Z-scan	CVT Glass	2.20 ± 10^{-5} m Multilayer	— 6.22 ± 10^{-2} (-) 1064 nm	Polycrystalline — —	1064 nm — 8.50 ± 10^{-16} W m^{-2} — 2.50 ± 10^{-11} s $2.00 \pm 10^{+1}$ Hz	[$(4.18 \sim 2.32) \pm 10^{-8}$ + i$(5.73 \sim 1.12) \pm 10^{-11}$] esu $(8.73 \sim 1.47) \pm 10^{-15}$ m^2 W^{-1} $(1.91 \sim 0.78) \pm 10^{-10}$ m W^{-1}	[Bikorimana2016] —

(Continued.)

Table 4B. (Continued.)

Third-Order Nonlinearities								
		Material Properties				**Measurement Details**	**Nonlinear Properties**	
Material	Method	Fabrication Solvent/ Substrate	Width Number of layers	Index Abs. coeff. Wavelength	Crystallinity Bandgap Doping Level	**Pump** Wavelength Peak power Peak irradiance Beam spot size Pulse width Rep. rate	$\chi(3)$ $n_{2,\text{eff}}$ α_2	Reference Additional parameters and comments
MoS_2	THG	Micromechanical exfoliation Si/SiO_2 (285 nm)	0.65 ± 10^{-9} m Monolayer	— — —	— — —	1560 nm $2.70 \pm 10^{+3}$ W — — 1.50 ± 10^{-13} s $5.00 \pm 10^{+7}$ Hz	3.60 ± 10^{-19} m^2 V^{-2} — —	[Autere2018b] Nonlinearity dependence[2] in figure 5 of the reference paper
MoS_2	THG	Micromechanical cleavage Si/SiO_2	— Monolayer	— Close to 0 1560 nm	— — —	1560 nm $8.00 \pm 10^{+3}$ W — 9.30 ± 10^{-7} m 1.50 ± 10^{-13} s $5.00 \pm 10^{+7}$ Hz	— — —	[Säynätjoki2017] Nonlinearity dependence[2, 3, 6] in figures 4 and 5 of reference paper η: 4.76 ± 10^{-8}%
MoS_2	THG imaging	CVD SiO_2/Si (300 nm)	7.00 ± 10^{-10} m Monolayer	— — —	— — —	1560 nm — — 1.80 ± 10^{-6} m 1.50 ± 10^{-13} s $8.90 \pm 10^{+5}$ Hz	2.40 ± 10^{-19} m^2 V^{-2} — —	[Woodward2016] Nonlinearity dependence[1] shown in figures 3(a) and (b) of the reference paper The authors provided also the sheet susceptibilities
MoS_2	Z-scan	Liquid-phase exfoliation technique Cyclohexyl pyrrolidinone	$>8 \pm 10^{-9}$ m 15	— $2.57 \pm 10^{+3}$ m^{-1} 532 nm	— Indirect: 1.2 eV/ direct: 1.8 eV —	532 nm — — — 1.00 ± 10^{-10} s $1.00 \pm 10^{+4}$ Hz	[$(14.1 \sim 6.5) \pm 10^{-11}$ $i(9.9 \sim 3.3) \pm 10^{-12}$] esu $(2.5 \sim 1.2)$ $\pm 10^{-16}$ m^2 W^{-1} $(26.2 \sim 8.8)$ $\pm 10^{-11}$ m W^{-1}	[Wang2014a] Saturation irradiance: $(1.13 \sim 0.52) \pm 10^{+13}$ W m^{-2} The authors also provided NLO parameters for measurements at 515 nm, 800 nm, 1030 nm and 1064 nm

MoS_2	I-scan with microscopic imaging	CVD SiO_2/Si and quartz (300 nm)	— 1, 4, 6	— — —	— — —	1030 nm — — 1.73 ± 10^{-5} m 3.40 ± 10^{-13} s $1.00 \pm 10^{+3}$ Hz	— — $(7.62 \sim 0.15) \pm 10^{-8}$ m W^{-1}	[Li2015] Saturation irradiance: $(64.5 \sim 1.53) \pm 10^{+13}$ W m^{-2}
MoS_2	Z-scan	CVT Glass	2.50 ± 10^{-5} m Multilayer	— 5.03 ± 10^{-1} (-) 1064 nm	Polycrystalline — —	1064 nm — 5.66 ± 10^{-15} W m^{-2} — 2.50 ± 10^{-11} s $2.00 \pm 10^{+1}$ Hz	$(8.71 \sim 1.59) \pm 10^{-10}$ i$(1.50 \sim 0.88) \pm 10^{-11}$ esu $(1.88 \sim 0.48) \pm 10^{-16}$ m^2 W^{-1} $(3.8 \sim 0.59) \pm 10^{-11}$ m W^{-1}	[Bikorimana2016] α_2 due to SA
$MoSe_2$	THG	Micromechanical exfoliation Si/SiO_2 (285 nm)	0.65 ± 10^{-9} m Monolayer	— — —	— — —	1560 nm $2.70 \pm 10^{+3}$ W — — 1.50 ± 10^{-13} s $5.00 \pm 10^{+7}$ Hz	2.20 ± 10^{-19} m^2 V^{-2} — —	[Autere2018b] Nonlinearity dependence^2 in figure 5 of the reference paper
$MoSe_2$	Z-scan	Liquid-phase exfoliation technique Cyclohexyl pyrrolidinone	— Mono or triple	— $7.93 \pm 10^{+2}$ m^{-1} 800 nm	— Indirect: 1.1 eV/ Direct: 1.5 eV —	800 nm — — — 1.00 ± 10^{-13} s $1.00 \pm 10^{+3}$ Hz	i$(1.45 \sim 0.34) \pm 10^{-15}$ esu — $(2.54 \sim 0.60) \pm 10^{-14}$ m W^{-1}	[Wang2014a] Saturation irradiance: $(590 \sim 225) \pm 10^{+13}$ W m^{-2} The authors also provided NLO parameters for measurements at 515 nm, 532 nm, 1030 nm and 1064 nm
$MoTe_2$	Z-scan	Liquid-phase exfoliation technique Cyclohexyl pyrrolidinone	— Mono or triple	— $1.07 \pm 10^{+2}$ m^{-1} 1064 nm	— Indirect: 1.0 eV/ direct: 1.0 eV —	1064 nm — — — 1.00 ± 10^{-10} s $1.00 \pm 10^{+4}$ Hz	[$(0.92 \sim 0.15) \pm 10^{-11}$ i$(2.27 \sim 0.39) \pm 10^{-12}$] esu $(0.160 \sim 0.027) \pm 10^{-16}$ m^2 W^{-1} $(2.99 \sim 0.52) \pm 10^{-11}$ m W^{-1}	[Wang2014a] Saturation irradiance: $(0.19 \sim 0.04) \pm 10^{+13}$ W m^{-2} The authors also provided NLO parameters for measurements at 515 nm, 532 nm, 800 nm and 1030 nm

(Continued.)

Table 4B. (Continued.)

Third-Order Nonlinearities									
		Material Properties				**Measurement Details**	**Nonlinear Properties**		
Material	Method	Fabrication Solvent/ Substrate	Width Number of layers	Index Abs. coeff. Wavelength	Crystallinity Bandgap Doping Level	**Pump** Wavelength Peak power Peak irradiance Beam spot size Pulse width Rep. rate	$\chi(3)$ $n_{2,\text{eff}}$ α_2	Reference Additional parameters and comments	
Reduced GO (rGO)	Z-scan	Self-assembly H_2SO_4/ H_2O_2/deionized water/methanol mixture	8 ± 10^{-7} m to 2 ± 10^{-6} m Thin film	— — —	— — —	800 nm — — 2.50 ± 10^{-6} m 1.00 ± 10^{-13} s —	— 1.00 ± 10^{-13} m^2 W^{-1} —	[Zheng2014] Fully rGO with no oxygen-containing group for optical fluence > 50 μJ cm^{-2} Nonlinearity dependence[4] in figure 4(a) of reference paper Information also for Graphene Oxide (GO)	
WS_2	THG	Micromechanical exfoliation Si/SiO_2 (285 nm)	0.65 ± 10^{-9} m Monolayer	— — —	— — —	1560 nm $2.70 \pm 10^{+3}$ W — — 1.50 ± 10^{-13} s $5.00 \pm 10^{+7}$ Hz	2.40 ± 10^{-19} m^2 V^{-2} — —	[Autere2018b] Nonlinearity dependence[2] in figure 5 of the reference paper	
WS_2	Z-scan	CVT Glass	2.00 ± 10^{-5} m Multilayer	— 2.54 ± 10^{-1} (-) 1064 nm	Polycrystalline — —	1064 nm — 2.30 ± 10^{-15} W m^{-2} — 2.50 ± 10^{-11} s $2.00 \pm 10^{+1}$ Hz	$[(2.31 \sim 0.21) \pm 10^{-8}$ i$(1.75 \sim 0.11) \pm 10^{-11}]$ esu $(5.83 \sim 0.18) \pm 10^{-15}$ m^2 W^{-1} $(5.1 \sim 0.26) \pm 10^{-11}$ m W^{-1}	[Bikorimana2016] α_2 due to SA	

WS_2	Z-scan	Vapor phase sulfurization of metal films Quartz	7.50 ± 10^{-10} m —	— $7.17 \pm 10^{+7}$ m^{-1} 1040 nm	— — —	1040 nm — $2.35 \pm 10^{+14}$ W m^{-2} — 3.40 ± 10^{-13} s $1.00 \pm 10^{+2}$ Hz	$(4.82 \pm 10^{-9} +$ i $1.49 \pm 10^{-8})$ esu 1.28 ± 10^{-14} m^2 W^{-1} 3.07 ± 10^{-8} m W^{-1}	[Dong2016a] Nonlinearity dependence[3] in table 2 and figure 4(d) of the reference paper
WS_2	Z-scan	Vapor phase sulfurization of metal films Fused quartz	— 1 to 3	— $7.17 \pm 10^{+7}$ m^{-1} 1030 nm	— — —	1030 nm — $3.80 \pm 10^{+14}$ W m^{-2} — 3.40 ± 10^{-13} s $1.00 \pm 10^{+2}$ Hz	i 4 ± 10^{-8} esu — 1.00 ± 10^{-7} m W^{-1}	[Zhang2015b] Nonlinearity dependence[1] in table 2 of the reference paper In reference paper, also values for pump and probe at 800 nm and 515 nm
WS_2	Z-scan	CVD Sapphire	7.00 ± 10^{-10} m Monolayer	— $8.88 \pm 10^{+9}$ m^{-1} 800 nm	— — —	800 nm — — 4.00 ± 10^{-7} m 1.00 ± 10^{-13} s $1.00 \pm 10^{+3}$ Hz	— 8.10 ± 10^{-13} m^2 W^{-1} 3.70 ± 10^{-6} m W^{-1}	[Zheng2015b] —
WSe_2	THG	Micromechanical exfoliation Si/SiO_2 (285 nm)	0.65 ± 10^{-9} m Monolayer	— — —	— — —	1560 nm $2.70 \pm 10^{+3}$ W — — 1.50 ± 10^{-13} s $5.00 \pm 10^{+7}$ Hz	1.00 ± 10^{-19} m^2 V^{-2} — —	[Autere2018b] Nonlinearity dependence[2] in figure 5 of the reference paper
WSe_2	THG	Micromechanical exfoliation Fused silica	1.17 ± 10^{-9} m Monolayer	— — —	— 1.65 eV —	1546 nm — — $(0.8 \sim 0.1) \pm 10^{-6}$ m 2.00 ± 10^{-13} s $8.00 \pm 10^{+7}$ Hz	$(0.9 \sim 0.2)$ $\pm 10^{-28}$ m^3 V^{-2} — —	[Rosa2018] Nonlinearity dependence[2, 3] in figures 2 and 4 of the reference paper The authors also provided information for 4, 5, 6, and 9 layers at 1546 nm Specified third-order nonlinearity is the sheet susceptibility

(Continued.)

Table 4B. (Continued.)

Third-Order Nonlinearities								
		Material Properties				**Measurement Details**	**Nonlinear Properties**	
Material	Method	Fabrication Solvent/ Substrate	Width Number of layers	Index Abs. coeff. Wavelength	Crystallinity Bandgap Doping Level	**Pump** Wavelength Peak power Peak irradiance Beam spot size Pulse width Rep. rate	$\chi(3)$ $n_{2,\text{eff}}$ α_2	Reference Additional parameters and comments
WSe_2	Z-scan	CVT Glass	2.20 ± 10^{-5} m Multilayer	— 1.55 ± 10^{-1} (-) 1064 nm	Polycrystalline — —	1064 nm — 8.50 ± 10^{-15} W m^{-2} — 2.50 ± 10^{-11} s $2.00 \pm 10^{+1}$ Hz	$(9.74 \sim 1.19) \pm 10^{-7}$ + i$(6.35 \sim 1.35)$ $\pm 10^{-12}$ esu $(2.47 \sim 1.23)$ $\pm 10^{-13}$ m^2 W^{-1} $(1.9 \sim 0.57)$ $\pm 10^{-11}$ m W^{-1}	[Bikorimana2016] —
WSe_2	Z-scan	Vapor phase sulfurization of metal films Quartz	1.14 ± 10^{-8} m —	— $1.13 \pm 10^{+8}$ m^{-1} 1040 nm	— — —	1040 nm — $8.11 \pm 10^{+13}$ W m^{-2} — 3.40 ± 10^{-13} s $1.00 \pm 10^{+2}$ Hz	(7.2 ± 10^{-10} + i 2.4 ± 10^{-8}) esu 1.87 ± 10^{-15} m^2 W^{-1} 4.80 ± 10^{-8} m W^{-1}	[Dong2016a] Nonlinearity dependence[3] in table 2 and figure 4(d) of the reference paper

Superscripts indicate the work reports the nonlinearity dependence on [1]wavelength/energy, [2]polarization, [3]sample size (width, diameter, thickness, number of layers), [4]input fluence, [5]doping level, [6]pulse length/peak power, [7]concentration.

3.4. Metamaterials: data table and discussion

Team: *Adam Ball, Ksenia Dolgaleva, Daniel Espinosa, Nathaniel Kinsey,* ***Mikko Huttunen (team leader),*** *Dragomir Neshev, Ray Secondo*

3.4.1. Introduction

3.4.1.1. Metamaterials definitions

Efficient NLO interactions are essential for many applications in modern optics. However, they typically require high-irradiance laser sources or long interaction lengths. These requirements cannot be satisfied in the small-footprint optical devices used in many applications. With the growing importance of PICs and ultracompact nanostructured optical devices, enabling efficient NLO interactions at the nanoscale is essential. This may be achieved in nanostructured optical devices with engineered NLO responses. Along these lines, metamaterials offer several advantages such as the ability to confine light for enhanced nonlinearities as well as to shape and control scattered light in new ways [Chen2018, Minovich2015, Husu2012, Litchinitser2018, BinHasan2014, Kauranen2012, Smirnova2016, Chang2018b, Butet2015, Huang2020, Gigli2019a, Reshef2019, DeAngelis2020]. It is also worth noting that in ultra-thin metasurfaces the phase-matching condition is largely relaxed. It is expressed in the form of transverse phase matching, together with mode-matching that replaces the conventional longitudinal phase matching for propagating waves in bulk materials. Recent work also demonstrates that stacked metasurface structures can be longitudinally phasematched by utilizing phase-engineered metasurfaces [Stolt2021].

In this section, we focus on highlighting recent achievements in the broader field of NLO metamaterials and NSMs. Metamaterials are artificial nanostructures comprised of building blocks called meta-atoms, which serve as their structural units. The constituent materials can be metallic [Kauranen2012, Husu2012, BinHasan2014, Litchinitser2018], semiconducting [Vabishchevich2018, Shcherbakov2017] or dielectric [Sain2019, Gigli2019a, Yan2020]. Moreover, one can choose the arrangement geometry of the building blocks in such a way as to change the enhancement mechanism. The structural units can be positioned in a regular or irregular 2D array to form a 2D metamaterial or a metasurface [Kauranen2012, Saad-Bin-Alam2021a]. Alternatively, they can comprise 3D metamaterials through structures such as extruded 2D arrays, multi-layer films [Stolt2021, Suresh2021], or fully 3D nanostructure arrays [Kadic2019]. The latter requires far more sophisticated fabrication approaches and is not discussed in this work. We focus instead on the NLO performance of more practical metasurfaces and planar nanostructures made of metal, semiconductor and dielectric materials.

Since metamaterials are manmade artificial materials different from all other material types considered in this article, a short tutorial on metamaterials is provided below.

3.4.1.2. Mechanisms of nonlinearity enhancement

The power of artificial nanostructures resides in their ability to manipulate the flow of light in a manner not accessible in bulk materials by engineering optical confinement, scattering and interference on a subwavelength scale. An artificial nanostructure thus represents a new material comprised of the structural elements (meta-atoms), which has an optical response that can be very different from that of its constituent materials. There are several mechanisms responsible for the enhancement, suppression and/or sign reversal of the NLO effects attainable in nanostructures. Although most of the mechanisms are based on the resonances associated with the meta-atoms, the origin and type of resonance differ depending on the type of metasurface, as discussed below. Moreover, there are some additional mechanisms of enhancement one can explore, which are briefly described as well.

Metal–dielectric nanostructures with meta-atoms built of noble metals, such as silver and gold, exhibit surface plasmon polaritons and localized surface plasmon resonances (LSPRs) associated with the meta-atoms (often referred to as antennae) [Chen2018, Gomes2020, Lis2014, Wurtz2008, Minovich2015, Krasavin2018, Husu2012, Litchinitser2018, BinHasan2014, Deka2017, Kauranen2012, Smirnova2016, Chang2018b, Butet2015, Huang2020, Gwo2016]. LSPRs are responsible for the localization, and subsequent increase, of the electric field strength in the vicinity of the meta-atoms, which contributes to the enhancement of the NLO interactions. While the metallic meta-atoms can themselves exhibit nonlinearities due to the strong fields outside of the meta-atom, plasmonic structures are typically employed to enhance the electric field within another nonlinear medium, such as lithium niobate or a nonlinear polymer. This allows for the separation and optimization of the confinement and nonlinear material. Yet, the Q- factors of LSPRs are generally very low (<10) due to high absorption losses associated with metals. High ohmic losses and Joule heating limit the applicability of the noble metal metasurfaces in practical NLO devices unless other mechanisms of enhancement are explored in addition to LSPRs [Reshef2019a, Saad-Bin-Alam2021a, Huttunen2019, Khurgin2013]. For example, in regular metal–dielectric metasurfaces, there exist collective resonances called surface lattice resonances (SLRs) [Michaeli2017], which exhibit much higher Q-factors on

the order of 10^3 [Saad-Bin-Alam2021a]. SLRs arise from the coherent scattering of light where the periodic structure introduces interference to amplify the resonance and its associated Q-factor. In this way, the collective scattering of the entire lattice, as opposed to the enhancement provided by a single meta-atom, contributes to the NLO processes much more efficiently.

Dielectric metasurfaces, including those made of semiconductors, have appeared in recent years as a solution to overcome limitations associated with the high losses of metals [Smirnova2016, Gigli2019a, Yan2020, Hopkins2015, Shcherbakov2017, Sain2019, Vabishchevich2018]. Dielectric metasurfaces are typically divided by the values of their refractive indices into high-index ($n > 3.5$), such as Si, GaAs, Ge, mid-index ($2 < n < 3.5$), such as TiO_2, Se, SiC, Si_3N_4, and low-index ($n < 2$), such as silica- and polymer-based metasurfaces, which are not commonly used in NLO due to their poor confinement or weak NLO characteristics [Yan2020]. The primary mechanisms of enhancement of the NLO interactions in dielectric metasurfaces are electric and magnetic Mie resonances associated with their individual building blocks. These resonances result in moderate Q-factors of 10–100, depending upon the index [Rybin2017], and fields localized within the antenna, enabling enhanced effective NLO responses. In this sense, their nonlinearity is derived from the nanoantenna's constituent material, coupling the linear index and nonlinearity. While this coupling generates some restrictions in the case of second-order nonlinearities, for third-order effects, higher index (needed for high-Q) materials also generally exhibit larger nonlinearities [Sheik-Bahae1990a]. High-quality-factor phase-gradient dielectric metasurfaces with a Q-factor around 2500 have recently been demonstrated and hold the potential for NLO applications and on-chip lasing [Lawrence2020]. Moreover, the NLO performance of dielectric metasurfaces can be boosted by exploiting multimode interference, resulting in Fano resonances [Hopkins2015] or non-radiative anapole modes [Yang2018a]. Dielectric metasurfaces hold promise for infrared imaging [Camacho-Morales2021], harmonic generation and other areas of application of NLO processes [Yan2020].

Photonic bound states in the continuum (BIC) structures create localized eigenstates with an infinite lifetime coexisting with the continuous spectrum of radiative modes [Bykov2020] and complement the more general photonic topological insulating structures [Khanikaev2013]. Localized types of practical BIC nanostructures are a subgroup of dielectric metamaterials where a special type of resonance, having an ultra-high Q-factor on the order of 10^7 and higher, is employed [Koshelev2019a, Wang2020a, Koshelev2019b, Koshelev2020, Bernhardt2020, Liu2019b, Azzam2021]. They represent localized states with energies embedded in the continuum of the radiating states. The basic idea behind BICs is the lack of coupling between the resonant mode and all the radiation channels of the surrounding space. Different BICs can be categorized based on the radiation suppression mechanisms. In practice, infinitely high Q-factors of BICs are limited by finite sample sizes, material absorption, symmetry breaking and fabrication imperfections. These limitations result in quasi-BICs with large but finite Q-factors, rendering the opportunity for radiation collection, important for practical nonlinear photonic devices. Dynamical nonlinear image tuning via polarization and wavelength tuning in BIC nanostructures has been experimentally demonstrated [Xu2019], opening the door for application of such nanostructures in tunable displays, nonlinear holograms and other areas.

Epsilon-near-zero (ENZ) nanostructures [Reshef2019, Neira2015, Alam2018, Suresh2021, Wen2018, Deng2020, Yang2019] represent a new group of metamaterials designed in such a way that the real part of the effective dielectric permittivity is vanishingly small at a certain wavelength called zero-permittivity wavelength λ_{ENZ}. In contrast, *near-zero-index* (NZI) metamaterials have the effective refractive index n_{eff} vanishing at a specific wavelength called zero-index wavelength λ_{ZI}. Such materials are generally achieved through the combination of metal and dielectric constituents or through the use of resonant structures [Kinsey2019]. There are several mechanisms of enhancement of the NLO interactions acting as the basis of ENZ and NZI metamaterials. First, near the ENZ/NZI wavelength, the strong dispersion of the index gives rise to slow-light propagation, which results in temporal compression and enhancement of the electric field [Khurgin2010]. Second, the small magnitude of the permittivity in the ENZ region gives rise to additional electric field-enhancement, through the continuity of the normal component of the displacement field $D_\perp$. Lastly, ENZ and NZI provide reduced phase advance within the bulk and facilitate easier phase matching. However, it should be noted that these properties result primarily from slow light effects and are not present in NZI schemes which maintain a finite group velocity [Khurgin2019, Khurgin2020].

3.4.1.3. Historical development

The precursors to the rise and development of the field of metal–dielectric NLO metasurfaces were the earlier demonstrations in the 1980s of the benefit of surface roughness in surface-emitted second- and third-order NLO processes [Chen1981, Shalaev1998] exhibiting several-orders-of-magnitude enhancement in comparison to harmonic generation from a smooth surface. Experiments on hyper-Rayleigh scattering (HRS), reported at the end of the 1990s, have served as the first formal demonstrations of incoherent SHG

from spherical gold and silver nanoparticles [Dadap1999, Vance1998]. Noble metal nanoparticles of different dimensions and shapes have been explored in later HRS studies [Hao2002, Nappa2006, Butet2010a, Butet2010b], performed in the 2000s, with an emphasis on the interplay between multipoles [Nappa2006, Butet2010a]. SHG from non-spherical plasmonic objects [Bouhelier2003, Nahata2003, Danckwerts2007, Hanke2012] (before 2012) and more advanced 3D plasmonic nanostructures [Zhang2011, Cai2011, Pu2010, Park2011] (after 2010) have also been investigated.

Structured plasmonic surfaces for efficient NLO interactions were proposed [Wokaun1981, Reinisch1983] and later experimentally demonstrated [Wokaun1981, Coutaz1985] in the 1980s by SHG generation off an extended metal grating into the first order of diffraction. The first experimental demonstration of the NLO effects in a plasmonic array of meta-atoms was SHG in an array of L-shaped gold nanoparticles [Lamprecht1997, Tuovinen2002, Canfield2004] (late 1990s–early 2000s), followed by a split-ring resonator (SRR) metasurface with magnetic resonances [Linden2012, Klein2006, Feth2008] (2006–2012). These works laid the foundation to the rapidly evolving field of plasmonic metasurfaces for efficient NLO interactions.

The study of resonant dielectric nanostructures is a relatively new research direction in the field of nanophotonics that started a decade ago [Zhao2009, Schuller2007]. Employing sub-wavelength dielectric nanoparticles with Mie resonances for engineering optical metasurfaces with strong NLO responses resulted in the demonstration of enhanced SHG, THG, FWM and other NLO interactions without paying the cost of high losses associated with metal–dielectric nanostructures [Minovich2015, Smirnova2016, Liu2018a, Liu2018b, Kivshar2018, Grinblat2017a, Grinblat2017b]. Mie-resonant silicon and AlGaAs nanoparticles have received considerable attention for nonlinear frequency generation [Liu2018a, Liu2018b].

Spurred by developments in solid-state physics, work in dielectric metasurfaces has more recently broadened to encompass the physical effects of optical topology, enabling robust unidirectional propagation and control over scattering [Khanikaev2013]. Such effects have been explored in the nonlinear regime to realize devices such as lasers [Bandres2018] and switches [Shalaev2019] for integrated photonics (see on-chip waveguiding materials category in section 3.6). Among the many physical effects being explored, BIC structures represent a special case for NLO due to their ability to achieve high Q-factors [Koshelev2019a, Wang2020a, Koshelev2019b, Koshelev2020, Bernhardt2020, Liu2019b, Azzam2021] and are being actively explored. Although BICs were mathematically predicted a long time ago and were investigated in other fields of physics in the 1960s–1970s [Fonda1963, Cumpsty1971], the first experimental demonstrations of BIC-based photonic devices were performed only in 2016 [Hsu2016].

ENZ and NZI metamaterials represent other emerging classes of NSMs for efficient NLO interactions. The research in the field started in the 2010s with a plethora of theoretical works [Ciattoni2010a, Ciattoni2010b, Vincenti2011, Ciattoni2012] predicting enhanced NLO interactions in media with vanishing permittivity, which preceded the first experimental demonstrations both in homogeneous thin films and effective ENZ metastructures [Alam2016, Kinsey2015a, Luk2015, Capretti2015, Caspani2016]. Following these works, ENZ nanostructures have been proposed, offering tunability and unprecedented strength and tailorability of NLO interactions [Neira2015, Alam2018, Suresh2021, Wen2018].

3.4.1.4. Metamaterial-related best practices and considerations when performing NLO measurements

Among the best experimental practices for a proper assessment of the NLO performances of a metamaterial, the following rules-of-thumb can be recommended. If possible, one needs to provide information about the estimated values of the nonlinearities per meta-atom. Since some of the described systems are fragile and can melt under even moderate levels of optical power in a free-space excitation setup, one must follow precautions to avoid optical damage, and to ensure reproducibility of the obtained NLO results. Additionally, as efforts to realize higher Q-factor structures emerge, analysis should also account for the strong dispersion near these resonances. For example, not all of the incident excitation power may be captured by the resonator [Shcherbakov2019] and the effect of pulse chirp near the resonance will begin to play a role in the analysis and extraction of effective NLO parameters. In the end, the caveats and best practices are the same as those listed in section 2, with enhanced focus on damage, thermal nonlinearities, etc due to the relatively strong absorption of plasmonic structures.

3.4.1.5. Description of general table outline

Tables 5A and B show a representative list of, respectively, second-order and third-order NLO properties of metamaterials taken from the literature since 2000, with the entries arranged in alphabetical order. Our aim has been to compile the most relevant advances in NLO metamaterials since 2000. Because numerous studies have been performed during the last two decades, not all of them could be tabulated and/or referenced here.

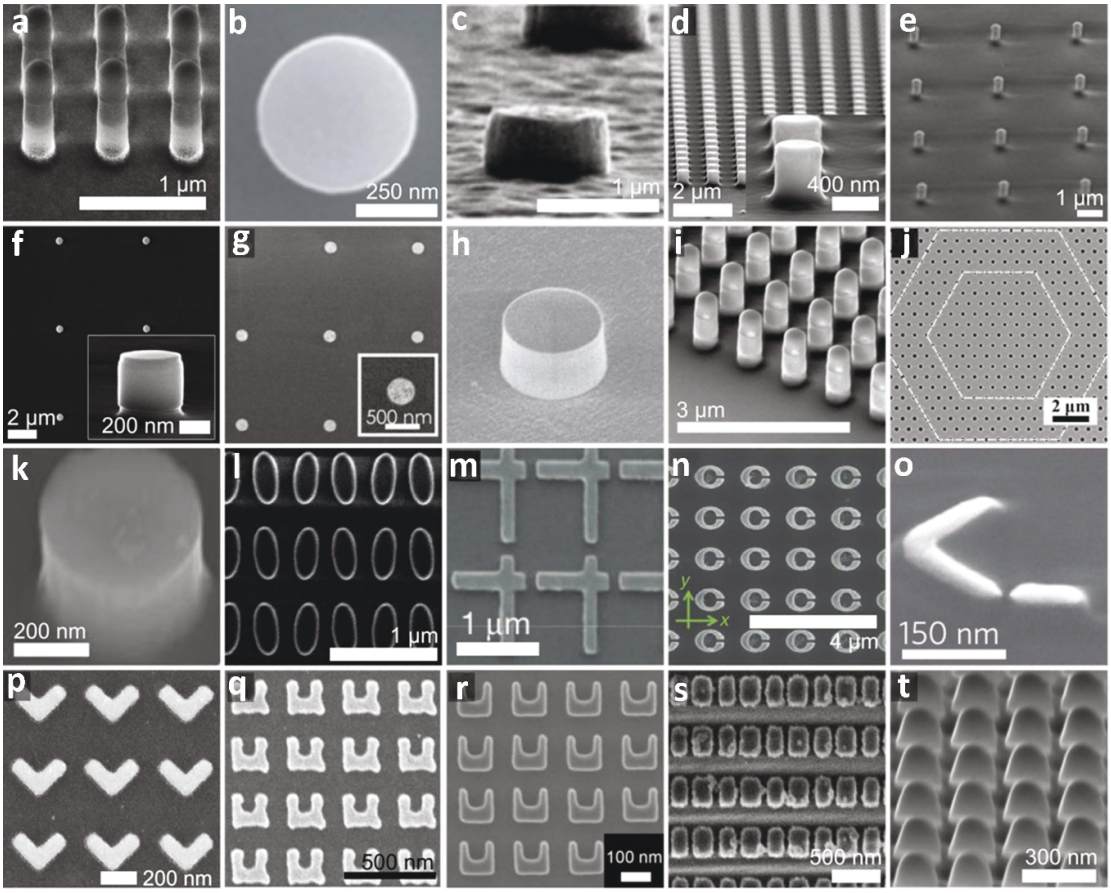

Figure 4. SEM images of metamaterial devices with second-order nonlinear properties. The labels of the sub-figures correspond to the labels given in table 5A. Panels (a)–(d), (g), (k), (l), (p), and (r)–(t) are reprinted with permission from [Liu2016a, Xu2020, Sautter2019, Marino2019a, Camacho-Morales2016, Cambiasso2017, Anthur2020, Czaplicki2018, Wen2018, Bernhardt2020, Semmlinger2018], ACS. Panels (m) and (o) are reprinted with permission from [Lee2014, Celebrano2015], Springer Nature. Panels (i) and (n) are reprinted under CC BY license from [Liu2018a, Wolf2015]. Panels (e), (f), (j) and (q) are reprinted with permission from [Gili2016, Gigli2019b, Wang2020a, Klein2007], ©2007, 2016, 2019, 2020 Optica Publishing Group. Panel (h) is reprinted with permission from [Koshelev2020], AAAS.

Instead, the studies highlighted here are only representative works, where extra care has been taken in the characterization of the investigated metamaterial following the recommendations in the section above and the best practices in section 2. Furthermore, our focus is on the studies that report NLO coefficients (e.g., $\chi^{(2)}$, $\chi^{(3)}$, $n_{2(\mathrm{eff})}$, α_2, etc). Many studies exist where the investigated metamaterial has been shown to result in enhancement of NLO signals when compared to some reference material/system. In order to restrict our scope, we chose not to tabulate works providing only enhancement factors, but instead focused on investigations also reporting NLO coefficients and/or conversion efficiencies. An interested reader is referred to [Chen2018, Minovich2015, Krasavin2018, Husu2012, Litchinitser2018, BinHasan2014, Kauranen2012, Smirnova2016, Chang2018b, Butet2015, Huang2020, Gigli2019a, Reshef2019, DeAngelis2020] for a broader perspective of the topic.

Tables 5A and B are subdivided into 'Material properties', 'Measurement details' and 'Nonlinear properties'. The main material properties that we have tabulated are the material(s), fabrication technique, sample thickness, material crystallinity, substrate and reference to the sub-figure in figures 4 and 5 showing the fabricated device. All reported experiments have nominally been performed at room temperature. Figure 4 shows SEM pictures of devices with second-order NLO responses, while figure 5 shows SEM pictures of devices with third-order NLO responses. The main pump parameters have also been tabulated, along with the enhancement mechanism utilized in the sample. Within each column the information is given in the order of the header description, and the NLO technique used is provided in the 'Method' column. In table 5A, we list the overall conversion efficiency η and/or absolute value of the effective susceptibility as the NLO parameters of key importance. In table 5B, in addition to the above parameters, the effective n_2 and α_2 values have also been listed where relevant.

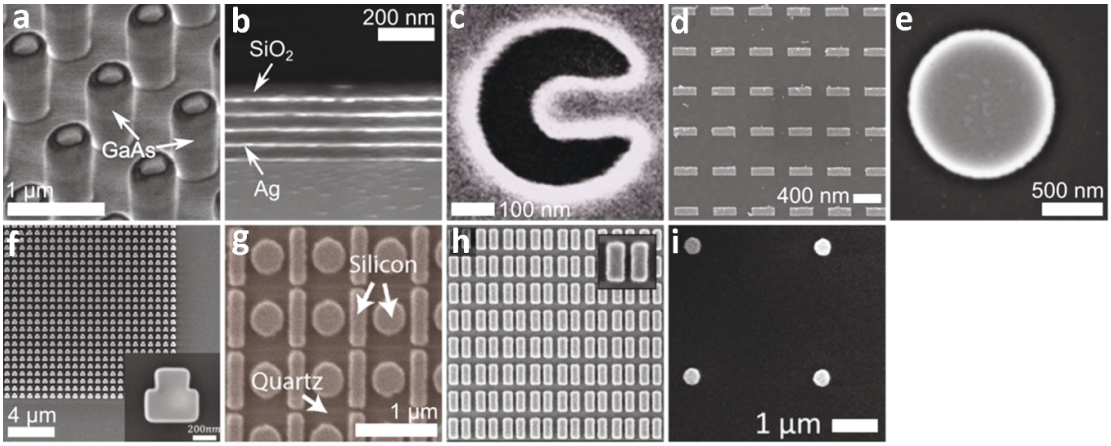

Figure 5. SEM images of metamaterial devices with third-order nonlinear properties. The labels of the sub-figures correspond to the labels given in table 5B. Panels (a), (b), (e), (g), (h), and (i) are reprinted with permission from [Zubyuk2019, Suresh2021, Grinblat2017b, Yang2015, Koshelev2019b, Shcherbakov2014], ACS. Panel (c) is reprinted with permission from [Melentiev2013], ©2013 Optica Publishing Group. Panel (d) is reprinted with permission from [Lee2014, Celebrano2015], Springer Nature. Panel (f) is reprinted under CC BY license from [Liu2019b].

3.4.2. Discussion

3.4.2.1. Advancements and remaining challenges for metamaterials

Because most of the early works were focused on metallic nanoparticles, *de facto* metamaterials of that era, a major advancement in the field of metamaterials can be seen to be the gradual shift from metals to the lower-loss semiconductors and dielectric nanomaterials [Grinblat2017a, Grinblat2017b, Semmlinger2018, Koshelev2019b]. New mechanisms of enhancement, associated with these new kinds of metamaterials, including ENZ, BIC and Fano resonances, have clearly diversified from the early approaches that were almost solely based on material resonances [Czaplicki2018, Koshelev2020]. Apart from the fundamental studies of NLO phenomena, dielectric metasurfaces have enabled the observation of such challenging effects as SPDC. Recently, for the first time, the generation of photon pairs via SPDC in lithium niobate quantum optical metasurfaces [Santiago-Cruz2021] and in a single AlGaAs nanocylinder [Marino2019b] has been demonstrated. By engineering the quantum optical metasurface, the authors demonstrated tailoring of the photon-pair spectrum in a controlled way [Santiago-Cruz2021]. These achievements lay the foundation for the application of dielectric metasurfaces in quantum light generation.

Furthermore, a generally progressing trend is visible in the achieved NLO parameters where newer NLO metamaterials seem to (clearly) outperform their earlier counterparts. As an example, many of the recent investigations of dielectric and semiconducting metasurfaces demonstrate conversion efficiencies on the order of $\sim 10^{-3}$ % for SHG [Lee2014, Gili2016, Sautter2019, Xu2020] and on the order of $\sim 10^{-4}$ % for THG [Grinblat2017b, Koshelev2019b]. In contrast, conversion efficiencies achieved in earlier works have been around 2×10^{-9} % for SHG and 3×10^{-10} % for THG [Klein2008].

NLO metasurfaces have recently started gaining popularity as efficient sources of THz radiation, as this frequency range is not easily attainable by conventional methods of light generation. There is a growing number of works where THz generation by DFG off a metasurface is reported [Luo2014, Keren-Zur2019, Polyushkin2011, Tal2020, McDonnell2021]. These results compare favorably with the more standard method of THz generation by DFG in bulk crystals. Specifically, the measured sheet NLO susceptibility $\sim 10^{-16}$ m^2 V^{-1} far exceeds that of thin films and bulk non-centrosymmetric materials [Luo2014]. On the other hand, the extraction of the associated NLO coefficients has only been performed in [Luo2014], leaving this a development area for future studies. There is very little knowledge about NLO parameters of metamaterials at THz frequencies, and it is highly advisable for research works to report such values for this frequency window.

On the design side, significant improvements have been made in the development of new analytical [Saad-Bin-Alam2021b] and numerical [Butet2016, Blechman2019, Noor2020] methods for designing NLO metasurfaces optimized for some specific NLO interactions.

Further work is in progress to make NLO metamaterials functional in real-life applications. A partly connected challenge is to develop nanofabrication techniques to the level where fabrication of 3D NLO metamaterials becomes a routine task [Stolt2021]. When these achievements can be combined with recent advances in phase-engineered metasurfaces [Chen2018], one could envisage 3D phase-matched metamaterials that could potentially boost efficiencies up to the levels adequate for practical applications. We

note that at that stage, linear absorption/scattering losses would start playing a role [Stolt2021], and actions to mitigate their detrimental effects should be taken.

3.4.2.2. Recommendations for future works on metamaterials

It would be extremely beneficial if future publications would in general report more extensive details of the experimental parameters alongside the NLO parameters of the studied metamaterials (see our earlier recommendations for 'best practices'). For example, oftentimes publications report only the relative NLO enhancement factors of the metamaterials, making it difficult to estimate the potential importance of the studies. Therefore, we recommend that, in future works, at least the parameters listed in the tables reported here be properly quantified and reported.

In many cases, it would also be important to quantitatively characterize individual meta-atoms acting as the building blocks in the metamaterials (see, for example, [Saad-Bin-Alam2021b]). If such information becomes more abundantly available, designing next-generation NLO metamaterials would become an easier task. Furthermore, such data would improve the transparency of the work because it would facilitate estimating the success of the demonstrated enhancement mechanism and the potential importance of the performed study.

Finally, we recommend the community to continue their effort to estimate the damage thresholds of various metamaterial platforms and to study their possible damage mechanisms. We consider such efforts particularly useful when NLO metamaterials reach the level of maturity where applications start to emerge. At that stage, the relevant parameters should not be limited only to conversion efficiency/susceptibility/n_2 values, but can include the measured power of frequency-converted light. In this case, such information becomes critical for an application-oriented researcher to be able to estimate whether the studied metamaterial system could be scaled up in area to be used with high-power pump lasers.

3.4.3. Data table for metamaterials

Table 5A. Second-order NLO properties of metamaterials from representative works since 2000. Legend for superscripts: see below the table.

Second-Order Nonlinearities								
Material Properties		**Measurement Details**		**Nonlinear Properties**				
			Pump					
Material Substrate Fabrication Thickness Crystallinity	SEM image	Method	Wavelength Peak irradiance Beam waist Pulse width Rep. rate	η (%)[a]	$\lvert\chi^{(2)}\rvert$ (m V^{-1})[a]	Enhancement mechanism	Additional parameters and comments	Reference
GaAs/AlGaO GaAs MBE/e-beam lithography 0.3 μm Monocrystalline/monocrystalline	Figure 4(a)	SHG	1020 nm 3.4 ± 10^7 MW m^{-2} 3 μm 0.12 ps 80 000 kHz	2 ± 10^{-3}%/ 1.5 ± 10^{-8} W^{-1}	—	Magnetic dipole resonance	—	[Liu2016a]
(110)-GaAs Fused silica MOCVD/e-beam lithography 0.4 μm Monocrystalline	Figure 4(b)	SHG	1450 nm 1.2 ± 10^7 MW m^{-2} 2 μm 0.255 ps 80 000 kHz	3.00 ± 10^{-3}	—	—	—	[Xu2020]
(111)-GaAs Fused silica MOCVD/e-beam lithography 0.4 μm Monocrystalline	Figure 4(c)	SHG	1556 nm 1.0 ± 10^7 MW m^{-2} — 0.1 ps 80 000 kHz	4.80 ± 10^{-3}	—	—	—	[Sautter2019]
$Al_{0.18}Ga_{0.82}As$/AlOx GaAs MBE/e-beam lithography 0.4/1.0 μm Monocrystalline/amorphous	—	SHG	1550 nm 1.6 ± 10^7 MW m^{-2} — 0.15 ps —	1 ± 10^{-3}%/ 1.5 ± 10^{-7} W^{-1}	—	—	—	[Ghirardini2017]

(Continued.)

Table 5A. (Continued.)

Second-Order Nonlinearities								
Material Properties		**Measurement Details**		**Nonlinear Properties**				
			Pump					
Material Substrate Fabrication Thickness Crystallinity	SEM image	Method	Wavelength Peak irradiance Beam waist Pulse width Rep. rate	η (%)[a]	$\lvert\chi^{(2)}\rvert$ (m V^{-1})[a]	Enhancement mechanism	Additional parameters and comments	Reference
$Al_{0.18}Ga_{0.82}As$/AlOx GaAs MBE/e-beam lithography 0.4/1.0 μm Monocrystalline/amorphous	Figure 4(d)	SHG	1550 nm 5 ± 10^6 MW m^{-2} 25 μm 0.16 ps 1000 kHz	2 ± 10^{-6} W^{-1}	—	—	—	[Marino2019a]
$Al_{0.18}Ga_{0.82}As$/AlOx GaAs MBE/e-beam lithography 0.4/1.0 μm Monocrystalline/amorphous	Figure 4(e)	SHG	1554 nm 1.6 ± 10^7 MW m^{-2} — 0.15 ps —	1.10 ± 10^{-3}	—	—	—	[Gili2016]
$Al_{0.18}Ga_{0.82}As$/AlOx GaAs MOCVD/e-beam lithography 0.35/1.0 μm Monocrystalline/amorphous	Figure 4(f)	SHG	1550 nm — 2.36 μm 0.16 ps 1000 kHz	6.5 ± 10^{-6} W^{-1}	—	—	—	[Gigli2019b]
$Al_{0.2}Ga_{0.8}As$ Fused silica MOCVD/e-beam lithography 0.3 μm Monocrystalline	Figure 4(g)	SHG	1556 nm 7.0 ± 10^7 MW m^{-2} 1.1 μm 0.5 ps 5000 kHz	8.50 ± 10^{-3}	—	—	—	[Camacho-Morales2016]
AlGaAs SiO_2/ITO/SiO_2 e-beam lithography 0.635 μm Monocrystalline	Figure 4(h)	SHG	1570 nm — 1.8 μm 2 ps 5144 kHz	1.3 ± 10^{-6} W^{-1}	—	Quasi-BIC, Mie resonance	—	[Koshelev2020]

GaAs/AlGaO GaAs MBE/e-beam lithography 0.45 μm Monocrystalline/monocrystalline	Figure 4(i)	SHG	1570 nm — 1.5 μm 0.04 ps 1 kHz	2.30 ± 10^{-4}	—	—	—	[Liu2018a]
GaN Silicon MOCVD, PECVD, e-beam lithography 0.2 μm Monocrystalline	Figure 4(j)	SHG	1543.55 nm — — CW —	2.4 ± 10^{-2} W^{-1}	—	Quasi-BIC at SH and cavity resonance at FH	—	[Wang2020a]
GaP nanoantennas GaP e-beam lithography 0.2 μm Monocrystalline	Figure 4(k)	SHG	910 nm 2 ± 10^{9} MW m^{-2} — 0.18 ps 100 kHz	2 ± 10^{-4}%/ 4 ± 10^{-9} W^{-1}	—	Scattering resonance and surface effect	—	[Cambiasso2017]
GaP nanodimers Sapphire MOCVD on GaAs then transfer-bonded to Sapphire, e-beam lithography 0.15 μm Monocrystalline	Figure 4(l)	SHG	1190–1220 nm 100 MW m^{-2} 50 μm CW —	2 ± 10^{-5}%/ 5 ± 10^{-7} W^{-1}	—	Quasi-BIC in arrays with slight asymmetry in nanoparticles	—	[Anthur2020]
GaP nanodimers Sapphire MOCVD on GaAs then transfer-bonded to Sapphire, e-beam lithography 0.15 μm Monocrystalline	Figure 4(l)	SHG	1190–1220 nm 1.0 ± 10^{5} MW m^{-2} 50 μm 0.2 ps —	4 ± 10^{-3}%/ 1 ± 10^{-3} W^{-1}	—	Quasi-BIC in arrays with slight asymmetry in nanoparticles	—	[Anthur2020]
Gold/InGaAs/AlInAs MQW InP MBE 0.1/0.03/0.656 μm Amorphous/monocrystalline/monocrystalline	Figure 4(m)	SHG	8000 nm 150 MW m^{-2} 17.5 μm 400 000 ps 250 kHz	2.00 ± 10^{-4}	55 ± 10^{-8} (yyy)	MQW enhancement	—	[Lee2014]

(Continued.)

Table 5A. (Continued.)

Second-Order Nonlinearities								
Material Properties		**Measurement Details**		**Nonlinear Properties**				
Material Substrate Fabrication Thickness Crystallinity	SEM image	Method	**Pump** Wavelength Peak irradiance Beam waist Pulse width Rep. rate	η (%)[a]	$\lvert\chi^{(2)}\rvert$ (m V^{-1})[a]	Enhancement mechanism	Additional parameters and comments	Reference
Gold/InGaAs/InAlAs MQW InP e-beam lithography 1 μm Amorphous/monocrystalline/monocrystalline	Figure 4(n)	SHG	10 100 nm — 50 μm 12 000 ps 1 kHz	2.3 ± 10^{-3}W W^{-2}	—	Resonators on MQWs	—	[Wolf2015]
Gold nanoantenna Fused silica Focused ion beam lithography 0.04 μm Monocrystalline	Figure 4(o)	SHG imaging	1560 nm 1.69 ± 10^{7} MW m^{-2} 0.7 μm 0.12 ps 80 000 kHz	5 ± 10^{-10} W^{-1}	—	Multiresonant antenna	—	[Celebrano2015]
Gold nanoparticle arrays Fused silica e-beam lithography 0.02 μm Amorphous	Figure 4(p)	SHG	1150 nm 1.2 ± 10^{5} MW m^{-2} — 0.2 ps 80 000 kHz	2.50 ± 10^{-9}	—	Collective lattice effect	—	[Czaplicki2018]
Gold nanoparticles Embedded in gelatin matrix e-beam lithography 0.15 μm —	—	SHG imaging	794 nm — — 0.18 ps 76 000 kHz	—	1 ± 10^{-23} (esu)	—	—	[Butet2010b]
Gold split-ring resonators Fused silica e-beam lithography 0.025 μm Amorphous	Figure 4(q)	SHG	1500 nm 0.0077 MW m^{-2} — 0.17 ps 81 000 kHz	2.00 ± 10^{-9}	—	—	—	[Klein2007]

TiN Sapphire Pulsed laser deposition/e-beam lithography 0.05 μm Monocrystalline	Figure 4(r)	SHG	1040 nm 1.2 ± 10^{8} MW m^{-2} 2 μm 0.2 ps 80 000 kHz	—	—	LSPR at the fundamental frequency, ENZ at the SH frequency	—	[Wen2018]
WS_2/Silicon BK-7 PECVD, e-beam lithography -/0.16 μm Monocrystalline	Figure 4(s)	SHG	832 nm — 6 μm 0.08 ps 80 000 kHz	—	—	Quasi-BIC	—	[Bernhardt2020]
ZnO nanodisks Soda lime glass Sputtering/focused ion beam lithography 0.15 μm Polycrystalline	Figure 4(t)	SHG	394 nm 1.68 ± 10^{7} MW m^{-2} 8.5 μm 0.205 ps 250 kHz	7.00 ± 10^{-7}	9.6 ± 10^{-13} (d-coefficient)	Magnetic dipole resonance	—	[Semmlinger2018]

[a] Units as illustrated unless otherwise indicated in the table.

Table 5B. Third-order NLO properties of metamaterials from representative works since 2000. Legend for superscripts: see below the table.

Third-Order Nonlinearities								
Material Properties		**Measurement Details**		**Nonlinear Properties**				
			Pump					
Material Substrate Fabrication Thickness Crystallinity	SEM image	Method	Wavelength Peak irradiance Beam waist Pulse width Rep. rate	η (%)[a] n_2 (m^2 W^{-1}) α_2 (m W^{-1})	$\chi^{(3)}$ (m^2 V^{-2})[a]	Enhancement mechanism	Additional parameters and Comments	Reference
(100)-GaAs/AlGaO GaAs MBE/e-beam lithography 0.3 μm Monocrystalline	Figure 5(a)	I-scan	830 nm 2.5 ± 10^7 MW m^{-2} 10 μm 0.06 ps 80 000 kHz	— — —	—	Higher free-carrier generation rate	Saturation irradiance: 1.6 ± 10^7 MW m^{-2}	[Zubyuk2019]
Ag nanoantenna/SiO_2 Fused silica e-beam evaporation 0.016/0.065 μm Amorphous	Figure 5(b)	Z-scan	410–560 nm — — 28 ps 0.05 kHz	— 1.2 ± 10^{-12} 1.5 ± 10^{-5}	—	ENZ	—	[Suresh2021]
Al split hole resonator/- 40 nm of fused silica e-beam lithography/FIB 0.2 μm Amorphous	Figure 5(c)	THG	1560 nm 10 MW m^{-2} 2.15 μm 0.2 ps 70 000 kHz	1.0 ± 10^{-3} — —	— — —	Plasmon resonance and lightning-rod effect	—	[Melentiev2013]
Au nanoantenna/ITO Fused silica e-beam lithography 0.05 μm —	Figure 5(d)	Z-scan	1240 nm 1.5 ± 10^6 MW m^{-2} — 0.14 ps —	— 3.7 ± 10^{-13} 2.4 ± 10^{-7}	—	ENZ + optimized field coupling and enhancement by antennae	—	[Alam2018]
Au nanoparticle Fused silica Electrodeposition 0.15 μm Amorphous	—	Z-scan	600 nm 8.0 ± 10^8 MW m^{-2} 1.5 μm 0.05 ps —	— 2.4 ± 10^{-15} 9.97 ± 10^{-8}	(0.28–1.48i) $\pm 10^{-16}$	ENZ + Au interband transition resonance	$\chi^{(3)}$ for 600 nm at 60° and (0.18–1.48i)$\pm 10^{-17}$ for 550 nm at 20°	[Neira2015]

Ge nanodisk Borosilicate glass e-beam lithography 0.2 μm Amorphous	Figure 5(e)	THG	1650 nm 0.8 MW m^{-2} — 0.18 ps 100 kHz	1.0 ± 10^{-3} — —	2.8 ± 10^{-16}	Higher-order (anapole) modes	—	[Grinblat2017b]
Si nanoblock Quartz e-beam lithography 0.5 μm Monocrystalline	Figure 5(f)	THG	1587 nm — — 5 ps —	1.4 ± 10^{-8} W^{-2} — —	—	Quasi-BIC in arrays with slight asymmetry in nanoparticles	—	[Liu2019b]
Si nanoantenna Quartz LPCVD/e-beam lithography 0.12 μm Polycrystalline	Figure 5(g)	THG	1350 nm 0.32 MW m^{-2} — 0.25 ps 1 kHz	1.2 ± 10^{-4} — —	—	High-Q Fano resonance	—	[Yang2015]
Si nanoantenna Fused silica PECVD, e-beam lithography 0.538 μm Amorphous	Figure 5(h)	THG	1425 nm — — 0.2 ps 80 000 kHz	1.0 ± 10^{-4} — —	—	Quasi-BIC in arrays with broken symmetry	—	[Koshelev2019b]
Si nanodisk SOI E-beam lithography 0.26 μm Monocrystalline	Figure 5(i)	THG	1260 nm 0.5 MW m^{-2} — 0.2 ps 80 000 kHz	0.8 ± 10^{-5} — —	—	Magnetic response	—	[Shcherbakov2014]

[a] Units as illustrated unless otherwise indicated in the table.

3.5. Fiber waveguiding materials: data table and discussion

***Team: John Ballato (team leader)**, Peter Dragic*

3.5.1. Introduction

3.5.1.1. Background information

Our understanding and use of NLO are very much intertwined with the history and development of fiber optics. This is because optical fibers are unique tools for studying and utilizing NLO phenomena due to their combination of low loss, long lengths, small core sizes and resulting small mode diameters. Indeed, the first observations of nonlinearities [Stolen1972, Ippen1972, Stolen1974, Hill1974] in fibers are contemporaneous with the first low loss fibers themselves [Keck1972a, Keck1972b]. Furthermore, phase matching of NLO processes in optical fibers can be achieved in more than one way [Stolen1974, Stolen1981]. First, in the case of a multimode fiber, different optical modes across a wide span of wavelengths, for example the signal and idler in FWM, may be found which possess the same propagation constant. Alternatively, the design of the fiber can be suitably tailored to control (e.g., 'flatten') the dispersion curve of a given mode (such as the fundamental mode) to compensate for bulk chromatic dispersion. Such fibers can take the form of both solid multilayered conventional and microstructured waveguides.

From a practical perspective, a key driver of nonlinear fiber optics was the concurrent development of commercial communications networks. As noted by Stolen, a pioneer in nonlinear fiber optics, '*Fiber nonlinear optics has grown from a novel medium for the study of nonlinear optical effects, through a period where these effects appeared as system impairments, to the present day where optical nonlinearities are an integral part of high-capacity optical systems*' [Stolen2008]. This sentiment is well-reflected in the history of nonlinearities and communication systems [Smith1972, Chraplyvy1990, Zhang1994, Li2001, Hasegawa2017, Winzer2018, Essiambre2021].

Other applications of modern consequence where fiber NLO is critical include fiber sensors and high power/high energy fiber lasers. Fiber lasers, of considerable interest for defense, security, remote sensing, and manufacturing uses, generally demand reduced nonlinearities, particularly those that are considered parasitic to power-scaling and beam quality [Richardson2010, Zervas2014, Dawson2008], such as stimulated Brillouin, Raman, and thermal Rayleigh scattering (which manifests as transverse mode instabilities) [Dong2013, Smith2011, Jauregui2020, Zervas2019], as well as thermal lensing [Dong2016b]. Fiber-based sensors, on the other hand, including distributed systems [Lu2019b] such as those designed for structural health [Barrias2016] and down-hole and geological [Schenato2017] temperature and pressure monitoring, tend to favor higher nonlinearities for enhanced signal-to-noise ratio and therefore higher measurement sensitivity [Bao2012]. 'Linear' systems, namely those based on fiber Bragg grating technology and Rayleigh scattering, have found wide commercial success, as have those based on the Raman scattering nonlinearity. The latter systems work on the principle that the ratio of the anti-Stokes to Stokes Raman scattered signals is a strong function of temperature, and therefore Raman scattering primarily is used for distributed temperature sensing. Both temperature and strain sensing are possible with Brillouin scattering, since the scattering frequency is a strong function of both the fiber thermal and mechanical environments. Unfortunately, Brillouin-based systems have not found wide commercial success due to their complexity and cost [Dragic2018].

3.5.1.2. Considerations for fibers when performing NLO measurements

All this said, care must be taken in assessing nonlinearities in optical fiber. This is because the measured nonlinearity is contributed to by both the materials comprising the fiber and the design of the fiber itself. Being a waveguide, the latter is important because fiber design influences the spatial (modal) and spectral (dispersion) properties of the propagating light. This, in turn, influences the relative contributions of the core and clad materials to the nonlinearities through their respective NLO coefficients. Representative examples of such fiber design influences on, for example, the nonlinear refractive index, n_2, can be found in [Kato1995a, Boskovic1996]. To this point, even the n_2 value of fused silica, the most canonical and well-studied fiber optic material, is not as precisely known as one would expect given the half-century since the first low loss fibers were reported (see section 1.1). Another case where considerable care is required when applied to waveguides is Brillouin scattering. Namely, the Brillouin gain coefficient $g_{\text{Brillouin}}$ has both material and waveguide influences. Depending on the waveguide design, one may dominate the other, or they may play a more cooperative role, often making it difficult to distinguish between the two. Materially, $g_{\text{Brillouin}}$ depends on refractive index, transverse photoelasticity, isothermal compressibility, Brillouin linewidth, and acoustic velocity such that each of these values should be carefully measured and reported for true completeness. More commonly, publications report the Brillouin shift and linewidth/lineshape but these can strongly be impacted by the fiber itself. These include factors such as the number of acoustic modes present and their relative confinement, whether the waveguide is acoustically anti-guiding or guiding, fiber

quality (loss) and length, and birefringence, to name just a few. All waveguide effects broaden the spectrum and reduce the observed Brillouin gain relative to the bulk material. In addition to these specific considerations for fibers, also the best practices described in section 2 should be taken into account when performing NLO measurements.

3.5.1.3. Description of general table outline

Table 6 provides a representative list of NLO properties of fiber waveguiding materials taken from the literature since 2000. Our goal has been to compile and highlight advancements in nonlinear materials in fiber form since 2000 with the above-mentioned caveats and the best practices of section 2 in mind. The publications included in table 6 were selected based on their representing measurements on fibers across the spectrum of reasonably common materials and respective nonlinearities. The included works nominally report data obtained at room temperature. The Table is subdivided into 'Fiber properties', 'Measurement details' and 'Nonlinear properties'. Within each column the information is given in the order of the header description, and the NLO technique used is provided in the 'Method' column. The Table compiles representative values for the following fiber material sub-categories: telecommunications-grade silica [Oguama2005, Oguama2005b, Deroh2020, Evert2012], silicate [Tuggle2017, Dragic2014, Lee2005, Cavillon2018], non-silica oxide (e.g., phosphate [Lee2007] and tellurite [Deroh2020]), and non-oxide (e.g., chalcogenides [Deroh2020, Florea2006, Tuniz2008, Fortier2008] and fluoride [Fortin2011, Lambin-Lezzi2013, Deroh2020]) optical fibers. For the more conventional silica and silica-based glass fibers, trends in Brillouin, Raman, and n_2 for a wide variety of dopants are provided in [Cavillon2018a] and references therein. Also noted are NLO properties of representative specialty optical fibers including polymer [Mizuno2010] and crystalline core optical fibers such as those made from sapphire [Harrington2014, Yin2008, Kim2008] and semiconductors [Ren2019, Shen2020]. Since second-order nonlinearities are generally precluded by symmetry in glass and cubic crystalline core fibers, the focus here is on third order $\chi^{(3)}$ wave-mixing as well as nonlinear scattering (e.g., Raman and Brillouin) phenomena. For completeness, second order nonlinearities in poled glass optical fiber also are noted [Canagasabey2009].

Two last points are noteworthy. First, the focus here is on the materials and material nonlinearities in conventional core-cladding configurations and not specifically on nonlinearity contributions from advanced waveguide design (e.g., microstructured or photonic-crystal fibers (PCFs), see, for example [Cordeiro2005, Dudley2009, Hu2019, Nizar2021]) as the range of those enabled influences is virtually endless. Indeed, one can make a very strong case that understanding/quantifying the relevant properties of a material should precede any attempts to design a waveguide from it. Second, nonlinearities can be materially enhanced or reduced (even negated), depending on the application. As such, both are generally treated here by way of discussing trends and ranges. The more fundamental materials science of optical nonlinearities in fibers has been recently reviewed [Ballato2018, Cavillon2018a].

3.5.2. Discussion

3.5.2.1. Advancements and remaining challenges for fibers

Not surprisingly, the range of NLO parameter values measured from optical fibers as shown in table 6 is nearly as expansive as the range of materials from which they are made. Ironically, it is this plenty that precludes an equally abundant coverage of all materials and values. Unless otherwise noted, table 6 is meant to provide generalized values, ranges, and trends for each fiber material family and associated nonlinearity.

Over the past twenty years, since approximately 2000, the dominant trend one observes is in the range of (strong and weak) NLO materials contained within or integrated into the fibers. Some of this growth is due to the expansion in applications employing fibers, such as power-scaled high energy lasers and sensors, as well as in new fiber processing methods that permit the fiberization of materials previously not possible [Sazio2006, Ballato2018a]. Arguably, this renaissance in fiber materials has driven rapid progress in the range of NLO parameter values. This said, beyond telecommunications grade silica, losses are still relatively high in most glass and crystal core fibers, thus potentially reducing their efficiencies and range of applications. However, markedly higher NLO parameter values offset issues of loss in some cases, such as with the semiconductor core optical fibers since a very large material nonlinearity shortens, often by several orders-of-magnitude, the required fiber lengths.

3.5.2.2. Recommendations for future works on fibers

The aforementioned renaissance in optical fiber materials has opened two particularly intriguing doors to the world of NLO. First, the wide range of new materials has greatly expanded the achievable range of NLO parameter values. When coupled with fiber design (e.g., microstructured fibers and PCFs) and post-processing (e.g., tapering), unquestionable benefits to future applications arise [Sylvestre2021]. Second, the availability of new fiber materials has generated new insights and concepts relevant to nonlinear fiber

optics. These include, for example, zero nonlinearity values based on carefully balanced fiber compositions. For instance, in the case of Brillouin scattering, positive and negative transverse photoelasticities [Ballato2018, Cavillon2018a] are balanced such that no spontaneous scattering occurs, thereby obviating its stimulated form. Such opportunities are not possible based only on fiber design. Needless to say, there are great possibilities ahead for fiber optics, both in terms of uniquely high and low nonlinearities. The Periodic Table can be construed to be a rich palette from which new materials with novel properties may be derived. Continued characterization sheds light on how to combine the base materials to achieve a desired outcome, be it using a hybrid or designer material approach. That being said, too few literature works go the extra mile to derive the relevant NLO material values from a system-level demonstration. For example, there are numerous examples of supercontinuum generation (SCG) from novel fibers/materials, but a large proportion of these papers lack sufficient detail from which the relevant nonlinearities may be quantified. Many other works, especially those in the area of hybrid fibers (see section 3.7), refer back to bulk values for the nonlinearities. It is important to remember that many materials, including glasses, undergo very different thermal histories when found in either bulk or fiber form. If a material's structural properties depend on its fabrication history, this may have a significant impact on its NLO behavior. In the case of hybrid materials, secondary effects such as material inter-diffusion during fabrication may have a similar impact.

It is fortunate that many of the works cited herein set out from the beginning to quantify the nonlinearities in fibers made from novel materials, but the difficulty in doing so is evident from table 6. The vast majority, with some exceptions, focus on one nonlinearity, while none have included three (i.e. n_2, Raman, and Brillouin together in the same work). That said, and even where there is a focus on a single nonlinearity, there are still gaps that can be seen in the table, though not following any particular trend, where information is lacking but desirable. Included in the Table are those parameters that generally are most important to be included in publications reporting NLO measurements in fibers. In other words, we consider the reporting of these parameters to be a 'best practice', in addition to the more general best practices described in section 2. To further complicate things, additional fiber-specific measurement complexities can arise from such characteristics as the number of propagating modes (not just a V-number alone), fiber splicing efficiency, fiber uniformity, attenuation at the operating wavelength(s), mode field diameter, mode index, dispersion, etc that can have a strong impact on the strength of a nonlinearity and deserve discussion where relevant. For completeness, it is ideal to also include the compositional profile across the core since each chemical constituent influences a given nonlinearity in differing ways; see, for example, table 1 in [Cavillon2018a], which qualifies changes in Raman, Brillouin, and n_2-mediated wave-mixing for a wide variety of glass components often used in silica-based optical fibers. This further epitomizes the need for all relevant data to be provided, through which a reader can at least formulate their own estimates of the NLO coefficients, or at least in the case of hybrid systems, an effective value for the nonlinearity (see section 3.7). Such data is of critical importance, as it is key to the design of next-generation fibers.

3.5.3. Data table for fiber waveguiding materials

Table 6. NLO properties of fiber waveguiding materials from representative works since 2000. Legend for superscripts: see below the table.

Material	Method	Fiber Properties: Length / Loss / Core index contrast / Cladding material / Core size / Effective area	Measurement Details: Wavelength / Peak power / Rep. rate / Pulse width	Nonlinear Properties: $n_{2,\mathrm{eff}}$ [a]	g_{Raman} / Frequency shift	$g_{\mathrm{Brillouin}}$ / Frequency shift / Linewidth	Reference
Commercial telecommunications fiber							
Pure SiO_2	IGA/SPM/SRS Threshold	20 m 0 dB m^{-1} — SiO_2 — 50 μm^2	1064 nm 5–25 W 100 MHz 50–70 ps	1.81 ± 10^{-20} m^2 W^{-1}	0.78 ± 10^{-13} m W^{-1} —	— — —	[Oguama2005b]
SMF-28	SpBS Linewidth	500 m 0.022 dB m^{-1} — SiO_2 8.2 μm 101 μm^2	2000 nm — CW	2.44 ± 10^{-20} m^2 W^{-1}	— —	2.525 ± 10^{-11} m W^{-1} 8.40 GHz 15 MHz	[Deroh2020]
SMF-28	SpBS Linewidth	500 m 0.0002 dB m^{-1} — SiO_2 8.2 μm 78 μm^2	1550 nm — CW	—	— —	2.262 ± 10^{-11} m W^{-1} 10.85 GHz 28 MHz	[Deroh2020]
DCF	IGA/SPM/SRS Threshold	20 m 0 dB m^{-1} — SiO_2 — 10.61 μm^2	1064 nm 5–25 W 100 MHz 50–70 ps	2.67 ± 10^{-20} m^2 W^{-1}	1.47 ± 10^{-13} m W^{-1} —	— — —	[Oguama2005b]
EDFAs	IGA/SPM	20 m 0 dB m^{-1} — SiO_2 — 8.9–27.2 μm^2	1064 nm 5–25 W 100 MHz 50–70 ps	1.82 to 3.04 ± 10^{-20} m^2 W^{-1}	— —	— — —	[Oguama2005]

(Continued.)

Table 6. (Continued.)

Material	Method	Fiber Properties: Length / Loss	Fiber Properties: Core index contrast / Cladding material / Core size / Effective area	Measurement Details: Wavelength / Peak power	Measurement Details: Rep. rate / Pulse width	Nonlinear Properties: $n_{2,\text{eff}}$ [a]	Nonlinear Properties: g_{Raman} / Frequency shift	Nonlinear Properties: $g_{\text{Brillouin}}$ / Frequency shift / Linewidth	Reference
GeO_2 doped SiO_2	SpBS Reference Fiber[b]	20 m 0.082 dB m^{-1}	$\leqslant 5 \pm 10^{-3}$ SiO_2 40 μm —	1534 nm —	CW	—	— —	0.53 ± 10^{-11} m W^{-1} 10.71 GHz 80 MHz	[Evert2012]
Silicate glass fibers									
Y_2O_3-Al_2O_2-SiO_2	FWM/SpBS Reference Fiber	4 m 0.78, 0.47 dB m^{-1}	$47.3, 32.9 \pm 10^{-3}$ SiO_2 11.2, 20.7 μm —	1542 nm 850 W	CW	1.8 to 2.0 ± 10^{-20} m^2 W^{-1}	— —	0.125 to 0.139 ± 10^{-11} m W^{-1} 11.40 to 12.5 GHz 200 to 500 MHz	[Tuggle2017]
La_2O_3-Al_2O_2-SiO_2	SpBS Reference Fiber	2 m 1.0 dB m^{-1}	100 ± 10^{-3} SiO_2 16 μm 5.8 μm MFD	1534 nm —	CW	—	— —	0.26 ± 10^{-11} m W^{-1} 11.476 GHz 82.0 MHz	[Dragic2014]
Bi_2O_3-SiO_2	Nonlinear phase shift/SBS Pump-Probe	1 m 0.8 dB m^{-1}	— SiO_2 — 3.08 μm^2	1550 nm —	CW	8.17 ± 10^{-19} m^2 W^{-1}	— —	6.43 ± 10^{-11} m W^{-1} — —	[Lee2005]
Other oxide glass fibers									
P_2O_5-based	SBS Threshold	1.245 m 5.47 dB m^{-1}	0.144 NA Phosphate 27.7 μm —	1064 nm $\leqslant$60 W	— 1 μs	—	— —	2.1 ± 10^{-11} m W^{-1} 27.7 GHz 219 MHz	[Lee2007]
Oxyfluoride	SpBS Reference Fiber, SpRS, FWM	800 m 0.65 dB m^{-1}	35 ± 10^{-3} SiO_2 18.6 μm —	1540 nm 430 W	— —	3 ± 10^{-20} m^2 W^{-1}	0.48 ± 10^{-13} m W^{-1} —	0.56 ± 10^{-11} m W^{-1} 10.75 GHz 52 MHz	[Cavillon2018]

Heavy metal oxides glass fibers									
GeO_2-SiO_2	SpBS Linewidth	3 m 0.1 dB m^{-1}	— SiO_2 2 μm 5 μm^2	2000 nm —	CW	4.97 ± 10^{-20} m^2 W^{-1}	— —	7.45 ± 10^{-12} m W^{-1} 6.00 GHz 76 MHz	[Deroh2020]
GeO_2-SiO_2	SpBS Linewidth	3 m 0.2 dB m^{-1}	— SiO_2 2 μm 3.5 μm^2	1550 nm —	CW	—	— —	1.05 ± 10^{-11} m W^{-1} 7.70 GHz 98 MHz	[Deroh2020]
TZN (TeO_2 based)	SpBS Linewidth	2 m 0.5 dB m^{-1}	— Tellurite 4 μm 10 μm^2	2000 nm —	CW	38 ± 10^{-20} m^2 W^{-1}	— —	13 ± 10^{-11} m W^{-1} 6.17 GHz 15 MHz	[Deroh2020]
TZN (TeO_2 based)	SpBS Linewidth	2 m 0.5 dB m^{-1}	— Tellurite 4 μm 8 μm^2	1550 nm —	CW	—	— —	16 ± 10^{-11} m W^{-1} 7.97 GHz 21 MHz	[Deroh2020]
Chalcogenide glass fibers									
As_2S_3	SBS Threshold	0.1 m 0.57 dB $^{-1}$	0.33 NA — 4.2 μm —	1548.4 nm $\leqslant$0.03 W	— —	—	— —	3.9 ± 10^{-9} m W^{-1} — —	[Florea2006]
As_2S_3	SpBS Linewidth	2 m 0.2 dB m^{-1}	0.26 NA As-S glass 6.1 μm 26 μm^2	2000 nm —	CW	—	— —	1.17 ± 10^{-9} m W^{-1} 6.21 GHz 25 MHz	[Deroh2020]
As_2S_3	SpBS Linewidth	2 m 0.2 dB m^{-1}	0.26 NA As-S glass 6.1 μm 20 μm^2	1550 nm —	CW	—	— —	1.54 ± 10^{-9} m W^{-1} 7.96 GHz 33 MHz	[Deroh2020]
As_2Se_3	SBS Threshold	0.1 m 0.9 dB m^{-1}	0.14 NA — 6.5 μm —	1548.4 nm $\leqslant$0.133 W	— —	—	— —	6.75 ± 10^{-9} m W^{-1} — —	[Florea2006]

(Continued.)

Table 6. (Continued.)

Material	Method	Fiber Properties: Length / Loss; Core index contrast / Cladding material / Core size / Effective area	Measurement Details: Wavelength / Peak power; Rep. rate / Pulse width	Nonlinear Properties: $n_{2,\mathrm{eff}}$ [a]	g_{Raman} / Frequency shift	$g_{\mathrm{Brillouin}}$ / Frequency shift / Linewidth	Reference
As_2Se_3	SPM, XPM	0.25 m 1 dB m^{-1}	Single mode, As-Se glass — 21 μm^2	1560, 1503, 1470 nm 73 W	100 MHz 15 ps	1.10 to 0.75 ± 10^{-17} m^2 W^{-1}	2 to 3 $\pm$ 10^{-11} m W^{-1} 7 THz	— — —	[Tuniz2008]
Ge-Sb-S	SpBS, SRS Pump-Probe	1.5 m 5.5 dB m^{-1}	— PCF 50 μm —	1553 nm $\leqslant$25 W	— 10 ns	—	1.8 ± 10^{-11} m W^{-1} 9.7 THz	8 ± 10^{-10} m W^{-1} 8.2 GHz —	[Fortier2008]
Fluoride glass fibers									
Fluoride	SBS Threshold	29 m 0.02 dB m^{-1}	0.23 NA — 6.5 μm —	1940 nm $\leqslant$7 W	CW	—	3.25 to 3.52 ± 10^{-14} m W^{-1} 17.35 THz	— — —	[Fortin2011]
ZBLAN	SBS Pump-Probe	10.4 m 0.25 dB m^{-1}	0.17 NA Fluoride glass — —	1550 nm $\leqslant$5 W	CW	—	— —	$4 \sim 3 \pm 10^{-12}$ m W^{-1} 7.76 GHz $<$38 MHz	[Lambin-Lezzi2013]
ZBLAN	SpBS Linewidth	5 m 0.25 dB m^{-1}	— Fluoride glass 9 μm 66 μm^2	2000 nm —	CW	2.93 ± 10^{-20} m^2 W^{-1}	— —	5.28 ± 10^{-12} m W^{-1} 6.00 GHz 35 MHz	[Deroh2020]
ZBLAN	SpBS Linewidth	5 m 0.125 dB m^{-1}	— Fluoride glass 9 μm 55 μm^2	1550 nm —	CW	—	— —	4.95 ± 10^{-12} m W^{-1} 7.75 GHz 59 MHz	[Deroh2020]

Representative specialty core phase fibers									
Perfluoro polymer	SBS Threshold	100 m 0.15 dB m^{-1}	0.185 NA Polymer 120 μm —	1550 nm $\leqslant$1 W	CW	—	— —	3.09 ± 10^{-11} m W^{-1} 2.83 GHz 105 MHz	[Mizuno2010]
Sapphire	SCG	0.001 m[c]	— Unclad 60 μm —	784 nm —	1 kHz 150 fs	3 ± 10^{-20} m^2 W^{-1}	— —	— — —	[Yin2008]
Sapphire	SCG	0.035 m[c]	— Unclad 115 μm —	2000 nm 3–16 MW	— 150 fs	2.8 ± 10^{-20} m^2 W^{-1}	— —	— — —	[Kim2008]
Silicon	SPM	0.008 m 0.2 to 3 dB cm^{-1}	3.9 NA SiO_2 Depends on taper —	1540 nm 0.04–1.2 kW	— 700 fs	3 ± 10^{-18} m^2 W^{-1}	— —	— — —	[Ren2019]
Silicon	SPM	0.01 m 2 dB cm^{-1}	3.9 NA SiO_2 Depends on taper —	2400 nm —	— 100 fs	1 ± 10^{-17} m^2 W^{-1}	— —	— — —	[Shen2020]
Poled germanosilicate	SHG	0.32 m 0 dB m^{-1}	0.11 NA SiO_2 6 μm —	1541 nm 200 W	3 MHz —	$\chi^{(2)}_{\text{eff}} = 0.054$ pm V^{-1}, 15.2% conversion efficiency			[Canagasabey2009]

[a] Sometimes the value of $n_{2,\text{eff}}$ should be multiplied by 9/8 when comparing to bulk measurements to account for the effects of polarization randomization that occurs for fibers longer than several meters [Buckland1996] (see section 1.1 on fused silica).

[b] The Brillouin gain coefficient was determined by comparing the strength of Brillouin scattering to a reference fiber of known $g_{\text{Brillouin}}$.

[c] Not noted in stated reference but attenuation values of 0.3 dB m^{-1} at a wavelength of 2.94 μm have been reported [Harrington2014].

3.6. On-chip waveguiding materials: data table and discussion

Team: *Philippe Boucaud, Ksenia Dolgaleva, Daniel Espinosa, Rich Mildren,* ***Minhao Pu (team leader),*** *Nathalie Vermeulen, Kresten Yvind*

3.6.1. Introduction

3.6.1.1. On-chip waveguiding materials and their NLO applications

Integrated photonics deals with miniaturization of bulk-component optical setups including all their key components (light-emitting devices, light-steering optics and detectors) and functionalities on small chips, typically with dimensions $< 1 \times 1$ cm^2. The on-chip miniaturization of photonic components allows building compact photonic integrated circuits (PICs) with high complexity, small footprint and potentially low cost when produced in large volumes. Thanks to the strong advancement in manufacturing technology over the past decades, a wide variety of materials can be combined nowadays through heterogeneous integration and bonding, thus covering a very wide spectral range and optimizing the performance of both active and passive devices by selecting the appropriate material platform for each on-chip functionality. Alternatively, monolithic photonic integration where active and passive integrated optical components are built on the same platform, with some variation of the material composition depending on the device functionality, is also possible using III–V semiconductor platforms.

Nonlinear integrated photonics exploits the NLO response of on-chip components. Some examples of on-chip nonlinear photonic structures include straight passive waveguides, micro-ring resonators or other compact structures, such as photonic-crystal waveguides. Fabrication of waveguides with dimensions smaller than the wavelength of operation [Karabchevsky2020] has enabled strong light confinement and, as such, high irradiances beneficial for efficient NLO interactions. Ultra-compact waveguides with large refractive index contrasts between the core and cladding can also exhibit strong waveguide dispersion, enabling dispersion engineering useful for establishing, e.g., phase-matched SHG or FWM. Finally, besides basic waveguide cross-sections consisting of three material layers (guiding layer or core, substrate and cladding), more advanced quantum-well waveguide geometries featuring enhanced NLO interactions have also emerged over the years [Wagner2009, Hutchings2010, Wagner2011].

In case the waveguide core material lacks inversion symmetry, NLO interactions of the second order can take place; otherwise, the waveguide will only exhibit a third-order NLO response. These two waveguide subcategories offer quite different NLO functionalities: whereas waveguides with a second-order nonlinearity allow, e.g., on-chip frequency doubling, DFG and EO modulation (the latter is not included in the tables), those with a third-order nonlinearity enable Kerr-based supercontinuum generation, Raman amplification, all-optical switching, etc. These functionalities are finding practical use in a wide variety of applications, ranging from on-chip biosensing, spectroscopy and LIDAR to optical datacom, signal processing, and quantum computing.

3.6.1.2. Background prior to 2000

The NLO properties of the majority of materials used for on-chip integration were already studied in bulk form well before 2000, and many NLO experiments in waveguide configurations were reported before the turn of the century. These early studies were primarily concerned with determining effective NLO coefficients of the materials in waveguide arrangements. Furthermore, efforts in optimizing the light confinement and tailoring various phase-matching techniques in waveguides already began before the new millennium. Nevertheless, the field has still experienced tremendous growth after 2000 facilitated by the maturing fabrication technologies for PICs [Ottaviano2016, Roland2020].

3.6.1.2.1. Background for on-chip waveguide materials with second-order nonlinearity

Second-order NLO effects generally require non-centrosymmetric materials. Although it is possible to induce these effects in centrosymmetric materials by means of strain [Cazzanelli2011], by applying all-optical poling techniques [Nitiss2022] or by exploiting surface effects, the strongest second-order nonlinearities are generally found in materials that intrinsically lack inversion symmetry. Before 2000, the following non-centrosymmetric crystalline waveguide materials were used for establishing $\chi^{(2)}$ effects: III–V semiconductors, aluminum gallium arsenide (AlGaAs) and gallium arsenide (GaAs) [Anderson1971, VanDerZiel1974, VanDerZiel1976, Yoo1995, Ramos1996, Fiore1997a, Street1997a, Street1997b, Xu1997, Fiore1998, Fiore1997b, Yoo1996, Bravetti1998, Xu1998]; III-nitrides, aluminum nitride (AlN) and gallium nitride (GaN) [Blanc1995, Zhang1996]; and some II–VI semiconductors such as zinc selenide (ZnSe), zinc telluride (ZnTe), and zinc sulfide (ZnS), grown epitaxially on a GaAs substrate [Angell1994, Wagner1995, Wagner1997, Kuhnelt1998]; as well as some other materials [Sugita1999, Chui1995, Azouz1995]. Most of the III–V semiconductor optical waveguides used to demonstrate $\chi^{(2)}$ effects before the 1990s [Anderson1971, VanDerZiel1974, VanDerZiel1976] as well as all AlN, GaN [Blanc1995, Zhang1996] and II–VI waveguide

demonstrations [Angell1994, Wagner1995, Wagner1997, Kuhnelt1998] were in slab waveguides with 1D confinement. As the means and tools for nanofabrication experienced further development, it became possible to routinely fabricate AlGaAs/GaAs channel or ridge waveguides with 2D confinement, exhibiting more efficient NLO interactions [Yoo1995, Ramos1996, Fiore1997a, Street1997a, Street1997b, Xu1997, Fiore1998, Fiore1997b, Yoo1996, Bravetti1998, Xu1998]. Among the specific second-order NLO effects in AlGaAs and GaAs, there were numerous experiments on SHG in the near-IR [VanDerZiel1974, VanDerZiel1976, Yoo1995, Fiore1997a, Street1997a, Street1997b, Xu1997, Fiore1998], mid-IR [Anderson1971], and visible (SHG of blue light) [Ramos1996]. There were also some DFG reports with generation of mid-IR [Fiore1997b, Bravetti1998], as well as near-IR radiation using 770 nm pump light [Yoo1996] and SFG of 780 nm red light with a near-IR pump [Xu1998]. AlN and GaN III-nitride and II–VI slab dielectric waveguides enabled the observation of SHG in the visible [Blanc1995, Zhang1996].

While crystalline birefringence is often used in bulk crystals to phase-match the widely spaced wavelengths in second-order NLO processes, other techniques are needed for materials that do not possess natural birefringence, such as GaAs and AlGaAs. Phase-matching techniques used to enhance the efficiency of second-order NLO effects include dispersion engineering of the slab waveguide structure [Anderson1971], and modal phase matching where the fundamental radiation occupied a lower-order mode and the second harmonic populated a higher-order mode for effective refractive index matching [VanDerZiel1974, Blanc1995, Wagner1995]. Most of the demonstrations of phase-matched $\chi^{(2)}$ effects employed various QPM approaches [VanDerZiel1976, Yoo1995, Fiore1997a, Street1997a, Street1997b, Xu1997, Yoo1996, Xu1998, Angell1994, Wagner1997, Kuhnelt1998, Azouz1995, Sugita1999]. Specifically, many reports explored periodic domain inversion (PDI) where the sign of $\chi^{(2)}$ was periodically modulated by crystalline domain reorientation achieved through wafer bonding and subsequent epitaxial (MOCVD or MBE) regrowth of the structure with the domain orientation following that of the template [Yoo1995, Xu1997, Yoo1996, Xu1998, Angell1994]. This approach featured high propagation losses of 50–120 dB cm^{-1}, except for one study reporting much lower propagation losses of 5.5 dB cm^{-1} at the 1460 nm fundamental and 25 dB cm^{-1} at the 730 nm second-harmonic [Yoo1995]. QPM by PDI through proton exchange followed by thermal annealing in $LiTaO_3$ [Azouz1995] and by periodic electric-field poling of MgO:$LiNbO_3$ (with a very high efficiency of 31%) [Sugita1999] were also demonstrated. QPM by a periodic modulation of the refractive index was achieved via a corrugation formed by a grating etched in one of the waveguide heterostructure interfaces [VanDerZiel1976]. Furthermore, QPM by periodic modulation of the values of $\chi^{(2)}$ (their periodic suppression) was achieved via asymmetric coupled quantum-well reorientation [Fiore1997a], quantum-well intermixing [Street1997a, Street1997b] selective wet oxidation of AlAs in AlGaAs/GaAs structures [Fiore1998, Fiore1997b, Bravetti1998], and maskless focused-ion-beam implantation in ZnTe and ZnSe waveguides [Wagner1997, Kuhnelt1998]. Thanks to the highest modulation contrast of $\chi^{(2)}$ achievable through PDI, this method has been shown to result in the highest conversion efficiencies despite the largest propagation losses. Some specific conversion efficiency figures are 1040% W^{-1} cm^{-2} for SHG [Xu1997] and 810% W^{-1} cm^{-2} for DFG [Xu1998] (PDI $Al_{0.6}Ga_{0.4}As$ core with $Al_{0.7}Ga_{0.3}As$ claddings, fundamental wavelengths around 1550 nm). Some other promising results include 190% W^{-1} [Fiore1998] (AlGaAs/AlAs with form birefringence by selective wet oxidation), 450% W^{-1} [Azouz1995] ($LiTaO_3$ formed by proton exchange), and 1500% W^{-1} [Sugita1999] (SHG of 426 nm in MgO:$LiNbO_3$ waveguide with a periodically patterned domain structure).

3.6.1.2.2. Background for on-chip waveguide materials with third-order nonlinearity

Third-order NLO interactions demonstrated in waveguide platforms before 2000 include a wide variety of phenomena such as SPM, XPM, THG, Raman, Brillouin and FWM. The dominant number of experimental demonstrations were performed in the 1990s in III–V semiconductor optical devices based on AlGaAs [Espindola1995, Peschel1999, Millar1999, Le1990, Hamilton1996, Kang1996b, Islam1992, Stegeman1994, Kang1995, Kang1998, Villeneuve1995a, Villeneuve1995b Villeneuve1995c, Le1992] and InGaAsP [Nakatsuhara1998, Day1994, DOttavi1995, Donnelly1996, Darwish1996, Tsang1991]. Waveguides of planar configuration (featuring 1D confinement) [Kang1996b, Day1994, Kang1998] and channel/rib waveguides (with 2D confinement) [Espindola1995, Stegeman1994, Nakatsuhara1998, Villeneuve1995c, DOttavi1995, Hamilton1996, Donnelly1996, Islam1992, Peschel1999, Le1990, Millar1999, Villeneuve1995b] were considered. The majority of studies were performed in waveguides with 2D confinement, while 1D structures were primarily used for spatial soliton demonstrations [Kang1996b, Kang1998]. The NLO phenomena studied in III–V semiconductors included SPM and XPM [Kang1996b, Day1994, Hamilton1996, Kang1998, Tsang1991, Villeneuve1995b], FWM [Espindola1995, DOttavi1995, Donnelly1996, Le1990, Darwish1996, Le1992], and other demonstrations of the third-order optical nonlinearity [Islam1992, Peschel1999, Millar1999].

InGaAsP-based works feature optical devices with both resonant [Day1994] and nonresonant [Nakatsuhara1998, DOttavi1995, Donnelly1996, Darwish1996, Tsang1991] nonlinearities in the vicinity of the bandgap. In contrast, AlGaAs-based works primarily concentrated on operation at wavelengths below half of the bandgap energy, typically the telecom C-band wavelengths, where it is possible to eliminate 2PA by manipulating the material compositions of the waveguide heterostructures [Kang1996b, Villeneuve1995c, Stegeman1994, Peschel1999, Kang1998, Villeneuve1995b]. InGaAsP- and AlGaAs-based quantum-well devices have been shown to exhibit strong nonlinearities due to band-filling and excitonic effects [Day1994, Donnelly1996, Darwish1996, Tsang1991, Islam1992].

Most of the studies on the third-order nonlinearities in III–V semiconductor waveguides before 2000 were focusing on measuring nonlinear coefficients such as $n_{2(\mathrm{eff})}$ and α_2. The values of $n_{2(\mathrm{eff})}$ in AlGaAs of various material compositions at various wavelengths have been reported to fall within the range between 2.1×10^{-18} and 3.3×10^{-17} m^2 W^{-1}, with the most cited values near half-the-bandgap of $(1.3–1.5) \times 10^{-17}$ m^2 W^{-1} in the telecom C-band [Espindola1995, Stegeman1994, Hamilton1996, Islam1992, Aitchison1997]. The 2PA coefficients α_2 of AlGaAs below half-the-bandgap have been reported to span between 2.6×10^{-13} and 6×10^{-13} m W^{-1} [Espindola1995, Islam1992, Aitchison1997]. The values of $n_{2(\mathrm{eff})}$ (in the range between 6×10^{-17} and 9.5×10^{-16} m^2 W^{-1}) and α_2 (3×10^{-11} to 6×10^{-10} m W^{-1}) typically measured in the vicinity of the bandgap, have been reported in InGaAsP waveguides [Donnelly1996, Darwish1996, Tsang1991]. The values of $\chi^{(3)}$ in AlGaAs [Le1990] and InGaAsP [Donnelly1996] waveguides have also been measured. A few studies report the conversion efficiencies for FWM processes in AlGaAs [Le1990, Le1992] and InGaAsP [Donnelly1996, Darwish1996] waveguides.

Organic polymers in waveguide configurations (not included in the data table) represent another large group of materials that has been extensively studied before 2000 [Prasad1987, Grabler1997, Rossi1991, Huang1999, Okawa1991, Chon1994, Muto1992, Hosoda1992, Driessen1998, Bartuch1997, Malouin1996, Malouin1998, Murata1998, Marques1991, Asobe1995, Lee1993, Konig1999]. Many studies report the effective values of $\chi^{(3)}$ of a variety of polymer-based waveguides [Huang1999, Okawa1991, Chon1994, Rossi1991, Hosoda1992, Lee1993]. The typical value ranges for the nonlinear coefficients n_2 of these waveguide materials are between 2.7×10^{-18} and 1.7×10^{-16} m^2 W^{-1}, while α_2 ranges between 8×10^{-13} and 5.8×10^{-11} m W^{-1} [Chon1994, Driessen1998, Bartuch1997, Malouin1998, Murata1998, Marques1991, Asobe1995, Malouin1996, Grabler1997]. Thanks to the wide transparency windows of the majority of the polymer waveguide platforms, most of these measurements have been performed in the visible wavelength range.

There were a few reports demonstrating third-order NLO interactions in waveguides made of other materials, namely: Si_3N_4 [Bertolotti1999], QPM KTP waveguides [Sundheimer1993], gelatin-gold nanoparticle composites [Bloemer1990], SiO_2-TiO_2 [Toruellas1991], and ChGs [Cerqua-Richardson1998]. Notably, there was also a series of works on planar iron-doped and titanium-indiffused $LiTaO_3$ and $LiNbO_3$ waveguides where phase conjugation by anisotropic FWM and two-wave mixing has been demonstrated [Kip1994, Popov1992, Normandin1979, Kip1992, Fujimura1999, Kip1995].

The dominant driver behind studying the third-order phenomena in waveguide configurations before 2000 was the potential of developing all-optical signal processing devices for optical communication networks and optical information processing. As the fastest response time associated with most of the nonresonant third-order processes is at the sub-femtosecond time scale, high-speed switching at moderate optical powers is possible. Many proof-of-principle all-optical-switching devices such as nonlinear directional couplers and asymmetric Mach–Zender interferometers [Kang1995, Stegeman1994, Villeneuve1995a] have been demonstrated before 2000. Optical bistable devices in various waveguide platforms have also been realized [Nakatsuhara1998, Huang1999]. Yet, despite this interest in datacom and information processing applications, the NLO properties of Si waveguides remained largely unexplored before 2000.

3.6.1.3. Considerations for on-chip waveguides when performing NLO measurements

Determining the irradiance inside the on-chip waveguide is not straightforward and can represent the main source of error in NLO measurements. Apart from the determination of the optical beam characteristics such as the pulse width and the peak power, a careful evaluation of the coupling efficiency and the effective mode area is crucial for the irradiance determination. If the waveguide's cross-sectional dimensions change along the propagation direction, as in the case of devices with tapers, the subsequent change in the irradiance and phase matching conditions must also be accounted for.

The propagation loss must be properly evaluated. It includes the linear absorption, which depends only on the constituent materials, the scattering off the waveguide's walls and the field leakage. The determining factors in the loss characteristics are the waveguide's fabrication process, its geometry, material composition,

and the quality of the substrate. Although most of the selected waveguide materials do not exhibit 2PA at the wavelength of interest in their bulk states, the large surface area of the waveguides may give rise to linear absorption from impurities and defects generating free carriers and/or excited impurity or defect states that subsequently absorb. This 2-step process mimics 2PA making it difficult to experimentally separate its effects from direct 2PA. However, this is a fluence dependent rather than an irradiance dependent process, and thus its effects are reduced in short-pulse measurements [Lin2007a, VanStryland1985, Christodoulides2010]. Using CW or long pulse high-repetition-rate sources helps to determine this contribution.

An effective NLO coefficient measured in heterostructure waveguides usually results from an irradiance-weighted average of the NLO coefficients of different layers. The contribution of the guiding layer is dominant in most cases. However, the precise effective NLO coefficient values depend on the confinement factor [Grant1996]. For this reason, the waveguide's NLO coefficients might deviate from the corresponding bulk values.

As for the measurements of the efficiency of the NLO process, the approach used to perform the calculation must be explicitly given. For example, one should state whether the power used in the calculation is the average or peak power, external or internal (coupled in), at the input or output of the device.

In multi-beam experiments, the group velocity mismatch (GVM) and phase mismatch, which depend on the material and waveguide dispersions, should also be properly quantified because for several NLO processes, such as FWM, these are some of the most crucial factors in determining the efficiency of the process. GVM is responsible for separating the probe pulse from the pump pulse in time as they propagate along the waveguide, while the phase mismatch between different wavelength components involved in the NLO process determines the coherence length of the process [Tishchenko2022]. The beauty of on-chip waveguides is that some of them enable dispersion engineering with the possibility of zero GVD at the wavelengths of interest to improve the efficiency of a NLO process [Pu2018, Dolgaleva2015, Meier2007]. Estimating the efficiency of the NLO process in a waveguide from the theoretical models that account for the dispersion, the irradiances, and NLO coefficients, and comparing it to the measured value is also a good practice [Espinosa2021a, Pu2018, Foster2007].

On-chip waveguides used in NLO are often quite short ($<$1 cm). For waveguide materials that are not highly nonlinear, one should test/account for possible nonlinearities in the rest of the characterization system by performing reference measurements. This is especially true for tapered fiber-coupled devices where a reference measurement without the device can be performed with the input power corrected for the insertion loss.

Besides the special considerations outlined here, also the general best practices of section 2 should be taken into account when performing NLO measurements with on-chip waveguides.

3.6.1.4. Description of general table outline

Tables 7A and B show a representative list of, respectively, second-order and third-order NLO properties of on-chip waveguiding materials taken from the literature since 2000. The selection of the papers included in the Tables has been based on the best practices in section 2 and the considerations outlined above. Table 7B has the entries grouped into five subcategories to facilitate the search for a specific waveguide composition: III–V semiconductors; silicon and silicon carbide, nitride, and oxide; ChGs; diamond; tantalum oxide and titanium oxide. Within each subcategory, the entries are ordered alphabetically. Tables 7A and B are subdivided into 'Material properties', 'Measurement details' and 'Nonlinear properties'. Within each column the information is given in the order of the header description. 'Material properties' include the waveguide dimensions (length and cross-section), fabrication methods, propagation loss, refractive index, and a reference to the sub-figure in figures 6 and 7 showing the fabricated device. Figure 6 shows SEM pictures of devices with second-order NLO responses, while figure 7 shows SEM pictures of devices with third-order NLO responses. The peak power values in the Tables are nominally incoupled powers as specified in the papers. The table entries cover various material platforms and compositions, as well as various waveguide configurations and phase-matching techniques. In some instances, the waveguide structure was rather complex, and it was difficult to fit its detailed description in the Tables. In these cases, simplified descriptions were provided with references to the more detailed descriptions in the corresponding papers. The NLO technique used in each of the papers is provided in the 'Method' column. Lastly, some papers specify the dependence of the NLO parameters or conversion efficiency η on wavelength, waveguide dimension, temperature, etc or have notes associated with their measurement/analysis. This information is listed within the 'Comments' column. The works included in the Tables nominally report data obtained at room temperature, unless specified otherwise in the 'Comments' column. If dispersive values for the NLO parameter were provided, the cited value represents the peak value for the material within the stated measurement range.

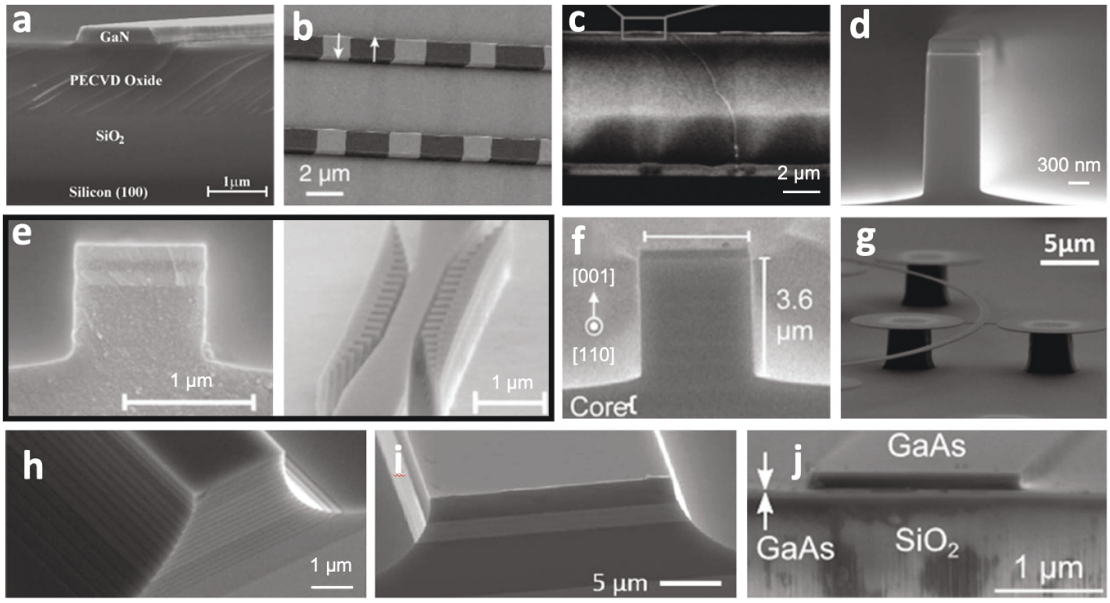

Figure 6. SEM images of integrated photonic devices for second-order nonlinear interactions. The labels of the sub-figures correspond to the labels given in table 7A. Panels (a)–(j) are reprinted with permission from [Xiong2011, Wang2018b, Yu2005, Duchesne2011, Scaccabarozzi2006, Han2009, Morais2017, Savanier2011b, Ozanam2014, Stanton2020], ©2005, 2006, 2009, 2011, 2014, 2017, 2018, 2020 Optica Publishing Group.

3.6.2. Discussion

The data in tables 7A and B indicate a clear trend towards the development of high-confinement waveguides because of the benefit of enhanced NLO interactions for both the second- and third-order NLO processes. Novel and improved fabrication procedures have been developed to ensure high-quality materials and low surface roughness. Several new waveguide material platforms have been entering the scene, bringing about excellent NLO performance. These platforms will further stimulate the development of practical NLO integrated devices.

3.6.2.1. Advancement since 2000 and remaining challenges

Over the past twenty years, there have been significant advancements in the methods of micro- and nanofabrication. Apart from the major progress in photo-lithography and electron-beam lithography, novel nanofabrication approaches and techniques have appeared, and also photonic foundries offering multi-project wafer runs at a reduced cost per chip have facilitated the field's growth. In the early 2000s, the NLO community turned its attention to silicon-on-insulator (SOI) photonics as a promising nonlinear platform because of its potentially lower cost and high compatibility with CMOS technology. Various SOI components for parametric amplification, wavelength conversion, and Raman lasing have been demonstrated in the telecom wavelength range.

The success of silicon photonics, inspired by CMOS silicon electronics, relies on the tight light confinement enabled by the combination of a high-index material (Si) surrounded by a low-index oxide cladding. Not surprisingly, this semiconductor-on-oxide approach has also been applied to other material systems, such as AlGaAs, resulting in NLO devices with improved performances. Another enabling factor in the new platform development is significant progress in bonding and substrate removal technologies, opening the route to various types of heterogeneous integration. Nonlinear photonics with suspended semiconductor membranes has consequently emerged. Below we provide more detailed insight into the progress since 2000, the remaining challenges and the applications of on-chip waveguides with second- and third-order NLO effects.

3.6.2.1.1. Advancement and challenges for on-chip waveguiding materials with second-order nonlinearity

There were many improvements in lowering the propagation losses and increasing conversion efficiencies of the second-order NLO interactions in the existing AlGaAs waveguide technologies. Specifically, selectively oxidized AlGaAs/Al_xO_y multilayer stacks with 2D-confined ridge waveguides with much lower propagation losses of 1.5–5 dB cm^{-1} featuring much higher conversion efficiencies ranging between 2.7 and 5% W^{-1} were demonstrated [Savanier2011b (SHG), Savanier2011a (SFG), Ozanam2014]. Moreover, 2D-confined AlGaAs waveguides with symmetric Bragg reflectors in their top and bottom claddings have been realized

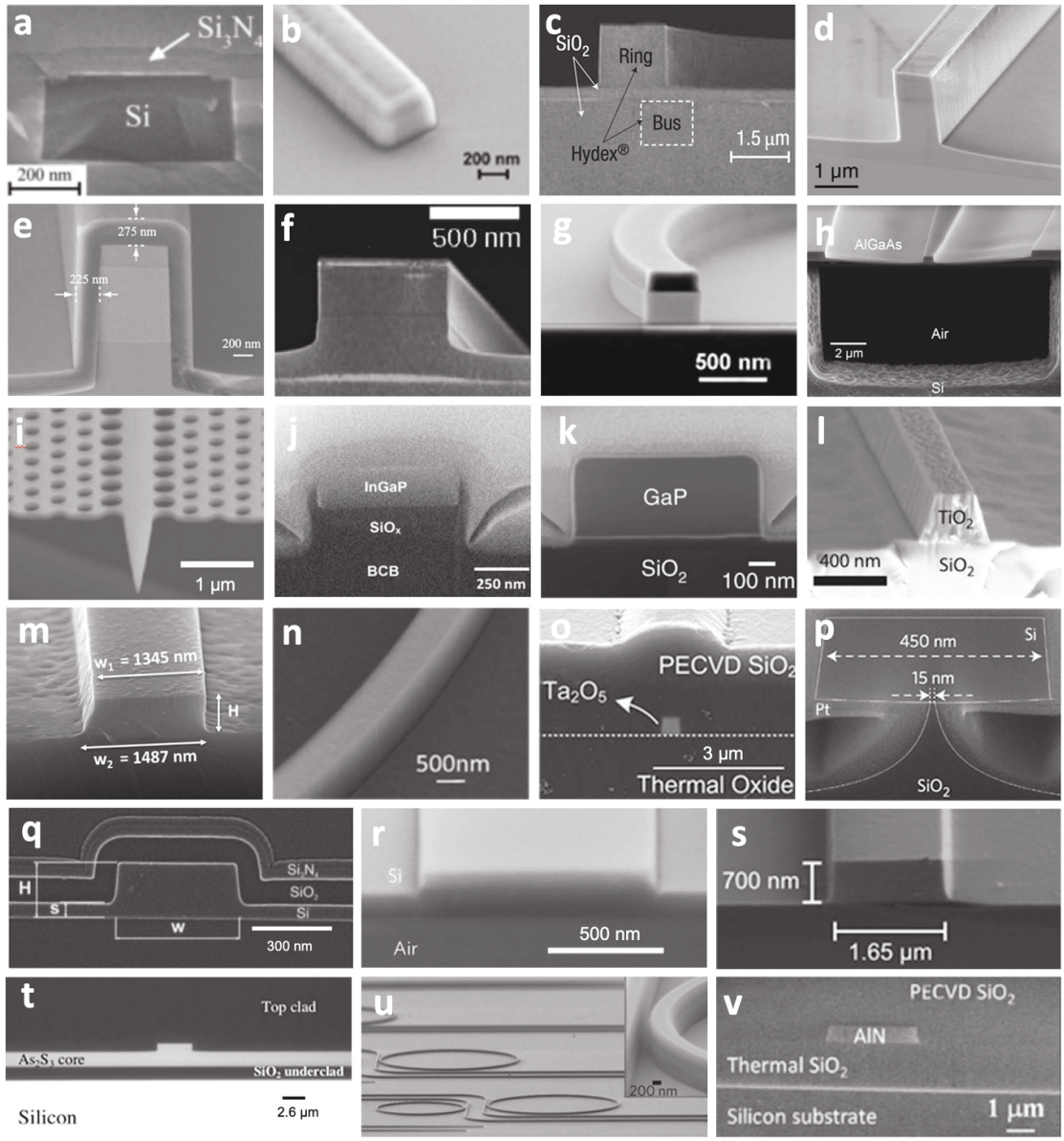

Figure 7. SEM images of integrated photonic devices for third-order NLO interactions. The labels of the sub-figures correspond to the labels given in table 7B. Panels (a), (b), (d), (e), (h), (i), (l), (n), (o), (q), (s), (t) and (v) are reprinted with permission from [Liu2011, Wang2012b, Wathen2014, Apiratikul2014, Chiles2019, Dave2015a, Evans2013, Zheng2019b, Wu2015, Gajda2012, Kruckel2015a, Madden2007, Jung2013], ©2007, 2011, 2012, 2013, 2014, 2015, 2019 Optica Publishing Group. Panels (c), (j), (k), (p), (r), and (u) are reprinted with permission from [Ferrera2008, Colman2010, Wilson2020, VanLaer2015, Kittlaus2016, Hausmann2014], Springer Nature. Panel (f) is reprinted with permission from [Espinosa2021a], Elsevier. Panels g and m are reprinted under CC BY license from [Stassen2019] and [Hammani2018].

[Han2009, Bijlani2008, Han2010, Abolghasem2009], exhibiting SHG and SFG conversion efficiencies around 9% W^{-1} [Han2009, Bijlani2008] and DFG conversion efficiencies of 5.2×10^{-4}% W^{-1} [Han2010]. Fabrication of QPM AlGaAs waveguides by PDI [Yu2005, Ota2009, Yu2007] and by a periodic suppression of $\chi^{(2)}$ (periodic domain disorientation) achieved through quantum-well intermixing [Wagner2011, Hutchings2010, Wagner2009] have seen significant improvements. PDI waveguides with propagation losses as low as 5 dB cm^{-1} and SHG conversion efficiencies over 40% W^{-1} [Yu2007] have been demonstrated.

Another advancement in the established AlGaAs waveguide technologies resides in the capability to fabricate deeply etched waveguides with sub-micrometer dimensions. An example of such a waveguide has been demonstrated in [Duchesne2011] where 300–1000 nm-wide ultracompact AlGaAs waveguides with tight light confinement were used for SHG with modal phase matching. The normalized conversion efficiency was moderate, 1.4×10^5% $(W\ m^{-2})^{-1}$, due to the high propagation losses of 18 dB cm^{-1} characteristic to such devices with exposed guiding-layer sidewalls.

In addition to the existing AlGaAs waveguide technologies, there appeared new waveguide platforms where an AlGaAs or GaAs guiding layer is surrounded by an insulator such as SiO_2 [Stanton2020,

Chang2019, Chang2018a] or air [Morais2017, Roland2020]. The propagation loss of 1.5–2 dB cm^{-1} in AlGaAs on SiO_2 is similar to that of the conventional AlGaAs strip-loaded waveguides, while conversion efficiencies as high as 40% W^{-1} [Stanton2020] and 250% W^{-1} [Chang2018a] in the CW regime have been reported. Simple type-II phase matching between a fundamental transverse-electric (TE) mode and a high-order second-harmonic transverse-magnetic (TM) mode was implemented, combined with directional QPM in [Morais2017]. Further advancements in the reduction of the propagation losses will lead to even more efficient AlGaAs devices for second-order NLO interactions. However, there exists another factor limiting the conversion efficiencies of longer waveguide structures. The narrow phase-matching bandwidth combined with an extreme sensitivity of the phase-matched wavelength to the waveguide dimensions (a precision on the order of a few nm is required) makes phase matching over a long distance technologically difficult [Stanton2020].

There are several reports on other waveguide platforms used for phase-matched second-order NLO interactions, among which are AlN on SiO_2 [Bruch2018], GaP on SiO_2 [Wilson2020], GaN on SiO_2 [Xiong2011], AlGaN [Gromovyi2017], and periodically polled $LiNbO_3$ [Wang2018b]. A remarkably high SHG conversion efficiency of 17 000% W^{-1} for the fundamental wavelength around 1550 nm has been achieved in a 2D-confined AlN ring resonator [Bruch2018]. The 2D confinement represents the most significant advancement in AlN- and GaN-based waveguides since only structures with 1D confinement (slab dielectric waveguides) were accessible before 2000. It was not until recently that the fabrication of 2D-confined channel waveguides based on these platforms became possible. AlN and GaN represent wide-bandgap semiconductors exhibiting large hardness and posing challenges in both epitaxial growth and defect-free nanofabrication. Further mitigation of the threading-dislocation density by optimizing the epitaxial growth and substrate choice [Awan2018] is expected to result in a significant improvement and more widespread use of such platforms in nonlinear photonics.

The observation of the second-order NLO interactions in waveguides is not limited to SHG or SFG. Spontaneous parametric down-conversion (SPDC) generating correlated photon pairs for applications in quantum technologies has been demonstrated in AlGaAs waveguides [Guo2017, Sarrafi2013]. OPO based on second-order processes has been demonstrated in GaAs/AlGaAs waveguides [Savanier2013], and, more recently, in AlN ring resonators [Bruch2019]. Supercontinuum generation (SCG) [Lu2019a, Zheng2021, Okawachi2020] and frequency comb generation [Zhang2019b] based on second-order processes have also been reported.

To illustrate the wide variety of components discussed here, figure 6 shows SEM images of some integrated waveguide devices used for second-order NLO interactions (see table 7A).

3.6.2.1.2. Advancement and challenges for on-chip waveguiding materials with third-order nonlinearity

There have been significant improvements in mitigating the propagation losses, optimizing the waveguide geometries, and achieving higher conversion efficiencies in the existing third-order nonlinear optical waveguide platforms, such as AlGaAs. Furthermore, there is a plethora of new works featuring novel waveguide materials that appeared after 2000 or waveguide materials that already existed but were not yet considered for NLO experiments until after 2000. These include various silicon-based platforms (SOI [Claps2002, Tsang2002, Liu2004, Rong2005, Zlatanovic2010, Turner-Foster2010, Liu2011, Kuyken2011, Liu2012b, VanLaer2015, Zhang2020b], Si_3N_4 [Levy2009, Tien2010, Kruckel2015b, Wang2018a], silicon-rich nitride [Wang2015, Kruckel2015a, Lacava2017, Ooi2017], SiC [Zheng2019b, Xing2019], amorphous silicon [Wang2012a, Wang2012b, Lacava2016, Girouard2020]), various ChGs [Madden2007, Lamont2008, Gai2010], TiO_2 [Evans2013, Guan2018, Hammani2018], Hydex glass [Ferrera2008, Ferrera2009, Duchesne2009], diamond [Hausmann2014, Latawiec2015, Latawiec2018], and additional III–V semiconductor platforms not previously explored for nonlinear photonic devices (GaP [Wilson2020], InGaAs/AlAsSb [Tsuchida2007, Cong2008, Lim2010, Feng2013]). The overall trend indicates that higher effective nonlinearities can be obtained in high-index-contrast waveguides, often with a low-index dielectric like silica or sapphire below the waveguide core. High-index-contrast silicon-based waveguides typically feature sub-micron dimensions [Wang2015, Lacava2017, Ooi2017, Turner-Foster2010, Kuyken2011, Liu2012b, VanLaer2015]. Furthermore, ultracompact AlGaAs waveguides with sub-micron dimensions, appearing after 2000, have also shown superior efficiencies of NLO interactions in comparison to their more conventional low-index-contrast counterparts [Apiratikul2014, Dolgaleva2015, Espinosa2021a]. Moreover, the SOI approach has been extended to other semiconductor platforms, enabling an increase in their refractive index contrasts and a decrease in the waveguide dimensions. Among those are AlGaAs-on-insulator (AlGaAs-OI) [Stassen2019, Pu2016, Pu2018, Kaminski2019, Hu2018, Ottaviano2016, Zheng2019a], GaP-OI [Wilson2020], and InGaP-OI [Colman2010, Dave2015a, Dave2015b]. Thanks to the strong light confinement, it became possible to push the effective nonlinear coefficient γ_{eff} to the level of 720 $m^{-1}\,W^{-1}$ in NLO waveguides based on these material platforms [Stassen2019]. Further enhancement of

the NLO interactions has been achieved through resonant effects in microring resonators [Absil2000, Li2021, Ramelow2019, Shi2021, Fu2020a, Zheng2019a, Zheng2019b, Ottaviano2016] and photonic-crystal structures [Jandieri2021, Monat2009 Liu2007, Zhu2006, Monat2010, Martin2017, Corcoran2009].

The effective nonlinearity is only one of the critical elements that determine the overall device performance. Another crucial parameter is propagation loss: the linear loss limits the effective nonlinear interaction length, while the nonlinear loss limits the maximum pump power that can be used for the specific NLO process. Significant efforts have been put into lowering both types of losses. As the linear loss is dominated by the scattering loss associated with the waveguide surface roughness and the refractive index contrast between the core and cladding, various approaches have been proposed to smoothen the waveguide surfaces (see, for example, [Awan2018, Liao2017]) and to passivate the waveguide surface for scattering reduction [Apiratikul2014, Wathen2014]. The nonlinear loss induced by multiphoton absorption is determined by the bandgap of the nonlinear material. The latter can be mitigated by using an appropriate material platform that lacks 2PA in the wavelength range of interest, which stimulated an effort in developing wide-bandgap NLO material platforms such as SiN, Hydex, Ta_2O_5 [Wu2015], SiC, AlN, and GaN. Some of the aforementioned platforms also exhibit modest index contrast compared to that associated with SOI and similar platforms. Although the effective nonlinearity that can be achieved in such low-index-contrast platforms is relatively low, their propagation losses are also extremely low. Ultra-low loss waveguides (with propagation losses <0.5 dB cm^{-1}) can be easily realized, allowing for much longer propagation lengths and ultra-high-Q microring resonators, thereby magnifying the efficiency of the NLO interactions. In contrast, the propagation losses in most high-index-contrast waveguides are much higher (>1 dB cm^{-1}) and do not permit long-length devices. Nevertheless, superior waveguide compactness and dispersion-management capability make them efficient NLO material platforms. Mitigating propagation losses, and improving waveguide designs, fabrication procedures, and NLO efficiencies continue to be the challenges on the path towards more practical integrated NLO devices.

Among the third-order NLO processes investigated after 2000, there are SPM, XPM, FWM, Raman effects, and Brillouin processes. If the works published before 2000 were focusing on determining the effective NLO coefficients of various waveguide structures, the trend after 2000 was partially shifted towards achieving higher NLO efficiencies with lower incident powers. The underlying idea is to push the proof-of-concept demonstrations towards practical implementations. In many emerging platforms, including AlGaAs-OI [Pu2016, Zheng2019a], SiN [Ramelow2019, Wu2021, Xue2016], Hydex [Reimer2014], SiC [Shi2021], and AlN [Jung2013, Jung2016], ultra-high-Q resonators have been realized to demonstrate FWM-based Kerr frequency comb generation, which has a wide variety of applications in spectroscopy, metrology, telecommunication, and quantum information processing. Furthermore, ultra-broadband (larger than half an octave) FWM bandwidths have been demonstrated [Pu2018, Moille2021], and supercontinuum generation (SCG) spanning more than an octave [Porcel2017, Lu2019a, Zhao2015, Liu2016b, Yu2019] has also been achieved in different waveguide platforms. All-optical signal processing operations and optical logic gates have been demonstrated [Pelusi2008, Willner2014, Koos2009, Yan2012b, Jandieri2018, Ma2016, Eggleton2012], targeting applications in optical communication networks and optical computing. An emerging application of on-chip nonlinear photonic devices that appeared after 2000 is to generate correlated photon pairs for use in quantum optics [Ma2018, Shi2019b, Kultavewuti2016, Kultavewuti2019].

To illustrate the variety of structures discussed above, figure 7 displays SEM images of some integrated waveguide devices used for third-order NLO interactions (see table 7B).

3.6.2.2. Recommendations for future works on on-chip waveguiding materials

Most papers noted in tables 7A and B present the measurements of one physical effect, e.g., SPM-induced spectral broadening, Raman scattering or harmonic generation. We encourage researchers to take into consideration the category-specific recommendations outlined above as well as the best practices in section 2. Following these tips will help eliminate possible errors encountered in the process of determining the values of NLO coefficients and conversion efficiencies.

We recommend that the authors of papers reporting on the NLO performance of waveguides specify at least those parameters that are included in tables 7A and B. Furthermore, the completeness of such works could benefit from adding additional information. For example, it is instructive to separate the absorption and scattering losses, and to add the thermo-optic coefficients in resonator structures, whenever it is possible. Self-heating is an important consideration in resonator-based applications, while these parameters are rarely provided in waveguide characterization papers.

Another point of concern is nonlinear losses. The parameter α_2 in the Tables is most often attributed to the 'instantaneous' 2PA that would have been retrieved from low-duty-cycle pulsed-source experiments. The highly nonlinear semiconductor waveguides with high refractive index contrast present a special challenge due to the high field amplitudes at the surfaces where surface states may be present [Espinosa2021b,

Viswanath2001]. The same applies to amorphous/polycrystalline materials where surface effects may dominate the losses [Wronski1981, Grillanda2015, Girouard2020]. In all cases, a detailed description of the fabrication and surface passivation (if performed) should be provided. These surface effects can result in significant linear absorption creating free carriers and/or excited impurity or defect states which may have long lifetimes. These carriers/excited states can subsequently absorb resulting in an effective 2PA process not easily distinguished from direct 2PA [Espinosa2021b, Grillanda2015]. Such processes may be best characterized using long pulses with high repetition rates and/or CW sources, where the average power makes these nonlinear processes dominant [Grillanda2015]. In addition, if energetically allowed, direct 2PA can also lead to free-carrier generation which results in a higher-order nonlinearity [VanStryland1985, Christodoulides2010].

Although many of the NLO PICs aim in the end to use integrated lasers which have a limited output power, it would be good if the authors report damage thresholds of the waveguides. Special attention should also be paid to quantifying the actual incoupled powers inside the waveguides rather than the incident powers.

Most of the NLO measurements performed in waveguide structures yield an effective NLO coefficient, which represents an irradiance-weighted average over various waveguide constituents [Grant1996]. We recommend performing an 'inverse' calculation to estimate nonlinear material parameters from the measured values. By comparing this result to the known bulk-material nonlinear coefficients, one can validate the model and determine a possible need for improvement.

3.6.3. Data table for on-chip waveguiding materials

Table 7A. Second-order NLO properties of on-chip waveguiding materials from representative works since 2000. Legend for superscripts: see below the table.

Second-Order Nonlinearities								
		Material Properties			Measurement Details		Nonlinear Properties	
					Pump	**Probe/Signal**		
Core	Method	Length[a]	Growth/	Refractive index	Wavelength	Wavelength	$\chi^{(2)}$ (m V^{-1})	Reference
Cladding	Phase matching	Cross-section[b] Width	Deposition	Propagation loss	Peak power	Peak power	d (m V^{-1})	Additional parameters and comments
Substrate		Height[c]	Lithography	Wavelength	Pulse width	Pulse width	η	
		SEM image[d]	Other fabrication		Polarization	Polarization	Normalized η	
					Rep. rate		Bandwidth	
$Al_{0.19}Ga_{0.81}As$	SHG	1.46 mm	MBE	—	1596 nm	—	—	[Morais2017]
Air (suspended)	Birefringent phase matching	Figures 1 and 2 0.9 μm 0.123 μm	E-beam, photolithography	4.5, 64 (SHG) cm^{-1}	8.0 ± 10^{-4} W CW TE	— — —	— 1.2 % W^{-1} —	Periodically bent (snake-like) waveguide.
GaAs (001)		Figure 6(g)	—	1593 nm	—		—	Conversion efficiency dependence on pump wavelength shown in figure 4(b) of the reference paper.
$Al_{0.19}Ga_{0.81}As$	SHG	1 mm	MBE	—	1593 nm	—	—	[Morais2017]
Air (suspended)	Birefringent phase matching	Figures 1 and 2 0.9 μm 0.123 μm	E-beam, photolithography	3.7, 38 (SHG) cm^{-1}	8.0 ± 10^{-4} W CW TE	— — —	— 2.7 % W^{-1} —	Straight waveguide.
GaAs (001)		—	—	1593 nm	—		—	Conversion efficiency dependence on pump wavelength shown in figure 4(b) of the reference paper.
$Al_{0.2}Ga_{0.8}As$	SHG	1.26 mm	—	—	1582.6 nm	—	—	[Duchesne2011]
$Al_{0.7}Ga_{0.3}As$	Modal phase matching	Figure 1 0.65 μm	E-beam	18.3 dB cm^{-1}	1.6 ± 10^{-4} W CW	— —	— —	
GaAs (001)		0.5 μm Figure 6(d)	—	1582 nm	TE and TM —	—	$1.4 \pm 10^{+5}$ % (W x m^2)$^{-1}$ —	

(Continued.)

Table 7A. (Continued.)

Second-Order Nonlinearities								
		Material Properties			**Measurement Details**		**Nonlinear Properties**	
					Pump	**Probe/Signal**		
Core Cladding Substrate	Method Phase matching	Length[a] Cross-section[b] Width Height[c] SEM image[d]	Growth/ Deposition Lithography Other fabrication	Refractive index Propagation loss Wavelength	Wavelength Peak power Pulse width Polarization Rep. rate	Wavelength Peak power Pulse width Polarization	$\chi^{(2)}$ (m V^{-1}) d (m V^{-1}) η Normalized η Bandwidth	Reference Additional parameters and comments
$Al_{0.4}Ga_{0.6}As$ $Al_{0.6}Ga_{0.4}As$ and $Al_{0.2}Ga_{0.8}As$ GaAs	SHG Bragg reflection waveguide	2.12 mm Figure 1 3 μm 4 μm —	MOCVD Photolithography —	— 5.9 cm^{-1} 1555 nm	1600 nm — 2.0 ± 10^{-12} s(FWHM) TE $7.6 \pm 10^{+7}$ Hz	— — — — —	— — 8.6 % W^{-1}[e] $2.1 \pm 10^{+6}$ % (W x m^2)$^{-1}$ $5.3 \pm 10^{+11}$ Hz (FWHM)	[Bijlani2008] The upper and lower reflectors are made of 8 and 10 periods, respectively. Each period: 278 nm of $Al_{0.6}Ga_{0.4}As$ and 118 nm of $Al_{0.2}Ga_{0.8}As$.
$Al_{0.5}Ga_{0.5}As$/ Al_xO_y multilayer Al_xO_y —	SHG Birefringent phase matching	0.6 mm Figure 1 0.8–1 μm — Figure 6(e)	MBE E-beam —	— 23 dB cm^{-1} 1550 nm	1570 nm 2.3 ± 10^{-5} W CW TE —	— — — — —	— — 5 % W^{-1}[e] — —	[Scaccabarozzi2006] Conversion efficiency dependence on pump wavelength shown in figure 2(b) of the reference paper. The reported pump power is taken at the waveguide's output. The Al_xO_y layers are obtained by thermal oxidation of the $Al_{0.93}Ga_{0.07}As$ layers.
$Al_{0.61}Ga_{0.39}As$ $Al_{0.70}Ga_{0.30}As$ and $Al_{0.25}Ga_{0.75}As$ GaAs (100)	DFG Bragg reflection waveguide	1.5 mm — 4.4 μm 3.6 μm —	MOCVD Photolithography —	— 2 (TE), 2.2 (TM) cm^{-1} 1550 nm	775 nm — 2.0 ± 10^{-12} s TM $7.6 \pm 10^{+7}$ Hz	1545.9 nm 2.9 ± 10^{-3} W CW TE	— — 1.2 ± 10^{-4} % W^{-1}[f] $5.4 \pm 10^{+1}$ % (W x m^2)$^{-1}$ $>5 \pm 10^{+12}$ Hz	[Han2010] The symmetric top and bottom Bragg reflectors are made of 6 periods of $Al_{0.70}Ga_{0.30}As$/ $Al_{0.25}Ga_{0.75}As$.

$Al_{0.61}Ga_{0.39}As$ $Al_{0.70}Ga_{0.30}As$ and $Al_{0.25}Ga_{0.75}As$ GaAs (100)	DFG Bragg reflection waveguide	1.5 mm — 4.4 μm 3.6 μm —	MOCVD Photolithography —	— 2 cm^{-1} 1550 nm	775 nm — 2.0 ± 10^{-12} s TE $7.6 \pm 10^{+7}$ Hz	1545.9 nm 2.9 ± 10^{-3} W CW TE	— — 5.2 ± 10^{-4} % W^{-1}[f] $2.3 \pm 10^{+2}$ % $(W \times m^2)^{-1}$ $>5 \pm 10^{+12}$ Hz	[Han2010] The symmetric top and bottom Bragg reflectors are made of 6 periods of $Al_{0.70}Ga_{0.30}As$/$Al_{0.25}Ga_{0.75}As$.
$Al_{0.61}Ga_{0.39}As$ $Al_{0.70}Ga_{0.30}As$ and $Al_{0.25}Ga_{0.75}As$ GaAs (100)	DFG Bragg reflection waveguide	1.5 mm — 4.4 μm 3.6 μm —	MOCVD Photolithography —	— 2 (TE), 2.2 (TM) cm^{-1} 1550 nm	775 nm 6.3 ± 10^{-2} W CW TM —	1545.9 nm 2.9 ± 10^{-3} W CW TE	— — 1.7 ± 10^{-4} % W^{-1}[f] $7.6 \pm 10^{+1}$ % $(W \times m^2)^{-1}$ $>5 \pm 10^{+12}$ Hz	[Han2010] The symmetric top and bottom Bragg reflectors are made of 6 periods of $Al_{0.70}Ga_{0.30}As$/$Al_{0.25}Ga_{0.75}As$.
$Al_{0.61}Ga_{0.39}As$ $Al_{0.70}Ga_{0.30}As$ and $Al_{0.25}Ga_{0.75}As$ GaAs (100)	DFG Bragg reflection waveguide	1.5 mm — 4.4 μm 3.6 μm —	MOCVD Photolithography —	— 2 cm^{-1} 1550 nm	775 nm 6.3 ± 10^{-2} W CW TE —	1545.9 nm 2.9 ± 10^{-3} W CW TE	— — 1.3 ± 10^{-3} % W^{-1}[f] $5.8 \pm 10^{+2}$ % $(W \times m^2)^{-1}$ $>5 \pm 10^{+12}$ Hz	[Han2010] The symmetric top and bottom Bragg reflectors are made of 6 periods of $Al_{0.70}Ga_{0.30}As$/$Al_{0.25}Ga_{0.75}As$.
$Al_{0.61}Ga_{0.39}As$ $Al_{0.70}Ga_{0.30}As$ and $Al_{0.25}Ga_{0.75}As$ GaAs (100)	SFG Bragg reflection waveguide	2.2 mm Figure 1(b) 4.4 μm 3.6 μm Figure 6(f)	— — —	— 2 (TE), 2.2 (TM) cm^{-1} 1550 nm	1555 nm 4.2 ± 10^{-3} W CW TM —	1552–1556 nm 3.5 ± 10^{-4} W CW TE	— 4.00 ± 10^{-11} 2.9 ± 10^{-2}% $3.0 \pm 10^{+6}$ (% $(W \times m^2)^{-1}$)[g] $>7.5 \pm 10^{+12}$ Hz (FWHM)	[Han2009] The effective mode areas: Pump: 6.7 ± 10^{-12} m^2 Probe: 6.6 ± 10^{-12} m^2 The symmetric top and bottom Bragg reflectors are made of 6 periods of $Al_{0.70}Ga_{0.30}As$/$Al_{0.25}Ga_{0.75}As$.
$Al_{0.67}Ga_{0.33}As$ $Al_{0.70}Ga_{0.30}As$ Ge-on-GaAs	SHG Orientation patterned	8 mm Figure 1 7 μm 1.1 μm —	MBE E-beam —	— 5.5, 25–45 (SHG) dB cm^{-1} 1550 nm	1550 nm 3.9 ± 10^{-3} W CW — —	— — — —	— — $4.3 \pm 10^{+1}$ % W^{-1} — —	[Yu2007] Conversion efficiency dependence on sample length shown in figure 4(b) of the reference paper. Quasi-phase matching periods from 4.7 ± 10^{-6} to 4.9 ± 10^{-6} m.

(Continued.)

Table 7A. (Continued.)

Second-Order Nonlinearities								
		Material Properties			Measurement Details		Nonlinear Properties	
					Pump	**Probe/Signal**		
Core Cladding Substrate	Method Phase matching	Length[a] Cross-section[b] Width Height[c] SEM image[d]	Growth/ Deposition Lithography Other fabrication	Refractive index Propagation loss Wavelength	Wavelength Peak power Pulse width Polarization Rep. rate	Wavelength Peak power Pulse width Polarization	$\chi^{(2)}$ (m V^{-1}) d (m V^{-1}) η Normalized η Bandwidth	Reference Additional parameters and comments
$Al_{0.67}Ga_{0.33}As$ $Al_{0.7}Ga_{0.3}As$ GaAs (001)	SHG Periodic domain disordering	5 mm Figure 1 6 μm 1.1 μm Figure 6(c)	MBE Photolithography —	— 6–7 dB cm^{-1} 1550 nm	1559.1 nm 1.9 ± 10^{-3} W CW TE —	— — — —	— — $2.3 \pm 10^{+1}$ % W^{-1} — —	[Yu2005]
AlGaAs/AlO_x multilayer GaAs GaAs	SHG Birefringent phase matching	1.5 mm Figure 1(a) 15.3 μm — Figure 6(i)	MBE E-beam —	Figure 1 1 cm^{-1} 4500 nm	4420 nm 1.6 ± 10^{-2} W 3.0 ± 10^{-7} s TE —	— — — —	— — — $4.4 \pm 10^{+3}$ (% (W m^2)$^{-1}$)[h] —	[Ozanam2014] The multilayer is formed by $Al_{0.19}Ga_{0.81}As$, GaAs and AlO_x. The AlO_x layers are obtained by oxidation of the $Al_{0.98}Ga_{0.02}As$ layers.
AlGaAs/AlO_x multilayer GaAs GaAs	DFG Birefringent phase matching	0.5 mm — 4 μm — —	MBE — —	— 1.6 cm^{-1} 1580 nm	773.2 nm — CW TE —	1559 nm — CW TE	— — — $9.7 \pm 10^{+4}$ (% (W m^2)$^{-1}$)[i] —	[Savanier2011a] The multilayer is formed by $Al_{0.2}Ga_{0.8}As/AlO_x$ and $Al_{0.25}Ga_{0.75}As/AlO_x$. The AlO_x layers are obtained by selective oxidation of the $Al_{0.98}Ga_{0.02}As$ layers.
AlGaAs/AlO_x multilayer GaAs GaAs	SFG Birefringent phase matching	0.5 mm — 4 μm — —	MBE — —	— 1.6 cm^{-1} 1580 nm	1543 nm 1.4 ± 10^{-3} W CW TE —	1550.4 nm 1.9 ± 10^{-4} W CW TE	— — 2.7 % W^{-1} $1.1 \pm 10^{+7}$ % (W m^2)$^{-1}$ 7.2 nm (at 3 dB)	[Savanier2011a] The multilayer is formed by $Al_{0.2}Ga_{0.8}As/AlO_x$ and $Al_{0.25}Ga_{0.75}As/AlO_x$. The AlO_x layers are obtained by selective oxidation of the $Al_{0.98}Ga_{0.02}As$ layers.

AlGaAs/AlO_x multilayer GaAs GaAs	SHG Birefringent phase matching	0.5 mm Figure 4 4 μm — Figure 6(h)	MBE — —	Figure 1 1.13 cm^{-1} 1550 nm	1550 nm 1.6 ± 10^{-2} W CW TE —	— — — —	— — 2.8 % W^{-1} $1.1 \pm 10^{+7}$ % $(W \times m^2)^{-1}$ 2.9 nm (at 3 dB)	[Savanier2011b] The multilayer is formed by $Al_{0.2}Ga_{0.8}As/AlO_x$ and $Al_{0.25}Ga_{0.75}As/AlO_x$. The AlO_x layers are obtained by post-etching lateral oxidation of the $Al_{0.98}Ga_{0.02}As$ layers.
AlN Sapphire and SiO_2 Sapphire c-plane	SHG Temperature tuning	0.188 mm — 1.2–1.3 μm 1.1 μm —	MOCVD E-beam —	— — —	1590 nm 2.6 ± 10^{-4} W CW TM —	— — — —	— — $1.7 \pm 10^{+4}$ % W^{-1}[e] — —	[Bruch2018] Conversion efficiency dependence on temperature shown in figure 3(b) of the reference paper.
AlN Sapphire and SiO_2 Sapphire c-plane	SHG Temperature tuning	0.188 mm — 1.2–1.3 μm 1.1 μm —	MOCVD E-beam —	— — —	1556 nm 2.6 ± 10^{-4} W CW TM —	— — — —	6.20 ± 10^{-12} — $1.5 \pm 10^{+4}$ % W^{-1}[e] — —	[Bruch2018] Conversion efficiency dependence on temperature shown in figure 3(b) of the reference paper.
GaAs Air and SiO_2 Silicon	SHG Birefringent phase matching	2.9 mm Figure 4(a) — 0.158 μm Figure 6(j)	MBE E-beam Wafer bonding	— 1.5 dB cm^{-1} 1968 nm	1968 nm — CW TE —	— — — —	— 1.80 ± 10^{-10} $3.95 \pm 10^{+3}$ % W^{-1}[e] — $1.48 \pm 10^{+11}$ Hz	[Stanton2020] Conversion efficiency dependence on pump wavelength and temperature shown in figure 7 of the reference paper. The linear loss at the SH wavelength is one order of magnitude larger than that at the FF wavelength.
GaAs SiO_2 Silicon	SHG Modal phase matching	1.4 mm Figure 1(a) 1.53 μm 0.15 μm —	MOCVD DUV Wafer bonding	— 2 dB cm^{-1} 2000 nm	2009.8 nm 2.5 ± 10^{-3} W CW TE —	— — — —	— — $2.5 \pm 10^{+2}$ % W^{-1} $1.3 \pm 10^{+8}$ (% $(W \times m^2)^{-1}$)[h] 0.93 nm (at 3 dB)	[Chang2018a] Conversion efficiency dependence on pump wavelength shown in figure 4(c) of the reference paper.

(Continued.)

Table 7A. (Continued.)

Second-Order Nonlinearities								
		Material Properties			**Measurement Details**		**Nonlinear Properties**	
					Pump	**Probe/Signal**		
Core Cladding Substrate	Method Phase matching	Length[a] Cross-section[b] Width Height[c] SEM image[d]	Growth/ Deposition Lithography Other fabrication	Refractive index Propagation loss Wavelength	Wavelength Peak power Pulse width Polarization Rep. rate	Wavelength Peak power Pulse width Polarization	$\chi^{(2)}$ (m V^{-1}) d (m V^{-1}) η Normalized η Bandwidth	Reference Additional parameters and comments
GaAs SiO_2 Silicon	SHG Ring resonator phase matching	— Figure 1(a) 1.3 μm 0.15 μm —	MOCVD DUV Wafer bonding	— 2 dB cm^{-1} 2000 nm	2000 nm 6.1 ± 10^{-5} W CW TE —	— — — — —	— — 4%, $6.5 \pm 10^{+4}$ % W^{-1} — —	[Chang2019] The efficiency reported is for a ring resonator device.
GaAs/$Al_{0.85}Ga_{0.15}As$ superlattice $Al_{0.56}Ga_{0.44}As$, $Al_{0.60}Ga_{0.40}As$ and $Al_{0.85}Ga_{0.15}As$ GaAs	DFG Periodic domain disordering	1 mm Figure 1 3 μm 0.6 μm —	MBE — —	— 1.8 (TE), 3.7 (TM) cm^{-1} 1550 nm	792.9 nm 3.1 ± 10^{-2} W CW TE —	1535–1555 nm 5.2 ± 10^{-2} W CW TE and TM	— — — $1.2 \pm 10^{+2}$ (% (W×m^2)$^{-1}$)[i] —	[Wagner2011] 14:14 GaAs:$Al_{0.85}Ga_{0.15}As$ monolayers superlattice.
GaAs/$Al_{0.85}Ga_{0.15}As$ superlattice $Al_{0.56}Ga_{0.44}As$, $Al_{0.60}Ga_{0.40}As$ and $Al_{0.85}Ga_{0.15}As$ GaAs	DFG Periodic domain disordering	1 mm Figure 1 3 μm 0.6 μm —	MBE — —	— 1.8 (TE), 3.7 (TM) cm^{-1} 1550 nm	791.7 nm 2.4 ± 10^{-2} W CW TM —	1535–1555 nm 4.9 ± 10^{-2} W CW TE	— — — $7.2 \pm 10^{+2}$ (% (W×m^2)$^{-1}$)[i] $>12.5 \pm 10^{+12}$ Hz	[Wagner2011] 14:14 GaAs:$Al_{0.85}Ga_{0.15}As$ monolayers superlattice. The conversion bandwidth is the maximum separation between the signal and idler.

GaN	SHG	4 mm	MBE, MOVPE	—	1263 nm	—	—	[Gromovyi2017]
$Al_{0.65}Ga_{0.35}N$	Modal phase matching	Figure 3	—	1 dB cm^{-1}	$9.0 \pm 10^{+1}$ W	—	—	
Sapphire		—			4.0 ± 10^{-9} s	—	2%	
		1.2 μm	—	1260 nm	TM	—	$1.5 \pm 10^{+3}$ % $(W \times m^2)^{-1}$	
		—			$1.0 \pm 10^{+3}$ Hz		—	
GaN	SHG	—	MOCVD, PECVD	2.3	1550 nm	—	1.60 ± 10^{-11}	[Xiong2011]
SiO_2	—	Figures 2(b) and 4(b), (c)	E-beam	—	1.2 ± 10^{-1} W	—	—	
Silicon		0.86 μm	Wafer bonding	1550 nm	CW	—	3.2 ± 10^{-3} %	
		0.4 μm			—	—	—	
		Figure 6(a)			—		—	
$LiNbO_3$	SHG	4 mm	—	—	1550 nm	—	—	[Wang2018b]
Air and SiO_2	Periodically poled	Figures 1(a) and (b)	Photolithography, e-beam	2.5 dB cm^{-1}	2 ± 10^{-3}–2.2 ± 10^{-1} W	—	—	Conversion efficiency dependence on pump wavelength shown in figure 3 of the reference paper.
LN-on-insulator		1.4 μm		1550 nm	CW	—	—	
		0.6 μm	—		TE	—	$2.6 \pm 10^{+7}$ (% $(W \times m^2)^{-1})^h$	
		Figure 6(b)			—		7 nm (at 3 dB)	

[a] The length of ring resonators was calculated from the ring radius.
[b] Figure of the reference paper showing the cross-section geometry.
[c] For heterostructure waveguides, the reported height is the guiding layer thickness.
[d] Selected SEM images presented in this work for each geometry and material platform.
[e] Conversion efficiency formula: $\eta = P_{SH}/P_{FF}^2$ [SH—Second Harmonic, FF—Fundamental Frequency].
[f] Conversion efficiency formula: $\eta = P_{DF}/(P_P P_S)$ [DF—Difference frequency, P—Pump, S—Signal].
[g] Conversion efficiency formula: $\eta = P_{SF}\lambda_{SF}/(P_S \lambda_S)$ [SF—Sum frequency, P—Pump, S—Signal].
[h] Normalized conversion efficiency formula: $\eta_N = P_{SH}/(P_{FF}L)^2$ [SH—Second Harmonic, FF—Fundamental Frequency, L—Length].
[i] Normalized conversion efficiency formula: $\eta_N = P_{DF}/(P_P P_S L^2)$ [DF—Difference frequency, P—Pump, S—Signal, L-Length].

Table 7B. Third-order NLO properties of on-chip waveguiding materials from representative works since 2000. Legend for superscripts: see below the table.

Third-Order Nonlinearities								
		Material Properties			Measurement Details		Nonlinear Properties	
					Pump	**Probe/signal**		
Core	Method	Length[a]	Crystallinity	Refractive index	Wavelength	Wavelength	n_2	Reference
Cladding		Cross section[b]	Growth/deposition	Propagation loss	Peak power	Peak power	α_2	Additional parameters and comments
Substrate		Width		Wavelength	Pulse width	Pulse width	γ_{eff}	
		Height[c]	Lithography	Bandgap	Polarization	Polarization	η	
		SEM image[d]	Other fab	GVD	Rep. rate	Rep. rate	Bandwidth	
				Dispersion curve[e]	Effective area	Effective area		
III–V semiconductors								
AlN	FWM	0.376 mm	—	—	—	—	2.3 ± 10^{-19} m^2 W^{-1}	[Jung2013]
SiO_2		Figure 1(c)	Sputtering	—	5.0 ± 10^{-1} W	—	—	
Silicon		3.5 μm		1555 nm	CW	—	—	
		0.65 μm	—	—	TE	—	—	
		Figure 7(v)	—	—	—	—	—	
				Figure 1(a)	1.3 ± 10^{-12} m^2	—		
$Al_{0.12}Ga_{0.88}As$	FWM	0.81 mm	—	—	1566 nm	1564 nm	—	[Zheng2019a]
SiO_2		—	MOVPE	1.2 dB cm^{-1}	3.8 ± 10^{-4} W	—	—	The device is a racetrack resonator, with 17 μm-radius curved waveguide and 700 μm-long straight waveguide parts.
Sapphire		0.44 μm	E-beam	1550 nm	CW	CW	—	
		0.3 μm		—	TE	—	19.8 dB[g]	
		—	Wafer bonding, substrate removal	—	—	—	—	
				—	—	—		
$Al_{0.18}Ga_{0.82}As$	FWM	1 mm	Monocrystalline	—	1470–1540 nm	1540–1560 nm	—	[Espinosa2021a]
$Al_{0.65}Ga_{0.35}As$ and $Al_{0.35}Ga_{0.65}As$		Figure 1	—	2 dB cm^{-1}	—	2.8 ± 10^{-2} W	—	The length of the 900 nm-wide part is 1 mm, but the total length is 5.26 mm, which includes the 2 μm-wide couplers.
		0.9 μm		1520 nm	3.0 ± 10^{-12}	CW	$5.1 \pm 10^{+1}$ m^{-1}W^{-1}	
		0.8 μm	E-beam	—	s(FWHM)	TE	15.8%[h]	
GaAs (100)		—	—	1.0 ± 10^{-24} s^2 m^{-1}	TE	—	$3.2 \pm 10^{+12}$ Hz	Conversion efficiency dependence on pump-probe detuning shown in figure 9 of the reference paper.
				Figure 5	$7.7 \pm 10^{+7}$ Hz	—	(at 20 dB)	
					1.4 ± 10^{-12} m^2			

$Al_{0.18}Ga_{0.82}As$ $Al_{0.65}Ga_{0.35}As$ GaAs [100]	FWM	2 mm Figure 1 0.6 μm 1.4 μm —	Monocrystalline — E-beam —	— 40 dB cm^{-1} 1520 nm — 7.5 ± 10^{-25} s^2 m^{-1} Figure 5	1470–1540 nm — 3.0 ± 10^{-12} s(FWHM) TE $7.7 \pm 10^{+7}$ Hz 3.2 ± 10^{-13} m^2	1540–1560 nm 2.8 ± 10^{-2} W CW TE — —	— — $1.8 \pm 10^{+2}$ m^{-1}W^{-1} 31.6%[h] $3.8 \pm 10^{+12}$ Hz (at 20 dB)	[Espinosa2021a] The length of the 600 nm-wide part is 2 mm, but the total length is 5.33 mm, which includes the 2 μm-wide couplers. Conversion efficiency dependence on pump-probe detuning shown in figure 9 of the reference paper.
$Al_{0.18}Ga_{0.82}As$ $Al_{0.65}Ga_{0.35}As$ GaAs [100]	FWM	1 mm Figure 1 0.8 μm 0.7 μm Figure 7(f)	Monocrystalline — E-beam —	— 7 dB cm^{-1} 1520 nm — 1.5 ± 10^{-24} s^2 m^{-1} Figure 5	1470–1540 nm — 3.0 ± 10^{-12} s(FWHM) TE $7.7 \pm 10^{+7}$ Hz 7.3 ± 10^{-13} m^2	1540–1560 nm 2.8 ± 10^{-2} W CW TE — —	— — $9.0 \pm 10^{+1}$ m^{-1}W^{-1} 12.6%[h] —	[Espinosa2021a] The length of the 800 nm wide part is 1 mm, but the total length is 5.87 mm, which includes the 2 μm-wide couplers. Conversion efficiency dependence on pump-probe detuning is shown in figure 9 of the reference paper.
$Al_{0.18}Ga_{0.82}As$ $Al_{0.7}Ga_{0.3}As$ GaAs	FWM	25 mm Figure 1 1.2 μm 1.7 μm —	Monocrystalline MBE Photolithography —	— 1.9 dB cm^{-1} 1550 nm 1.64 eV 9.0 ± 10^{-25} s^2 m^{-1} —	1550.5 nm 8.0 ± 10^{-1} W CW TE — 7.3 ± 10^{-13} m^2	1551.9 nm — CW TE — —	1.1 ± 10^{-17} m^2 W^{-1} 5.0 ± 10^{-13} m W^{-1} — 10%[f] —	[Apiratikul2014] Conversion efficiency dependence on pump power is shown in figure 4 of the reference paper.
$Al_{0.18}Ga_{0.82}As$ $Al_{0.7}Ga_{0.3}As$ GaAs	FWM	25 mm Figure 1 1.35 μm 1.7 μm —	Monocrystalline MBE Photolithography Reflown resist	— 0.56 dB cm^{-1} 1550 nm 1.64 eV 9.0 ± 10^{-25} s^2 m^{-1} Figure 6	1550.5 nm 8.0 ± 10^{-1} W CW TE — 8.2 ± 10^{-13} m^2	1551.9 nm — CW TE — —	7.0 ± 10^{-18} m^2 W^{-1} 3.0 ± 10^{-13} m W^{-1} — 22.9%[f] —	[Apiratikul2014] Photoresist reflow was used to achieve smoother sidewalls.
$Al_{0.18}Ga_{0.82}As$ $Al_{0.7}Ga_{0.3}As$ GaAs	FWM	5 mm Figure 1 0.69 μm 1.7 μm —	Monocrystalline MBE Photolithography —	— — 1550 nm 1.64 eV 2.2 ± 10^{-25} s^2 m^{-1} Figure 6	1550.5 nm 8.0 ± 10^{-1} W CW TE — 4.4 ± 10^{-13} m^2	1551.9 nm — CW TE — —	— — — 0.16%[f] $8.0 \pm 10^{+12}$ Hz (at 3 dB)	[Apiratikul2014] Uncoated.

(Continued.)

Table 7B. (Continued.)

Third-Order Nonlinearities								
		Material Properties			Measurement Details		Nonlinear Properties	
					Pump	**Probe/signal**		
Core Cladding Substrate	Method	Length[a] Cross section[b] Width Height[c] SEM image[d]	Crystallinity Growth/deposition Lithography Other fab	Refractive index Propagation loss Wavelength Bandgap GVD Dispersion curve[e]	Wavelength Peak power Pulse width Polarization Rep. rate Effective area	Wavelength Peak power Pulse width Polarization Rep. rate Effective area	n_2 α_2 γ_{eff} η Bandwidth	Reference Additional parameters and comments
$Al_{0.18}Ga_{0.82}As$ $Al_{0.7}Ga_{0.3}As$ GaAs	FWM	5 mm Figure 1 0.69 μm 1.7 μm figure 7(e)	Monocrystalline MBE Photolithography —	— — 1550 nm 1.64 eV 4.4 ± 10^{-25} s^2 m^{-1} Figure 6	1550.5 nm 8.0 ± 10^{-1} W CW TE — 4.7 ± 10^{-13} m^2	1551.9 nm — CW TE — —	— — — 0.25%[f] $5.5 \pm 10^{+12}$ Hz (at 3 dB)	[Apiratikul2014] Coated with SiN_x.
$Al_{0.20}Ga_{0.80}As$ $Al_{0.50}Ga_{0.50}As$ and $Al_{0.24}Ga_{0.76}As$ GaAs	Nonlinear transm./refl.	10 mm Figure 1 2 μm 1.2 μm —	Monocrystalline MOCVD E-beam, photolithography —	— 3.2 dB cm^{-1} 1550 nm — 1.2 ± 10^{-24} s^2 m^{-1} —	1550 nm $1.5 \pm 10^{+2}$ W 2.0 ± 10^{-12} s(FWHM) — $3.6 \pm 10^{+7}$ Hz 4.4 ± 10^{-12} m^2	— — — — — — —	— — — — — — —	[Dolgaleva2011] 3PA coefficient = 8 ± 10^{-26} m^3 W^{-2} at 1550 nm.
$Al_{0.21}Ga_{0.79}As$ SiO_2 and HSQ SOI	FWM	9 mm Figure 1 0.63 μm 0.29 μm —	— Epitaxy, PECVD E-beam Wafer bonding	— 1.5 dB cm^{-1} 1549.5 nm 1.69 eV 250 ps (nm × km)$^{-1}$ figure 3	1549.5 nm 1.1 ± 10^{-1} W CW TE — —	— — — — — —	— — — 12 dB[i] 55 nm (at 3 dB)	[Ros2017] Conversion efficiency dependence on length, pump power and signal—pump spacing shown in figure 5 of the reference paper.
$Al_{0.23}Ga_{0.77}As$ $Al_{0.7}Ga_{0.3}As$ and SiN_x GaAs	FWM	10.8 mm Figure 1 0.2–1 μm 2.1 μm —	Monocrystalline — Projection lithography —	— 5.1 dB cm^{-1} 1550 nm — — —	1538–1563 nm 1.2 ± 10^{-1} W CW TM — 6.2 ± 10^{-13} m^2	1565 nm 3.2 ± 10^{-2} W CW TM — —	— — — 0.2%[j] $1.0 \pm 10^{+12}$ Hz (at 3 dB)	[Mahmood2014] Conversion efficiency dependence on pump—probe detuning shown in figure 2 of the reference paper.

$Al_{0.26}Ga_{0.74}As$ PhC Air —	SRS Pump Probe	1 mm — — — —	Monocrystalline — —	— 9.1 cm^{-1} 1606 nm — — —	1550 nm 4.4 W 5.0 ± 10^{-12} s TE $2.0 \pm 10^{+7}$ Hz —	1605.8 nm 2.8 ± 10^{-4} W CW TE — —	— — — — — —	[Oda2008] g_{Raman}: 5.1 ± 10^{-11} m W^{-1} Raman shift: $2.85 \pm 10^{+4}$ m^{-1} Linewidth: $3.6 \pm 10^{+2}$ m^{-1} The lattice constant, thickness, and hole diameter are 452, 260, and 120 nm, respectively.
$Al_{0.32}Ga_{0.68}As$ Air Silicon	SPM/XPM spectral broadening	4 mm Figures 1(a) and (b) 0.48 μm 0.54 μm Figure 7(h)	Monocrystalline Epitaxy E-beam Wafer bonding	— 0.45 dB cm^{-1} 2400 nm 1.82 eV 20 ps $(nm \times km)^{-1}$ Figures 4(c) and 5(c)	1560 nm — 6.1 ± 10^{-14} s TE $1.6 \pm 10^{+8}$ Hz 2.2 ± 10^{-13} m^2	— — — — — —	— — — — 1200 nm (at 20 dB)	[Chiles2019] The reported bandwidth is for the supercontinuum generation (from 1100 nm to 2300 nm). Supercontinuum generation bandwidth dependence on pulse energy shown in figure 4(a) of the reference paper.
$Al_{0.32}Ga_{0.68}As$ Air Silicon	SPM/XPM spectral broadening	2.3 mm Figures 1(a) and (b) 2.15 μm 0.54 μm Figure 7(h)	Monocrystalline Epitaxy E-beam Wafer bonding	— 0.45 dB cm^{-1} 2400 nm 1.82 eV 20 ps $(nm \times km)^{-1}$ Figures 4(c) and 5(c)	3060 nm — 8.5 ± 10^{-14} s TE $1.0 \pm 10^{+8}$ Hz 1.2 ± 10^{-12} m^2	— — — — — —	— — — — 4200 nm (at 20 dB)	[Chiles2019] The reported bandwidth is for the supercontinuum generation (from 2300 nm to 6500 nm). Supercontinuum generation bandwidth dependence on pulse energy shown in figure 5(a) of the reference paper.
AlGaAs $Al_{0.7}Ga_{0.3}As$ GaAs	FWM	10 mm Figures 1 and 2 — — Figure 7(d)	Monocrystalline — — —	— 1.5 dB cm^{-1} 1550 nm 1.6 eV 1.1 ± 10^{-24} s^2 m^{-1} —	1552.45 nm 1.0 ± 10^{-1} W CW TE — —	1551.9 nm — CW TE — —	2.3 ± 10^{-17} m^2 W^{-1} 3.3 ± 10^{-11} m W^{-1} — 1.6%[f] —	[Wathen2014] The 2PA coefficient was measured at 1550 nm by the nonlinear transmittance technique with: Pulse width: 1.26 ± 10^{-12} s Rep. rate: $1 \pm 10^{+7}$ Hz Peak irradiance: $<3.5 \pm 10^{+13}$ W m^{-2}

(Continued.)

Table 7B. (Continued.)

Third-Order Nonlinearities									
		Material Properties			Measurement Details		Nonlinear Properties		
					Pump	**Probe/signal**			
Core Cladding Substrate	Method	Length[a] Cross section[b] Width Height[c] SEM image[d]	Crystallinity Growth/deposition Lithography Other fab	Refractive index Propagation loss Wavelength Bandgap GVD Dispersion curve[e]	Wavelength Peak power Pulse width Polarization Rep. rate Effective area	Wavelength Peak power Pulse width Polarization Rep. rate Effective area	n_2 α_2 γ_{eff} η Bandwidth	Reference Additional parameters and comments
AlGaAs $Al_{0.7}Ga_{0.3}As$ GaAs	FWM	10 mm Figures 1 and 2 — — Figure 7(d)	Monocrystalline — — —	— 0.74 dB cm^{-1} 1550 nm 1.66 eV — —	1552.45 nm 1.0 ± 10^{-1} W CW TE — —	1551.9 nm — CW TE — —	1.5 ± 10^{-17} m^2 W^{-1} — — 0.6%[f] —	[Wathen2014] 3PA coefficient = 8.3 ± 10^{-26} m^3 W^{-2} at 1550 nm, measured by nonlinear transmittance with: Pulse width: 1.26 ± 10^{-12} s Rep. rate: $1 \pm 10^{+7}$ Hz Peak irradiance $<8 \pm 10^{+13}$ W m^{-2}
AlGaAs $Al_{0.7}Ga_{0.3}As$ GaAs	FWM	25 mm Figures 1 and 2 — — Figure 7(d)	Monocrystalline — — —	— 0.56 dB cm^{-1} 1550 nm 1.77 eV — —	1552.45 nm 1.0 ± 10^{-1} W CW TE — —	1551.9 nm — CW TE — —	9.0 ± 10^{-18} m^2 W^{-1} — — 22.9%[f] $1.6 \pm 10^{+12}$ Hz (at 3 dB)	[Wathen2014] —
AlGaAs $Al_{0.7}Ga_{0.3}As$ GaAs	FWM	5 mm Figures 1 and 2 — — Figure 7(d)	Monocrystalline — — —	— 3 dB cm^{-1} 1550 CW 1.79 eV 4.5 ± 10^{-25} s^2 m^{-1} —	1552.45 nm 1.0 ± 10^{-1} W CW TE — —	1551.9 nm — — TE — —	8.5 ± 10^{-18} m^2 W^{-1} — — 0.4%[f] $5.5 \pm 10^{+12}$ Hz (at 3 dB)	[Wathen2014]
AlGaAs SiO_2 and HSQ SOI	FWM	3 mm Figure 1(c) 0.465 μm 0.29 μm Figure 7(g)	— MOVPE, PECVD E-beam Wafer bonding, substrate removal	— 2 dB cm^{-1} 1545 nm — — —	1543.6 nm — CW TE — —	1538.2 nm — CW TE — —	— — $7.2 \pm 10^{+2}$ $m^{-1}W^{-1}$ 16 dB 130 nm (at 3 dB)	[Stassen2019] The nonlinear coefficient was measured on a straight waveguide device, while the FWM efficiency was measured on a microring. The conversion bandwidth is the same for the waveguide and microring.

AlGaAs SiO_2 and HSQ SOI	FWM	3 mm Figure 1(b) 0.64 μm 0.28 μm —	— MOVPE, PECVD E-beam Wafer bonding, Substrate removal	3.3 1.3 dB cm^{-1} — — 46 ps (nm km)$^{-1}$ —	1550 nm 4.0 ± 10^{-1} W CW TE — —	1549 nm 1.0 ± 10^{-4} W CW TE — —	— — $6.3 \pm 10^{+2}$ m^{-1}W^{-1} 4.2 dB 750 nm (at 3 dB)	[Pu2018]
AlGaAs SiO_2 and HSQ SOI	FWM	9 mm — — — —	— MOVPE, PECVD E-beam Wafer bonding, Substrate removal	— 8 dB cm^{-1} — — 164 ps (nm km)$^{-1}$ —	1550 nm 1.6 ± 10^{-1} W CW TE — —	1545 nm — CW TE — —	— — $3.5 \pm 10^{+2}$ m^{-1}W^{-1} 15 dB —	[Kaminski2019] Conversion efficiency dependence on signal wavelength shown in figure 4 of the reference paper. The authors also reported a conversion efficiency of 23 dB for a 3 mm-long waveguide.
AlGaAs SiO_2 and HSQ SOI	SPM/XPM spectral broadening	5 mm Figure 1(b) 0.6 μm 0.28 μm —	— Epitaxy, PECVD E-beam Wafer bonding, Substrate removal	— 1.5 dB cm^{-1} 1542 nm — — Figure S1	1542 nm 5.6 W 1.5 ± 10^{-12} s(FWHM) TE $1.0 \pm 10^{+10}$ Hz —	— — — — — —	— — — 66%[k] 44 nm (at 20 dB)	[Hu2018] The generated comb wavelength ranges from 1520 nm to 1539.8 nm, and from 1546.1 nm to 1570 nm, as informed in the supplementary material.
GaAs/$Al_{0.85}Ga_{0.15}As$ superlattice $Al_{0.56}Ga_{0.44}As$ and $Al_{0.60}Ga_{0.40}As$ GaAs	SPM/XPM spectral broadening	5.7 mm — 3 μm 1 μm —	Monocrystalline MBE — —	— 0.65 cm^{-1} 1550 nm — — —	1545 nm $4.0 \pm 10^{+2}$ W 2 ± 10^{-12} s(FWHM) TE, TM $7.6 \pm 10^{+7}$ Hz 4.5 ± 10^{-12} m^2	— — — — — —	7.5 ± 10^{-18} m^2 W^{-1} — — — — —	[Wagner2009] Nonlinearities dependence on wavelength shown in figure 3 of the reference paper.
GaAs/AlAs superlattice $Al_{0.56}Ga_{0.44}As$ and $Al_{0.60}Ga_{0.40}As$ GaAs	SPM/XPM spectral broadening	12 mm Figure 1 3 μm 0.8 μm —	Monocrystalline MBE Photolithography —	— 0.25 cm^{-1} 1500–1600 nm — 1.0 ± 10^{-24} s^2 m^{-1} —	1545 nm $3.0 \pm 10^{+2}$ W 2 ± 10^{-12} s(FWHM) TE $7.6 \pm 10^{+7}$ Hz 9.7–11.2 $\pm 10^{-12}$ m^2	— — — — — —	3.2 ± 10^{-17} m^2 W^{-1} 2.0 ± 10^{-11} m W^{-1} — — —	[Wagner2007] Nonlinearities dependence on wavelength shown in figures 2, 5, 8 and 10 of the reference paper.

(Continued.)

Table 7B. (Continued.)

Third-Order Nonlinearities									
		Material Properties			Measurement Details		Nonlinear Properties		
					Pump	**Probe/signal**			
Core	Method	Length[a]	Crystallinity	Refractive index	Wavelength	Wavelength	n_2	Reference	
Cladding		Cross section[b]	Growth/deposition	Propagation loss	Peak power	Peak power	α_2	Additional parameters and comments	
Substrate		Width		Wavelength	Pulse width	Pulse width	γ_{eff}		
		Height[c]	Lithography	Bandgap	Polarization	Polarization	η		
		SEM image[d]	Other fab	GVD	Rep. rate	Rep. rate	Bandwidth		
				Dispersion curve[e]	Effective area	Effective area			
GaAs/AlAs superlattice	SPM/XPM spectral broadening	12 mm Figure 1 3 μm 0.8 μm —	Monocrystalline MBE Photolithography —	— 0.7 cm^{-1} 1500–1600 nm — — —	1545 nm $3.0 \pm 10^{+2}$ W 2 ± 10^{-12} s(FWHM) TM $7.6 \pm 10^{+7}$ Hz $16\text{–}24 \pm 10^{-12}$ m^2	— — — — — —	1.7 ± 10^{-17} m^2 W^{-1} 1.0 ± 10^{-11} m W^{-1} — — —	[Wagner2007] Nonlinearities dependence on wavelength shown in figures 2, 5, 8 and 10 of the reference paper.	
$Al_{0.56}Ga_{0.44}As$ and $Al_{0.60}Ga_{0.40}As$									
GaAs									
$In_{0.53}Ga_{0.47}As/AlAs_{0.56}Sb_{0.44}$ CDQW	SPM/XPM spectral broadening	0.25 mm Figure 1 3 μm — —	— — — — —	— — — — — —	1560 nm — 2.0 ± 10^{-12} s TM $1.0 \pm 10^{+10}$ Hz —	1360 nm — CW TE — —	— — — — — —	[Cong2008] XPM efficiency = 2.0 ± 10^{11} rad J^{-1}. See the reference paper for quantum well layers thicknesses.	
—									
InP									
InGaAs/AlAs/AlAsSb CDQW	SPM/XPM spectral broadening	0.24 mm — — — —	— — — — —	— 278 cm^{-1} 1600 nm — — Figure 2	1550 nm — 7.0 ± 10^{-13} s TM $8.0 \pm 10^{+7}$ Hz —	1539.67 nm — CW TE — —	— — — — — —	[Lim2010] XPM efficiency = 5.2 ± 10^{10} rad J^{-1} See the reference paper for quantum well layers thicknesses. $I_{\text{sat}} = 19$ J m^{-2}	
InAlAs and InP									
InP									
InGaAs/AlAs/AlAsSb CDQW	SPM/XPM spectral broadening	0.24 mm — 2 μm — —	— — — — —	— — — — — —	1550.1 nm — 2.3 ± 10^{-12} s TM $1.0 \pm 10^{+10}$ Hz —	1559.9 nm — CW TE — —	— — — — — —	[Tsuchida2007] XPM efficiency = 4.9 ± 10^{11} rad J^{-1} See the reference paper for quantum well layers thicknesses.	
InAlAs									
—									

InGaAs/ AlAsSb CDQW AlGaAsSb and InP InP	SPM/XPM spectral broadening	0.25 mm Figure 1(b) 2 μm — —	— — — —	— 400 cm^{-1} 1560 nm — — Figures 2(d) and (e)	1560 nm — 2.0 ± 10^{-12} s TM $1.0 \pm 10^{+10}$ Hz —	1541 nm — CW TE — —	— — — — — —	[Cong2009] XPM efficiency = 3.3 ± 10^{11} rad J^{-1} See the reference paper for quantum well layers thicknesses. XPM efficiency dependence on doping density shown in figure 2(c) of the reference paper
InGaAs/AlAsSb CDQW InP InP	SPM/XPM spectral broadening	1 mm — 1.3 μm — —	— MBE E-beam —	— — — — — —	1560 nm — 2.4 ± 10^{-12} s TM $1.0 \pm 10^{+10}$ Hz —	1545 nm — CW TE — —	— — — — — —	[Feng2013] XPM efficiency = 9.3 ± 10^{11} rad J^{-1} The experimental setup and the waveguide fabrication details given in Feng *et al* [Feng2012].
GaP SiO_2 Silicon	FWM	0.314 mm Figure 2(d) 0.5 μm 0.3 μm Figure 7(k)	Monocrystalline MOCVD — Wafer bonding	3.1 1.2 dB cm^{-1} 1560 nm 2.1 eV — Figure 2(e)	1560 nm — CW — — 1.5 ± 10^{-13} m^2	— — —— — —	1.1 ± 10^{-17} m^2 W^{-1} — $2.4 \pm 10^{+2}$ m^{-1}W^{-1} — —	[Wilson2020]
InGaP SiO_2 —	SPM/XPM spectral broadening	1.3 mm Figure 1(a) — — Figure 7(j)	— — — —	3.13 10 dB cm^{-1} 1544 nm 1.9 eV 1.1 ± 10^{-21} s^2 m^{-1} Figure 1(b)	1551 nm — 3.2 ± 10^{-12} s(FWHM) — $2.2 \pm 10^{+7}$ Hz —	— — — — — —	— — $9.2 \pm 10^{+2}$ m^{-1}W^{-1} — —	[Colman2010] The GVD in the table is for 1555 nm.
InGaP SiO_2 Silicon	FWM	2 mm Figure 1 0.63 μm 0.25 μm Figure 7(i)	— MOCVD E-beam Wafer bonding	— 12 dB cm^{-1} 1540 nm 1.9 eV 5.0 ± 10^{-25} s^2 m^{-1} figure 2	1552.4 nm 3.8 ± 10^{-2} W CW TE — 2.4 ± 10^{-13} m^2	1551.1 nm 1.5 ± 10^{-3} W CW TE — 2.4 ± 10^{-13} m^2	— — $4.8 \pm 10^{+2}$ m^{-1}W^{-1} 0.08%[f] —	[Dave2015a] 3PA coefficient = 2.5 ± 10^{-26} m^3 W^{-2}

(Continued.)

Table 7B. (Continued.)

Third-Order Nonlinearities								
		Material Properties			**Measurement Details**		**Nonlinear Properties**	
					Pump	**Probe/signal**		
Core Cladding Substrate	Method	Length[a] Cross section[b] Width Height[c] SEM image[d]	Crystallinity Growth/deposition Lithography Other fab	Refractive index Propagation loss Wavelength Bandgap GVD Dispersion curve[e]	Wavelength Peak power Pulse width Polarization Rep. rate Effective area	Wavelength Peak power Pulse width Polarization Rep. rate Effective area	n_2 α_2 γ_{eff} η Bandwidth	Reference Additional parameters and comments
InGaP SiO_2 Silicon	SPM/XPM spectral broadening	2 mm Figures 1 and 3 0.7 μm 0.25 μm —	— MOCVD E-beam Wafer bonding	— 12 dB cm^{-1} 1550 nm — 6.0 ± 10^{-25} s^2 m^{-1} figure 1	1550 nm $1.1 \pm 10^{+1}$ W 1.7 ± 10^{-13} s(FWHM) TE $8.2 \pm 10^{+7}$ Hz 2.1 ± 10^{-13} m^2	— — — — — — —	— — — — $1.6 \pm 10^{+14}$ Hz (at 30 dB)	[Dave2015b] Supercontinuum generation bandwidth dependence on waveguide width shown in figure 2 of the reference paper.
$In_{0.63}Ga_{0.37}As_{0.8}P_{0.2}$ InP InP	FWM	8 mm Figure 1 1.7 μm 0.9 μm —	Monocrystalline MOCVD E-beam —	3.4 3 dB cm^{-1} 1568 nm — 2.2 ± 10^{-23} s^2 m^{-1} —	1568 nm 9.0 W 3.0 ± 10^{-12} s TM $7.6 \pm 10^{+7}$ Hz 1.1 ± 10^{-12} m^2	1551 nm 5.0 ± 10^{-1} W CW TM — —	1.0 ± 10^{-17} m^2 W^{-1} — — 0.001%[f] $5.5 \pm 10^{+12}$ Hz	[Saeidi2018] Conversion bandwidth calculated as the maximum signal-to-idler wavelength separation
$In_{0.63}Ga_{0.37}As_{0.8}P_{0.2}$ InP InP	Nonlinear transm./refl.	8 mm Figure 1 1.7 μm 0.9 μm —	Monocrystalline MOCVD E-beam —	3.4 3 dB cm^{-1} 1568 nm — 2.2 ± 10^{-23} s^2 m^{-1} —	1568 nm $4.8 \pm 10^{+1}$ W 3.0 ± 10^{-12} s TM $7.6 \pm 10^{+7}$ Hz 1.1 ± 10^{-12} m^2	— — — — — —	— 1.90 ± 10^{-10} m W^{-1} — — — —	[Saeidi2018]
InGaAsP QW InP InP	FWM	10 mm — — — —	Monocrystalline — — — —	— — — 0.83 eV — —	1548 nm 2.5 ± 10^{-2} W CW — — —	10-nm shift — CW — — —	— — — 0.16% — —	[Thoen2000] 10 nm-thick InGaAsP quantum wells with 15 nm InP barriers centered in InGaAsP guiding layer

Silicon and silicon carbide, nitride, and oxide								
a-Si SiO_2 Silicon	FWM	18.3 mm — 0.48 μm 0.225 μm —	— PECVD E-beam —	3.39 6 dB cm^{-1} 1550 nm — — —	1602 nm 2.3 ± 10^{-1} W CW TE — —	1-nm shift — CW — — —	1.5 ± 10^{-17} m^2 W^{-1} — — 3.39%[f] — 	[Girouard2020]
a-Si SiO_2 Silicon	FWM	1 mm Figure 1 0.48 μm 0.22 μm —	— PECVD E-beam —	— 4.7 dB cm^{-1} 1550 nm — 4.8 ± 10^{-25} s^2 m^{-1} —	1550 nm 7.0 ± 10^{-2} W CW TE — —	1550.5 nm — CW TE — —	— — $8.0 \pm 10^{+2}$ m^{-1}W^{-1} 0.25%[f] $6.0 \pm 10^{+12}$ Hz (at 3 dB)	[Lacava2016]
a-Si SiO_2 Silicon	FWM	8 mm Figure 1 0.5 μm 0.205 μm —	— PECVD E-beam —	— 7.2 dB cm^{-1} 1550 nm — 1.6 ± 10^{-25} s^2 m^{-1} —	1540 nm 3.0 ± 10^{-4} W CW TE — —	— — CW TE — —	7.4 ± 10^{-17} m^2 W^{-1} — — 0.1%[f] $2.0 \pm 10^{+13}$ Hz (at 3 dB)	[Wang2012a] Conversion efficiency dependence on converted wavelength shown in figure 2 of the reference paper.
a-Si SiO_2 Silicon	FWM	— — 0.5 μm 0.205 μm —	— PECVD E-beam —	— 7.2 dB cm^{-1} 1550 nm — — —	1560 nm 1.3 ± 10^{-2} W 2.8 ± 10^{-12} s TE $1.0 \pm 10^{+10}$ Hz —	1540 nm — 2.8 ± 10^{-12} s TE $1.0 \pm 10^{+10}$ Hz —	7.4 ± 10^{-17} m^2 W^{-1} — — 5%[f] $2.0 \pm 10^{+13}$ Hz (at 3 dB)	[Wang2012a]
a-Si SiO_2 Silicon	FWM	6 mm figure 1 0.5 μm 0.198 μm Figure 7(b)	— PECVD E-beam —	— 3.5 dB cm^{-1} 1550 nm — 1.3 ± 10^{-26} s^2 m^{-1} Figure 1	1550 nm 6.3 ± 10^{-2} W 1.9 ± 10^{-12} s TE $1.0 \pm 10^{+10}$ Hz —	1560 nm 8.0 ± 10^{-4} W 2.1 ± 10^{-12} s TE $1.0 \pm 10^{+10}$ Hz —	— — $3.0 \pm 10^{+3}$ m^{-1}W^{-1} 5%[f] —	[Wang2012b]

(Continued.)

Table 7B. (Continued.)

Third-Order Nonlinearities									
		Material Properties			Measurement Details		Nonlinear Properties		
					Pump	**Probe/signal**			
Core Cladding Substrate	Method	Length[a] Cross section[b] Width Height[c] SEM image[d]	Crystallinity Growth/deposition Lithography Other fab	Refractive index Propagation loss Wavelength Bandgap GVD Dispersion curve[e]	Wavelength Peak power Pulse width Polarization Rep. rate Effective area	Wavelength Peak power Pulse width Polarization Rep. rate Effective area	n_2 α_2 γ_{eff} η Bandwidth	Reference Additional parameters and comments	
Si and PIN SiO_2 and Si_3N_4 Silicon	FWM	40 mm — 0.5 μm 0.22 μm Figure 7(q)	— — Photolithography —	— 2 dB cm^{-1} 1552.5 nm — 1.3 ± 10^{-24} s^2 m^{-1} —	1552.5 nm 4.0 ± 10^{-1} W CW TE — —	— — CW TE — —	— 9.0 ± 10^{-12} m W^{-1} $2.0 \pm 10^{+2}$ m^{-1}W^{-1} 79.4%[f] —	[Gajda2012]	
Si — —	Nonlinear transm./ refl.	24 mm — — —	Monocrystalline — — —	— 0.46 cm^{-1} — 1560 nm — — —	1560 nm $4.0 \pm 10^{+2}$ W 9.0 ± 10^{-13} s — $2.5 \pm 10^{+7}$ Hz 8.1 ± 10^{-12} m^2	— — — — — —	— 4.4 ± 10^{-12} m W^{-1} — — —	[Claps2003]	
Si Air (suspended) Silicon	SBS Pump Probe	2.9 mm Figures 1 (a)–(g) 1 μm 0.08 μm Figure 7(r)	Monocrystalline — E-beam —	— 0.18 dB cm^{-1} 1550 nm — — —	1550 nm 6.2 ± 10^{-2} W CW TE — —	— — — — — —	— — — — —	[Kittlaus2016] Forward Brillouin amplification $\gamma_{\text{Brillouin}} = 1152$ m^{-1} W^{-1} Brillouin shift = 4.35 GHz Linewidth = 7 MHz. Free-carrier lifetime = 2.2 ± 10^{-9} s	
Si Air and SiO_2 Silicon	SBS Pump Probe	2.7 mm Figure 1(c) 0.45 μm 0.23 μm Figure 7(p)	Monocrystalline — Photolithography —	— 2.6 dB cm^{-1} 1550 nm — — —	1550 nm 2.5 ± 10^{-2} W CW TE — —	— — — — — —	— — — — —	[VanLaer2015] Forward Brillouin amplification. $\gamma_{\text{Brillouin}} = 3218$ m^{-1} W^{-1} Brillouin shift = 9.2 GHz Linewidth = 30 MHz Free-carrier lifetime = 5.7 ± 10^{-9} s	

Si Air and SiO_2 Silicon	SBS Pump Probe	20 mm Figure 1(c) 0.45 μm 0.23 μm Figure 7(p)	Monocrystalline — Photolithography —	— 2.6 dB cm^{-1} 1550 nm — — —	1550 nm 1.2 ± 10^{-2} W CW TE — —	— — — — — —	— — — — — —	[VanLaer2015] Backward Brillouin amplification. $\gamma_{Brillouin} = 359\ m^{-1}\ W^{-1}$ Brillouin shift = 13.66 GHz Linewidth = 15 MHz Free-carrier lifetime = 5.7 ± 10^{-9} s
Si SiO_2 and air Silicon	SRS Pump Probe	48 mm Figure 1 1.52 μm 1.45 μm —	Monocrystalline — Photolithography —	— 0.22 dB cm^{-1} 1550 nm — — —	1545 nm 4.7 ± 10^{-1} W 1.7 ± 10^{-8} s(FWHM) TE $1.0 \pm 10^{+4}$ Hz 1.6 ± 10^{-12} m^2	1680 nm 2.0 ± 10^{-3} W CW TM — 1.4 ± 10^{-12} m^2	— — — — — —	[Liu2004] $g_{Raman} = 1.05 \pm 10^{-10}\ m\ W^{-1}$ Raman shift = $5.2 \pm 10^{+4}\ m^{-1}$ Pump peak irradiance = $3 \pm 10^{11}\ W\ m^{-2}$ Free-carrier lifetime = 2.5 ± 10^{-8} s
Si SiO_2 and air Silicon	SRS Pump Probe	48 mm Figure 1(a) 1.5 μm 1.55 μm —	Monocrystalline — Photolithography —	— 0.35 dB cm^{-1} 1550 nm — — —	1536 nm 2.0 W 1.3 ± 10^{-7} s — $1.0 \pm 10^{+4}$ Hz 1.6 ± 10^{-12} m^2	— — — — — —	— — — 10% — —	[Rong2005] $g_{Raman} = 7.5 \pm 10^{-11}\ m\ W^{-1}$ Raman shift = $5.2 \pm 10^{+4}\ m^{-1}$ Free-carrier lifetime = 1 ± 10^{-8} s The conversion efficiency is the slope efficiency of average Raman lasing output vs average input power.
Si SiO_2 and air Silicon	SpRS cross-section	24 mm Figure 2 5 μm 2.5 μm —	Monocrystalline — — —	— 2.8 dB cm^{-1} 1542 nm — — —	1427 nm 1.0 W CW TE — —	— — — — — —	— — — — — —	[Claps2002] $g_{Raman} = 7.6 \pm 10^{-10}\ m\ W^{-1}$ Raman shift = $5.2 \pm 10^{+4}\ m^{-1}$
Si SiO_2 and air Silicon	Raman Laser Threshold	2.8 mm Figure 1(f) 2 μm 0.22 μm —	Monocrystalline — Photolithography —	— 0.51 dB cm^{-1} 1325 nm — — —	1240 nm 1.0 ± 10^{-3} W CW TE — 3.7 ± 10^{-13} m^2	— — — — — —	— — — — — —	[Zhang2020b] $g_{Raman} = 3.66 \pm 10^{-10}\ m\ W^{-1}$ Raman shift = $5.2 \pm 10^{+4}\ m^{-1}$ Gain dependence on pump wavelength shown in figure 6(b) of the reference paper.

(Continued.)

Table 7B. (Continued.)

Third-Order Nonlinearities									
		Material Properties			Measurement Details		Nonlinear Properties		
					Pump	**Probe/signal**			
Core Cladding Substrate	Method	Length[a] Cross section[b] Width Height[c] SEM image[d]	Crystallinity Growth/deposition Lithography Other fab	Refractive index Propagation loss Wavelength Bandgap GVD Dispersion curve[e]	Wavelength Peak power Pulse width Polarization Rep. rate Effective area	Wavelength Peak power Pulse width Polarization Rep. rate Effective area	n_2 α_2 γ_{eff} η Bandwidth	Reference Additional parameters and comments	
Si SiO_2 and Si_3N_4 Silicon	Nonlinear transm./refl.	4 mm Figures 1(a)–(c) 0.6 μm 0.22 μm Figure 7(a)	Monocrystalline — Photolithography —	— 4.5–7.0 dB cm^{-1} 1800–2300 nm — — —	2200 nm 6.0 W 2.0 ± 10^{-12} s(FWHM) TE $7.6 \pm 10^{+7}$ Hz —	— — — — — —	— 3.0 ± 10^{-13} m W^{-1} — — —	[Liu2011] Nonlinearity dependence on wavelength shown in table 1 of the reference paper	
Si SiO_2 Silicon	FWM	20 mm Figure 1(b) 0.9 μm 0.22 μm —	— — — —	— 2.6 dB cm^{-1} 1810–2410 nm — 5.0 ± 10^{-25} s^2 m^{-1} Figure S4(b)	1946 nm $3.7 \pm 10^{+1}$ W 2.0 ± 10^{-12} s TE $7.6 \pm 10^{+7}$ Hz —	2440 nm 3.5 ± 10^{-5} W CW TE — —	— — $2.8 \pm 10^{+2}$ $m^{-1}W^{-1}$ 8912.5%[j] $6.2 \pm 10^{+13}$ Hz	[Liu2012b] The conversion efficiency refers to the parametric gain Parametric gain dependence on wavelength shown in figure 2 of the reference paper	
Si SiO_2 Silicon	FWM	20 mm — 0.9 μm 0.22 μm —	— — — —	— 2.8 dB cm^{-1} 2173 nm — 6.0 ± 10^{-25} s^2 m^{-1} —	2173 nm $1.4 \pm 10^{+1}$ W 2.0 ± 10^{-12} s TE $7.6 \pm 10^{+7}$ Hz —	2209–2498 nm 6.0 ± 10^{-5} W CW TE — —	— — $1.5 \pm 10^{+2}$ $m^{-1}W^{-1}$ 1000 000% 580 nm	[Kuyken2011] The conversion efficiency refers to the parametric gain Parametric gain dependence on wavelength shown in figure 3 of the reference paper	
Si SiO_2 Silicon	FWM	3.8 mm Figure S1 1.06 μm 0.25 μm —	— — E-beam —	— 2.8 dB cm^{-1} 2025 nm — — —	2025 nm 1.8 ± 10^{-1} W 1.0 ± 10^{-9} s TE $1.0 \pm 10^{+6}$ Hz 3.5 ± 10^{-13} m^2	1912–1994 nm — CW TE — —	1.1 ± 10^{-17} m^2 W^{-1} — $9.7 \pm 10^{+1}$ $m^{-1}W^{-1}$ 0.5%[f] 292 nm (at 3 dB)	[Zlatanovic2010] Conversion efficiency dependence on pump-signal detuning shown in figure 2(b) of the reference paper	

Si SiO_2 Silicon	FWM	15 mm Figure 1 0.55 μm 0.3 μm — —	— — E-beam —	— — 1554 nm — —	1554 nm 1.1 ± 10^{-1} W CW TE — —	1555–2078 nm 2.5 ± 10^{-4} W CW TE — — —	— — — 1.58%[f] $9.7 \pm 10^{+13}$ Hz (at 3 dB)	[Turner-Foster2010] Conversion efficiency dependence on converted wavelength shown in figure 2 of the reference paper
Si SiO_2 Silicon	Nonlinear transm./refl.	17 mm Figure 1 — — —	Monocrystalline — — —	— 0.1 dB cm^{-1} 1540 nm — 1.2 ± 10^{-24} s^2 m^{-1} Figure 5	1540 nm $2.0 \pm 10^{+1}$ W 5.4 ± 10^{-11} s(FWHM) — — 6.2 ± 10^{-12} m^2	— — — — — — —	— 4.5 ± 10^{-12} m W^{-1} — — — —	[Tsang2002]
4H-SiC SiO_2 Silicon	FWM	3 mm — 0.51 μm 0.5 μm Figure 7(n)	— — E-beam Wafer bonding	2.4 — 1565 nm >2.4 eV 325 ps (nm km)$^{-1}$ Figure 5(a)	1565 nm 1.3 ± 10^{-1} W CW TE — —	— 1.0 ± 10^{-3} W — TE — —	6.0 ± 10^{-19} m^2 W^{-1} — 7.4 $m^{-1}W^{-1}$ 0.00032%[f] $1.6 \pm 10^{+13}$ Hz (at 3 dB)	[Zheng2019b] Nonlinearity dependence on waveguide width shown in figure 4 of the reference paper
a-SiC SiO_2 Silicon	SPM/XPM spectral broadening	12 mm Figure 2(a) 1.2 μm 0.35 μm —	— PECVD E-beam —	2.45 3 dB cm^{-1} 1550 nm 2.3 eV 400 ps (nm km)$^{-1}$	1550 nm $1.3 \pm 10^{+1}$ W — — — 4.2 ± 10^{-13} m^2	— — — — — —	4.8 ± 10^{-18} m^2 W^{-1} — $4.0 \pm 10^{+1}$ $m^{-1}W^{-1}$ — —	[Xing2019]
Si_3N_4 SiO_2 Silicon	FWM	1000 mm Figure 1(a) 2.8 μm 0.1 μm —	— — — —	— 0.06 dB cm^{-1} 1550 nm — 5.0 ± 10^{-25} s^2 m^{-1} —	1563 nm 2.1 W CW TE — —	1562 nm 7.7 ± 10^{-2} W CW TE — —	— — 2.9 ± 10^{-1} $m^{-1}W^{-1}$ 0.245%[f] $6.2 \pm 10^{+11}$ Hz (at 3 dB)	[Kruckel2015b]

(Continued.)

Table 7B. (Continued.)

Third-Order Nonlinearities								
		Material Properties			Measurement Details		Nonlinear Properties	
					Pump	**Probe/signal**		
Core	Method	Length[a]	Crystallinity	Refractive index	Wavelength	Wavelength	n_2	Reference
Cladding		Cross section[b]	Growth/deposition	Propagation loss	Peak power	Peak power	α_2	Additional parameters and comments
Substrate		Width		Wavelength	Pulse width	Pulse width	γ_{eff}	
		Height[c]	Lithography	Bandgap	Polarization	Polarization	η	
		SEM image[d]	Other fab	GVD	Rep. rate	Rep. rate	Bandwidth	
				Dispersion curve[e]	Effective area	Effective area		
Si_3N_4	FWM	22 mm	—	—	1550 nm	1550.8 nm	6.9 ± 10^{-19} m^2 W^{-1}	[Wang2018a]
SiO_2		Figure 2(a)	PECVD	0.58 dB cm^{-1}	1.6 ± 10^{-1} W	1.1 ± 10^{-1} W	—	
Silicon		2 μm	Photolithography	1550 nm	CW	CW	2.6 m^{-1}W^{-1}	
		0.72 μm		3.27 eV	TE	TE	0.00012%[j]	
		—	—	—	—	—	—	
			—	—	1.1 ± 10^{-12} m^2	—		
Si_3N_4	FWM	61 mm	—	—	1550 nm	1470–1630 nm	2.5 ± 10^{-19} m^2 W^{-1}	[Levy2009]
SiO_2		Figure 2(a)	LPCVD, PECVD	0.5 dB cm^{-1}	$2.4 \pm 10^{+1}$ W	—	—	The reported conversion efficiency is the parametric OPO gain achieved in microresonators
Silicon		1.45 μm	E-beam	1550 nm	1.0 ± 10^{-11} s	CW	—	
		0.725 μm		—	TE	TE	229%[f]	
		—	—	6.4 ± 10^{-27} s^2 m^{-1}	$1.0 \pm 10^{+9}$ Hz	—	150 nm	Signal gain dependence on wavelength shown in figure 2(b) of the reference paper
			—	Figure 2(a)	—	—	(at 3.6 dB)	
Si_3N_4	SPM/XPM spectral broadening	6000 mm	—	—	1549.9 nm	1550.3 nm	9.0 ± 10^{-20} m^2 W^{-1}	[Tien2010]
SiO_2		Figure 1(a)	LPCVD	—	4.0 ± 10^{-1} W	4.0 ± 10^{-1} W	—	Nonlinearity dependence on core thickness shown in figure 2 of the reference paper
Silicon		2.8 μm	—	1550 nm	CW	CW	6.0 ± 10^{-2} m^{-1}W^{-1}	
		0.08 μm	—	—	TE	TE	—	
		—	—	—	—	—	—	
			—	—	—	—		
Si_7N_3	FWM	7 mm	—	3.1	1555 nm	—	—	[Ooi2017]
SiO_2		—	PECVD	4.5 dB cm^{-1}	2.3 ± 10^{-2} W	2.3 ± 10^{-4} W	—	Conversion efficiency dependence on pump wavelength shown in figure 3(b) of the reference paper
Silicon		0.55 μm	E-beam	1550 nm	CW	CW	$5.0 \pm 10^{+2}$ m^{-1}W^{-1}	
		0.3 μm		2 eV	TE	TE	0.323%	
		—	—	2.5 ± 10^{-25} s^2 m^{-1}	—	—	$2.2 \pm 10^{+13}$ Hz	
				Figure 2(b)	—	—	(at 3 dB)	

Si_7N_3 SiO_2 Silicon	SPM/XPM spectral broadening	7 mm — 0.6 μm 0.3 μm —	— PECVD E-beam —	3.1 10 dB cm^{-1} 1550 nm 2.05 eV 2.4 ± 10^{-25} s^2 m^{-1} Figure 2(c)	1550 nm $1.4 \pm 10^{+2}$ W 1.8 ± 10^{-12} s TE $2.0 \pm 10^{+7}$ Hz 2.1 ± 10^{-13} m^2	— — — — — —	2.8 ± 10^{-17} m^2 W^{-1} — $5.5 \pm 10^{+2}$ m^{-1}W^{-1} — $7.7 \pm 10^{+13}$ Hz (at 30 dB)	[Wang2015]
Si_xN_y SiO_2 Silicon	FWM	— — 0.7 μm 0.22 μm —	— PECVD E-beam —	2.49 1.5 dB cm^{-1} 1550 nm — — —	1550.1 nm 3.2 ± 10^{-1} W CW TE — 4.0 ± 10^{-13} m^2	1550 nm 3.2 ± 10^{-2} W CW TE — —	1.6 ± 10^{-18} m^2 W^{-1} 8.0 ± 10^{-12} m W^{-1} $1.6 \pm 10^{+1}$ m^{-1}W^{-1} 0.0032%[f] —	[Lacava2017] Conversion efficiency dependence on waveguide width shown in figure 6 of the reference paper. The reference paper also reports the nonlinearities for a standard Si_3N_4 waveguide, and for a Si_xN_y waveguide with a different silicon content.
Si_xN_y SiO_2 Silicon	FWM	9.4 mm Figure 1(b) 1.65 μm 0.7 μm Figure 7(s)	— PECVD E-beam —	2.1 1.2 dB cm^{-1} 1570 nm 2.3 eV 2.0 ± 10^{-26} s^2 m^{-1} Figure 3(b)	1563 nm 1.0 W CW TE — 9.0 ± 10^{-13} m^2	1562 nm 7.9 ± 10^{-2} W CW TE — —	1.4 ± 10^{-18} m^2 W^{-1} — 6.1 m^{-1}W^{-1} 0.016%[f] $2.0 \pm 10^{+12}$ Hz (at 3 dB)	[Kruckel2015a]
Hydex SiO_2 and air SiO_2	FWM	0.3 mm Figure 1 1.5 μm 1.45 μm Figure 7(c)	Amorphous CVD Photolithography —	1.7 0.06 dB cm^{-1} 1550 nm — — —	1553.38 nm 5.0 ± 10^{-3} W CW TM — 2.0 ± 10^{-12} m^2	1558.02 nm 5.5 ± 10^{-4} W CW TM — —	1.2 ± 10^{-19} m^2 W^{-1} — 2.3 ± 10^{-1} m^{-1}W^{-1} 0.0013% —	[Ferrera2008] Ring radius around 48 μm, Q—factor of 65 000, FSR 575 GHz.
Hydex SiO_2 and air SiO_2	FWM	0.85 mm — — — —	Amorphous CVD Photolithography —	1.7 0.06 dB cm^{-1} 1550 nm — 1.0 ± 10^{-26} s^2 m^{-1} Figure 3	1551 nm 8.8 ± 10^{-3} W CW TE — —	1553 nm 1.3 ± 10^{-3} W CW TE — —	— — — 0.25% — —	[Ferrera2009] Ring radius 135 μm, FSR 200 GHz.

(Continued.)

Table 7B. (Continued.)

Third-Order Nonlinearities								
		Material Properties			**Measurement Details**		**Nonlinear Properties**	
					Pump	**Probe/signal**		
Core Cladding Substrate	Method	Length[a] Cross section[b] Width Height[c] SEM image[d]	Crystallinity Growth/deposition Lithography Other fab	Refractive index Propagation loss Wavelength Bandgap GVD Dispersion curve[e]	Wavelength Peak power Pulse width Polarization Rep. rate Effective area	Wavelength Peak power Pulse width Polarization Rep. rate Effective area	n_2 α_2 γ_{eff} η Bandwidth	Reference Additional parameters and comments
Hydex SiO_2 SiO_2	SPM/XPM spectral broadening	450 mm Figure 1 1.5 μm 1.45 μm —	Amorphous CVD Photolithography —	1.7 0.06 dB cm^{-1} 1550 nm — 2 ± 10^{-25} s^2 m^{-1} —	1560 nm $3.9 \pm 10^{+1}$ W 1.7 ± 10^{-12} s(FWHM) — $1.7 \pm 10^{+7}$ Hz 2.0 ± 10^{-12} m^2	— — — — — —	1.1 ± 10^{-19} m^2 W^{-1} — 2.2 ± 10^{-1} m^{-1}W^{-1} — —	[Duchesne2009] Peak irradiance $<25 \pm 10^{+13}$ W m^{-2}
Chalcogenide glasses								
As_2S_3 SiO_2 Silicon	SPM/XPM spectral broadening	60 mm Figure 1 2 μm 0.87 μm —	Amorphous Thermal evaporation — —	2.38 0.6 dB cm^{-1} 1550 nm — 3.7 ± 10^{-26} s^2 m^{-1} Figure 2	1550 nm $6.8 \pm 10^{+1}$ W 6.1 ± 10^{-13} s(FWHM) TM $1.0 \pm 10^{+7}$ Hz 1.2 ± 10^{-12} m^2	— — — — — — —	— 6.2 ± 10^{-15} m W^{-1} $1.0 \pm 10^{+1}$ m^{-1}W^{-1} — 750 nm (at 30 dB)	[Lamont2008]
As_2S_3 SiO_2 Silicon	FWM	70 mm Figure 1(a) 2 μm 0.85 μm — —	Amorphous Thermal evaporation Photolithography —	4 dB cm^{-1} 1550 nm — 28 ps (nm km)$^{-1}$ — —	1547 nm 1.35 ± 10^{-1} W CW — — 1 ± 10^{-12} m^2	1554–1564 nm — CW — — —	— — 10 m^{-1}W^{-1} 37.8 dB —	[Pelusi2010] Broadband all-optical wavelength conversion of high-speed Differential Phase-Shift Keyed and On-Off Keyed signals with bit rates of 40–160 Gb s^{-1} was demonstrated

$Ge_{11.5}As_{24}Se_{64.5}$	FWM	18 mm	Amorphous	2.66	1550.8 nm	1552.6 nm	—	[Gai2010]
SiO_2 and polymer		Figure 3(a) 0.63 μm	Thermal evaporation	2.6 dB cm^{-1} 1550 nm	135 ± 10^{-3} W CW	2.8 ± 10^{-3} W CW	9.3 ± 10^{-14} m W^{-1} $1.36 \pm 10^{+2}$ $m^{-1}W^{-1}$	$n_2 = 8.6 \pm 10^{-14}$ cm^2 W^{-1} quoted from other paper
		0.5 μm	E-beam	—	TM	TM	—	Supercontinuum generation in the range between 1200 and 2400 nm was demonstrated.
Silicon		—		—	—	—	—	
			—	—	0.27 ± 10^{-12} m^2	—		
Diamond								
Diamond	Raman Laser Threshold	0.188 mm	Monocrystalline	—	750 nm	—	—	[Latawiec2018]
SiO_2 and air		Figure 2(a) 0.3 μm	—	— —	2.0 ± 10^{-2} W CW	— —	— —	$g_{Raman} = 3.2 \pm 10^{-11}$ m W^{-1} Raman shift $= 1.33 \pm 10^{+5}$ m^{-1}
		0.3 μm	E-beam	5.5 eV	TE	—	1.7%	
Silicon		—		—	—	—	—	The conversion efficiency is the external Raman lasing slope efficiency.
			—	—	—	—		
Diamond	FWM	0.125 mm	Monocrystalline	—	1600 nm	—	8.2 ± 10^{-20} m^2 W^{-1}	[Hausmann2014]
SiO_2		Figure 1(a) 0.875 μm	HPHT	0.34 dB cm^{-1} 1545.1 nm	7.8 ± 10^{-2} W CW	— —	— —	OPO based on FWM.
Silicon		0.85 μm Figure 7(u)	E-beam	5.5 eV —	TE —	— —	5%[l] —	
			—	Figures 1(b) and 5	5.0 ± 10^{-13} m^2	—		
Diamond	Raman Laser Threshold	0.6 mm	Monocrystalline	—	1575 nm	—	—	[Latawiec2015]
SiO_2		Figure 1(b) 0.8 μm	CVD	— —	8.5 ± 10^{-2} W CW	— —	— —	$g_{Raman} = 2.5 \pm 10^{-11}$ m W^{-1} Raman shift $= 1.33 \pm 10^{+5}$ m^{-1}
Silicon		0.7 μm	E-beam	5.5 eV	TE	—	0.43%	
		—		—	—	—	—	The conversion efficiency is the external Raman lasing slope efficiency.
			—	—	—	—		

(Continued.)

Table 7B. (Continued.)

Third-Order Nonlinearities								
		Material Properties			**Measurement Details**		**Nonlinear Properties**	
					Pump	**Probe/signal**		
Core	Method	Length[a]	Crystallinity	Refractive index	Wavelength	Wavelength	n_2	Reference
Cladding		Cross section[b]	Growth/deposition	Propagation loss	Peak power	Peak power	α_2	Additional parameters and comments
Substrate		Width		Wavelength	Pulse width	Pulse width	γ_{eff}	
		Height[c]	Lithography	Bandgap	Polarization	Polarization	η	
		SEM image[d]	Other fab	GVD	Rep. rate	Rep. rate	Bandwidth	
				Dispersion curve[e]	Effective area	Effective area		
Tantalum oxide, titanium oxide								
Ta_2O_5	FWM	12.6 mm	—	2.1	1555.465 nm	1556.08 nm	1.0 ± 10^{-18} m^2 W^{-1}	[Wu2015]
SiO_2		Figure 1	Sputtering, PECVD	1.5 dB cm^{-1}	3.5 ± 10^{-2} W	4.0 ± 10^{-3} W	—	
Silicon		0.7 μm	E-beam	1550 nm	CW	CW	5.2 m^{-1}W^{-1}	
		0.4 μm		—	TE	TE	0.001%[j]	
		Figure 7(o)	—	1400 ps (nm km)$^{-1}$	—	—	—	
				Figure 5(a)	7.7 ± 10^{-13} m^2	—		
TiO_2	FWM	11 mm	—	2.31	1550.1 nm	1551.3 nm	3.6 ± 10^{-18} m^2 W^{-1}	[Guan2018]
SiO_2		Figure 2	Sputtering	5.4 dB cm^{-1}	6.0 ± 10^{-1} W	1.9 ± 10^{-2} W	—	
Silicon		1.15 μm	E-beam	1550 nm	CW	CW	$3.4 \pm 10^{+1}$ m^{-1}W^{-1}	
		0.38 μm		3.4 eV	TE	TE	0.024%[f]	
		—	—	50 ps (nm km)$^{-1}$	—	—	—	
				Figure 7	4.3 ± 10^{-13} m^2	—		
TiO_2	SPM/XPM spectral broadening	22 mm	—	2.35	1640 nm	—	—	[Hammani2018]
SiO_2		Figure 1	Sputtering	5.5 dB cm^{-1}	$1.3 \pm 10^{+3}$ W	—	—	
Silicon		1.345 μm		1640 nm	9.0 ± 10^{-14} s	—	—	
		0.45 μm	Photolithography	3.4 eV	TE	—	—	
		Figure 7(m)		20 ps (nm km)$^{-1}$	$8.0 \pm 10^{+7}$ Hz	—	860 nm	
			—	Figure 4(a)	5.4 ± 10^{-13} m^2	—	(at 20 dB)	
TiO_2	SPM/XPM spectral broadening	9 mm	—	2.4	1565 nm	—	1.6 ± 10^{-19} m^2 W^{-1}	[Evans2013]
SiO_2		Figure 1	Sputtering	8 dB cm^{-1}	$2.9 \pm 10^{+4}$ W	—	—	
Silicon		0.9 μm		1560 nm	1.7 ± 10^{-13} s	—	1.5 m^{-1}W^{-1}	Broadening factor 3.8 at 15 dB
		0.25 μm	E-beam	3.1–3.3 eV	TE	—	—	
		Figure 7(l)		1.5 ± 10^{-24} s^2 m^{-1}	$8.0 \pm 10^{+7}$ Hz	—	—	
			—	—	4.3 ± 10^{-13} m^2	—		

TiO_2	SPM/XPM	6 mm	—	2.4	794 nm	—	1.6 ± 10^{-18} m^2 W^{-1}	[Evans2013]	
SiO_2	spectral broadening	Figure 1	Sputtering	8 dB cm^{-1}	$2.9 \pm 10^{+4}$ W	—	7.0 ± 10^{-12} m W^{-1}	Broadening factor 3.8 at	15 dB
Silicon		0.9 μm		794 nm	8.5 ± 10^{-14} s	—	$7.9 \pm 10^{+1}$ $m^{-1}W^{-1}$		
		0.25 μm	E-beam	3.1–3.3 eV	TM	—	—		
		Figure 7(l)		1.5 ± 10^{-24} s^2 m^{-1}	$1.1 \pm 10^{+7}$ Hz	—	—		
			—	—	1.6 ± 10^{-13} m^2	—			

[a] The length of ring resonators was calculated from the ring radius.
[b] Figure of the reference paper with the cross-section image or drawing.
[c] For heterostructure waveguides, the reported height is the guiding layer thickness.
[d] Selected SEM images presented in this work for each geometry and material platform.
[e] Figure of the reference paper showing a dispersion curve.
[f] Conversion efficiency formula: $\eta = P_{\text{I, output}}/P_{\text{S, output}}$ [I–Idler, and S—Signal for this and the following formulas].
[g] Conversion efficiency formula: $\eta = 10\log\left(P_{\text{I, output}}/P_{\text{S, input}}\right)$.
[h] Conversion efficiency formula: $\eta = P_{\text{I, output, peak}}/P_{\text{S, input}}$.
[i] Conversion efficiency formula: $\eta = 10\log\left(P_{\text{I, output}}/P_{\text{S, output}}\right)$.
[j] Conversion efficiency formula: $\eta = P_{\text{I, output}}/P_{\text{S, input}}$.
[k] Conversion efficiency formula: $\eta = \Sigma P_{\text{all comb lines}}/P_{\text{pump}}$.
[l] Conversion efficiency formula: $\eta = \Sigma P_{\text{side bands}}/P_{\text{pump}}$.

3.7. Hybrid waveguiding systems: data table and discussion

Team: *John Ballato, Peter Dragic, Minhao Pu,* ***Nathalie Vermeulen (team leader)****, Kresten Yvind*

3.7.1. Introduction

3.7.1.1. Hybrid waveguiding systems and their NLO applications

Optical fibers and on-chip waveguides are often employed for NLO applications as the strong light confinement enabled by these waveguiding structures benefits the efficiency of NLO phenomena. At the same time, NLO researchers have been exploring whether fibers and on-chip waveguides, typically made of glasses or semiconductor materials, can be combined with very different materials, such as low-dimensional materials, metals, organic solids, liquids, gasses, etc. The goal of adding other materials to the waveguiding structures is to modify, and in most cases to enhance, the efficiency of a given NLO process. The resulting hybrid waveguiding systems find applications in the same domains as their 'bare' counterparts (see sections 3.5 and 3.6) but can also acquire other NLO functionalities, depending on the properties of the added material. For example, whereas 'bare' fibers have always been the preferred medium when targeting low-loss NLO applications, hybrid fibers enhanced with low-dimensional materials such as carbon nanotubes or graphene can also fulfill absorptive functionalities such as fiber-based saturable absorption in laser cavities with pulsed operation [Liu2020, Teng2020]. As such, the development of hybrid fibers and hybrid on-chip waveguides has allowed combining the best of both worlds, i.e. the intrinsic strengths of the bare waveguiding structures plus the special NLO properties of the added materials. Further details on the importance of NLO hybrid fibers and NLO hybrid on-chip waveguides can be found in several recent review papers (see, for example, [Li2018, Debord2019, Guo2019, Liu2020, Teng2020, Tuniz2021, Steglich2021, Vermeulen2022]).

3.7.1.2. Background prior to 2000

3.7.1.2.1. Background for hybrid fibers

Research on NLO hybrid fibers started already in the 1970s, with a focus on hollow fiber capillaries filled with NLO solids [Stevenson1974, Babai1977]. Around the same period, light guidance in fiber capillaries with liquid cores was demonstrated by several groups [Ogilvie1972, Payne1972, Stone1972]. In contrast, laser transmission in fiber capillaries containing gasses became a subject of study from the 1990s onward [Olshanii1993]. Not only can hollow fiber structures be employed for realizing NLO hybrid fibers, but also solid-core fibers with their cross-sectional geometry modified by, e.g., side polishing or tapering can be used for this purpose. Because of their modified cross-section the added NLO material can be brought in close proximity to the light-guiding fiber core, such that it can interact with the evanescent tails of the fiber mode. The first demonstrations of this concept date back to the 1980s [Bergh1980, Lamouroux1983, Lacroix1986]. Both the hybrid fibers based on hollow capillaries and those relying on side-polished or tapered solid-core fibers were successfully employed in various NLO experiments before the turn of the century (see, e.g., [Stevenson1974, Kanbara1992, Nesterova1996, Lee1998]). Nevertheless, the research area of NLO hybrid fibers has experienced the strongest growth after 2000, thanks to the emergence of new special fiber structures as well as new exotic materials that can enhance the fibers' NLO response (see further on).

3.7.1.2.2. Background for hybrid on-chip waveguides

Similarly as for hybrid fibers, the first hybrid on-chip waveguides developed for NLO applications comprised NLO organics, and this approach allowed demonstrating the EO effect on a silicon chip already in the 1990s [Faderl1995]. Also here, the evanescent tails of the waveguide mode allowed 'sensing' the presence of the NLO organics deposited on top, even when working with a standard strip waveguide geometry [Faderl1995]. Due to their planar structure, photonic chips in fact provided a very suitable platform for the deposition of NLO solids on top, whereas NLO liquids and gasses were more easily combined with hollow fiber structures. Nevertheless, the most important breakthroughs in the development of hybrid on-chip waveguides would be triggered by major advancements in both waveguide technology and material science shortly after 2000 (see further on).

3.7.1.3. Considerations for hybrid waveguiding systems when performing NLO measurements

When characterizing hybrid fibers and hybrid on-chip waveguides, both the considerations for the bare fibers/waveguides (see sections 3.5.1.2 and 3.6.1.3) and those for the added materials need to be taken into account. For NLO measurements requiring phase matching, it is important to account for the phase matching conditions of the entire hybrid system. Also interfacial aspects such as (lack of) adhesion of the added materials, uniformity and/or diffusion are important to verify prior to the NLO experiments. From the measured NLO response, the effective nonlinearity for the hybrid system as a whole can be extracted. If, however, one wants to go one step further and assess the contributions from each constituent to the overall NLO response, careful analysis is required: the cross-sectional distribution of the modal power in the hybrid

waveguiding structure needs to be evaluated, and this information subsequently fed into a weighted contributions model to extract the individual nonlinear properties of the fiber/waveguide structure and the added material (see, e.g., [Vermeulen2016a] and appendix of [Vermeulen2016b]). Here, it is also important to keep in mind that the different NLO contributions do not always add up. For example, when studying NLR in a silicon waveguide covered with undoped graphene while using excitation wavelengths in the near-IR telecom domain, the silicon will have a positive nonlinearity whereas the graphene top layer will exhibit a negative nonlinearity [Vermeulen2016a, CastelloLurbe2020]. Therefore, in the weighted contributions analysis, it is crucial to implement the correct nonlinearity signs for each of the constituting media. In case the signs are not known upfront, this information can be obtained, for example, using a phase-sensitive NLO technique such as SPM-based spectral broadening and by comparing the NLO response of the hybrid waveguiding structure to that of the bare waveguide/fiber [Vermeulen2016a]. This allows evaluating whether there are nonlinearities of opposite sign present in the hybrid system.

3.7.1.4. Description of general table outline

Tables 8A and B show a representative list of NLO properties of, respectively, hybrid fibers and hybrid on-chip waveguides taken from the literature since 2000, with the entries arranged in alphabetical order. The selection of works included in the Tables has been based on the general best practices in section 2 and the considerations outlined above. Taking into account that an extremely large number of material combinations are possible in hybrid systems, this selection has been limited to just a few representative works for different combinations of bare fibers/waveguides with other media, and therefore does not provide an extensive overview. The selection also contains a few papers with organic solids, liquids and gasses, although in this article the focus is rather on inorganic solids, as mentioned in the general introduction. The included works nominally report data obtained at room temperature. Tables 8A and B are subdivided into 'Material properties', 'Measurement details' and 'Nonlinear properties'. Within each column the information is given in the order of the header description. 'Material properties' include the characteristics of both constituents of the hybrid system, as well as references to the sub-figures in figure 8 showing SEM images of the fabricated structures. The peak power values in the Tables are nominally incoupled powers as specified in the papers. The NLO technique used in each of the papers is provided in the 'Method' column. As most works report on third-order NLO effects, the focus in the Tables is on third-order NLO parameters such as $|\mathrm{Re}(\gamma_{\mathrm{eff}})|$ and the effective saturation irradiance $I_{\mathrm{sat,eff}}$ together with the saturable loss, extracted from the hybrid system as a whole. That said, also a limited number of papers reporting on second-order NLO parameters are included in the Tables, with their parameter values specified in a separate 'Comments' column. Also included in the 'Comments' column are individual nonlinearity contributions that could be separately determined per constituent material, when stated as such. Lastly, some papers specify the dependence of the NLO parameters on wavelength, waveguide/fiber dimension, doping level expressed as Fermi level (eV) or carrier concentration (m^{-2}), etc or have notes associated with their measurement/analysis such as the formulas used to calculate conversion efficiencies η. This information is listed within the 'Comments' column.

3.7.2. Discussion

In view of the relatively recent emergence of low-dimensional materials, their combination with on-chip waveguides and fibers is quite a new development with most progress being made over the last 5 to 10 years. Within this short period of time, a wide variety of 2D materials has been explored for this purpose, as can be seen in tables 8A and B. At the same time, the Tables also show that organic solids, liquids and gasses still are very interesting NLO media for constructing hybrid waveguiding systems.

3.7.2.1. Advancement since 2000 and remaining challenges

3.7.2.1.1. Advancement and challenges for hybrid fibers

Table 8A for NLO hybrid fibers shows two distinct novelties as compared to the works before 2000, the first novelty being the emergence of SiO_2 hollow-core photonic-crystal fibers (PCFs) [Russell2014]. In contrast to hollow fiber capillaries which intrinsically are leaky waveguides even when filled with, e.g., gasses, hollow-core PCFs efficiently trap light within their hollow core by exploiting the physics of photonic bandgaps [Russell2014]. As such, various NLO effects have been demonstrated in hollow-core PCFs filled with liquids and gasses [Baghwat2008, Russell2014], exhibiting strong NLO responses as shown by the examples listed in the Table [Benabid2002, Vieweg2010, Renninger2016, Yang2020]. That said, combining ultra-low loss and truly robust single-mode propagation in a hollow-core PCF still represents a challenge and requires special design approaches [Amrani2021]. It should also be noted that, because of the intrinsic

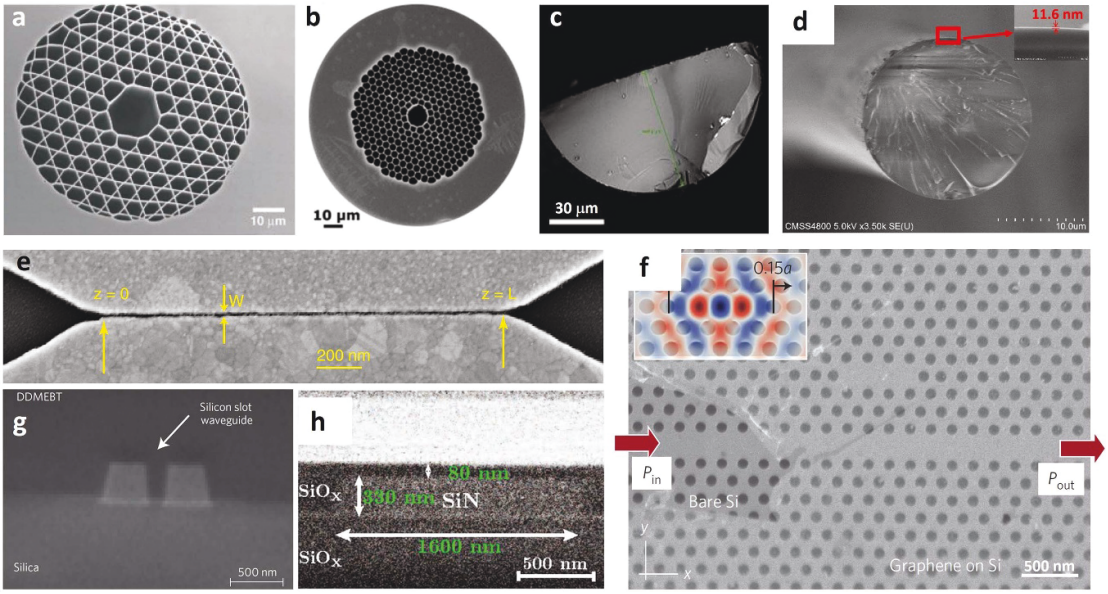

Figure 8. SEM images of NLO hybrid fibers and hybrid on-chip waveguides. The labels of the sub-figures correspond to the labels given in tables 8A and 8B. Panels (a) and (e) are reprinted with permission from [Benabid2002, Nielsen2017], AAAS. Panels (b), (f), and (g) are reprinted with permission from [Yang2020, Gu2012, Koos2009], Springer Nature. Panels (c) and (h) are reprinted with permission from [An2020, Alexander2017], ACS. Panel (d) is reprinted with permission from [Wang2018], CLP Publishing.

simplicity of fiber capillaries as compared to PCFs, several research groups continued using capillaries after 2000 to realize hybrid fibers for different NLO functionalities [Schneebeli2013, Chemnitz2017].

A second important novelty in NLO hybrid fiber development after 2000 has been the rise of low-dimensional materials [Liu2020]. Both 1D carbon nanotubes and 2D materials such as graphene, graphene oxide, black phosphorus and several types of Transition Metal Dichalcogenides (TMDs) were deposited on side-polished or tapered fibers (see, for example, [Xu2013, Park2015, Lee2015, Martinez2017, Steinberg2018, Wang2018, Chen2019b, An2020]). The low-dimensional materials either enhanced the already present NLO response of the bare fibers [Xu2013, An2020] and sometimes even made them tunable by means of electrical gating [An2020], or they enriched the fiber components with additional NLO functionalities such as frequency doubling [Chen2019b] and saturable absorption [Park2015, Lee2015, Martinez2017, Steinberg2018, Wang2018]. The latter is particularly useful for the development of pulsed fiber lasers [Liu2020]. Still, transferring low-dimensional materials onto side-polished or tapered fiber surfaces can be quite challenging. Efforts for the direct growth of, e.g., graphene on dielectrics such as glass are currently ongoing [Khan2018] and could circumvent the need for complex material transfer procedures while improving standardization and upscaling of the hybrid fiber fabrication. To assess the quality of fabricated hybrid fibers, careful characterization is required [Vermeulen2022]. Note that particularly for graphene-based devices it is important to know the doping level of the graphene layer as the latter determines whether or not a strong NLO response can be expected from the 2D sheet [CastelloLurbe2020]. Finally, as shown in table 8A, the strong nonlinear refractive response of fibers enriched with low-dimensional materials is often accompanied by high linear losses [Xu2013, An2020]. At the same time, taking into account that NLO research with low-dimensional materials still is at a relatively early stage, it is remarkable how much progress has been made over the past few years on the implementation of these materials in NLO hybrid fibers.

3.7.2.1.2. Advancement and challenges for hybrid on-chip waveguides

A first novelty seen in table 8B for NLO hybrid on-chip waveguides is that NLO organics are nowadays combined with advanced waveguiding structures such as plasmonic or slot waveguides [Nielsen2017, Koos2009]. This advancement has been enabled by the major progress in photonic chip fabrication technology over the past decades. Both plasmonic and slot waveguides intensify the electromagnetic field in the NLO polymer: the former by focusing the light down to the nanoscale inside a metallic structure close to the polymer [Nielsen2017, Tuniz2021], the latter by having its waveguide mode centered around the polymer located within the slot [Koos2009, Steglich2021]. These two approaches give rise to a strong enhancement of the electromagnetic field strength yielding very high NLO efficiencies, albeit with significant propagation

losses in the waveguides. Today's research on hybrid plasmonic or slot waveguides mainly focuses on how to maintain such a strong field enhancement while keeping the losses low [Tuniz2021, Steglich2021].

Hybrid on-chip waveguide development has also greatly benefitted from the emergence of NLO 2D materials [Li2018]. Similarly to the case of hybrid fibers, the combination of on-chip waveguides with graphene, graphene oxide, and TMDs either strengthened the already present NLO response of the waveguides [Gu2012, Vermeulen2016a, Alexander2017, Vermeulen2018, Yang2018b, Zhang2020c, Qu2020] and sometimes made the response electrically tunable [Alexander2017], or they introduced additional NLO functionalities such as saturable absorption [Demongodin2019], frequency doubling [Chen2017a] and difference frequency generation [Yao2018]. Most on-chip waveguides used in these experiments were Si or Si_3N_4 waveguides with a standard strip geometry. Transferring 2D materials onto such waveguides embedded within a planar photonic chip poses fewer practical challenges as compared to the transfer onto fiber surfaces. Nevertheless, direct synthesis of the 2D materials on the waveguides would be beneficial from the point of view of standardization and upscaling [Khan2018]. Just like their fiber-based counterparts, hybrid on-chip waveguides require careful material characterization of their constituents [Vermeulen2022], and for graphene-based devices this also includes evaluating the doping level of the 2D layer (see section above). Finally, as shown in table 8B, the strong nonlinear refractive response of on-chip waveguides covered with 2D materials often comes with high losses (see, for example, [Vermeulen2016a, Alexander2017, Vermeulen2018, Yang2018b, Zhang2020c]). That said, the obtained results are promising, and further progress can be expected in the coming years as the fabrication of photonic chips and 2D materials will continue to improve and the fundamental understanding of the NLO physics of 2D materials will be further extended.

3.7.2.2. Recommendations for future works on hybrid waveguiding systems

Our general recommendation for future works on NLO hybrid waveguides is to report at least those parameters that are included in tables 8A and B, as these provide essential information on the hybrid systems. So, including these parameters in future publications can be considered as a best practice in addition to the more general best practices described in section 2.

To maximize the impact of future works, it is of particular importance to extract the actual nonlinearity, e.g., γ_{eff}, of the hybrid system (rather than just specifying the relative NLO enhancement enabled by the added material) and to study the dependence of the nonlinearity on, e.g., wavelength. Ideally, one could also go the extra mile of determining the individual nonlinearities (magnitude and sign) of the fiber/waveguide medium and the added medium along the considerations outlined above. By then comparing the retrieved NLO coefficients with measurements of the same materials in a 'stand-alone' configuration, it is possible to evaluate if combining them in a hybrid waveguiding system leaves their individual NLO properties unchanged or not.

We would also like to point out the need for a detailed description of the material properties (including the doping level when relevant) and of the linear optical properties of all constituents in the hybrid system. This is not always done in the existing literature, which makes it difficult to properly interpret and reproduce the reported results. For example, in addition to specifying the linear optical loss for the complete hybrid system, one should also quantify the initial optical loss of the bare fiber/waveguide. In a similar way, the material to be added needs to be optically characterized beforehand. To allow for reproducibility, future works should also provide a detailed description of the fabrication procedure for realizing the hybrid system and specify its geometrical outline, both in the cross-sectional plane and along the optical axis. The latter comprises specifying the length over which the added material is present as well as the remaining length of bare fiber/waveguide. This way, the reader can get the full picture of the system under study, which is essential in view of the inherent complexity of hybrid waveguiding structures. As such, the research community will be able to efficiently build upon state-of-the-art results so that the 'best of both worlds' idea behind hybrid waveguiding systems can be exploited to its full potential.

3.7.3. Data table for hybrid waveguiding systems

Table 8A. NLO properties of hybrid fibers from representative works since 2000. Legend for superscripts: see below the table.

Hybrid Fibers										
Material Properties			**Measurement Details**			**Nonlinear Properties**				
Constituent 1 Fiber type	**Constituent 2** Added material Thickness Fabrication	**Hybrid fiber** Length Loss/wavelength[a] Effective area SEM image[b]	**Method**	**Pump** Wavelength Peak power Pulse width Rep. rate	**Probe** Wavelength Peak power Pulse width	$\lvert\mathrm{Re}(\gamma_{\mathrm{eff}})\rvert$ ($\mathrm{m^{-1}\,W^{-1}}$)	$I_{\mathrm{sat,eff}}$ ($\mathrm{W\,m^{-2}}$)	Saturable loss (%)	Additional parameters and comments	Reference
SiO_2 hollow-core fiber Capillary	B-carotene — —	500 mm — — 8 ps	IRS Pump-Probe	1550 nm — 3 ps 50 MHz	— — 8 ps	—	—	—	g_{Raman}: 6.00 ± 10^{-13} m $\mathrm{W^{-1}}$ Raman shift: $1.16 \pm 10^{+5}$ $\mathrm{m^{-1}}$ 5 μm core diameter	[Schneebeli2013]
SiO_2 hollow-core fiber Capillary	CCl_4 — —	1 m — — —	IRS Pump-Probe	1550 nm — 3 ps 50 MHz	— — 3 ps	—	—	—	g_{Raman}: 1.50 ± 10^{-12} m $\mathrm{W^{-1}}$ Raman shift: $4.59 \pm 10^{+4}$ $\mathrm{m^{-1}}$ 32 mW average pump power; 10 μm core diameter	[Schneebeli2013]
SiO_2 hollow-core fiber Capillary	CS_2 — —	450 mm — — —	IRS Pump-Probe	1550 nm — 3 ps 50 MHz	— — 8 ps	—	—	—	g_{Raman}: 3.00 ± 10^{-11} m $\mathrm{W^{-1}}$ Raman shift: $6.6 \pm 10^{+4}$ $\mathrm{m^{-1}}$ 1.5 mW average pump power; 2 μm core diameter	[Schneebeli2013]
SiO_2 hollow-core fiber Capillary	CS_2 — —	140 mm — — —	Other	1950 nm — 460 fs 5.6 MHz	— — —	2.80 ± 10^{-1}	—	—	Supercontinuum generation; 14 nJ pump pulse energy; 4.7 μm core diameter	[Chemnitz2017]
SiO_2 hollow-core fiber PCF	Air — —	1.61 m — — —	Two-color SBS Pump-Probe	1535 nm 48 mW CW —	— — —	1.60 ± 10^{-4}	—	—	$\gamma_{\mathrm{Brillouin}}$: 9.00 ± 10^{-4} $\mathrm{W^{-1}\,m^{-1}}$ Brillouin shift: $3.50 \pm 10^{+7}$ Hz, Linewidth: $4.00 \pm 10^{+6}$ Hz Forward Brillouin scattering; 1 atm air pressure; 5.65 μm core diameter	[Renninger2016]

SiO_2 hollow-core fiber PCF	CCl_4 — —	190 mm — — —	Other	1030 nm — 210 fs 44 MHz	— — —	3.70 ± 10^{-1}	—	—	Supercontinuum generation; 330 mW average pump power; 2.5 μm core diameter	[Vieweg2010]
SiO_2 hollow-core fiber PCF	CO_2 — —	50 m — 80 μm^2 Figure 8(b)	Two-color SBS Pump-Probe	1550 nm 6 mW CW —	— — —	—	—	—	$\gamma_{Brillouin}$: 1.68 W^{-1} m^{-1} Brillouin shift: $3.20 \pm 10^{+8}$ Hz, Linewidth: $3.65 \pm 10^{+6}$ Hz Backward Brillouin scattering; 41 bar CO_2 pressure; 10 μm core diameter	[Yang2020]
SiO_2 hollow-core fiber PCF	H_2 — —	320 mm — — Figure 8(a)	SRS	532 nm — 6 ns 20 Hz	— — —	—	—	—	30% pump-to-Stokes conversion efficiency for 4.5 uJ pump pulse energy; 17 bar H_2 pressure; 15 μm core diameter	[Benabid2002]
SiO_2 solid-core fiber Side polished	Black phosphorus 10 nm Mechanical exfoliation	100 mm 73.6% /1566 nm — —	Nonlinear transm./refl.	1566 nm — 1.2 ps 14.2 MHz	— — —	—	$1.25 \pm 10^{+11}$	3.31	—	[Park2015]
SiO_2 solid-core fiber Side polished	Graphene Monolayer CVD	500 μm 47% /1561 nm 40 μm^2 Figure 8(c)	FWM	1561 nm 300 W 265 fs 37.8 MHz	1480–1610 nm 10 mW CW	1.14	—	—	Graphene doping: variable (values here for 0.2 eV) $\lvert\chi^{(3)}\rvert$: 8 ± 10^{-17} m^2 V^{-2} Nonlinearity dependence on graphene doping level shown in figure 2 of reference paper	[An2020]
SiO_2 solid-core fiber Side polished	Graphene 2 layers CVD	5 mm 8.7% /1550 nm — —	Nonlinear transm./refl.	1609 nm — 423 fs 30.9 MHz	— — —	—	$2.57 \pm 10^{+12}$	1.06	Graphene doping: variable (values here for 1.2 V gate voltage)	[Lee2015]

(Continued.)

Table 8A. (Continued.)

Hybrid Fibers										
Material Properties			**Measurement Details**			**Nonlinear Properties**				
Constituent 1 Fiber type	**Constituent 2** Added material Thickness Fabrication	**Hybrid fiber** Length Loss/wavelength[a] Effective area SEM image[b]	**Method**	**Pump** Wavelength Peak power Pulse width Rep. rate	**Probe** Wavelength Peak power Pulse width	$\lvert\mathrm{Re}(\gamma_{\mathrm{eff}})\rvert$ ($\mathrm{m}^{-1}\,\mathrm{W}^{-1}$)	$I_{\mathrm{sat,eff}}$ ($\mathrm{W\,m}^{-2}$)	Saturable loss (%)	Additional parameters and comments	Reference
SiO_2 solid-core fiber Side polished	Graphene oxide 100 nm Modified Hummers method	10 mm 42% /1550 nm — —	Nonlinear transm./refl.	1550 nm 19.4 kW 150 fs 89 MHz	— — — —	—	—	22	Saturation fluence: 7 ± 10^{-2} $\mathrm{J\,m}^{-2}$	[Steinberg2018]
SiO_2 solid-core fiber Tapered	Carbon nanotubes — High-pressure CO process	100 mm 68% /1550 nm 50 μm^2 —	FWM	1550 nm 1.6 W CW —	1552 nm — 0.1 ns —	1.82	—	—	Semiconducting nanotubes; 1ppm in PTFEMA Conversion efficiency: 0.2% Conversion efficiency formula: $\mathrm{idler_{out}/signal_{in}}$ Conversion bandwidth: 9 nm	[Xu2013]
SiO_2 solid-core fiber Tapered	Carbon nanotubes — High-pressure CO process	4 mm 34% /1550 nm — —	Nonlinear transm./refl.	1550 nm — 600 fs 25 MHz	— — — —	—	—	8.5	Semiconducting nanotubes; 50% in PTFEMA; variable fiber diameter (values here for 3 μm) Average saturation power: 4.50 ± 10^{-4} W Nonlinearity dependence on diameter of tapered fiber shown in table II of reference paper	[Martinez2017]
SiO_2 solid-core fiber Tapered	$MoTe_2$ 11.6 nm Magnetron sputtering deposition	10 mm 44.6% /1572.4 nm — Figure 8(d)	Nonlinear transm./refl.	1572.4 nm — 642 fs 50.12 MHz	— — — —	—	$9.60 \pm 10^{+10}$	25.5	—	[Wang2018]

SiO_2 solid-core fiber Tapered	$MoTe_2$ 11.6 nm Magnetron sputtering deposition	10 mm 43.3% /1915.5 nm — Figure 8(d)	Nonlinear transm./refl.	1915.5 nm — 1.25 ps 18.72 MHz	— — —	—	$1.23 \pm 10^{+11}$	22.1	—	[Wang2018]
SiO_2 solid-core fiber Tapered	WS_2 Monolayer CVD	60 μm <25% /1530–1590 nm — —	SHG	1550 nm — 10 ns 1 MHz	— — —	—	—	—	20-fold enhancement of SHG signal as compared to bare fiber for 50 mW average pump power	[Chen2019b]

[a] Wavelength at which the specified loss has been measured.
[b] Selected SEM images presented in this work.

Table 8B. NLO properties of hybrid on-chip waveguides from representative works since 2000. Legend for superscripts: see below the table.

Hybrid On-Chip Waveguides									
Material Properties			Measurement Details			Nonlinear Properties			
Constituent 1 Waveguide (wg) Lithography	**Constituent 2** Added material Thickness Fabrication	**Hybrid wg** Length Loss/wavelength[a] Effective area SEM image[b]	**Method**	**Pump** Wavelength Peak power Pulse width Rep. rate Polarization	**Probe** Wavelength Peak power Pulse width Polarization	$\lvert\mathrm{Re}(\gamma_{\mathrm{eff}})\rvert$ $(\mathrm{m}^{-1}\,\mathrm{W}^{-1})$	η (%)	Additional parameters and comments	Reference
Hydex wg Photolith.	Graphene oxide 2 layers Solution-based process	15 mm 0.2 dB mm^{-1}/ 1550 nm — —	FWM	1550 nm 160 mW CW — TE mode	1551 nm 160 mW CW TE mode	9.00 ± 10^{-1}	2.00 ± 10^{-3}	Conversion efficiency formula: $\mathrm{idler}_{\mathrm{out}}/\mathrm{signal}_{\mathrm{out}}$ Conversion bandwidth: 2.50 ± 10^{12} Hz Nonlinearity dependence on wavelength detuning and length shown in figure 4 of reference paper	[Yang2018b]
Plasmonic (gold) wg E-beam lith.	Polymer MEH-PPV — Spin-coating	2 μm — — Figure 8(e)	FWM	1480 nm 30 W 1.04 ps 10 kHz TE mode	1450 nm — 1.11 ps TE mode	$3.09 \pm 10^{+4}$	4.60	$\mathrm{Im}(\gamma_{\mathrm{eff}})$: 7.00 ± 10^{2} $\mathrm{m}^{-1}\,\mathrm{W}^{-1}$ Conversion efficiency formula: $\mathrm{idler}_{\mathrm{out}}/\mathrm{signal}_{\mathrm{in}}$	[Nielsen2017]
Si photonic-crystal wg Photolith.	Graphene Monolayer CVD	1.5826 μm (cavity length) — — Figure 8(f)	FWM	1562.36 nm 0.6 mW CW — TE mode	1562.09 nm 600 μW CW TE mode	—	1.00 ± 10^{-1}	Graphene doping: 5.00 ± 10^{16} m^{-2} Free-carrier lifetime: 2.00 ± 10^{-10} s $\lvert n_{2,\mathrm{eff}}\rvert$: 4.80 ± 10^{-17} $\mathrm{m}^{2}\,\mathrm{W}^{-1}$	[Gu2012]
Si slot wg Photolith.	Organic molecules DDMEBT — Molecular beam deposition	4 mm 1.6 dB mm^{-1}/ 1550 nm — Figure 8(g)	FWM	1548 nm 375 mW 3 ps 42.7 GHz TE mode	1556 nm — 3.00 ps TE mode	$1.04 \pm 10^{+2}$	6.00 ± 10^{-2}	Conversion efficiency formula: $\mathrm{idler}_{\mathrm{out}}/\mathrm{signal}_{\mathrm{out}}$	[Koos2009]

Si wg Photolith.	Graphene Monolayer CVD	400 μm 132 dB mm^{-1}/ 1550 nm — —	SPM/XPM spectral broadening	1553 nm 1.68 W 3 ps 80 MHz TE mode	— — — —	1.40 $\pm$ 10^{+3}	—	Graphene doping: 0.2 eV $n_{2,\text{eff}}$ of graphene only: 1 $\pm$ 10^{-13} m^2 W^{-1}	[Vermeulen2016a]
Si wg E-beam lith.	MoS_2 3 nm CVD	1.6 mm 5.5 dB mm^{-1}/ 1560 nm — —	FWM	1550 nm — CW — TM mode	1550.4 nm — CW TM mode	—	6.00 $\pm$ 10^{-2}	Conversion efficiency formula: idler$_{\text{out}}$/signal$_{\text{out}}$ Nonlinearity dependence on wavelength detuning shown in figure 6 of reference paper	[Zhang2020c]
Si_3N_4 wg Photolith.	Graphene oxide Monolayer Solution- based process	20 mm 0.61 dB mm^{-1}/ 1550 nm — —	FWM	1549 nm 63 mW CW — TE mode	1550 nm 63 mW CW TE mode	1.31 $\pm$ 10^{+1}	1.40 $\pm$ 10^{-4}	Conversion efficiency formula: idler$_{\text{out}}$/signal$_{\text{in}}$ Conversion bandwidth: 1.25 $\pm$ 10^{12} Hz Nonlinearity dependence on graphene-oxide layer number shown in figure 8 of reference paper	[Qu2020]
Si_3N_4 wg Photolith.	Graphene Monolayer CVD	100 μm 50 dB mm^{-1}/ 1550.18 nm — Figure 8(h)	FWM	1550.18 nm 11.2 mW CW — TM mode	1550.7 nm — CW TM mode	6.40 $\pm$ 10^{+3}	1.00 $\pm$ 10^{-3}	Graphene doping: variable (values here for 0.35 eV, i.e. 0.5 V gate voltage) Conversion efficiency formula: idler$_{\text{out}}$/signal$_{\text{out}}$ Nonlinearity dependence on graphene doping level and wavelength detuning shown in figure 4 of reference paper	[Alexander2017]
Si_3N_4 wg Photolith.	Graphene Monolayer —	3.2 mm 12.6 dB mm^{-1}/ 1540 nm 0.81 μm^2 —	Nonlinear transm./refl.	1547 nm — 200 fs 20 MHz TE mode	— — — —	—	—	Graphene doping: 0.3 eV Free-carrier lifetime: 1.50 $\pm$ 10^{-13} s Saturation density: 1.30 $\pm$ 10^{+16} m^{-2} Non-saturable loss: 7.5 dB mm^{-1}	[Demongodin2019]
Si_3N_4/SiO_2 wg Photolith.	Graphene Monolayer CVD	1.1 mm 20 dB mm^{-1}/ 1563 nm — —	SPM/XPM spectral broadening	1563 nm 2.7 W 3 ps 80 MHz TE mode	— — — —	Proportional to free-carrier refraction coefficient	—	Graphene doping: 6.50 $\pm$ 10^{16} m^{-2} Free-carrier lifetime: 1.00 $\pm$ 10^{-12} s Free-carrier refraction coefficient: 1.00 $\pm$ 10^{-5} (-)	[Vermeulen2018]
a-Si wg E-beam lith.	$MoSe_2$ Monolayer Mechanical exfoliation	22 μm — — —	SHG	1550 nm — 82 fs 80 MHz TE mode	— — — —	—	—	5-fold enhancement of SHG signal as compared to free-space excitation of $MoSe_2$ Pump irradiance: 150 TW m^{-2}	[Chen2017a]

(Continued.)

Table 8B. (Continued.)

Hybrid On-Chip Waveguides									
Material Properties			**Measurement Details**			**Nonlinear Properties**			
Constituent 1	**Constituent 2**	**Hybrid wg**	**Method**	**Pump**	**Probe**				
Waveguide (wg)	Added material	Length		Wavelength	Wavelength	$\lvert\mathrm{Re}(\gamma_{\mathrm{eff}})\rvert$	η (%)	Additional parameters and comments	Reference
Lithography	Thickness	Loss/wavelength[a]		Peak power	Peak power	($\mathrm{m}^{-1}\ \mathrm{W}^{-1}$)			
	Fabrication	Effective area		Pulse width	Pulse width				
		SEM image[b]		Rep. rate	Polarization				
				Polarization					
Si_3N_4 wg	Graphene	80 μm	DFG	1531.9 nm	1593.2 nm	—	4.00 ± 10^{-3} W^{-1}	Plasmon-enhanced DFG	[Yao2018]
Photolith.	Monolayer	100 dB mm^{-1}/		200 W	1.6 W			Graphene doping: variable (values here for 0.05 eV)	
	CVD	1550 nm		2.2 ps	CW			$\chi^{(2)}$: 1.20 ± 10^{-6} esu	
		—		39.1 MHz	TM mode			Conversion efficiency formula: $\mathrm{idler}_{\mathrm{out}}$/(signal*pump)	
		—		TM mode				Nonlinearity dependence on graphene doping shown in figure 4 of reference paper	

[a] Wavelength at which the specified loss has been measured.

[b] Selected SEM images presented in this work.

3.8. THz NLO: data table and discussion

***Team**: Dmitry Turchinovich*

3.8.1. Introduction

3.8.1.1. THz NLO mechanisms

As already mentioned in sections 3.1.1 and 3.3.1, some materials exhibit pronounced nonlinear responses not only at optical wavelengths but also in the THz domain. These THz nonlinearities can originate from various physical processes. The free carrier response typically constitutes the strongest, and most broadband, contribution to the dielectric function of materials at THz frequencies [Dressel and Grüner2002, Huber2001, Jepsen2011, Ulbricht2011]. Consequently, the strongest NLO response at THz frequencies is also usually dominated by free-carrier effects, and hence is characteristic of conductive materials, or materials that become conductive under intense THz excitation (see, for example, [Blanchard2011, Cheng2020, Deinert2021, Fan2013, Giorgianni2016, Grady2013, Hafez2018, Hafez2020, Hirori2011, Hoffmann2009a, Hoffmann and Turchinovich2010, Hohenleutner2015, Hwang2013, Jadidi2016, Junginger2012, König-Otto2017, Kovalev2020, Kovalev2021, Lee2020, Liu2012a, Matsunaga2013, Mayer2015, Mics2015, Schubert2014, Sharma2010, Shimano2012, Turchinovich2012]). Here, the THz electromagnetic field couples to the free carriers via optical conductivity mechanisms, leading to absorption of a part of the electromagnetic energy by the electronic system of the material. This energy transfer from the driving THz field to the free electrons typically results in heating of the electron population of the material, or quasi-coherent ponderomotive acceleration of carriers within the band structure, both leading to the concomitant temporal modification of the THz optical conductivity of the material, and hence to its nonlinear response to the driving THz field.

THz nonlinearities may also arise from THz-driven phase transitions (e.g., [Liu2012a]), or from direct, quasi-resonant excitation of THz intersubband transitions in semiconductor nanostructures such as quantum wells or superlattices (e.g., [Houver2019, Kuehn2011, Raab2019, Raab2020]). IR-active optical phonons with resonant frequencies in the THz range also contribute to the THz nonlinearity in crystals [Dekorsy2003, Lu2021, Mayer and Keilmann1986a].

The THz nonlinearities resulting from the direct THz excitation of electrons or IR-active phonon modes in crystals are dissipative in nature, as the driving THz field is physically absorbed by the material in the first steps of the light-matter interaction. The materials exhibiting the strongest nonlinearities at THz frequencies are, typically, doped semiconductors, superconductors, and doped quantum materials such as graphene, topological insulators, and 3D Dirac semimetals (see, for example, [Blanchard2011, Cheng2020, Deinert2021, Fan2013, Giorgianni2016, Grady2013, Hafez2018, Hafez2020, Hirori2011, Hoffmann2009a, Hoffmann and Turchinovich2010, Hohenleutner2015, Hwang2013, Jadidi2016, Junginger2012, König-Otto2017, Kovalev2020, Kovalev2021, Lee2020, Matsunaga2013, Mayer2015, Mics2015, Schubert2014, Sharma2010, Shimano2012, Turchinovich2012]). Doped graphene was shown to have by far the strongest electronic nonlinearity at THz frequencies [Hafez2018]. Its nonlinear coefficients at THz frequencies surpass those of all other known materials by many orders of magnitude, and this possibly holds for other spectral ranges as well [Hafez2018, Hafez2020].

The non-dissipative THz nonlinearities such as the THz Kerr effect [Hoffmann2009a, Sajadi2015] or the THz-driven QCSE [Hoffmann2010], also reported in the literature, are usually weaker in strength than the dissipative electronic nonlinearities. These non-dissipative nonlinear effects are typically observed in a THz pump—optical probe arrangement, where the strong THz field modifies the conditions of light-matter interactions for the optical-frequency probe in the material. For THz Kerr measurements, optically transparent solids and liquids are typically used as samples, whereas for the observation of THz QCSE, quantum nanostructures featuring resonant absorption at the optical probe wavelength are used. A somewhat related type of THz NLO experiment is the THz-driven side-band generation on a CW optical carrier wave, which propagates through a THz-nonlinear material or device [Dhillon2007, Zaks2012]. These experiments are usually performed in a quasi-CW mode, and the THz sideband generation is registered in the spectrum of the carrier probe signal at optical frequencies.

3.8.1.2. Brief history of THz NLO research

THz NLO is a relatively young discipline. The key reason for this is the relative difficulty of generating strong fields at THz frequencies, as compared to visible and IR optical signals. In the early works on THz NLO from the 1980–1990s gas lasers and THz free-electron lasers (FELs) were used as sources, and the experiments were performed in a quasi-CW mode (see, for example, [Bewley1993, Van Dantzig and Planken1999, Dekorsy2003, Ganichev and Prettl2006, Heyman1994, Markelz1994a, Markelz1994b, Mayer and Keilmann1986a, Mayer and Keilmann1986b, Pellemans and Planken1998, Winnerl2000]). Almost all these experiments were performed on semiconductors, both bulk and nanostructured.

Since the 1990s THz spectroscopy is dominated by the THz time-domain spectroscopy (THz-TDS) method (see, for example, [Grischkowsky1990, Jepsen2011, Tonouchi2007, Ulbricht2011]). In THz-TDS, single-cycle THz pulses are generated from femtosecond laser pulses in photoconductive antennas or via optical rectification in $\chi^{(2)}$-nonlinear crystals. The detection of such THz transients in THz-TDS is enabled via photoconductive detection, or via free-space electrooptic sampling (FEOS) in $\chi^{(2)}$-nonlinear crystals [Gallot and Grischkowsky1999, Planken2001, Zhang and Turchinovich2021]. Both of these techniques involve a femtosecond laser pulse as a time gate, providing for the field-resolved detection of THz electromagnetic transients with sub-cycle temporal resolution. Importantly, FEOS also permits the calibrated detection of THz fields, yielding the temporal evolution of the instantaneous electric field strength in absolute units within the detected THz field transient [Gallot and Grischkowsky1999, Planken2001, Zhang and Turchinovich2021]. If certain conditions are observed, the recorded FEOS signals can be rigorously reconstructed back to the electric field evolution in the propagating THz signal, and even to the initial polarization or magnetization dynamics in the THz emitter (see, for example, [Hafez2018, Zhang2020a, Zhang and Turchinovich2021]). We note that standard table-top THz generation via photoconductive mechanisms or via optical rectification yields THz fields not exceeding a few kV cm^{-1} in strength, thus only providing for spectroscopy in the linear regime.

In 2002 highly efficient strong-field THz generation via optimized optical rectification by tilted pulse front pumping (TPFP) of $\chi^{(2)}$-nonlinear crystals was proposed by Hebling *et al* [Hebling2002], which later led to the demonstration of THz pulses with peak field strengths reaching 250 kV cm^{-1} by Yeh *et al* [Yeh2007]. This demonstration paved the way to modern nonlinear THz spectroscopy using table-top sources. Since then, the TPFP of lithium niobate (LN) crystals by mJ-level femtosecond laser pulses dominates the table-top strong-field THz generation, typically yielding single-cycle THz pulses with the spectrum covering the range 0–3 THz, and with (sub-)MV cm^{-1} peak electric fields. Amplified Ti:Sapphire femtosecond lasers, delivering mJ-level femtosecond pulses with 800 nm central wavelength remain the most popular pumping sources for strong-field THz generation via the TPFP method in LN, however other types of femtosecond lasers, e.g., Yb-based [Hoffmann2007], can also be used. Other modern methods of table-top strong-field THz generation include air-plasma THz generation [Tani2012], typically yielding ultrabroadband single-cycle THz pulses with the spectrum covering the range of 0–20 THz or even broader, and optical rectification in organic nonlinear crystals [Shalaby and Hauri2015]. We refer the reader to the following reviews and article collections on modern methods of strong-field THz generation and nonlinear THz spectroscopy [Elsaesser2019, Hafez2016, Hoffmann and Fülöp2011, Hwang2015, Kampfrath2013, Leitenstorfer2014].

Furthermore, latest-generation relativistic accelerator-based sources, such as those at the TELBE facility at Helmholtz-Zentrum Dresden-Rossendorf [Green2016], are also actively used in modern THz NLO research. They deliver quasi-monochromatic multi-cycle THz pulses with peak fields currently reaching 100s kV cm^{-1} (and with the potential to reach MV cm^{-1} levels), and are precisely synchronized to a table-top femtosecond laser [Kovalev2017], thus enabling calibrated FEOS of the THz fields in the experiment [Hafez2018, Kovalev2021].

3.8.1.3. Considerations for THz NLO research

Since the strongest THz nonlinearities are based on the physical absorption of the driving THz field by the electrons or polar phonons in the materials, such THz nonlinear effects are therefore dissipative. Furthermore, almost all reported THz nonlinearities are based on field effects. Therefore, the THz field strength is the key parameter characterizing the pump signal in THz NLO, and not the integrated THz pulse energy, power or irradiance, as is common in 'traditional' NLO.

Interestingly, almost all reported strong THz nonlinearities are generally non-perturbative, i.e., they do not follow a clear power law scaling over the entire range of applied THz peak fields, and often demonstrate saturation behavior. However, in certain cases it is possible to observe a clear perturbative, power law scaling over a considerable range of pumping THz field strengths, usually around the lower end of pumping strengths. In this case it is possible to use this small-signal nonlinearity regime and establish the effective nonlinear coefficients of the material similar to 'traditional' NLO [Cheng2020, Deinert2021, Hafez2018].

Owing to a generally dissipative nature of THz NLO processes, 'classical' phase matching between the pump wave and the generated NLO signal is not the dominating concept dictating the conversion efficiency in THz NLO. The conversion efficiency here is rather dependent on the efficiency of energy transfer from the pump signal to the material itself (pump absorption), reabsorption of the generated THz NLO signal within the material, and the outcoupling efficiency of the generated NLO signal.

Finally, and in stark contrast to 'traditional' NLO, most of the experiments on THz NLO are performed using strong-field single-cycle THz pulses, usually produced via TPFP in LN. Such single-cycle pulses are per default ultra-broadband, and contain many octaves of frequencies. This often leads to the observation of

frequency-dependent effective nonlinearities, sometimes even of different signs (see, e.g., [Turchinovich2012]), co-existing within the ultrabroadband bandwidth of a single-cycle THz pulse. However, observation of THz nonlinearities in a multi-cycle, quasi-monochromatic THz pumping regime is also possible. Such THz pump fields are either generated at large-scale facilities such as FELs (see, e.g., [Jadidi2016, König-Otto2017, Zaks2012]) and TELBE (see, e.g., [Deinert2021, Hafez2018, Kovalev2020, Kovalev2021]), or are produced via the monochromatization of a strong-field LN-generated single-cycle THz pulse using bandwidth filtering [Cheng2020].

3.8.1.4. Description of general table outline

Table 9 shows a representative list of THz nonlinearities taken from the literature since 2000. As THz NLO is quite different from 'traditional' NLO, table 9 has been organized in a different way as compared to the previously presented tables and contains the following columns:

- Material type and relevant material information such as doping level (specified either as doping concentration N_c or Fermi energy E_F) and type (electrons or holes)
- Additional material information if available
- Material dimensionality (dim.) which can be 0D/1D/2D/3D
- Parameters of THz pump signal used in the measurement: source type, signal type namely single-cycle/few cycle/quasimonochromatic, central frequency (for quasimonochromatic/few cycle pulses) or frequency range (for single-cycle THz pulses), and peak THz field strength
- Physical mechanism of THz nonlinearity
- Nonlinearity type: dissipative (diss.)/non-dissipative (non-diss.)
- Type of observed nonlinear effect, such as nonlinear absorption, high-harmonics generation (HHG) etc.
- Measured nonlinear coefficients. Note that the coefficients $\chi^{(n)}$ are reported for the pumping field range corresponding to the perturbative nonlinearity regime.

Within each column the information is given in the order of the header description.

In table 9 we only listed papers presenting nonlinear coefficients of various materials, measured and quantified in a fashion compatible with 'traditional' NLO ($\chi^{(n)}$ coefficients, conversion efficiency, saturable absorption parameters, nonlinear refractive index or refractive index modulation etc). We thus did not include papers demonstrating the nonlinear effect, but not quantifying its strength, nor papers that only report a relative transmission change of the THz field through the material.

Furthermore, we only listed papers where the THz pump field was characterized using the calibrated FEOS [Gallot and Grischkowsky1999, Planken2001, Zhang and Turchinovich2021] method at the sample position, with one exception of an FEL signal where the THz field at the sample position could be precisely calibrated from the power measurement [König-Otto2017]. We thus excluded papers reporting only the integrated power/energy/irradiance as the characteristic of the pump THz signal, since it is the THz field that is key for the THz nonlinearity. In addition, we excluded the works reporting on THz Z-scans, especially those using single-cycle ultrabroadband THz pulses. The focal spot for such an ultrabroadband pulse is per definition strongly frequency-dependent, and the measurement of a precise spot shape is highly nontrivial since the THz cameras usually have a rather limited, and strongly frequency-dependent sensitivity. As a result, the precise quantitative determination of NLO coefficients of materials using THz Z-scan is a highly challenging task, prone to too many experimental uncertainties. Finally, we remark that the works included in table 9 nominally report data obtained at room temperature, unless denoted otherwise.

3.8.2. Discussion

Most, and also the strongest nonlinearities presented in table 9 are dissipative and are based on nonlinear conduction of free electrons in strong THz fields. These nonlinearities are observed directly in the THz field interacting with the material. The non-dissipative nonlinearities such as the THz Kerr effect or THz-driven QCSE, are rather observed in THz pump—optical probe measurements, where the THz field modifies the propagation conditions for the optical-frequency probe in the material, such as its polarization state (Kerr effect) or resonant absorption coefficient (QCSE).

3.8.2.1. Advancement and remaining challenges in THz NLO research

The major advancement in THz NLO since the demonstration of table-top generation of strong-field THz pulses via TPFP of LN around 2002–2007 is the ability to implement a nonlinear THz-TDS scheme. Here one is able to 'look inside an optical cycle' during the NLO interaction, i.e., to time-resolve the nonlinear propagation of a THz field transient with sub-cycle resolution. Such a type of measurement, giving an unprecedented direct look into the initiation and development of an optical nonlinearity at the level of the

light field, is presently unattainable at other frequency ranges featuring much faster oscillating optical fields, that are therefore more problematic to directly sample in the time domain.

The future progress in THz NLO will be most likely driven by the wider availability of strong-field THz sources in combination with highly sensitive field- and time-resolved THz signal detection, the development of novel nonlinear spectroscopy techniques, and the availability of novel nonlinear materials. The following factors will contribute: (a) broader availability of strong-field single-cycle and multi-cycle THz field sources, both table-top and at large-scale facilities; (b) improved sensitivity in the THz field detection, in particular by increasing the repetition rate of the experiment using high-pulse-energy (multi-mJ level), high-repetition-rate (100 kHz or higher) femtosecond lasers; (c) development of more advanced data acquisition and analysis protocols; (d) further development of novel nonlinear THz spectroscopy techniques, e.g., multi-dimensional THz spectroscopy (see, e.g., [Elsaesser2019, Grechko2018, Junginger2012, Kuehn2011, Woerner2013]), and (e) broader availability of novel nonlinear materials such as quantum materials with higher potential for nonlinear ultrafast electron conduction.

3.8.2.2. Recommendations for future works on THz NLO research

In the future works on THz NLO, we do strongly recommend to precisely characterize the THz field at the position of the sample via calibrated FEOS and to provide this calibrated field transient in the publication. Once all the THz signals in the experiment—pump and nonlinear product(s)—are calibrated, it becomes rather straightforward to quantify the parameters of the NLO interaction, such as the effective nonlinear coefficient, in the fashion used in 'traditional' NLO.

For example, a broader use of quasi-monochromatic strong-field pumping, either at large-scale facilities such as TELBE (e.g., [Deinert2021, Hafez2018, Kovalev2021]), or via table-top quasi-monochromatic strong-field generation (e.g., [Cheng2020, Lee2020]), combined with fully calibrated FEOS [Gallot and Grischkowsky1999, Planken2001, Zhang and Turchinovich2021] detection, should lead to more rigorously calibrated experiments on discrete THz HHG in various materials (see [Deinert2021, Hafez2018, Kovalev2021]). Such measurements allow in particular to extract the THz nonlinear susceptibility coefficients $\chi^{(n)}$ by measuring the conversion efficiency from the pump field to the nth harmonic, over a wide range of pumping field strengths and frequencies [Hafez2018, Hafez2020, Cheng2020].

Finally, we strongly recommend providing comprehensive information on the nonlinear material used, on the details of the experimental setups, and on the protocols of data processing. This should allow for the reproducibility of the THz NLO results by the broader community.

3.8.3. Data table for THz NLO

Table 9. THz nonlinearities from representative works since 2000. Legend for superscripts: see below the table.

Material Type; Fabrication; Key Material Properties;	Dim.	THz Source; Single-Cycle/Quasimonochromatic; THz Pump Frequency Range (for Single Cycle) or Central Pump Frequency (for Quasimonochromatic); THz Peak Field Strength Range	Physical Mechanism of THz-induced NLO Effect	Diss./ Non-diss.	Observed Nonlinear Effects	Measured THz Nonlinear Coefficients	Reference
Al_2O_3	3D	TPFP of LN; Single-cycle; 0–3 THz; max. 2.1 MV cm^{-1}	THz-induced Kerr effect in bulk material probed by an 800 nm probe pulse	Non-diss.	Transient birefringence at optical probe wavelength of 800 nm, measured via optical polarization evolution	n_2 (1 THz) $= 0.7 \pm 10^{-16}$ cm^2 W^{-1}; max. Δn (800 nm) $= 0.6 \pm 10^{-6}$	[Sajadi2015]
Benzene (liquid)	3D	TPFP of LN; Single-cycle; 0–3 THz; 30–150 kV cm^{-1}	THz-induced Kerr effect in liquid, probed by an 800 nm probe pulse	Non-diss.	Transient birefringence at optical probe wavelength of 800 nm, measured via optical polarization evolution	$\chi^{(3)} = 0.22 \pm 10^{-20}$ m^2 V^{-2}; $n_2 = 56 \pm 10^{-16}$ cm^2 W^{-1}; $K = 0.26 \pm 10^{-14}$ m V^{-2} (Kerr coefficient*)	[Hoffmann2009a]
CCl_4 (liquid)	3D	TPFP of LN; Single-cycle; 0–3 THz; 30–150 kV cm^{-1}	THz-induced Kerr effect in liquid, probed by an 800 nm probe pulse	Non-diss.	Transient birefringence at optical probe wavelength of 800 nm, measured via optical polarization evolution	$\chi^{(3)} = 0.10 \pm 10^{-20}$ m^2 V^{-2}; $n_2 = 27 \pm 10^{-16}$ cm^2 W^{-1}; $K = 0.12 \pm 10^{-14}$ m V^{-2} (Kerr coefficient*)	[Hoffmann2009a]
$CHCl_3$ (liquid)	3D	TPFP of LN; Single-cycle; 0–3 THz; 30–150 kV cm^{-1}	THz-induced Kerr effect in liquid, probed by an 800 nm probe pulse	Non-diss.	Transient birefringence at optical probe wavelength of 800 nm, measured via optical polarization evolution	$\chi^{(3)} = 0.04 \pm 10^{-20}$ m^2 V^{-2}; $n_2 = 10 \pm 10^{-16}$ cm^2 W^{-1}; K $= 0.045 \pm 10^{-14}$ m V^{-2} (Kerr coefficient*)	[Hoffmann2009a]

(Continued.)

Table 9. (Continued.)

Material Type; Fabrication; Key Material Properties;	Dim.	THz Source; Single-Cycle/Quasimonochromatic; THz Pump Frequency Range (for Single Cycle) or Central Pump Frequency (for Quasimonochromatic); THz Peak Field Strength Range	Physical Mechanism of THz-induced NLO Effect	Diss./ Non-diss.	Observed Nonlinear Effects	Measured THz Nonlinear Coefficients	Reference
CH_2I_2 (liquid)	3D	TPFP of LN; Single-cycle; 0–3 THz; 30–150 kV cm^{-1}	THz-induced Kerr effect in liquid, probed by an 800 nm probe pulse	Non-diss.	Transient birefringence at optical probe wavelength of 800 nm, measured via optical polarization evolution	$\chi^{(3)} = 0.70 \pm 10^{-20}$ m^2 V^{-2}; $n_2 = 140 \pm 10^{-16}$ cm^2 W^{-1}; $K = 0.75 \pm 10^{-14}$ m V^{-2} (Kerr coefficient*)	[Hoffmann2009a]
CS_2 (liquid)	3D	TPFP of LN; Single-cycle; 0–3 THz; 30–150 kV cm^{-1}	THz-induced Kerr effect in liquid, probed by an 800 nm probe pulse	Non-diss.	Transient birefringence at optical probe wavelength of 800 nm, measured via optical polarization evolution	$\chi^{(3)} = 2.08 \pm 10^{-20}$ m^2 V^{-2}; $n_2 = 440 \pm 10^{-16}$ cm^2 W^{-1}; $K = 2.4 \pm 10^{-14}$ m V^{-2} (Kerr coefficient*)	[Hoffmann2009a]
Diamond; Polycrystalline	3D	TPFP of LN; Single-cycle; 0–3 THz; max. 2.1 MV cm^{-1}	THz-induced Kerr effect in bulk material probed by an 800 nm probe pulse	Non-diss.	Transient birefringence at optical probe wavelength of 800 nm, measured via optical polarization evolution	n_2 (1 THz) $= 3.0 \pm 10^{-16}$ cm^2 W^{-1}; max. Δn (800 nm) $= 1.03 \pm 10^{-6}$	[Sajadi2015]
GaAs; Doped, $N_c = 8 \pm 10^{15}$ cm^{-3} (electrons), Thickness $d = 0.4$ mm;	3D	TPFP of LN; Single-cycle; 0.2–2.5 THz; 9–292 kV cm^{-1}	Intervalley transfer and increase of effective mass of THz-driven free electrons	Diss.	Frequency-dependent nonlinear conductivity and saturable absorption	Frequency-dependent index change $\Delta n =$ 0.13–0.08; Reduction of power absorption coefficient by ca. 50% across the whole measurement spectrum	[Turchinovich2012]
GaAs; Doped, $N_c = 8 \pm 10^{15}$ cm^{-3} (electrons), Thickness $d = 0.4$ mm;	3D	TPFP of LN; Single-cycle; 0.2–2.5 THz; 9–292 kV cm^{-1}	Intervalley transfer and increase of effective mass of THz-driven free electrons	Diss.	Frequency-integrated saturable absorption; nonlinear pulse group delay	Saturation fluence $= 8.2$ μJ cm^{-2}; Max. nonlinear pulse compression $\Delta T/T$ 0.1; Max. group index change Δn_g 0.1	[Hoffmann and Turchinovich2010]

GaAs in external electric field; Intrinsic, photoexcited at 400 nm to create conductivity;	3D	Unspecified source; Single-cycle, monochromatized using bandpass filter; Quasimonochromatic; 0.6 THz; 50 kV cm^{-1};	THz EFISH in static applied symmetry-breaking electric bias field up to $E_b = 15$ kV cm^{-1}	Diss.	SHG and THG	Maximum effective $\chi^{(2)} = \chi^{(3)} * E_b = 1.7 \pm 10^{-7}$ m V^{-1}, corresponding to natural $\chi^{(3)} = 1 \pm 10^{-14}$–$1 \pm 10^{-13}$ m^2 V^{-2}; Max power conversion efficiency η_{SHG} 5 ± 10^{-5}; η_{THG} 1 ± 10^{-5}, at optical pump fluence $F_p = 4$ μJ cm^{-2}	[Lee2020]
GaP; Doped, $N_c = 1 \pm 10^{16}$ cm^{-3} (electrons), Thickness $d = 0.3$ mm;	3D	TPFP of LN; Single-cycle; 0.2–2.5 THz; 9–292 kV cm^{-1}	Intervalley transfer and increase of effective mass of THz-driven free electrons	Diss.	Frequency-integrated saturable absorption; nonlinear pulse group delay	Saturation fluence = 20.9 μJ cm^{-2}; Max. nonlinear pulse compression $\Delta T/T$ 5 ± 10^{-2}; Max. group index change Δn_g 0.05	[Hoffmann and Turchinovich2010]
Ge; Doped, $N_c = 1 \pm 10^{14}$ cm^{-3} (electrons), Thickness $d = 6$ mm;	3D	TPFP of LN; Single-cycle; 0.2–2.5 THz; 9–292 kV cm^{-1}	Intervalley transfer and increase of effective mass of THz-driven free electrons	Diss.	Frequency-integrated saturable absorption; nonlinear pulse group delay	Saturation fluence = 3.1 μJ cm^{-2}; Max. nonlinear pulse compression $\Delta T/T$ 5 ± 10^{-2}; Max. group index change Δn_g 2 ± 10^{-3}	[Hoffmann and Turchinovich2010]
Graphene; Produced by thermal decomposition of SiC on the C-face of 4 H-SiC; n-doped (inhomogeneously within the sample)	2D	FEL (FELBE); Quasimonochromatic; 19 THz; max. 25 kV cm^{-1}	FWM in Landau-quantized graphene (under 4.5 T magnetic field and 10 K cryogenic temperature)	Diss.	Degenerate FWM and transient grating generation	$\chi^{(3)}$ 9.2 ± 10^{-20} m^3 V^{-2} (bulk susceptibility) Temperature = 10 K	[König-Otto2017]
Graphene; CVD-grown; Doped, $E_F = 0.2$ eV (holes);	2D	air-plasma source; Single-cycle; 0–15 THz; 100–300 kV cm^{-1}	THz-driven impact ionization of carriers	Diss.	Modulation of optical density at 800 nm probe wavelength	Optical density change ΔOD 0.01–0.1 at 800 nm	[Tani2012]

(Continued.)

Table 9. (Continued.)

Material Type; Fabrication; Key Material Properties;	Dim.	THz Source; Single-Cycle/Quasimonochromatic; THz Pump Frequency Range (for Single Cycle) or Central Pump Frequency (for Quasimonochromatic); THz Peak Field Strength Range	Physical Mechanism of THz-induced NLO Effect	Diss./ Non-diss.	Observed Nonlinear Effects	Measured THz Nonlinear Coefficients	Reference
Graphene; CVD-grown; doped, $N_c = 2.1 \pm 10^{12}$ cm^{-2} (holes), $E_F = 0.17$ eV	2D	TELBE; Quasimonochromatic; 0.3 THz, 0.37 THz, 0.68 THz; 0–100 kV cm^{-1}	Thermodynamic response of free electrons	Diss.	HHG (odd): 3, 5, 7	$\chi^{(3)}$ 1 ± 10^{-9} m^2 V^{-2}; $\chi^{(5)}$ 1 ± 10^{-22} m^4 V^{-4}; $\chi^{(7)}$ 1 ± 10^{-38} m^6 V^{-6}; Max. field conversion efficiencies: THG: $\eta = 2 \pm 10^{-3}$; 5HG: $\eta = 2.5 \pm 10^{-4}$; 7HG: $\eta = 8 \pm 10^{-5}$	[Hafez2018]
Graphene; CVD-grown; doped, $N_c = 6 \pm 10^{11}$ cm^{-2} (holes), $E_F = 0.07$ eV	2D	TPFP of LN; Single-cycle; 0.3–2 THz; 2–120 kV cm^{-1}	Thermodynamic response of free electrons	Diss.	Frequency-dependent nonlinear conductivity and saturable absorption	Power loss = 12.5%, non-saturable power loss = 12.5%	[Mics2015]
Graphene	2D	TPFP of LN, monochromatization using bandpass filter; Quasimonochromatic; 0.8 THz; 12–31 kV cm^{-1}	Thermodynamic response of free electrons	Diss.	THG	$\chi^{(3)}$ 1 ± 10^{-9} m^2 V^{-2};	[Cheng2020]
InGaAs/GaAs QD-based SESAM for 1040 nm; MBE-grown, 80 QD layers; intrinsic;	0D	TPFP of LN; Single-cycle; 0.2–3.0 THz; 10–100 kV cm^{-1}	THz-driven QCSE in QDs	Non-diss.	Modulation of absorption at 1040 nm probe wavelength	Absorption change $\Delta\alpha = 3\%$ at 1040 nm	[Hoffmann2010]
LDPE (low-density polyethylene)	3D	TPFP of LN; single-cycle; 0–3 THz; max. 2.1 MV cm^{-1}	THz-induced Kerr effect in bulk material probed by an 800 nm probe pulse	Non-diss.	Transient birefringence at optical probe wavelength of 800 nm, measured via optical polarization evolution	n_2 (1 THz) $= 2.0 \pm 10^{-16}$ cm^2 W^{-1}; max. Δn (800 nm) $= 3.15 \pm 10^{-6}$	[Sajadi2015]

$LiNbO_3$	3D	TPFP of LN; few-cycle; 0.35 THz and 1.1 THz; max. 10 kV cm^{-1}	THz DFG at 0.76 THz	Diss.	DFG	$\chi^{(2)} > 1.5 \pm 10^{-6}$ m V^{-1}	[Lu2021]
Metamaterial based on GaAs; Metallic (Au/Cr) split-ring resonators deposited on n-doped ($N_c = 1 \pm 10^{16}$ cm^{-3}) and semi-insulating GaAs.	3D	TPFP of LN; Single-cycle; 0.2–1.2 THz; 24–400 kV cm^{-1}	THz-driven intervalley scattering and impact ionization in GaAs	Diss.	Modulation of THz relative permittivity ε	Relative permittivity change at the metamaterial resonant frequency. Doped GaAs: $\varepsilon =$ 2.5 – 1 at $f = 0.82$ THz, THz field range 24–400 kV cm^{-1}; Semi-insulating GaAs: $\varepsilon =$ 12.5 – 1 at $f = 0.85$ THz, THz field range 100–400 kV cm^{-1}	[Fan2013]
Metamaterial based on golden grating deposited on graphene; CVD-grown graphene; Doped, E_F 0.1 eV (holes)	2D	TELBE; Quasimonochromatic; 0.7 THz; 5–70 kV cm^{-1}	Thermodynamic response of free electrons; plasmonic THz field concentration in a grating	Diss.	THG	$\chi^{(3)}$ 3 $\pm 10^{-8}$ m^2 V^{-2}; Field conversion efficiency η 1 $\pm 10^{-2}$	[Deinert2021]
MgO	3D	TPFP of LN; Single-cycle; 0–3 THz; max. 2.1 MV cm^{-1}	THz-induced Kerr effect in bulk material probed by an 800 nm probe pulse	Non-diss.	Transient birefringence at optical probe wavelength of 800 nm, measured via optical polarization evolution	n_2 (1 THz) $= 0.5 \pm 10^{-16}$ cm^2 W^{-1}; max. Δn (800 nm) $= 0.7 \pm 10^{-6}$	[Sajadi2015]
Semiconducting SWCNT; Produced by CoMoCAT-process; Nominally intrinsic	1D	TPFP of LN; Single-cycle; 0.2–3 THz; 50–420 kV cm^{-1}	THz-driven QCSE and interband transitions in CNTs	Non-diss.	Modulation of absorption at 1.2–1.25 eV probe energy	Absorption change $\Delta\alpha = 4\%$ at 1.2–1.25 eV	[Shimano2012]
Si; Nominally intrinsic	3D	TPFP of LN; Single-cycle; 0–3 THz; max. 2.1 MV cm^{-1}	THz-induced Kerr effect in bulk material probed by an 800 nm probe pulse	Non-diss.	Transient birefringence at optical probe wavelength of 800 nm, measured via optical polarization evolution	n_2 (1 THz) $= 56 \pm 10^{-16}$ cm^2 W^{-1}; Δn (800 nm) $= 65 \pm 10^{-6}$	[Sajadi2015]

(Continued.)

Table 9. (Continued.)

Material Type; Fabrication; Key Material Properties;	Dim.	THz Source; Single-Cycle/Quasimonochromatic; THz Pump Frequency Range (for Single Cycle) or Central Pump Frequency (for Quasimonochromatic); THz Peak Field Strength Range	Physical Mechanism of THz-induced NLO Effect	Diss./ Non-diss.	Observed Nonlinear Effects	Measured THz Nonlinear Coefficients	Reference
SiN	3D	TPFP of LN; Single-cycle; 0–3 THz; max. 2.1 MV cm^{-1}	THz-induced Kerr effect in bulk material probed by an 800 nm probe pulse	Non-diss.	Transient birefringence at optical probe wavelength of 800 nm, measured via optical polarization evolution	n_2 (1 THz) $= 0.08 \pm 10^{-16}$ cm^2 W^{-1}; max. Δn (800 nm) $= 0.05 \pm 10^{-6}$	[Sajadi2015]
TPX (polymethylpentene)	3D	TPFP of LN; single-cycle; 0–3 THz; max. 2.1 MV cm^{-1}	THz-induced Kerr effect in bulk material probed by an 800 nm probe pulse	Non-diss.	Transient birefringence at optical probe wavelength of 800 nm, measured via optical polarization evolution	n_2 (1 THz) $= 0.3 \pm 10^{-16}$ cm^2 W^{-1}; max. Δn (800 nm) $= 0.36 \pm 10^{-6}$	[Sajadi2015]

*Kerr coefficient is defined in the paper as $K = \Delta n/\lambda E^2$.

4. Conclusion

We have identified general best practices for performing and reporting NLO measurements regardless of the NLO technique used, and have also highlighted several technique-specific best practices. Furthermore, we have introduced a set of tables with representative NLO data from the literature since 2000 for bulk materials, solvents, 0D–1D–2D materials, metamaterials, fiber waveguiding materials, on-chip waveguiding materials, hybrid waveguiding systems, and materials suitable for THz NLO. The data were selected based on the identified best practices and on special considerations for the different material types. For each of the material categories, we have also discussed the background prior to 2000, highlighted the recent advancements and remaining challenges, and concluded with recommendations for future NLO studies.

As shown in the discussions, the field of NLO has gained considerable momentum over the past two decades thanks to major breakthroughs in material science and technology. This has given rise to an enormous growth in NLO publications. However, many of them were not included in the tables presented here as they provided too limited information to comply with the best practices. The publications that brought most value to the tables are those that provide one or several NLO coefficients—and possibly also conversion efficiencies—for one or several materials, wavelengths, pulse durations, etc, measured and reported along the best practices. The dependence of NLO coefficients on wavelength, pulse duration, etc is very insightful information not only from a fundamental science perspective (as it allows distinguishing NLO processes while ruling out, e.g., thermal effects) but also from an application point of view. To assess the practical applicability of a NLO material, it is key that papers also clearly specify the material properties and fabrication details, and provide information on both the nonlinear and linear optical characteristics, such as the linear loss. This will allow evaluating the suitability of the material for specific NLO applications along well-defined figures-of-merit.

We encourage the NLO community to take all these aspects into account and implement the presented best practices in future works. In fact, there is still much to be discovered in NLO research, and in the coming years we intend to update the data tables by considering additional NLO processes and by adding materials that are currently not included or yet to be investigated. Hence, for those future investigations we want to stimulate the use of the listed best practices to allow a more adequate comparison, interpretation and practical implementation of the published parameters and as such further the fundamental understanding of NLO as well as its exploitation in real-life applications.

5. Description of author contributions

In the order of the author list:

Nathalie Vermeulen: co-coordinated the data table initiative together with Eric Van Stryland; contributed to the data collection and text of hybrid waveguiding systems (as team leader), on-chip waveguiding materials, and 0D–1D–2D materials; compiled the data table for hybrid waveguiding systems; contributed to the general introduction and conclusion; wrote the best practices sections 2.2.2.1 and 2.2.3, and the introductory part of section 3; compiled the manuscript and contributed to the final editing of the manuscript.

Daniel Espinosa: contributed to the data collection and text of bulk materials, 0D–1D–2D materials, metamaterials, and on-chip waveguiding materials; compiled the data table for on-chip waveguiding materials.

Adam Ball: contributed to the data collection and text of bulk materials and metamaterials.

John Ballato: contributed to the data collection and text of fiber waveguiding materials (as team leader) and hybrid waveguiding systems; compiled the data table for fiber waveguiding materials; contributed to the final editing of the manuscript.

Philippe Boucaud: contributed to the data collection and text of bulk materials and on-chip waveguiding materials.

Georges Boudebs: contributed to the data collection and text of bulk materials.

Cecília Campos: contributed to the text of 0D–1D–2D materials; compiled the data table for 0D–1D–2D materials.

Peter Dragic: contributed to the data collection and text of fiber waveguiding materials and hybrid waveguiding systems.

Anderson Gomes: contributed to the data collection and text of 0D–1D–2D materials (as team leader), and bulk materials; contributed to the best practices section 2.2.2.4.

Mikko Huttunen: contributed to the data collection and text of metamaterials (as team leader) and 0D–1D–2D materials; compiled the data table for metamaterials; wrote the best practices sections 2.2.1.1, 2.2.1.2 and 2.2.2.6.

Nathaniel Kinsey: contributed to the data collection and text of bulk materials (as team leader) and metamaterials; compiled the data table for bulk materials; contributed to the best practices section 2.2.2.4.

Rich Mildren: contributed to the data collection and text of bulk materials and on-chip waveguiding materials; wrote the best practices section 2.2.2.2.

Dragomir Neshev: contributed to the data collection and text of 0D–1D–2D materials and metamaterials.

Lázaro Padilha: contributed to the data collection and text of 0D–1D–2D materials.

Minhao Pu: contributed to the data collection and text of on-chip waveguiding materials (as team leader) and hybrid waveguiding systems.

Ray Secondo: contributed to the data collection and text of bulk materials and metamaterials.

Eiji Tokunaga: contributed to the data collection and text of bulk materials and solvents; wrote the best practices section 2.2.2.5.

Dmitry Turchinovich: collected the data and wrote the text for THz NLO (as team leader); compiled the data table for THz NLO.

Jingshi Yan: contributed to the data collection and text of 0D–1D–2D materials.

Kresten Yvind: contributed to the data collection and text of on-chip waveguiding materials and hybrid waveguiding systems.

Ksenia Dolgaleva: contributed to the data collection and text of bulk materials and 0D–1D–2D materials; contributed to the data collection and wrote most of the text of metamaterials and on-chip waveguiding materials.

Eric Van Stryland: co-coordinated the data table initiative together with Nathalie Vermeulen; collected the data and wrote the text for fused silica and solvents (as team leader); compiled the data tables for fused silica and solvents; contributed to the data collection and text of bulk materials; contributed to the general introduction, conclusion and the best practices section 2.2.2.4; wrote the best practices section 2.2.2.3; contributed to the final editing of the manuscript.

Acknowledgments

N V acknowledges the financial support from Fonds Wetenschappelijk Onderzoek (FWO) under Grants G005420N and G0F6218N (EOS-convention 30467715).

J B acknowledges support from the J. E. Sirrine Foundation.

P B acknowledges the French National Research Agency (Agence Nationale de la Recherche, ANR)—OPOINt project (ANR-19-CE24-0015).

G B acknowledges the support from the University of Angers and from the NNN-TELECOM Program, region des Pays de la Loire, Contract No. 2015 09036.

P D acknowledges the U.S. Department of Defense Directed Energy Joint Transition Office (DE JTO) (N00014-17-1-2546) and the Air Force Office of Scientific Research (FA9550-16-1-0383).

A S L G and C L A V C acknowledge support from Brazilian INCT of Photonics (CNPq, CAPES, FACEPE), and Air Force Office of Scientific Research (AFOSR) under Grant FA9550-20-1-0381.

M J H acknowledges the support of the Flagship of Photonics Research and Innovation (PREIN) funded by the Academy of Finland (Grant No. 320165).

N K, A B, R S acknowledge support from Air Force Office of Scientific Research (FA9550-18-1-0151) and the National Science Foundation (1808928).

R P M acknowledges funding from AFOSR FA2386-21-1-4030 and Australian Research Council LP200301594.

D N and J Y acknowledge the support by the Australian Research Council through the Centres of Excellence program (CE20010001) and NATO SPS program (OPTIMIST).

M P and K Y acknowledge the financial support from Danish National Research Foundation through the Research Centre of Excellence, Silicon Photonics for Optical Communications (SPOC) (ref. DNRF123). M P also acknowledges the financial support from the European Union's Horizon 2020 research and innovation programme (Grant Agreement No. 853522 REFOCUS).

D T acknowledges the financial support from European Union's Horizon 2020 research and innovation programme (Grant Agreement No. 964735 EXTREME-IR), and from Deutsche Forschungsgemeinschaft (DFG) within the project 468501411–SPP2314 INTEGRATECH under the framework of the priority programme SPP2314—INTEREST.

K D and D E are grateful to Roberto Morandotti and Sisira Suresh for suggesting relevant references for the tables. K D and D E acknowledge the financial support from Canada Research Chairs program and Natural Science and Engineering Council's Discovery program RGPIN-2020-03989.

ORCID iDs

Nathalie Vermeulen https://orcid.org/0000-0001-9676-0095
Daniel Espinosa https://orcid.org/0000-0003-0156-6623
Adam Ball https://orcid.org/0000-0003-1816-7813
John Ballato https://orcid.org/0000-0001-5910-3504
Philippe Boucaud https://orcid.org/0000-0002-4192-9030
Georges Boudebs https://orcid.org/0000-0002-0269-4689
Cecília L A V Campos https://orcid.org/0000-0001-5882-2670
Anderson S L Gomes https://orcid.org/0000-0001-6536-6570
Mikko J Huttunen https://orcid.org/0000-0002-0208-4004
Nathaniel Kinsey https://orcid.org/0000-0002-3825-5434
Rich Mildren https://orcid.org/0000-0002-1521-2423
Dragomir Neshev https://orcid.org/0000-0002-4508-8646
Lázaro A Padilha https://orcid.org/0000-0002-8825-6611
Minhao Pu https://orcid.org/0000-0002-4993-4299
Eiji Tokunaga https://orcid.org/0000-0001-8614-8898
Dmitry Turchinovich https://orcid.org/0000-0003-0054-7092
Kresten Yvind https://orcid.org/0000-0001-8013-1606
Ksenia Dolgaleva https://orcid.org/0000-0003-3643-679X
Eric W Van Stryland https://orcid.org/0000-0001-6200-8700

References

[Abbott2016] Abbott B P *et al* 2016 Observation of gravitational waves from a binary black hole merger *Phys. Rev. Lett.* **116** 061102
[Aber2000] Aber J E, Newstein M C and Garetz B A 2000 Femtosecond optical Kerr effect measurements in silicate glasses *J. Opt. Soc. Am.* B **17** 120–7
[Abolghasem2009] Abolghasem P, Han J, Bijlani B J, Arjmand A and Helmy A S 2009 Continuous-wave second harmonic generation in Bregg reflection waveguides *Opt. Express* **17** 9460
[Absil2000] Absil P P, Hryniewicz J V, Little B E, Cho P S, Wilson R A, Joneckis L G and Ho P-T 2000 Wavelength conversion in GaAs microring resonator *Opt. Lett.* **25** 554
[Abudurusuli2021] Abudurusuli A, Li J and Pan S 2021 A review on the recently developed promising infrared nonlinear optical materials *Dalton Trans.* **50** 3155
[Adair1992] Adair R, Chase L L and Payne S A 1992 Dispersion of the nonlinear refractive index of optical crystals *Opt. Mater.* **1** 185–94
[Agrawal2001] Agrawal G P 2001 *Nonlinear Fiber Optics* 3rd edn (New York: Academic)
[Agrawal2013] Agrawal G P 2013 *Nonlinear Fiber Optics* 5th edn (New York: Academic)
[Ahmed 2021] Ahmed S *et al* 2021 An insightful picture of nonlinear photonics in 2D materials and their applications: recent advances and future prospects *Adv. Opt. Mater.* **9** 2001671
[Ahn2014] Ahn H, Lee M-T and Chang Y-M 2014 Spectral dependence of third-order nonlinear optical properties in InN *Appl. Phys. Lett.* **104** 17
[Aitchison1997] Aitchison J S, Hutchings D C, Kang J U, Stegeman G I and Villeneuve A 1997 The nonlinear optical properties of AlGaAs at the half band gap *IEEE J. Quantum Electron.* **33** 341
[Alam2016] Alam M Z, De Leon I and Boyd R W 2016 Large optical nonlinearity of indium tin oxide in its epsilon-near-zero region *Science* **352** 795
[Alam2018] Alam M Z, Schulz S A, Upham J, De Leon I and Boyd R W 2018 Large optical nonlinearity of nanoantennas coupled to an epsilon-near-zero material *Nat. Photon.* **12** 79
[Alekseev1980] Alekseev N E, Gapontsev V P, Zhabotinskii M E, Kravchenko V B and Rudnitskii I P 1980 Laser Phosphate Glasses *Moscow, Izdatel'stvo Nauka* 352
[Alexander2017] Alexander K, Savostianova N A, Mikhailov S A, Kuyken B and Van Thourhout D 2017 Electrically tunable optical nonlinearities in graphene-covered SiN waveguides characterized by four-wave mixing *ACS Photonics* **4** 3039–44
[Alfano1986] Alfano R R, Li Q X, Jimbo T, Manassah J T and Ho P P 1986 Induced spectral broadening of a weak picosecond pulse in glass produced by an intense picosecond pulse *Opt. Lett.* **11** 626–8
[Allen1987] Allen P B 1987 Theory of thermal relaxation of electrons in metals *Phys. Rev. Lett.* **59** 1460
[Almeida2017] Almeida J M P, Oncebay C, Siqueira J P, Muniz S R, De Boni L and Mendonça C R 2017 Nonlinear optical spectrum of diamond at femtosecond regime *Sci. Rep.* **7** 1
[Almeida2019] Almeida G F B, Santos S N C, Siqueira J P, Dipold J, Voss T and Mendonça C R 2019 Third-order nonlinear spectrum of GaN under femtosecond-pulse excitation from the visible to the near infrared *Photonics* **6** 69
[Alms1975] Alms G R, Burnham A K and Flygare W H 1975 Small nuclear dispersion references: measurement of the dispersion in polarizability anisotropies *J. Chem. Phys.* **63** 3321–6
[Alo2020] Alo A, Barros L W T, Nagamine G, Vieira L B, Chang J H, Jeong B G, Bae W K and Padilha L A 2020 Simple yet effective method to determine multiphoton absorption cross section of colloidal semiconductor nanocrystals *ACS Photonics* **7** 1806–12
[Amrani2021] Amrani F,Osório J H, Delahaye F, Giovanardi F, Vincetti L, Debord B, Gérôme F and Benabid F 2021 Low-loss single-mode hybrid-lattice hollow-core photonic-crystal fibre *Light Sci. Appl.* **10** 7
[An2020] An N *et al* 2020 Electrically tunable four-wave-mixing in graphene heterogeneous fiber for individual gas molecule detection *Nano Lett.* **20** 6473–80
[Anderson1971] Anderson D B and Boyd J T 1971 Wideband CO_2 laser second harmonic generation phase matched in GaAs thin-film waveguides *Appl. Phys. Lett.* **19** 266

[Angell1994] Angell M J, Emerson R M, Hoyt J L, Gibbons J F, Eyres L A, Bortz M L and Fejer M M 1994 Growth of alternating <100>/<111>-oriented II-VI regions for quasi-phasematched nonlinear optical devices on GaAs substrates *Appl. Phys. Lett.* **64** 3107
[Anisimov1974] Anisimov S I, Kapeliovich B L and Perel'man T L 1974 Electron emission from metal surfaces exposed to ultrashort laser pulses *J. Exp. Theor. Phys.* **39** 375
[Anthur2020] Anthur A P, Zhang H, Paniagua-Dominguez R, Kalashnikov D A, Ha S T, Maß T W W, Kuznetsov A I and Krivitsky L 2020 Continuous wave second harmonic generation enabled by Quasi-Bound-States in the continuum on gallium phosphide metasurfaces *Nano Lett.* **20** 8745
[Apiratikul2014] Apiratikul P, Wathen J J, Porkolab G A, Wang B, He L, Murphy T E and Richardson C J K 2014 Enhanced continuous-wave four-wave mixing efficiency in nonlinear AlGaAs waveguides *Opt. Express* **22** 26814
[Armstrong1962] Armstrong J A, Bloembergen N, Ducuing J and Pershan P S 1962 Interactions between light waves in a nonlinear dielectric *Phys. Rev.* **127** 1918
[Asobe1995] Asobe M, Yokohama I, Kaino T, Tomari S and Kurihara T 1995 Nonlinear absorption and refraction in an organic dye functionalized main chain polymer waveguide in the 1.5 μm wavelength region *Appl. Phys. Lett.* **67** 891
[Asobe1997] Asobe M 1997 Nonlinear optical properties of chalcogenide glass fibers and their application to all-optical switching *Opt. Fiber Technol.* **3** 142
[Autere2017] Autere A *et al* 2017 Rapid and large-area characterization of exfoliated black phosphorus using third-harmonic generation microscopy *J. Phys. Chem. Lett.* **8** 1343–50
[Autere2018a] Autere A, Jussila H, Dai Y, Wang Y, Lipsanen H and Sun Z 2018 Nonlinear optics with 2D layered materials *Adv. Mater.* **30** 1705963
[Autere 2018b] Autere A *et al* 2018 Optical harmonic generation in monolayer group-VI transition metal dichalcogenides *Phys. Rev.* B **98** 115426
[Awan2018] Awan K M, Muhammad M M, Sivan M, Bonca S, Roqan I S and Dolgaleva K 2018 Fabrication and optical characterization of GaN waveguides on (-201)-oriented Ga_2O_3 *Opt. Mater. Express* **8** 88
[Azouz1995] Azouz A, Stelmakh N, Lourtioz J-M, Delacourt D, Papillon D and Lehoux J 1995 High second-harmonic conversion efficiency of quasi-phase-matched $LiTaO_3$ waveguides pumped by single-mode pulsed AlGaAs laser diodes *Appl. Phys. Lett.* **67** 2263
[Azzam2021] Azzam S I and Kildishev A V 2021 Photonic bound states in the continuum: from basics to applications *Adv. Opt. Mater.* **9** 16
[Babai1977] Babai F H, Dyott R B and White E A D 1977 Crystal growth of organic materials in glass capillaries *J. Mater. Sci.* **12** 869–72
[Baghwat2008] Bhagwat A R and Gaeta A L 2008 Nonlinear optics in hollow-core photonic bandgap fibers *Opt. Express* **16** 5035–47
[Bai2020] Bai Z, Williams R J, Kitzler O, Sarang S, Spence D J, Wang Y, Lu Z and Mildren R P 2020 Diamond brillouin laser in the visible *APL Photonics* **5** 3
[Baig 2021] Baig N, Kammakakam I and Falath W 2021 Nanomaterials: a review of synthesis methods, properties, recent progress, and challenges *Mater. Adv.* **2** 1821–71
[BalaMuraliKrishna2013] Bala Murali Krishna M and Narayana Rao D 2013 Influence of solvent contribution on nonlinearities of near infra-red absorbing croconate and squaraine dyes with ultrafast laser excitation *J. Appl. Phys.* **114** 133103-1–133103-8
[Ballato2018] Ballato J, Cavillon M and Dragic P 2018 A unified materials approach to mitigating optical nonlinearities in optical fiber: I. thermodynamics of optical scattering *Int. J. Appl. Glass Sci.* **9** 263
[Ballato2018a] Ballato J and Peacock A C 2018 Perspective: molten core optical fiber fabrication—a route to new materials and applications *APL Photonics* **3** 120903
[Balu2004] Balu M, Hales J, Hagan D and Van Stryland E 2004 White-light continuum Z-scan technique for nonlinear materials characterization *Opt. Express* **12** 3820–6
[Bandres2018] Bandres M A, Wittek S, Harari G, Parto M, Ren J, Segev M, Christodoulides D N and Khajavikhan M 2018 Topological insulator laser: experiments *Science* **359** 1231
[Bao2012] Bao X and Chen L 2012 Recent progress in distributed fiber optic sensors *Sensors* **12** 8601
[Barbillon 2017] Barbillon G 2017 *Nanoplasmonics–Fundamentals and Applications* (Rijeka: InTech)
[Barrias2016] Barrias A, Casas J R and Villalba S 2016 A review of distributed optical fiber sensors for civil engineering applications *Sensors* **16** 748
[Bartuch1997] Bartuch U, Peschel U, Gabler T, Waldhäusl R and Hörhold H-H 1997 Experimental investigations and numerical simulations of spatial solitons in planar polymer waveguides *Opt. Commun.* **134** 49
[Basiev1999a] Basiev T T, Sobol A A, Zverev P G, Ivleva L I, Osiko V V and Powell R C 1999 Raman spectroscopy of crystals for stimulated Raman scattering *Opt. Mater.* **11** 307–14
[Basiev1999b] Basiev T T, Sobol A A, Zverev P G, Osiko V V and Powell R C 1999 Comparative spontaneous Raman spectroscopy of crystals for Raman lasers *Appl. Opt.* **38** 594–8
[Bassani1991] Bassani F and Scandolo S 1991 Dispersion relations and sum rules in nonlinear optics *Phys. Rev.* B **44** 8446
[Bautista2021] Bautista J E Q, da Silva-neto M L, Campos C L A V, Maldonado M, de Araujo C B and Gomes A S L 2021 Thermal and non-thermal intensity dependent optical nonlinearities in ethanol at 800 nm, 1480 nm, and 1560 nm *J. Opt. Soc. Am.* B **38** 1104–11
[Bechtel1976] Bechtel J and Smith W 1976 Two-photon absorptionin semiconductors with picosecond laser pulses *Phys. Rev.* B **13** 3515–22
[Benabid2002] Benabid F, Knight J C, Antonopoulos G and Russell P S J 2002 Stimulated Raman scattering in hydrogen-filled hollow-core photonic crystal fiber *Science* **298** 399–402
[Benis2017] Benis S, Zhao P, Hagan D J and Van Stryland E W 2017 Nondegenerate, transient nonlinear refraction of indium tin oxide excited at epsilon-near-zero *Nonlinear Optics* p NW1A.3
[Benis2019] Benis S, Munera N, Van Stryland E W and Hagan D J 2019 Z-scan and beam-deflection measurements of indium-tin-oxide at epsilon-near-zero *Nonlinear Optics* p NTu3B.2
[Benis2020] Benis S, Cirloganu C M, Cox N, Ensley T, Hu H, Nootz G and Van Stryland E W 2020 Three-photon absorption spectra and bandgap scaling in direct-gap semiconductors *Optica* **7** 888
[Bergfeld2003] Bergfeld S and Daum W 2003 Second-harmonic generation in GaAs: experiment versus theoretical predictions of $\chi^{(2)}{}_{xyz}$ *Phys. Rev. Lett.* **90** 036801
[Bergh1980] Bergh R A, Lefevre H C and Shaw H J 1980 Single-mode fiber-optic polarizer *Opt. Lett.* **5** 479–81

[Bernhardt2020] Bernhardt N, Koshelev K, White S J U, Meng K W C, Fröch J E, Kim S, Tran T T, Choi D Y, Kivshar Y and Solntsev A S 2020 Quasi-BIC resonant enhancement of second-harmonic generation in WS_2 monolayers *Nano Lett.* **20** 5309
[Bertolotti1999] Bertolotti M, D'Andrea A, Fazio E, Zitelli M, Carrera A, Chiaretti G and Sanvito N G 1999 Experimental observation of spatial soliton dragging in a planar glass waveguide *Opt. Commun.* **168** 399
[Bewley1993] Bewley W W, Felix C L, Plombon J J, Sherwin M S, Sundaram M, Hopkins P F and Gossard A C 1993 Far-infrared second-harmonic generation in GaAs/AlGaAs heterostructures: perturbative and nonperturbative response *Phys. Rev.* B **48** 2376
[Bhattacharya1997] Bhattacharya P 1997 *Semiconductor Optoelectronic Devices* 2nd edn (New York: Prentice-Hall)
[Bierlein1989] Bierlein J D and Vanherzeele H 1989 Potassium titanyl phosphate: properties and new applications *J. Opt. Soc. Am.* B **6** 622
[Bijlani2008] Bijlania B, Abolghasem P and Helmy A S 2008 Second harmonic generation in ridge Bragg reflection waveguides *Appl. Phys. Lett.* **92** 101124
[Bikorimana2016] Bikorimana S, Lama P, Walser A, Dorsinville R, Anghel S, Mitioglu A, Micu A and Kulyuk L 2016 Nonlinear optical responses in two-dimensional transition metal dichalcogenide multilayer: WS_2, WSe_2, MoS_2 and $Mo_{0.5}W_{0.5}S_2$ *Opt. Express* **24** 20685
[BinHasan2014] Bin Hasan S, Lederer F and Rockstuhl C 2014 Nonlinear plasmonic antennas *Mater. Today* **17** 478
[Birnbaum2005] Birnbaum K M, Boca A, Miller R, Boozer A D, Northup T E and Kimble H J 2005 Photon blockade in an optical cavity with one trapped atom *Nature* **436** 87
[Blanc1995] Blanc D, Bouchoux A M, Plumereau C, Cachard A and Roux J F 1995 Phase-matched frequency doubling in an aluminum nitride waveguide with a tunable laser source *Appl. Phys. Lett.* **66** 659
[Blanchard2011] Blanchard F *et al* 2011 Effective mass anisotropy of hot electrons in nonparabolic conduction bands of n-doped InGaAs films using ultrafast terahertz pump-probe techniques *Phys. Rev. Lett.* **107** 107401
[Blechman2019] Blechman Y, Almeida E, Sain B and Prior Y 2019 Optimizing the nonlinear optical response of plasmonic metasurfaces *Nano Lett.* **19** 261
[Bloembergen1962] Bloembergen N and Pershan P S 1962 Light waves at the boundary of nonlinear media *Phys. Rev.* **128** 606–22
[Bloembergen1968] Bloembergen N, Chang R K, Jha S S and Lee C H 1968 Optical second-harmonic generation in reflection from media with inversion symmetry *Phys. Rev.* **174** 813
[Bloembergen1969] Bloembergen N, Burns W K and Matsuoka M 1969 Reflected third harmonic generated by picosecond laser pulses *Opt. Commun.* **1** 195
[Bloembergen1996] Bloembergen N 1996 *Nonlinear Optics* 4th edn (Singapore: World Scientific Printing)
[Bloemer1990] Bloemer M J, Ashley P R, Haus J W, Kalyaniwalla N and Christenses C R 1990 Third-order optical nonlinearities of composites in wavegude geometry *IEEE J. Quantum. Electron.* **26** 1075
[Boling1978] Boling N L, Glass A J and Owyoung A 1978 Empirical Relationships for predicting nonlinear refractive index changes in optical solids *IEEE J. Quantum. Electron.* **14** 601
[Bonner2014] Bonner G M, Lin J, Kemp A J, Wang J, Zhang H, Spence D J and Pask H M 2014 Spectral broadening in continuous-wave intracavity Raman lasers *Opt. Express* **22** 7492
[Boskovic1996] Boskovic A, Chernikov S V, Taylor J R, Gruner-Nielsen L and Levring O A 1996 Direct continuous-wave measurement of n_2 in various types of telecommunication fiber at 1.55 μm *Opt. Lett.* **21** 1966
[Bosshard2020] Bosshard C, Sutter K, Pretre P, Hulliger H, Florsheimer M, Kaatz P and Gunter P 2020 *Organic Nonlinear Optical Materials* 1st edn (London: CRC Press)
[Bouhelier2003] Bouhelier A, Beversluis M, Hartschuh A and Novotny L 2003 Near-field second-harmonic generation induced by local field enhancement *Phys. Rev. Lett.* **90** 13903
[Boyd2020] Boyd R W 2020 *Nonlinear Optics* 4th edn (New York: Academic)
[Boyd1969] Boyd G D, Johnston W D and Kaminow I P 1969 Optimization of the stimulated Raman scattering threshold *IEEE J. Quantum Electron.* **5** 203–6
[Boyko2018] Boyko A A, Schunemann P G, Guha S, Kostyukova N Y, Kolker D B, Panyutin V L and Petrov V 2018 Optical parametric oscillator pumped at 1 μm with intracavity mid-IR difference-frequency generation in OPGaAs *Opt. Mater. Express* **8** 549
[Bravetti1998] Bravetti P, Fiore A, Berger V, Rosencher E, Nagle J and gauthier-lafaye O 1998 5.2–5.6-um source tunable by frequency conversion in a GaAs-based waveguide *Opt. Lett.* **23** 331
[Bridges1995] Bridges R E, Fischer G L and Boyd R W 1995 Z-scan measurement technique for non-Gaussian beams and arbitrary sample thicknesses *Opt. Lett.* **17** 1821–3
[Bristow2007] Bristow A D, Rotenberg N and Van Driel H M 2007 Two-photon absorption and Kerr coefficients of silicon for 850–2200 nm *Appl. Phys. Lett.* **90** 191104
[Brorson1990] Brorson S D, Kazeroonian A, Moodera J S, Face D W, Cheng T K, Ippen E P and Dresselhaus G 1990 Femtosecond room-temperature measurement of the electron-phonon coupling constant in metallic superconductors *Phys. Rev. Lett.* **64** 2172
[Bruch2018] Bruch A W, Liu X, Guo X, Surya J B, Gong Z, Zhang L, Wang J, Yan J and Tang H X 2018 17 000%/W second-harmonic conversion efficiency in single-crystalline aluminum nitride microresonator *Appl. Phys. Lett.* **113** 131102
[Bruch2019] Bruch A W, Liu X, Surya J B, Zou C-L and Tang H X 2019 On-chip $X^{(2)}$ microring optical parametric oscillator *Optica* **6** 1361
[Brunhes2000a] Brunhes T, Boucaud P, Sauvage S, Lemaître A, Gérard J-M, Glotin F, Prazeres R and Ortega J-M 2000 Infrared second-order optical susceptibility in InAs/GaAs self-assembled quantum dots *Phys. Rev.* B **61** 5562–70
[Brunhes2000b] Brunhes T, Boucaud P, Sauvage S, Lemaître A, Gérard J-M, Thierry-Mieg V, Glotin F, Prazeres R and Ortega J-M 2000 Second-harmonic generation in InAs/GaAs self-assembled quantum dots *Physica* E **7** 155–8
[Bruno2020] Bruno V, Devault C, Vezzoli S, Kudyshev Z, Huq T, Mignuzzi S and Shalaev V M 2020 Negative refraction in time-varying strongly coupled plasmonic-antenna-epsilon-near-zero systems *Phys. Rev. Lett.* **124** 43902
[Brus1984] Brus L E 1984 Electron–electron and electron-hole interactions in small semiconductor crystallites: the size dependence of the lowest excited electronic state *J. Chem. Phys.* **80** 4403–9
[Buckland1996] Buckland E L and Boyd R W 1996 Electrostrictive contribution to the intensity-dependent refractive index of optical fibers *Opt. Lett.* **21** 1117–9
[Burris1985] Burris J and McIlrath T J 1985 Theoretical study relating the two-photon absorption cross section to the susceptibility controlling four-wave mixing *J. Opt. Soc. Am.* B **2** 1313–7
[Butet2010a] Butet J, Bachelier G, Russier-Antoine I, Jonin C, Benichou E and Brevet P-F 2010 Interference between selected dipoles and octupoles in the optical second-harmonic generation from spherical gold nanoparticles *Phys. Rev. Lett.* **105** 77401
[Butet2010b] Butet J, Duboisset J, Bachelier G, Russier-Antoine I, Benichou E, Jonin C and Brevet P-F 2010 Optical second harmonic generation of single metallic nanoparticles embedded in a homogeneous medium *Nano Lett.* **10** 1717

[Butet2015] Butet J, Brevet P F and Martin O J F 2015 Optical second harmonic generation in plasmonic nanostructures: from fundamental principles to advanced applications *ACS Nano* **9** 10545
[Butet2016] Butet J and Martin O J F 2016 Evaluation of the nonlinear response of plasmonic metasurfaces: Miller's rule, nonlinear effective susceptibility method, and full-wave computation *J. Opt. Soc. Am.* B **33** A8
[Bykov2020] Bykov D A, Bezus E A and Doskolovich L L 2020 Bound states in the continuum and strong phase resonances in integrated gires-tournois interferometer *Nanophotonics* **9** 83
[Cai2009] Cai W and Shalaev V M 2009 *Optical Metamaterials: Fundamentals and Applications* (Berlin: Springer)
[Cai2011] Cai W, Vasudev A P and Brongersma M L 2011 Electrically controlled nonlinear generation of light with plasmonics *Science* **333** 1720
[Camacho-Morales2016] Camacho-Morales R *et al* 2016 Nonlinear generation of vector beams from AlGaAs nanoantennas *Nano Lett.* **16** 7191
[Camacho-Morales2021] Camacho-Morales R *et al* 2021 Infrared upconversion imaging in nonlinear metasurfaces *Adv. Photonics* **3** 036002
[Cambiasso2017] Cambiasso J, Grinblat G, Li Y, Rakovich A, Cortés E and Maier S A 2017 Bridging the gap between dielectric nanophotonics and the visible regime with effectively lossless gallium phosphide antennas *Nano Lett.* **17** 1219
[Canagasabey2009] Canagasabey A *et al* 2009 High-average-power second-harmonic generation from periodically poled silica fibers *Opt. Lett.* **34** 2483
[Canfield2004] Canfield B K, Kujala S, Jefimovs K, Turunen J and Kauranen M 2004 Linear and nonlinear optical responses influenced by broken symmetry in an array of gold nanoparticles *Opt. Express* **12** 5418
[Capretti2015] Capretti A, Negro L D, Engheta N and Wang Y 2015 Enhanced third-harmonic generation in Si-compatible epsilon-near-zero indium tin oxide nanolayers *Opt. Lett.* **40** 1500
[Capretti2015a] Capretti A, Wang Y, Engheta N and Dal Negro L 2015 Comparative study of second-harmonic generation from epsilon-near-zero indium tin oxide and titanium nitride nanolayers excited in the near-infrared spectral range *ACS Photonics* **2** 1584
[Carnemolla2018] Carnemolla E G, Caspani L, DeVault C, Clerici M, Vezzoli S, Bruno V and Ferrera M 2018 Degenerate optical nonlinear enhancement in epsilon-near-zero transparent conducting oxides *Opt. Mater. Express* **8** 3392
[Caspani2016] Caspani L, Kaipurath R P M, Clerici M, Ferrera M, Roger T, Kim J and Faccio D 2016 Enhanced nonlinear refractive index in ϵ -near-zero materials *Phys. Rev. Lett.* **116** 233901
[CastelloLurbe2020] Castello-Lurbe D, Thienpont H and Vermeulen N 2020 Predicting graphene's nonlinear-optical refractive response for propagating pulses *Laser Photonics Rev.* **14** 1900402
[Cavillon2018] Cavillon M, Kucera C J, Hawkins T W, Runge A F, Peacock A C, Dragic P D and Ballato J 2018 Oxyfluoride core silica-based optical fiber with intrinsically low nonlinearities for high energy laser applications *J. Lightwave Technol.* **36** 284
[Cavillon2018a] Cavillon M, Kucera C, Hawkins T, Dawson J, Dragic P D and Ballato J 2018 A unified materials approach to mitigating optical nonlinearities in optical fiber: III. Canonical examples and materials road map *Int. J. Appl. Glass Sci.* **9** 447
[Celebrano2015] Celebrano M *et al* 2015 Mode matching in multiresonant plasmonic nanoantennas for enhanced second harmonic generation *Nat. Nanotechnol.* **10** 412
[Cerqua-Richardson1998] Cerqua-Richardson K A, McKinley J M, Lawrence B, Joshi S and Villeneuve A 1998 Comparison of nonlinear optical properties of sulfide glasses in bulk and thin film form *Opt. Mater.* **10** 155
[Chang1965] Chang J, Ducuing J and Bloembergen N 1965 Relative phase measurement between fundamental and second-harmonic light *Phys. Rev. Lett.* **15** 6–8
[Chang2018a] Chang L *et al* 2018 Heterogeneously integrated GaAs waveguides on insulator for efficient frequency conversion *Laser Photonics Rev.* **12** 1800149
[Chang2018b] Chang S, Guo X and Ni X 2018 Optical metasurfaces: progress and applications *Annu. Rev. Mater. Res.* **48** 279
[Chang2019] Chang L, Boes A, Pintus P, Peters J D, Kennedy M J, Guo X-W, Volet N, Yu S-P, Papp S B and Bowers J E 2019 Strong frequency conversion in heterogeneously integrated GaAs resonators *APL Photonics* **4** 036103
[Chase1994] Chase L and Van Stryland E 1994 Nonlinear refractive index: inorganic materials *Handbook of Laser Science and Technology* ed M Weber (Boca Raton, FL: CRC Press) pp 269–88 (supplement 2, section 8)
[Chemla1985] Chemla D S and Miller D A B 1985 Room-temperature excitonic nonlinear-optical effects in semiconductor quantum-well structures *J. Opt. Soc. Am.* B **2** 1155–73
[Chemnitz2017] Chemnitz M, Gebhardt M, Gaida C, Stutzki F, Kobelke J, Limpert J, Tünnermann A and Schmidt M A 2017 Hybrid soliton dynamics in liquid-core fibres *Nat. Commun.* **8** 42
[Chen1981] Chen C K, De Castro A R B and Shen Y R 1981 Surface-enhanced second-harmonic generation *Phys. Rev. Lett.* **46** 145
[Chen1987] Chen C, Fan Y X, Eckardt R C and Byer R L 1987 Recent developments in Barium Borate *Proc. SPIE* **0681**
[Chen2002] Chen Y-C, Raravikar N R, Schadler L S, Ajayan P M, Zhao Y-P, Lu T-M, Wang G-C and Zhang X-C 2002 Ultrafast optical switching properties of single-wall carbon nanotube polymer composites at 1.55 μm *Appl. Phys. Lett.* **81** 975
[Chen2007] Chen Y-H, Varma S, Alexeev I and Milchberg H M 2007 Measurement of transient nonlinear refractive index in gases using xenon supercontinuum single-shot spectral interferometry *Opt. Express* **15** 7458
[Chen2010] Chen R, Crankshaw S, Tran T, Chuang L C, Moewe M and Chang-Hasnain C 2010 Second-harmonic generation from a single wurtzite GaAs nanoneedle *Appl. Phys. Lett.* **96** 051110
[Cheng2014] Cheng J L, Vermeulen N and Sipe J E 2014 Third order optical nonlinearity of graphene *New J. Phys.* **16** 053014
[Chen2015] Chen W, Wang Y and Ji W 2015 Two-photon absorption in graphene enhanced by the excitonic Fano resonance *J. Phys. Chem.* C **119** 16954–61
[Chen2017a] Chen H, Corboliou V, Solntsev A, Choi D-Y, Vincenti M A, de Ceglia D, de Angelis C, Lu Y and Neshev D N 2017 Enhanced second-harmonic generation from two-dimensional $MoSe_2$on a silicon waveguide *Light Sci. Appl.* **6** e17060
[Chen2017b] Chen H, Huang X, Fu H, Lu Z, Zhang X, Montes J A and Zhao Y 2017 Characterizations of nonlinear optical properties on GaN crystals in polar, nonpolar, and semipolar orientations *Appl. Phys. Lett.* **110** 1
[Chen2018] Chen S, Li G, Cheah K W, Zentgraf T and Zhang S 2018 Controlling the phase of optical nonlinearity with plasmonic metasurfaces *Nanophotonics* **7** 1013
[Chen2019a] Chen L, Su B and Jiang L 2019 Recent advances in one-dimensional assembly of nanoparticles *Chem. Soc. Rev.* **48** 8–21
[Chen2019b] Chen J-H, Tan J, Wu G-X, Zhang X-J, Xu F and Lu Y-Q 2019 Tunable and enhanced light emission in hybrid WS_2-optical-fiber-nanowire structures *Light Sci. Appl.* **8** 8

[Chen2020] Chen F, Zhang J, Cassagne C and Boudebs G 2020 Large third-order optical nonlinearity of chalcogenide glasses within gallium-tin-selenium ternary system *J. Am. Ceram. Soc.* **103** 5050–55
[Chen2021] Chen P, Han W, Zhao M, Su J, Li Z, Li D, Pi L, Zhou X and Zhai T 2021 Recent advances in 2D rare earth materials *Adv. Funct. Mater.* **31** 2008790
[Cheng2018] Cheng J-X and Xie X S (eds) 2018 *Coherent Raman Scattering Microscopy* (London: CRC Press)
[Cheng2020] Cheng B, Kanda N, Ikeda T N, Matsuda T, Xia P, Schumann T, Stemmer S, Itatani J, Armitage N P and Matsunaga R 2020 Efficient terahertz harmonic generation with coherent acceleration of electrons in the Dirac semimetal Cd_3As_2 *Phys. Rev. Lett.* **124** 117402
[Cherukulappurath2004] Cherukulappurath S, Guignard M, Marchand C, Smektala F and Boudebs G 2004 Linear and nonlinear optical characterization of tellurium based chalcogenide glasses *Opt. Commun.* **242** 313
[Chi2020] Chi S, Liang F, Chen H, Tian W, Zhang H, Yu H and Zhang H 2020 Surface nonlinear optics on centrosymmetric dirac nodal-line semimetal ZrSiS *Adv. Mater.* **32** 1
[Chiles2019] Chiles J *et al* 2019 Multifunctional integrated photonics in the mid-infrared with suspended AlGaAs on silicon *Optica* **6** 1246
[Chon1994] Chon J C and Mickelson A R 1994 Fabrication and characterization of a third-order nonlinear organic-polymer composite glass waveguide: a self-phase modulator *Appl. Opt.* **33** 6935
[Chraplyvy1990] Chraplyvy A R 1990 Limitations on lightwave communications imposed by optical-fiber nonlinearities *J. Lightwave Technol.* **8** 1548
[Christodoulides2010] Christodoulides D N, Khoo I C, Salamo G J, Stegeman G I and Van Stryland E W 2010 Nonlinear refraction and absorption: mechanisms and magnitudes *Adv. Opt. Photonics* **2** 60
[Chui1995] Chui H C, Woods G L, Fejer M M, martinet E L and Harris J S 1995 Tunable mid-infrared generation by difference frequency mixing of diode laser wavelengths in intersubband InGaAs/AlAs quantum wells *Appl. Phys. Lett.* **66** 265
[Ciattoni2010a] Ciattoni A, Rizza C and Palange E 2010 Extreme nonlinear electrodynamics in metamaterials with very small linear dielectric permittivity *Phys. Rev.* A **81** 43839
[Ciattoni2010b] Ciattoni A, Rizza C and Palange E 2010 Transmissivity directional hysteresis of a nonlinear metamaterial slab with very small linear permittivity *Opt. Lett.* **35** 2130
[Ciattoni2012] Ciattoni A and Spinozzi E 2010 Efficient second-harmonic generation in micrometer-thick slabs with indefinite permittivity *Phys. Rev.* A **85** 043806
[Cirloganu2008] Cirloganu C M, Olszak P D, Padilha L A, Webster S, Hagan D J and Van Stryland E W 2008 Three-photon absorption spectra of zinc blende semiconductors: theory and experiment *Opt. Lett.* **33** 22
[Claps2002] Claps R, Dimitropoulos D, Han Y and Jalali B 2002 Observation of Raman emission in silicon waveguides at 1.54 μm *Opt. Express* **10** 1305
[Claps2003] Claps R, Dimitropoulos D, Raghunathan V, Han Y and Jalali B 2003 Observation of stimulated Raman amplification in silicon waveguides *Opt. Express* **11** 1731
[Clays1991] Clays K and Persoons A 1991 Hyper-Rayleigh scattering in solution *Phys. Rev. Lett.* **66** 2980–3
[Clerici2017] Clerici M, Kinsey N, DeVault C, Kim J, Carnemolla E G, Caspani L and Ferrera M 2017 Controlling hybrid nonlinearities in transparent conducting oxides via two-colour excitation *Nat. Commun.* **8** 15829
[Colin1996] Colin S, Contesse E, Boudec P L, Stephan G and Sanchez F 1996 Evidence of a saturable-absorption effect in heavily erbium-doped fibers *Opt. Lett.* **21** 1987–9
[Colman2010] Colman P, Husko C, Combrié S, Sagnes I, C W W and de Rossi A 2010 Temporal solitons and pulse compression in photonic crystal waveguides *Nat. Photon.* **4** 862
[Cong2008] Cong G W, Akimoto R, Nagase M, Mozume T, Hasama T and Ishikawa H 2008 Mechanism of ultrafast modulation of the refraction index in photoexcited $In_xGa_{1-x}As/AlAs_ySb_{1-y}$ quantum well waveguides *Phys. Rev.* B **78** 075308
[Cong2009] Cong G W, Akimoto R, Akita K, Gozu S, Mozume T, Hasama T and Ishikawa H 2009 Experimental and theoretical study of cross-phase modulation in InGaAs/AlAsSb coupled double quantum wells with a AlGaAs coupling barrier *Phys. Rev.* B **80** 035306
[Constant2016] Constant T J, Hornett S M, Chang D E and Hendry E 2016 All-optical generation of surface plasmons in graphene *Nat. Phys.* **12** 124–7
[Corcoran2009] Corcoran B, Monat C, Grillet C, Moss D J, Eggleton B J, White T P, O'Faolain L and Krauss T F 2009 Green light emission in silicon through slow-light enhanced third-harmonic generation in photonic-crystal waveguides *Nat. Photon.* **3** 206
[Cordeiro2005] Cordeiro C M, Wadsworth W J, Birks T A and Russell P S 2005 Engineering the dispersion of tapered fibers for supercontinuum generation with a 1064 nm pump laser *Opt. Lett.* **30** 1980
[Cotter1989] Cotter D, Ironside C N, Ainslie B J and Girdlestone H P 1989 Picosecond pump–probe interferometric measurement of optical nonlinearity in semiconductor-doped fibers *Opt. Lett.* **14** 317
[Coutaz1985] Coutaz J L, Neviere M, Pic E and Reinisch R 1985 Experimental study of surface-enhanced second-harmonic generation on silver gratings *Phys. Rev.* B **32** 2227
[Cumpsty1971] Cumpsty N A and Whitehead D S 1971 The excitation of acoustic resonances by vortex shedding *J. Sound Vib.* **18** 353
[Czaplicki2018] Czaplicki R, Kiviniemi A, Huttunen M J, Zang X, Stolt T, Vartiainen I, Butet J, Kuittinen M, Martin O J F F and Kauranen M 2018 Less is more: enhancement of second-harmonic generation from metasurfaces by reduced nanoparticle density *Nano Lett.* **18** 7709
[Da Silva-Neto2020] Da Silva-Neto M L, Barbosa-Silva R, de Araújo C B, de Matos C J S, Jawaid A M, Ritter A J, Vaia R A and Gomes A S L 2020 Hyper-Rayleigh scattering in 2D redox exfoliated semi-metallic ZrTe2 transition metal dichalcogenide *Phys. Chem. Chem. Phys.* **22** 27845–9
[Dadap1999] Dadap J I, Shan J, Eisenthal K B and Heinz T F 1999 Second-harmonic rayleigh scattering from a sphere of centrosymmetric material *Phys. Rev. Lett.* **83** 4045
[Danckwerts2007] Danckwerts M and Novotny L 2007 Optical frequency mixing at coupled gold nanoparticles *Phys. Rev. Lett.* **98** 26104
[Darwish1996] Darwish A M, Ippen E P, Le H Q, Donnelly J P, Groves S H and Swanson E A 1996 Short-pulse wavelength shifting by four wave mixing in passive InGaAsP/InP waveguides *Appl. Phys. Lett.* **68** 2038
[Dave2015a] Dave U D, Kuyken B, Leo F, Gorza S-P, Combrie S, De Rossi A, Raineri F and Roelkens G 2015 Nonlinear properties of dispersion engineered InGaP photonic wire waveguides in the telecommunication wavelength range *Opt. Express* **23** 4650
[Dave2015b] Dave U D, Ciret C, Gorza S-P, Combrie S, De Rossi A, Raineri F, Roelkens G and Kuyken B 2015 Dispersive-wave-based octave-spanning supercontinuum generation in InGaP membrane waveguides on a silicon substrate *Opt. Lett.* **40** 3584
[Dawson2008] Dawson J, Messerly M, Beach R, Shverdin M, Stappaerts E, Sridharan A, Pax P, Heebner J, Siders C and Barty C 2008 Analysis of the scalability of diffraction-limited fiber lasers and amplifiers to high average power *Opt. Express* **16** 13240

[Day1994] Day I E, Snow P A, Pentry R V, White I H, Grant R S, Kennedy G T, Sibbett W, Davies D A O, Fisher M A and Adams M J 1994 Bias dependent recovery time of all-optical resonant nonlinearity in an InGaAsP/InGaAsP multiquantum well waveguide *Appl. Phys. Lett.* **65** 2657
[De Araújo2005] De Araújo C B, Falcão-Filho E L, Humeau A, Guichaoua D, Boudebs G and Kassab L R P 2005 Picosecond third-order nonlinearity of lead-oxide glasses in the infrared *Appl. Phys. Lett.* **87** 1
[De Araújo2016] De Araújo C B, Gomes A S L and Boudebs G 2016 Techniques for nonlinear optical characterization of materials: a review *Rep. Prog. Phys.* **79** 036401
[DeAngelis2020] De Angelis C, Leo G and Neshev D N 2020 *Nonlinear Meta-Optics* (Boca Raton, FL: CRC Press)
[DesAutels2008] DesAutels G L, Brewer C, Walker M, Juhl S, Finet M, Ristich S, Whitaker M and Powers P 2008 Femtosecond laser damage threshold and nonlinear characterization in bulk transparent SiC materials *Proc. SPIE* **6875** 68751M
[Debord2019] Debord B, Amrani F, Vincetti L, Gerome F and Benabid F 2019 Hollow-core fiber technology: the rising of 'gas photonics' *Fibers* **7** 16
[Deinert2021] Deinert J-C *et al* 2021 Grating-graphene metamaterial as a platform for terahertz nonlinear photonics *ACS Nano* **15** 1145
[Deka2017] Deka G, Sun C K, Fujita K and Chu S W 2017 Nonlinear plasmonic imaging techniques and their biological applications *Nanophotonics* **6** 31
[Dekorsy2003] Dekorsy T, Yakovlev V A, Seidel W, Helm M and Keilmann F 2003 Infrared-phonon–polariton resonance of the nonlinear susceptibility in GaAs *Phys. Rev. Lett.* **90** 055508
[Del Coso2004] Del Coso R and Solis J 2004 Relation between nonlinear refractive index and third-order susceptibility in absorbing media *J. Opt. Soc. Am.* B **21** 640–4
[Demongodin2019] Demongodin P *et al* 2019 Ultrafast saturable absorption dynamics in hybrid graphene/Si3N4waveguides *APL Photonics* **4** 076102
[Deng2020] Deng J, Tang Y, Chen S, Li K, Zayats A V and Li G 2020 Giant enhancement of second-order nonlinearity of epsilon-near-zero medium by a plasmonic metasurface *Nano Lett.* **20** 5421
[Deroh2020] Deroh M, Beugnot J-C, Hammani K, Finot C, Fatome J, Smektala F, Maillotte H, Sylvestre T and Kibler B 2020 Comparative analysis of stimulated Brillouin scattering at 2 μm in various infrared glass-based optical fibers *J. Opt. Soc. Am.* B **37** 3792
[DeSalvo1992] DeSalvo R J, Hagan D J, Sheik-Bahae M, Stegeman G, Vanherzeele H and Van Stryland E W 1992 Self-focusing and defocusing by cascaded second order effects in KTP *Opt. Lett.* **17** 28–30
[DeSalvo1996] DeSalvo R, Said A A, Hagan D J, Van Stryland E W and Sheik-Bahae M 1996 Infrared to ultraviolet measurements of two-photon absorption and n_2 in wide bandgap solids *IEEE J. Quantum. Electron.* **32** 1324–33
[Dhillon2007] Dhillon S S, Sirtori C, Alton J, Barbieri S, de Rossi A, Beere H E and Ritchie D A 2007 Terahertz transfer onto a telecom optical carrier *Nat. Photon.* **1** 411
[Dietel1983] Dietel W, Fontaine J J and Diels J-C 1983 Intracavity pulse compression with glass: a new method of generating pulses shorter than 60 fsec *Opt. Lett.* **8** 1324
[Dinu2003a] Dinu M 2003 Dispersion of phonon-assisted nonresonant third-order nonlinearities *IEEE J. Quantum. Electron.* **39** 1498
[Dinu2003b] Dinu M, Quochi F and Garcia H 2003 Third-order nonlinearities in silicon at telecom wavelengths *Appl. Phys. Lett.* **82** 2954
[Dmitriev1999] Dmitriev V G, Gurzadyan G G and Nikogosyan D N 1999 *Handbook of Nonlinear Optical Crystals* 3rd edn (Berlin: Springer)
[Dolgaleva2011] Dolgaleva K, Ng W C, Qian L and Aitchison J S 2011 Compact highly-nonlinear AlGaAs waveguides for efficient wavelength conversion *Opt. Express* **19** 12440
[Dolgaleva2015] Dolgaleva K, Sarrafi P, Kultavewuti P, Awan K M, Feher N, Aitchison J S, Qian L, Volatier M, Arès R and Aimez V 2015 Tunable four-wave mixing in AlGaAs nanowires *Opt. Express* **23** 22477
[Dong2013] Dong L 2013 Stimulated thermal Rayleigh scattering in optical fibers *Opt. Express* **21** 2642
[Dong 2016a] Dong N, Li Y, Zhang S, McEvoy N, Zhang X, Cui Y, Zhang L, Duesberg G S and Wang J 2016 Dispersion of nonlinear refractive index in layered WS_2 and WSe_2 semiconductor films induced by two-photon absorption *Opt. Lett.* **41** 3936–9
[Dong2016b] Dong L 2016 Thermal lensing in optical fibers *Opt. Express* **24** 19841
[Dong2018] Dong Y, Chertopalov S, Maleski K, Anasori B, Hu L, Bhattacharya S, Rao A M, Gogotsi Y, Mochalin V N and Podila R 2018 Saturable absorption in 2D Ti_3C_2 Mxene thin films for passive photonic diodes *Adv. Mater.* **30** 1705714
[Donnelly1996] Donnelly J P, Le H Q, Swanson E A, Groves S H, Darwish A and Ippen E P 1996 Nondegenerate four-wave mixing wavelength conversion in low-loss passive InGaAsP-InP quantum-well waveguides *IEEE Photonics Technol. Lett.* **8** 623
[DOttavi1995] D'Ottavi A, Mecozzi A, Scotti S, Cara Romeo F, Martelli F, Spano P, Dall'Ara R, Eckner J and Guekos G 1995 Four-wave mixing efficiency in traveling wave semiconductor optical amplifiers at high saturation *Appl. Phys. Lett.* **67** 2753
[Dragic2014] Dragic P D, Kucera C, Ballato J, Litzkendorf D, Dellith J and Schuster K 2014 Brillouin scattering properties of lanthano–aluminosilicate optical fiber *Appl. Opt.* **53** 5660
[Dragic2018] Dragic P D and Ballato J 2018 A brief review of specialty optical fibers for Brillouin-scattering-based distributed sensors *Appl. Sci.* **8** 1996
[Dremetsika2017] Dremetsika E and Kockaert P 2017 Enhanced optical Kerr effect method for a detailed characterization of the third-order nonlinearity of two-dimensional materials applied to graphene *Phys. Rev.* B **96** 235422
[Dressel and Grüner2002] Dressel M and Grüner G 2002 Electrodynamics of solids *Optical Properties of Electrons in Matter* (Cambridge: Cambridge University Press)
[Driessen1998] Driessen A, Hoekstra J W M, Blom F C, Horst F, Krijnen G J M, van Schoot J B P, Lambeck P V, Popma T J A and Diemeer M B 1998 Evaluation of polymer based third order nonlinear integrated optics devices *Opt. Mater.* **9** 329
[Dubikovskiy2008] Dubikovskiy V, Hagan D J and Van Stryland E W 2008 Large nonlinear refraction in InSb at 10 μm and the effects of Auger recombination *J. Opt. Soc. Am.* B **25** 223
[Duchesne2009] Duchesne D, Ferrera M, Razzari L, Morandotti R, Little B E, Chu S T and Moss D J 2009 Efficient self-phase modulation in low loss, high index doped silica glass integrated waveguides *Opt. Express* **17** 1865
[Duchesne2011] Duchesne D *et al* 2011 Second harmonic generation in AlGaAs photonic wires using low power continuous wave light *Opt. Express* **19** 12408
[Dudley2009] Dudley J M and Taylor J R 2009 Ten years of nonlinear optics in photonic crystal fibre *Nat. Photon.* **3** 85
[Dudley2010] Dudley J and Taylor R 2010 *Supercontinuum Generation in Optical Fibers* (Cambridge: Cambridge University Press)
[Duguay1969] Duguay M A and Hansen J W 1969 An ultrafast light gate *Appl. Phys. Lett.* **15** 192–4
[Efros1982] Efros A and Efros A 1982 Interband absorption of light in a semiconductor sphere *Sov. Phys.-Semiconduct.* **16** 772–5
[Eggleton2012] Eggleton B J, Vo T D, Pant R, Schr J, Pelusi M D, Choi Y D, Madden S J and Luther-Davies B 2012 Photonic chip based ultrafast optical processing based on high nonlinearity dispersion engineered chalcogenide waveguides *Laser Photonics Rev.* **6** 97

[Eggleton2019] Eggleton B J 2019 Nonlinear optics in 2D materials *APL Photonics* **4** 034101
[Ekimov1988] Ekimov A I and Efros A L 1988 Nonlinear optics of semiconductor-doped glasses *Phys. Status Solidi* b **150** 627
[Elsaesser2019] Elsaesser T, Reimann K and Woerner M 2019 *Concepts and Applications of Nonlinear Terahertz Spectroscopy* (San Rafael, CA: Morgan & Claypool Publishers/IOP Concise Physics)
[Elsayed-Ali1987] Elsayed-Ali H E, Norris T B, Pessot M A and Mourou G A 1987 Time-resolved observation of electron-phonon relaxation in copper *Phys. Rev. Lett.* **58** 1212
[Ensley2019] Ensley T R and Bambha N K 2019 Ultrafast nonlinear refraction measurements of infrared transmitting materials in the mid-wave infrared *Opt. Express* **27** 37940
[Espindola1995] Espindola R P, Udo M K and Ho S T 1995 Nearly-degenerate frequency technique for simultaneous measurement of n_2, α_2, and FWM gain coefficient in waveguides *Opt. Commun.* **119** 682
[Espinosa2021a] Espinosa D H G, Awan K M, Odungide M, Harrigan S R, Sanchez D R and Dolgaleva K 2021 Tunable four-wave mixing in AlGaAs waveguides of three different geometries *Opt. Commun.* **479** 126450
[Espinosa2021b] Espinosa D H G, Harrigan S R, Awan K M, Rasekh P and Dolgaleva K 2021 Geometry-dependent two-photon absorption followed by free-carrier absorption in AlGaAs waveguides *J. Opt. Soc. Am.* B **38** 3765
[Essiambre2021] Essiambre R and Tkach R 2021 Capacity trends and limits of optical communication networks *Proc. IEEE* **100** 1035
[Evans2013] Evans C C, Shtyrkova K, Bradley J D B, Reshef O, Ippen E and Mazur E 2013 Spectral broadening in anatase titanium dioxide waveguides at telecommunication and near-visible wavelengths *Opt. Express* **21** 18582
[Evert2012] Evert A, James A, Hawkins T W, Foy P, Stolen R, Dragic P, Dong L, Rice R and Ballato J 2012 Longitudinally-graded optical fibers *Opt. Express* **20** 17393
[Faderl1995] Faderl L, Labeye P, Gidon P and Mottier P 1995 Integration of an electrooptic polymer in an integrated optics circuit on silicon *J. Lightwave Technol.* **13** 2020–6
[Falcão-Filho2004] Falcão-Filho E L, De Araújo C B, Bosco C A C, Acioli L H, Poirier G, Messaddeq Y, Boudebs G and Poulain M 2004 Nonlinear optical properties of tungstate fluorophosphate glasses *J. Appl. Phys.* **96** 2525
[Falconieri1999] Falconieri M and Salvetti G 1999 Simultaneous measurement of pure-optical and thermo-optical nonlinearities induced by high-repetition-rate, femtosecond laser pulses: application to CS *Appl. Phys.* B **69** 133
[Fan2013] Fan K, Hwang H Y, Liu M, Strikwerda A C, Sternbach A, Zhang J, Zhao X, Zhang X, Nelson K A and Averitt R D 2013 Nonlinear terahertz metamaterials via field-enhanced carrier dynamics in GaAs *Phys. Rev. Lett.* **110** 217404
[Fang2015] Fang Y, Xiao Z, Wu X, Zhou F, Yang J, Yang Y and Song Y 2015 Optical nonlinearities and ultrafast all-optical switching of m-plane GaN in the near-infrared *Appl. Phys. Lett.* **106** 251903
[Faraday1857] Faraday M 1857 X. The Bakerian lecture—experimental relations of gold (and other metals) to light *Phil. Trans. R. Soc.* **147** 145–81
[Feaver2013] Feaver R K, Peterson R D and Powers P E 2013 Longwave-IR optical parametric oscillator in orientation-patterned GaAs pumped by a 2 μm Tm,Ho:YLF laser *Opt. Express* **21** 16104
[Fedorov2020] Fedorov V V *et al* 2020 Gallium phosphide nanowires in a free-standing, flexible, and semitransparent membrane for large-scale infrared-to-visible light conversion *ACS Nano* **14** 10624–32
[Fedus2010] Fedus K, Boudebs G, Coulombier Q, Troles J and Zhang X H 2010 Nonlinear characterization of GeS_2-Sb_2S_3-CsI glass system *J. Appl. Phys.* **107** 023108
[Feng2012] Feng J, Akimoto R, Gozu S I, Mozume T, Hasama T and Ishikawa H 2012 Ultrafast all-optical switch with cross-phase modulation by area-selective ion implantation in InGaAs/AlAsSb coupled double quantum wells *Optics Express* **20** B279–87
[Feng2013] Feng J, Akimoto R, Gozu S-I, Mozume T, Hasama T and Ishikawa H 2013 Band edge tailoring of InGaAs/AlAsSb coupled double quantum wells for a monolithically integrated all-optical switch *Opt. Express* **21** 15840
[Ferdinandus2013] Ferdinandus M R, Hu H, Reichert M, Hagan D J and Van Stryland E W 2013 Beam deflection measurement of time and polarization resolved ultrafast nonlinear refraction *Opt. Lett.* **38** 3518–21
[Ferdinandus2017] Ferdinandus M R, Reed J M, Averett K L, Hopkins F K and Urbas A 2017 Analysis of beam deflection measurements in the presence of linear absorption *Opt. Mater. Express* **7** 1598–605
[Ferrera2008] Ferrera M, Razzari L, Duchesne D, Morandotti R, Yang Z, Liscidini M, Sipe J E, Chu S, Little B E and Moss D J 2008 Low-power continuous-wave nonlinear optics in doped silica glass integrated waveguide structures *Nat. Photon.* **2** 737
[Ferrera2009] Ferrera M *et al* 2009 Low power four wave mixing in an integrated, micro-ring resonator with Q = 1.2 million *Opt. Express* **17** 14098
[Feth2008] Feth N *et al* 2008 Second-harmonic generation from complementary split-ring resonators *Opt. Lett.* **33** 1975
[Fiore1997a] Fiore A, Beaulieu Y, Janz S, McCaffrey J P, Wasilewski Z R and Xu D X 1997 Quasiphase matched surface emitting second harmonic generation in periodically reversed asymmetric GaAs/AlGaAs quantum well waveguide *Appl. Phys. Lett.* **70** 2655
[Fiore1997b] Fiore A, Berger V, Rosencher E, Bravetti P, Laurent N and Nagle J 1997 Phase-matched mid-infrared difference frequency generation in GaAs-based waveguides *Appl. Phys. Lett.* **71** 3622
[Fiore1998] Fiore A, Janz S, Delobel L, van der Meer P, Bravetti P, Berger V, Rosencher E and Nagle J 1998 Second-harmonic generation at $\lambda = 1.6$ μm in AlGaAs/Al_2O_3 waveguides using birefringence phase matching *Appl. Phys. Lett.* **72** 2942
[Fishman2011] Fishman D A, Cirloganu C M, Webster S, Padilha L A, Monroe M, Hagan D J and Van Stryland E W 2011 Sensitive mid-infrared detection in wide-bandgap semiconductors using extreme non-degenerate two-photon absorption *Nat. Photon.* **5** 561
[Flom2015] Flom S R, Beadie G, Bayya S S, Shaw B and Auxier J M 2015 Ultrafast Z-scan measurements of nonlinear optical constants of window materials at 772, 1030, and 1550 nm *Appl. Opt.* **54** 123–8
[Florea2006] Florea C, Bashkansky M, Dutton Z, Sanghera J, Pureza P and Aggarwal I D 2006 Stimulated Brillouin scattering in single-mode As_2S_3 and As_2Se_3 chalcogenide fibers *Opt. Express* **14** 12063
[Fonda1963] Fonda L 1963 Bound states embedded in the continuum and the formal theory of scattering *Ann. Phys.* **22** 123
[Fortier2008] Fortier C, Fatome J, Pitois S, Smektala F, Millot G, Troles J, Desevedavy F, Houizot P, Brilland L and Traynor N 2008 Experimental investigation of Brillouin and Raman scattering in a 2SG sulfide glass microstructured chalcogenide fiber *Opt. Express* **16** 9398
[Fortin2011] Fortin V, Bernier M, Carrier J and Vallée R 2011 Fluoride glass Raman fiber laser at 2185 nm *Opt. Lett.* **36** 4152
[Foster2007] Foster M A, Turner A C, Salem R, Lipson M and Gaeta A L 2007 Broad-band continuous-wave parametric wavelength conversion in silicon nanowaveguides *Opt. Express* **15** 12949
[Fox1996] Fox A M 1996 Optoelectronics in quantum well structures *Contemp. Phys.* **37** 111–25
[Fox2001] Fox M 2001 *Optical Properties of Solids* (Oxford: Oxford University Press)
[Franken1961] Franken P A, Hill A E, Peters C W and Weinreich G 1961 Generation of optical harmonics *Phys. Rev. Lett.* **7** 118

[Fraser2015] Fraser S, Zheng X, Qiu L, Li D and Jia B 2015 Enhanced optical nonlinearities of hybrid graphene oxide films functionalized with gold nanoparticles *Appl. Phys. Lett.* **107** 031112
[Friberg1987] Friberg S and Smith P 1987 Nonlinear optical glasses for ultrafast optical switches *IEEE J. Quantum Electron.* **23** 2089–94
[Fryett2018] Fryett T, Zhan A and Majumdar A 2018 Cavity nonlinear optics with layered materials *Nanophotonics* **7** 355
[Fu2018] Fu Q, Xu L, Liang S, Shepherd D P, Richardson D J and Alam S-U 2018 Widely tunable, narrow-linewidth, high-peak-power, picosecond midinfrared optical parametric amplifier *IEEE J. Sel. Top. Quantum Electron.* **24** 1
[Fu2020a] Fu M, Zheng Y, Li G, Hu H, Pu M, Oxenlowe L K, Frandsen L H, Li X and Guan X 2020 High-Q titanium dioxide micro-ring resonators for integrated nonlinear photonics *Opt. Express* **28** 39084
[Fu2020b] Fu Q, Xu L, Liang S, Shardlow P C, Shepherd D P, Alam S-U and Richardson D J 2020 High-average-power picosecond mid-infrared OP-GaAs OPO *Opt. Express* **28** 5741
[Fujimura1999] Fujimura M, Suhara T and Nishihara H 1999 Periodically domain-inverted $LiNbO_3$ for waveguide quasi-phase matched nonlinear optic wavelength conversion devices *Bull. Mater. Sci.* **22** 413
[Fujita2000] Fujita T, Hasegawa T, Haraguchi M, Okamoto T, Fukui M and Nakamura S 2000 Determination of second-order nonlinear optical susceptibility of GaN films on sapphire *Jpn. J. Appl. Phys.* **39** 2610
[Gagarskiĭ2008] Gagarskiĭ S V and Prikhod'ko K V 2008 Measuring the parameters of femtosecond pulses in a wide spectral range on the basis of the multiphoton-absorption effect in a natural diamond crystal *J. Opt. Technol.* **75** 139
[Gai2010] Gai X, Madden S, Choi D-Y, Bulla D and Davies B L 2010 Dispersion engineered $Ge_{11.5}As_{24}Se_{64.5}$ nanowires with a nonlinear parameter of $136W^{-1}m^{-1}$ at 1550nm *Opt. Express* **18** 18866
[Gai2013] Gai X, Yu Y, Kuyken B, Ma P, Madden S J, Van Campenhout J, Verheyen P, Roelkens G, Baets R and Luther-Davies B 2013 Nonlinear absorption and refraction in crystalline silicon in the mid-infrared *Laser Photonics Rev.* **7** 1054
[Gajda2012] Gajda A, Zimmermann L, Jazayerifar M, Winzer G, Tian H, Elschner R, Richter T, Schubert C, Tillack B and Petermann K 2012 Highly efficient CW parametric conversion at 1550 nm in SOI waveguides by reverse biased p-i-n junction *Opt. Express* **20** 13100
[Gallot and Grischkowsky1999] Gallot G and Grischkowsky D 1999 Electro-optic detection of terahertz radiation *J. Opt. Soc. Am.* B **16** 1204
[Ganeev2004] Ganeev R A, Ryasnyansky A I, Baba M, Suzuki M, Ishizawa N, Turu M, Sakakibara S and Kuroda H 2004 Nonlinear refraction in CS_2 *Appl. Phys.* B **78** 433–8
[Ganichev and Prettl2006] Ganichev S D and Prettl W 2006 *Intense Terahertz Excitation of Semiconductors* (Oxford: Oxford University Press)
[Gannaway1978] Gannawa J N and Sheppard C J R 1978 Second-harmonic imaging in the scanning optical microscope *Opt. Quantum Electron.* **10** 435–9
[García de Arquer2021] García de Arquer F P, Talapin D V, Klimov V I, Arakawa Y, Bayer M and Sargent E H 2021 Semiconductor quantum dots: technological progress and future challenges *Science* **373** eaaz8541
[Garcia2000] Garcia H, Johnson A M and Trivedi S 2000 Photorefractive beam-coupling measurement of the nonlinear refractive index of semiconductor films *Phys. Status Solidi* b **220** 47
[Garcia2003] Garcia H, Johnson A M, Oguama F A and Trivedi S 2003 A new approach to the measurement of the nonlinear refractive index of short (25 m) lengths of silica and erbium doped fibers *Opt. Lett.* **28** 1796–8
[Garcia2012] Garcia H and Avanaki K N 2012 Direct and indirect two-photon absorption in Ge within the effective mass approximation *Appl. Phys. Lett.* **100** 131105
[Garmire1998] Garmire E and Kost A 1998 *Nonlinear Optics in Semiconductors I* (New York: Academic)
[Gattass2012] Gattass R R, Brandon Shaw L, Nguyen V Q, Pureza P C, Aggarwal I D and Sanghera J S 2012 All-fiber chalcogenide-based mid-infrared supercontinuum source *Opt. Fiber Technol.* **18** 345
[Cazzanelli2011] Cazzanelli M *et al* 2011 Second-harmonic generation in silicon waveguides strained by silicon nitride *Nat. Mater.* **11** 148
[George2019] George H, Reed J, Ferdinandus M, DeVault C, Lagutchev A, Urbas A, Norris T B, Shalaev V M, Boltasseva A and Kinsey N 2019 Nonlinearities and carrier dynamics in refractory plasmonic TiN thin films *Opt. Mater. Express* **9** 345
[Georges1991] Georges A T and Dixit S N 1991 Dependence of broadband Raman amplification in dispersive media on the pump–Stokes input correlation *J. Opt. Soc. Am.* B **8** 780
[Ghirardini2017] Ghirardini L *et al* 2017 Polarization properties of second-harmonic generation in AlGaAs optical nanoantennas *Opt. Lett.* **42** 559
[Gigli2019a] Gigli C, Marino G, Borne A, Lalanne P and Leo G 2019 All-dielectric nanoresonators for $\chi(2)$ nonlinear optics *Front. Phys.* **7** 1
[Gigli2019b] Gigli C, Marino G, Suffit S, Patriarche G, Beaudoin G, Pantzas K, Sagnes I, Favero I and Leo G 2019 Polarization- and diffraction-controlled second-harmonic generation from semiconductor metasurfaces *J. Opt. Soc. Am.* B **36** E55
[Gili2016] Gili V F *et al* 2016 Monolithic AlGaAs second-harmonic nanoantennas *Opt. Express* **24** 15965
[Giorgianni2016] Giorgianni F *et al* 2016 Strong nonlinear terahertz response induced by Dirac surface states in Bi_2Se_3 topological insulator *Nat. Commun.* **7** 11421
[Girouard2020] Girouard P, Frandsen L H, Galili M and Oxenløwe L K 2020 Record-high continuous-wave nonlinear performance of amorphous silicon waveguides *Conference on Lasers and Electro-Optics* (OSA Technical Digest) p SW3N.5
[Golubev2018] Golubev A A, Khlebtsov B N, Rodriguez R D, Chen Y and Zahn D R T 2018 Plasmonic heating plays a dominant role in the plasmon-induced photocatalytic reduction of 4-nitrobenzenethiol *J. Phys. Chem.* C **122** 5657
[Gomes2007] Gomes A S L, Falcão Filho E L, De Araújo C B, Rativa D, De Araujo R E, Sakaguchi K and Kazansky P G 2007 Third-order nonlinear optical properties of bismuth-borate glasses measured by conventional and thermally managed eclipse Z scan *J. Appl. Phys.* **101** 033115
[Gomes2020] Gomes A S L *et al* 2020 Linear and third-order nonlinear optical properties of self-assembled plasmonic gold metasurfaces *Nanophotonics* **9** 725
[Gonzalez2009] Gonzalez L P, Murray J M, Krishnamurthy S and Guha S 2009 Wavelength dependence of two photon and free carrier absorptions in InP *Opt. Express* **17** 8741
[Gordon1993] Gordon L, Woods G L, Eckardt R C, Route R, Feigelson R S, Fejer M M and Byer R L 1993 Diffusion-bonded stacked GaAs for quasiphase- matched second-harmonic generation of a carbon dioxide laser *Electron. Lett.* **29** 1942
[Grabler1997] Gabler T, Waldhäusl R, Bräuer A, Michelotti F, Hörhold H-H and Bartuch U 1997 Spectral broadening measurements in poly(phenylene vinylene) polymer *Appl. Phys. Lett.* **70** 928
[Grady2013] Grady N K *et al* 2013 Nonlinear high-temperature superconducting terahertz metamaterials *New J. Phys.* **15** 105016
[Grant1996] Grant R S 1996 Effective non-linear coefficients of optical waveguides *Opt. Quantum Electron.* **28** 1161

[Granzow2011] Granzow N, Stark S P, Schmidt M A, Tverjanovich A S, Wondraczek L and Russell P S J 2011 Supercontinuum generation in chalcogenide-silica step-index fibers *Opt. Express* **19** 21003
[Grasyuk1998] Grasyuk A, Kurbasov S V, Losev L L, Lutsenko A P, Kaminski A A and Semenov V B 1998 Determination of the Raman gain coefficient in leucosapphire *Quantum Electron.* **28** 162–6
[Grechko2018] Grechko M, Hasegawa T, D'Angelo F, Ito H, Turchinovich D, Nagata Y and Bonn M 2018 Coupling between intra- and intermolecular motions in liquid water revealed by two-dimensional terahertz-infrared-visible spectroscopy *Nat. Commun.* **9** 885
[Green2016] Green B *et al* 2016 High-field high-repetition-rate sources for the coherent THz control of matter *Sci. Rep.* **6** 22256
[Grillanda2015] Grillanda S and Morichetti F 2015 Light-induced metal-like surface of silicon photonic waveguides *Nat. Commun.* **6** 8182
[Grinblat2017a] Grinblat G, Li Y, Nielsen M P, Oulton R F and Maier S A 2017 Degenerate four-wave mixing in a multiresonant germanium nanodisk *ACS Photonics* **4** 2144
[Grinblat2017b] Grinblat G, Li Y, Nielsen M P, Oulton R F and Maier S A 2017 Efficient third harmonic generation and nonlinear subwavelength imaging at a higher-order anapole mode in a single germanium nanodisk *ACS Nano* **11** 953
[Grinblat2019] Grinblat G, Nielsen M P, Dichtl P, Li Y, Oulton R F and Maier S A 2019 Ultrafast sub–30-fs all-optical switching based on gallium phosphide *Sci. Adv.* **5** 1
[Grischkowsky1990] Grischkowsky D, Keiding S R, van Exter M and Fattinger C 1990 Far-infared time-domain spectroscopy with terahertz beams of dielectrics and semiconductors *J. Opt. Soc. Am.* B **7** 2006
[Gromovyi2017] Gromovyi M, Brault J, Courville A, Rennesson S, Semond F, Feuillet G, Baldi P, Boucaud P, Duboz J-Y and De Micheli M P 2017 Efficient second harmonic generation in low-loss planar GaN waveguides *Opt. Express* **25** 23035
[Gu2005] Gu B, Chen J, Fan Y-X, Ding J and Wang H-T 2005 Theory of Gaussian beam Z scan with simultaneous third- and fifth-order nonlinear refraction based on a Gaussian decomposition method *J. Opt. Soc. Am.* B **22** 2651–9
[Gu2006] Gu B, Fan Y-X, Wang J, Chen J, Ding J, Wang H-T and Guo B 2006 Characterization of saturable absorbers using an open-aperture Gaussian-beam Z scan *Phys. Rev.* A **73** 065803-1–4
[Gu2012] Gu T, Petrone N, McMillan J F, van der Zande A, Yu M, Lo G Q, Kwong D L, Hone J and Wong C W 2012 Regenerative oscillation and four-wave mixing in graphene optoelectronics *Nat. Photon.* **6** 554–9
[Guan2018] Guan X, Hu H, Oxenløwe L K and Frandsen L H 2018 Compact titanium dioxide waveguides with high nonlinearity at telecommunication wavelengths *Opt. Express* **26** 1055
[Guo2017] Guo X, Zou C-L, Schuck C, Jung H, Cheng R and Tang H X 2017 Parametric down-conversion photon-pair source on a nanophotonic chip *Light Sci. Appl.* **6** e16249
[Guo2019] Guo B, Xiao Q-L, Wang S-H and Zhang H 2019 2D layered materials: synthesis, nonlinear optical properties, and device applications *Laser Photonics Rev.* **13** 1800327
[Guo2021] Guo X, Peng Z, Ding P, Li L, Chen X, Wei H, Tong Z and Guo L 2021 Nonlinear optical properties of 6H-SiC and 4H-SiC in an extensive spectral range *Opt. Mater. Express* **11** 4
[Gwo2016] Gwo S, Wang C-Y, Chen H-Y, Lin M-H, Sun L, Li X, Chen W-L, Chang Y-M and Ahn H 2016 Plasmonic metasurfaces for nonlinear optics and quantitative SERS *ACS Photonics* **3** 1371
[Hafez2016] Hafez H A, Chai X, Ibrahim A, Mondal S, Férachou D, Ropagnol X and Ozaki T 2016 Intense terahertz radiation and their applications *J. Opt.* **18** 093004
[Hafez2018] Hafez H A *et al* 2018 Extremely efficient terahertz high-harmonic generation in graphene by hot Dirac fermions *Nature* **561** 507
[Hafez2020] Hafez H A, Kovalev S, Tielrooij K-J, Bonn M, Gensch M and Turchinovich D 2020 Terahertz nonlinear optics of graphene: from saturable absorption to high-harmonics generation *Adv. Opt. Mater.* **8** 1900771
[Hall1985] Hall T J, Jaura R, Connors L M and Foote P D 1985 The photorefractive effect—a review *Prog. Quantum Electron.* **10** 77
[Hamazaki2004] Hamazaki J, Matsui S, Kunugita H, Ema K, Kanazawa H, Tachibana T, Kikuchi A and Kishino K 2004 Ultrafast intersubband relaxation and nonlinear susceptibility at 1.55 μm in GaN/AlN multiple-quantum wells *Appl. Phys. Lett.* **84** 1102–4
[Hamilton1996] Hamilton C J, Marsh J H, Hutchings D C, Aitchison J S, Kennedy G T and Sibbett W 1996 Localized Kerr-type nonlinearities in GaAs/AlGaAs multiple quantum well structures at 1.55 um *Appl. Phys. Lett.* **68** 3078
[Hammani2018] Hammani K, Markey L, Lamy M, Kibler B, Arocas J, Fatome J, Dereux A, Weeber J-C and Finot C 2018 Octave spanning supercontinuum in titanium dioxide waveguides *Appl. Sci.* **8** 543
[Han2009] Han J, Abolghasem P, Bijlani B J and Helmy A S 2009 Continuous-wave sum-frequency generation in AlGaAs Bragg reflection waveguides *Opt. Lett.* **34** 3656
[Han2010] Han J B, Kang D P, Abolghasem P, Bijlani B J and Helmy A S 2010 Pulsed- and continuous-wave difference-frequency generation in AlGaAs Bragg reflection waveguides *J. Opt. Soc. Am.* B **27** 2488
[Hanke2012] Hanke T, Cesar J, Knittel V, Trügler A, Hohenester U, Leitenstorfer A and Bratschitsch R 2012 Tailoring spatiotemporal light confinement in single plasmonic nanoantennas *Nano Lett.* **12** 992
[Hao2002] Hao E C, Schatz G C, Johnson R C and Hupp J T 2002 Hyper-Rayleigh scattering from silver nanoparticles *J. Chem. Phys.* **117** 5963
[Hardy2007] Hardy J and Shamir J 2007 Optics inspired logic architecture *Opt. Express* **15** 150
[Harrington2014] Harrington J A 2014 Single-crystal fiber optics: a review *Proc. SPIE* **8959** 895902
[Hasegawa2017] Hasegawa T, Yamamoto Y and Hirano M 2017 Optimal fiber design for large capacity long haul coherent transmission *Opt. Express* **25** 706
[Hausmann2014] Hausmann B J M, Bulu I, Venkataraman V, Deotare P and Lončar M 2014 Diamond nonlinear photonics *Nat. Photon.* **8** 369
[He2005] He J, Qu Y, Li H, Mi J and Ji W 2005 Three-photon absorption in ZnO and ZnS crystals *Opt. Express* **13** 23
[Hebling2002] Hebling J, Almasi G, Kozma I and Kuhl J 2002 Velocity matching by pulse front tilting for large area THz-pulse generation *Opt. Express* **10** 1161
[Heiligtag 2013] Heiligtag F J and Niederberger M 2013 The fascinating world of nanoparticle research *Mater. Today* **16** 262–71
[Heiman1979] Heiman D, Hellwarth R W and Hamilton D S 1979 Raman scattering and nonlinear refractive index measurements of optical glasses *J. Non-Cryst. Solids* **34** 63–79
[Hellwarth1975] Hellwarth R, Cherlow J and Yang -T-T 1975 Origin and frequency dependence of nonlinear optical susceptibilities of glasses *Phys. Rev.* B **11** 964–7
[Hellwarth1977] Hellwarth R 1977 Third-order optical susceptibilities of liquids and solids *Prog. Quantum Electron.* **5** 1–68

[Heyman1994] Heyman J N, Craig K, Galdrikian B, Sherwin M S, Campman K, Hopkins P F, Fafard S and Gossard A C 1994 Resonant harmonic generation and dynamic screening in a double quantum well *Phys. Rev. Lett.* **72** 2183
[Hill1974] Hill K, Johnson D, Kawasaki B and MacDonald R 1974 CW three-wave mixing in single-mode optical fibers *J. Appl. Phys.* **49** 5098
[Hirori2011] Hirori H, Shinokita K, Shirai M, Tani S, Kadoya Y and Tanaka K 2011 Extraordinary carrier multiplication gated by a picosecond electric field pulse *Nat. Commun.* **2** 594
[Hoffmann and Fülöp2011] Hoffmann M C and Fülöp J A 2011 Intense ultrashort terahertz pulses: generation and applications *J. Phys. D: Appl. Phys.* **44** 083001
[Hoffmann and Turchinovich2010] Hoffmann M C and Turchinovich D 2010 Semiconductor saturable absorbers for ultrafast terahertz signals *Appl. Phys. Lett.* **96** 151110
[Hoffmann2007] Hoffmann M C, Yeh K-L, Hebling J and Nelson K A 2007 Efficient terahertz generation by optical rectification at 1035 nm *Opt. Express* **15** 11706
[Hoffmann2009a] Hoffmann M C, Brandt N C, Hwang H Y, Yeh K-L and Nelson K A 2009 Terahertz Kerr effect *Appl. Phys. Lett.* **95** 231105
[Hoffmann2010] Hoffmann M C, Monozon B S, Livshits D, Rafailov E U and Turchinovich D 2010 Terahertz electro-absorption effect enabling femtosecond all-optical switching in semiconductor quantum dots *Appl. Phys. Lett.* **97** 231108
[Hohenleutner2015] Hohenleutner M, Langer F, Schubert O, Knorr M, Huttner U, Koch S W, Kira M and Huber R 2015 Real-time observation of interfering crystal electrons in high-harmonic generation *Nature* **523** 572
[Hohlfeld2000] Hohlfeld J, Wellershoff S-S, Güdde J, Conrad U, Jähnke V and Matthias E 2000 Electron and lattice dynamics following optical excitation of metals *Chem. Phys.* **251** 237
[Hopkins2015] Hopkins B, Filonov D S, Miroshnichenko A E, Monticone F, Alù A and Kivshar Y S 2015 Interplay of magnetic responses in all-dielectric oligomers to realize magnetic fano resonances *ACS Photonics* **2** 724
[Hosoda1992] Hosoda M, Wada T, Yamamoto T, Kaneko A, Garito A F and Sasabe H 1992 Enhancement of third-order nonlinearities of soluble vanadyl phthalocyanines in doped polymer films *Jpn. J. Appl. Phys.* **31** 1071
[Houver2019] Houver S *et al* 2019 Giant optical nonlinearity interferences in quantum structures *Sci. Adv.* **5** eaaw7554
[Hsu2016] Hsu C W, Zhen B, Stone A D, Joannopoulos J D and Soljačić M 2016 Bound states in the continuum *Nat. Rev. Mater.* **1** 16048
[Hu2018] Hu H *et al* 2018 Single-source chip-based frequency comb enabling extreme parallel data transmission *Nat. Photon.* **12** 469
[Hu2019] Hu D J, Xu Z and Shum P P 2019 Review on photonic crystal fibers with hybrid guiding mechanisms *IEEE Access* **7** 67469
[Huang1999] Huang Y, Sun Z, Ding L and Wang Z 1999 A new polymeric material for optical switching *Appl. Phys.* B **68** 217
[Huang2020] Huang T, Zhao X, Zeng S, Crunteanu A, Shum P P and Yu N 2020 Planar nonlinear metasurface optics and their applications *Rep. Prog. Phys.* **83** 126101
[Huber2001] Huber R, Tauser F, Brodschelm A, Bichler M, Abstreiter G and Leitenstorfer A 2001 How many-particle interactions develop after ultrafast excitation of an electron–hole plasma *Nature* **414** 286
[Hum2007] Hum D S and Fejer M M 2007 Quasi-phasematching *C. R. Physique* **8** 180
[Hurlbut2007] Hurlbut W C, Vodopyanov K L, Kuo P S, Fejer M M and Lee Y S 2007 Multi-photon absorption and nonlinear refraction of GaAs in the mid-infrared *Opt. Lett.* **32** 668
[Husu2012] Husu H, Siikanen R, Mäkitalo J, Lehtolahti J, Laukkanen J, Kuittinen M and Kauranen M 2012 Metamaterials with tailored nonlinear optical response *Nano Lett.* **12** 673
[Hutchings1992] Hutchings D C, Sheik-Bahae M, Hagan D J and Van Stryland E W 1992 Kramers-Kronig relations in nonlinear optics *Opt. Quantum Electron.* **24** 1–30
[Hutchings2010] Hutchings D C, Wagner S J, Holmes B M, Younis U, Helmy A S and Aitchison J S 2010 Type-II quasi phase matching in periodically intermixed semiconductor superlattice waveguides *Opt. Lett.* **35** 1299
[Huttunen2019] Huttunen M J, Reshef O, Stolt T, Dolgaleva K, Boyd R W and Kauranen M 2019 Efficient nonlinear metasurfaces by using multiresonant high-Q plasmonic arrays *J. Opt. Soc. Am.* B **36** E30
[Hwang2013] Hwang H Y, Brandt N C, Farhat H, Hsu A L, Kong J and Nelson K A 2013 Nonlinear THz conductivity dynamics in p-type CVD-grown graphene *J. Phys. Chem.* B **117** 15819
[Hwang2015] Hwang H Y, Fleischer S, Brandt N C, Perkins B G, Liu M, Fan K, Sternbach A, Zhang X, Averitt R D and Nelson K A 2015 A review of non-linear terahertz spectroscopy with ultrashort tabletop-laser pulses *J. Mod. Opt.* **62** 1447
[Iliopoulos2015] Iliopoulos K, Potamianos D, Kakkava E, Aloukos P, Orfanos I and Couris S 2015 Ultrafast third order nonlinearities of organic solvents *Opt. Express* **23** 24171–6
[Imeshev2006] Imeshev G, Fermann M E, Vodopyanov K L, Fejer M M, Yu X, Harris J S, Bliss D and Lynch C 2006 High-power source of THz radiation based on orientation-patterned GaAs pumped by a fiber laser *Opt. Express* **14** 4439
[Ippen1972] Ippen E P and Stolen R H 1972 Stimulated Brillouin scattering in optical fibers *Appl. Phys. Lett.* **21** 539
[Islam1992] Islam M N, Soccolich C E, Slusher R E, Levi A F J, Hobson W S and Young M G 1992 Nonlinear spectroscopy near half-gap in bulk and quantum well GaAs/AlGaAs waveguides *J. Appl. Phys.* **71** 1927
[Jadidi2016] Jadidi M M, König-Otto J C, Winnerl S, Sushkov A B, Drew H D, Murphy T E and Mittendorff M 2016 Nonlinear terahertz absorption of graphene plasmons *Nano Lett.* **16** 2734
[Jain1979] Jain R K and Klein M B 1979 Degenerate four-wave mixing near the band gap of semiconductors *Appl. Phys. Lett.* **35** 454
[Jandieri2018] Jandieri V, Khomeriki R and Ern D 2018 Realization of true all-optical AND logic gate based on nonlinear coupled air-hole type photonic crystal waveguides *Opt. Express* **26** 19845
[Jandieri2021] Jandieri V, Khomeriki R, Onoprishvili T, Erni D, Chotorlishvili L, Werner D H and Berakdar J 2021 Band-gap solitons in nonlinear photonic crystal waveguides and their application for functional all-optical logic gating *Photonics* **8** 250
[Janisch2014] Janisch C, Wang Y, Ma D, Mehta N, Elías A L, Perea-López N, Terrones M, Crespi V and Liu Z 2014 Extraordinary second harmonic generation in tungsten disulfide monolayers *Sci. Rep.* **4** 5530
[Jasim 2019] Jasim K E 2019 Third-order nonlinear optical properties of quantum dots *Standards, Methods and Solutions of Metrology* (London: IntechOpen)
[Jauregui2020] Jauregui C, Stihler C and Limpert J 2020 Transverse mode instability *Adv. Opt. Photonics* **12** 429
[Jepsen2011] Jepsen P U, G C D and Koch M 2011 Terahertz spectroscopy and imaging–modern techniques and applications *Laser Photonics Rev.* **5** 124
[Jiang2010] Jiang Y, Ding Y J and Zotova I B 2010 Power scaling of widely-tunable monochromatic terahertz radiation by stacking high-resistivity GaP plates *Appl. Phys. Lett.* **96** 031101

[Jiang2011] Jiang Y, Li D, Ding Y J and Zotova I B 2011 Terahertz generation based on parametric conversion: from saturation of conversion efficiency to back conversion *Opt. Lett.* **36** 1608
[Jiang2018a] Jiang X, Gross S, Withford M J, Zhang H, Yeom D-I, Rotermund F and Fuerbach A 2018 Low-dimensional nanomaterial saturable absorbers for ultrashort-pulsed waveguide lasers *Opt. Mater. Express* **8** 3055
[Jiang2018b] Jiang T *et al* 2018 Gate-tunable third-order nonlinear optical response of massless Dirac fermions in graphene *Nat. Photon.* **12** 430–6
[Johnson2002] Johnson J C, Yan H, Schaller R D, Petersen P B, Yang P and Saykally R J 2002 Near-field imaging of nonlinear optical mixing in single zinc oxide nanowires *Nano Lett.* **2** 279–83
[Jung1997] Jung I D, Kärtner F X, Matuschek N, Sutter D H, Morier-Genoud F, Shi Z, Scheuer V, Tilsch M, Tschudi T and Keller U 1997 Semiconductor saturable absorber mirrors supporting sub-10-fs pulses *Appl. Phys.* B **65** 137
[Jung2013] Jung H, Xiong C, Fong K Y, Zhang X and Tang H X 2013 Optical frequency comb generation from aluminum nitride microring resonator *Opt. Lett.* **38** 2810
[Jung2016] Jung H and Tang H X 2016 Aluminum nitride as nonlinear optical material for on-chip frequency comb generation and frequency conversion *Nanophotonics* **5** 263
[Junginger2012] Junginger F, Mayer B, Schmidt C, Schubert O, Mährlein S, Leitenstorfer A, Huber R and Pashkin A 2012 Nonperturbative interband response of a bulk InSb semiconductor driven off resonantly by terahertz electromagnetic few-cycle pulses *Phys. Rev. Lett.* **109** 147403
[Kadic2019] Kadic M, Milton G W, Van Hecke M and Wegener M 2019 3D metamaterials *Nat. Rev. Phys.* **1** 198
[Kadlec2004] Kadlec F, Nemec H and Kužel P 2004 Optical two-photon absorption in GaAs measured by optical-pump terahertz-probe spectroscopy *Phys. Rev.* B **70** 125205
[Khan2018] Khan A, Islam S M, Ahmed S, Kumar R R, Habib M R, Huang K, Hu M, Yu X and Yang D 2018 Direct CVD growth of graphene on technologically important dielectric and semiconducting substrates *Adv. Sci.* **5** 1800050
[Kairdolf2013] Kairdolf B A, Smith A M, Stokes T H, Wang M D, Young A N and Nie S 2013 Semiconductor quantum dots for bioimaging and biodiagnostic applications *Annu. Rev. Anal. Chem.* **6** 143–62
[Kaiser1961] Kaiser W and Garrett C G B 1961 Two-Photon Excitation in CaF_2:Eu^{2+} *Phys. Rev. Lett.* **7** 229–31
[Kaminski2019] Kaminski P M *et al* 2019 Characterization and optimization of four-wave-mixing wavelength conversion system *J. Lightwave Technol.* **37** 5636
[Kampfrath2013] Kampfrath T, Tanaka K and Nelson K A 2013 Resonant and nonresonant control over matter and light by intense terahertz transients *Nat. Photon.* **7** 680
[Kanbara1992] Kanbara H, Asobe M, Kubodera K, Kaino T and Kurihara T 1992 All-optical picosecond switch using organic single-mode fiber waveguide *Appl. Phys. Lett.* **61** 2290
[Kang1995] Kang J U, Stegeman G I and Aitchison J S 1995 All-optical multiplexing of femtosecond signals using AlGaAs nonlinear directional coupler *Electron. Lett.* **31** 118
[Kang1996a] Kang I, Smolorz S, Krauss T, Wise F, Aitken B G and Borrelli N F 1996 Time-domain observation of nuclear contributions to the optical nonlinearities of glasses *Phys. Rev.* B **54** 641–4
[Kang1996b] Kang J U, Stegeman G I, Villeneuve A and Aitchison J S 1996 AlGaAs below half-bandgap: a laboratory for spatial soliton physics *Pure Appl. Opt.* **5** 583
[Kang1998] Kang J U, Aitchison J S, Stegeman G I and Akhmediev N 1998 One-dimensional spatial solitons in AlGaAs waveguides *Opt. Quantum Electron.* **30** 649
[Karabchevsky2020] Karabchevsky A, Katiyi A, Ang A S and Hazan A 2020 On-chip integrated nanophotonics and future challenges *Nanophotonics* **9** 3733
[Karvonen2017] Karvonen L *et al* 2017 Rapid visualization of grain boundaries in monolayer MoS_2 by multiphoton microscopy *Nat. Commun.* **8** 15714
[Kato1995a] Kato T, Suetsugu Y and Nishimura M 1995 Estimation of nonlinear refractive index in various silica-based glasses for optical fibers *Opt. Lett.* **20** 2279
[Kato1995b] Kato T, Suetsugu Y, Takagi M, Sasaoka E and Nishimura M 1995 Measurement of the nonlinear refractive index in optical fiber by the cross-phase-modulation method with depolarized pump light *Opt. Lett.* **20** 988
[Kauranen2012] Kauranen M and Zayats A V 2012 Nonlinear plasmonics *Nat. Photon.* **6** 737
[Keck1972a] Keck D B and Tynes A R 1972 Spectral response of low-loss optical waveguides *Appl. Opt.* **11** 1502
[Keck1972b] Keck D B, Schultz P C and Zimar F 1972 Attenuation of multimode glass optical waveguides *Appl. Phys. Lett.* **21** 215
[Keller1996] Keller U, Weingarten K J, Kartner F X, Kopf D, Braun B, Jung I D, Fluck R, Honninger C, Matuschek N and Aus der Au J 1996 Semiconductor saturable absorber mirrors (SESAM's) for femtosecond to nanosecond pulse generation in solid-state lasers *IEEE J. Sel. Top. Quantum Electron.* **2** 435
[Keren-Zur2019] Keren-Zur S, Tal M, Fleischer S, Mittleman D M and Ellenbogen T 2019 Generation of spatiotemporally tailored terahertz wavepackets by nonlinear metasurfaces *Nat. Commun.* **10** 1778
[Khanikaev2013] Khanikaev A B, Hossein Mousavi S, Tse W-K, Kargarian M, MacDonald A H and Shvets G 2013 Photonic topological insulators *Nat. Mater.* **12** 233
[Khurgin2010] Khurgin J B 2010 Slow light in various media: a tutorial *Adv. Opt. Photonics* **2** 287
[Khurgin2013] Khurgin J B, Sun G, Armstrong J A, Bloembergen N, Ducuing J and Pershan P S 2013 Plasmonic enhancement of the third order nonlinear optical phenomena: figures of merit *Opt. Express* **21** 27460
[Khurgin2019] Khurgin J and Kinsey N 2019 Nonlinear epsilon-near-zero materials explained: opinion *Opt. Mater. Express* **9** 2793
[Khurgin2020] Khurgin J B, Clerici M, Bruno V, Caspani L, DeVault C, Kim J and Kinsey N 2020 Adiabatic frequency shifting in epsilon-near-zero materials: the role of group velocity *Optica* **7** 226
[Khurgin2021] Khurgin J B, Clerici M and Kinsey N 2021 Fast and slow nonlinearities in epsilon-near-zero materials *Laser Photonics Rev.* **15** 2000291
[Kiessling2013] Kiessling J, Breunig I, Schunemann P G, Buse K and Vodopyanov K L 2013 High power and spectral purity continuous-wave photonic THz source tunable from 1 to 4.5 THz for nonlinear molecular spectroscopy *New J. Phys.* **15** 105014
[Kim1989] Kim B G, Garmire E, Hummel S G and Dapkus P D 1989 Nonlinear Bragg reflector based on saturable absorption *Appl. Phys. Lett.* **54** 1095
[Kim1994] Kim K S, Stolen R H, Reed W A and Quoi K W 1994 Measurement of the nonlinear index of silica-core and dispersion-shifted fibers *Opt. Lett.* **19** 257
[Kim2008] Kim J H, Chen M K, Yang C E, Lee J, Yin S S, Ruffin P, Edwards E, Brantley C and Luo C 2008 Broadband IR supercontinuum generation using single crystal sapphire fibers *Opt. Express* **16** 4085

[Kinsey2015a] Kinsey N, DeVault C, Kim J, Ferrera M, Shalaev V M and Boltasseva A 2015 Epsilon-near-zero Al-doped ZnO for ultrafast switching at telecom wavelengths *Optica* **2** 616–22
[Kinsey2015b] Kinsey N, Syed A A, Courtwright D, DeVault C, Bonner C E, Gavrilenko V I and Boltasseva A 2015 Effective third-order nonlinearities in metallic refractory titanium nitride thin films *Opt. Mater. Express* **5** 2395
[Kinsey2019] Kinsey N, DeVault C, Boltasseva A and Shalaev V M 2019 Near-zero-index materials for photonics *Nat. Rev. Mater.* **4** 742
[Kip1992] Kip D and Krätzig E 1992 Anisotropic four-wave mixing in planar LiNbO3 optical waveguides *Opt. Lett.* **17** 1563
[Kip1994] Kip D, Bartholomäus T, Garcia P M and Krätzig F 1994 Anisotropic two- and four-wave mixing in planar $LiTaO_3$:Ti:Fe optical waveguides *J. Opt. Soc. Am.* B **11** 1736
[Kip1995] Kip D and Krätzig R 1995 Phase-conjugate waves generated by anisotropic four-wave mixing in $LiNbO_3$ and $LiTaO_3$ optical waveguides *Radiat. Eff. Defects Solids* **136** 123
[Kishida 2000] Kishida H, Matsuzaki H, Okamoto H, Manabe T, Yamashita M, Taguchi Y and Tokura Y 2000 Gigantic optical nonlinearity in one-dimensional Mott-Hubbard insulators *Nature* **405** 929–32
[Kittlaus2016] Kittlaus E A, Shin H and Rakich P T 2016 Large Brillouin amplification in silicon *Nat. Photon.* **10** 463
[Kityk2002] Kityk I V, Wasylak J, Benet S, Dorosz D, Kucharski J, Krasowski J and Sahraoui B 2002 Synthesized rare-earth doped oxide glasses for nonlinear optics *J. Appl. Phys.* **92** 2260
[Kivshar2018] Kivshar Y 2018 All-dielectric meta-optics and non-linear nanophotonics *Natl Sci. Rev.* **5** 144
[Klein2006] Klein M W, Enkrich C, Wegener M and Linden S 2006 Second-harmonic generation from magnetic metamaterials *Science* **313** 502
[Klein2007] Klein M W, Wegener M, Karlsruhe D, Feth N and Linden S 2007 Experiments on second- and third-harmonic generation from magnetic metamaterials *Opt. Express* **15** 5238
[Klein2008] Klein M W, Wegener M, Feth N-A and Linden S 2008 Experiments on second- and third-harmonic generation from magnetic metamaterials: erratum *Opt. Express* **16** 8055
[Knight2003] Knight J C 2003 Photonic crystal fibres *Nature* **424** 847
[Kobayashi2007] Kobayashi Y, Yoshitomi D, Iwata K, Takada H and Torizuka K 2007 Ultrashort pulse characterization by ultra-thin ZnO, GaN, and AlN crystals *Opt. Express* **15** 9748
[Konig1999] König S, Blau W and Giorgetti E 1999 Nonlinear optical behavior of polydiacetylene coated glass waveguides *Int. J. Polym. Mater.* **44** 197
[König-Otto2017] König-Otto J C, Wang Y, Belyanin A, Berger C, De Heer W A, Orlita M, Pashkin A, Schneider H, Helm M and Winnerl S 2017 Four-wave mixing in Landau-quantized graphene *Nano Lett.* **17** 2184
[Koos2009] Koos C *et al* 2009 All-optical high-speed signal processing with silicon–organic hybrid slot waveguides *Nat. Photon.* **3** 216–9
[Koshelev2019a] Koshelev K, Bogdanov A and Kivshar Y 2019 Meta-optics and bound states in the continuum *Sci. Bull.* **64** 836
[Koshelev2019b] Koshelev K, Tang Y, Li K, Choi D-Y, Li G and Kivshar Y 2019 Nonlinear metasurfaces governed by bound states in the continuum *ACS Photonics* **6** 1639
[Koshelev2020] Koshelev K, Kruk S, Melik-Gaykazyan E, Choi J-H, Bogdanov A, Park H-G and Kivshar Y 2020 Subwavelength dielectric resonators for nonlinear nanophotonics *Science* **367** 288
[Kovalev2017] Kovalev S, Green B, Golz T, Maehrlein S, Stojanovic N, Fisher A S, Kampfrath T and Gensch M 2017 Probing ultra-fast processes with high dynamic range at 4th-generation light sources: arrival time and intensity binning at unprecedented repetition rates *Struct. Dyn.* **4** 024301
[Kovalev2020] Kovalev S *et al* 2020 Non-perturbative terahertz high-harmonic generation in the three-dimensional Dirac semimetal Cd_3As_2 *Nat. Commun.* **11** 2451
[Kovalev2021] Kovalev S *et al* 2021 Electrical tunability of terahertz nonlinearity in graphene *Sci. Adv.* **7** eabf9809
[Kozák2012] Kozák M, Trojánek F, Dzurňák B and Malý P 2012 Two- and three-photon absorption in chemical vapor deposition diamond *J. Opt. Soc. Am.* B **29** 1141
[Krasavin2018] Krasavin A V, Ginzburg P and Zayats A V 2018 Free-electron optical nonlinearities in plasmonic nanostructures: a review of the hydrodynamic description *Laser Photonics Rev.* **12** 1700082
[Krasavin2019] Krasavin A V, Gingburg P and Zayats. A V 2019 *Quantum Photonics: Pioneering Advances and Emerging Applications* (Switzerland: springer) Nonlinear nanoplasmonics eds Robert W B, Svetlana G L, Victor N Z pp 264–316
[Kravetsky2000] Kravetsky I V, Tiginyanu I M, Hildebrandt R, Marowsky G, Pavlidis D, Eisenbach A and Hartnagel. H L 2000 Nonlinear optical response of GaN layers on sapphire: the impact of fundamental beam interference *Appl. Phys. Lett.* **76** 810
[Krotkus2010] Krotkus A 2010 Semiconductors for terahertz photonics applications *J. Phys. D: Appl. Phys.* **43** 273001
[Kruckel2015a] Krückel C J, Fülöp A, Klintberg T, Bengtsson J, Andrekson P A and Torres-Company V 2015 Linear and nonlinear characterization of low-stress high-confinement silicon-rich nitride waveguides *Opt. Express* **23** 25827
[Kruckel2015b] Krückel C J, Torres-Company V, Andrekson P A, Spencer D T, Bauters J F, Heck M J R and Bowers J E 2015 Continuous wave-pumped wavelength conversion in low-loss silicon nitride waveguides *Opt. Lett.* **40** 875
[Kuehn2011] Kuehn W, Reimann K, Woerner M, Elsaesser T and Hey R 2011 Two-dimensional terahertz correlation spectra of electronic excitations in semiconductor quantum wells *J. Phys. Chem.* B **115** 5448
[Kuhnelt1998] Kuhnelt M, Leichtner T, Kaiser S, Hahn B, Wagner H P, Eisert D, Bacher G and Forchel A 1998 Quasiphase matched second harmonic generation in ZnSe waveguide structures modulated by focused ion beam implantation *Appl. Phys. Lett.* **73** 584
[Kultavewuti2016] Kultavewuti P, Zhu E Y, Qian L, Pusino V, Sorel M and Aitchison J S 2016 Correlated photon pair generation in AlGaAs nanowaveguides via spontaneous four-wave mixing *Opt. Express* **24** 3365
[Kultavewuti2019] Kultavewuti P, Y Z E, Zing X, Qian L, Pusino V, Sorel M and Aitchison J S 2019 Polarization-entangled photon pair sources based on spontaneous four wave mixing assisted by polarization mode dispersion *Sci. Rep.* **7** 1
[Kumar2013] Kumar N, Najmaei S, Cui Q, Ceballos F, Ajayan P M, Lou J and Zhao H 2013 Second harmonic microscopy of monolayer MoS_2 *Phys. Rev.* B **87** 161403
[Kuo2006] Kuo P S, Vodopyanov K L, Fejer M M, Simanovskii D M, Yu X, Harris J S and Weyburne D 2006 Optical parametric generation of a mid-infrared continuum in orientation-patterned GaAs *Opt. Lett.* **31** 71
[Kuyken2011] Kuyken B, Liu X, Roelkens G, Baets R, Osgood J R M and Green W M J 2011 50 dB parametric on-chip gain in silicon photonic wires *Opt. Lett.* **36** 4401
[Lacava2016] Lacava C, Ettabib M A, Cristiani I, Fedeli J M, Richardson D J and Petropoulos P 2016 Ultra-compact amorphous silicon waveguide for wavelength conversion *IEEE Photonics Technol. Lett.* **28** 410
[Lacava2017] Lacava C, Stankovic S, Khokhar A Z T, Bucio D, Gardes F Y, Reed G T, Richardson D J and Petropoulos P 2017 Si-rich silicon nitride for nonlinear signal processing applications *Sci. Rep.* **7** 22

[Lacroix1986] Lacroix S, Black R J, Veilleux C and Lapierre J 1986 Tapered single-mode fibers: external refractive-index dependence *Appl. Opt.* **25** 2468–9
[Lambin-Lezzi2013] Lambin-Lezzi V, Loranger S, Saad M and Kashyap R 2013 Stimulated Brillouin scattering in SM ZBLAN fiber *J. Non-Cryst. Solids* **359** 65
[Lamont2008] Lamont M R E, Luther-Davies B, Choi D-Y, Madden S and Eggleton B J 2008 Supercontinuum generation in dispersion engineered highly nonlinear ($\gamma = 10$/W/m) As_2S_3 chalcogenide planar waveguide *Opt. Express* **16** 14938
[Lamouroux1983] Lamouroux B F, Orszag A G, Prade B S and Vinet J Y 1983 Continuous laser amplification in a monomode fiber longitudinally pumped by evanescent field coupling *Opt. Lett.* **8** 504–5
[Lamprecht1997] Lamprecht S, Leitner A and Aussenegg F R 1997 Femtosecond decay-time measurement of electron-plasma oscillation in nanolithographically designed silver particles *Appl. Phys.* B **64** 269
[Larciprete2006] Larciprete M C, Centini M, Belardini A, Sciscione L, Bertolotti M, Sibilia C and Potì B 2006 Second harmonic generation in GaN/Al 50Ga 50N films deposited by metal-organic chemical vapor deposition *Appl. Phys. Lett.* **89** 131105
[Latawiec2015] Latawiec P, Venkataraman V, Burek M J, Hausmann B J M, Bulu I and Lončar M 2015 On-chip diamond Raman laser *Optica* **2** 924
[Latawiec2018] Latawiec P, Venkataraman V, Shams-Ansari A, Markham M and Lončar M 2018 Integrated diamond Raman laser pumped in the near-visible *Opt. Lett.* **43** 318
[Lawrence2020] Lawrence M, Barton D R, Dixon J, Song J H, van de Groep J, Brongersma M L and Dionne J A 2020 High quality factor phase gradient metasurfaces *Nat. Nanotechnol.* **15** 956
[Le1990] Le H Q, Bossi D E, Nichols K B and Goodhue W D 1990 Observation of maker fringes and estimation of $\chi(3)$ using picosecond nondegenerate four-wave mixing in AlGaAs waveguides *Appl. Phys. Lett.* **56** 1008
[Le1992] Le H Q and Di Cecca S 1992 Ultrafast, multi-THz-detuning, third-order frequency conversion in semiconductor quantum-well waveguides *IEEE Photonics Technol. Lett.* **4** 878
[Lee1993] Lee K-S, Wung C J, Prasad P N, Kim J-C, Park C K, Lin J-I and Shim H-K 1993 Sol-gel processed conjugated polymers for optical waveguides *Mol. Cryst. Liq. Cryst.* **224** 33
[Lee1998] Lee S G, Sokoloff J P, McGinnis B P and Sasabe H 1998 Polymer waveguide overlays for side-polished fiber devices *Appl. Opt.* **37** 453–62
[Lee2005] Lee J H, Tanemura T, Kikuchi K, Nagashima T, Hasegawa T, Ohara S and Sugimoto N 2005 Experimental comparison of a Kerr nonlinearity figure of merit including the stimulated Brillouin scattering threshold for state-of-the-art nonlinear optical fibers *Opt. Lett.* **30** 1698
[Lee2007] Lee Y W, Urbanek K E, Digonnet M J, Byer R L and Jiang S 2007 Measurement of the stimulated Brillouin scattering gain coefficient of a phosphate fiber *Proc. SPIE* **6469** 64690L
[Lee2010] Lee K C, Sussman B J, Nunn J, Lorenz V O, Reim K, Jaksch D and Prawer S 2010 Comparing phonon dephasing lifetimes in diamond using Transient Coherent Ultrafast Phonon Spectroscopy *Diam. Relat. Mater.* **19** 1289
[Lee2014] Lee J, Tymchenko M, Argyropoulos C, Chen P Y, Lu F, Demmerle F and Belkin M A 2014 Giant nonlinear response from plasmonic metasurfaces coupled to intersubband transitions *Nature* **511** 65
[Lee2015] Lee E *et al* 2015 Active control of all-fibre graphene devices with electrical gating *Nat. Commun.* **6** 6851
[Lee2017] Lee K F, Hensley C J, Schunemann P G and Fermann M E 2017 Midinfrared frequency comb by difference frequency of erbium and thulium fiber lasers in orientation-patterned gallium phosphide *Opt. Express* **25** 17411
[Lee2020] Lee K, Park J, Kang B J, Kim W T, Kim H, Baek S, Ahn K J, Min B and Rotermund F 2020 Electrically controllable terahertz second-harmonic generation in GaAs *Adv. Opt. Mater.* **8** 2000359
[Leitenstorfer2014] Leitenstorfer A, Nelson K A, Reimann K and Tanaka K 2014 Focus on nonlinear terahertz studies *New J. Phys.* **16** 045016
[Levenson1974] Levenson M D 1974 Feasibility of measuring the nonlinear index of refraction by third-order frequency mixing *J. Quantum Electron.* **10** 110–5
[Levy2009] Levy J S, Gondarenko A, Foster M A, Turner-Foster A C, Gaeta A L and Lipson M 2010 CMOS-compatible multiple-wavelength oscillator for on-chip optical interconnects *Nat. Photon.* **4** 37
[Li2001] Li M J and Nolan D A 2001 Optical transmission fiber design evolution *J. Lightwave Technol.* **26** 1079
[Li2015] Li Y, Dong N, Zhang S, Zhang X, Feng Y, Wang K, Zhang L and Wang J 2015 Giant two-photon absorption in monolayer MoS_2: giant two-photon absorption in monolayer MoS_2 *Laser Photonics Rev.* **9** 427–34
[Li2018] Li M, Zhang L, Tong L-M and Dai D-X 2018 Hybrid silicon nonlinear photonics *Photon. Res.* **6** B13–B22
[Li2019] Li X, Liu W, Song Y, Zhang C, Long H, Wang K, Wang B and Lu P 2019 Enhancement of the second harmonic generation from WS_2 monolayers by cooperating with dielectric microspheres *Adv. Opt. Mater.* **7** 1801270
[Li2021] Li Y, Wang X, Davidson R, Little B E and Chu S T 2021 Four-wave mixing in silicon-nanocrystal embedded high-index doped silica micro-ring resonator *J. Semiconduct.* **42** 042302
[Liang2017] Liang J *et al* 2017 Monitoring local strain vector in atomic-layered $MoSe_2$ by second-harmonic generation *Nano Lett.* **17** 7539–43
[Liao2017] Liao Z and Aitchison J S 2017 Precision etching for multi-level AlGaAs waveguides *Opt. Mater. Express* **7** 895
[Liaros2013] Liaros N, Aloukos P, Kolokithas-Ntoukas A, Bakandritsos A, Szabo T, Zboril R and Couris S 2013 Nonlinear optical properties and broadband optical power limiting action of graphene oxide colloids *J. Phys. Chem.* C **117** 6842–50
[Liberal2017] Liberal I and Engheta N 2017 Near-zero refractive index photonics *Nat. Photon.* **11** 149
[Lim1989] Lim E J, Fejer M M, Byer R L and Kozlovsky W J 1989 Blue light generation by frequency doubling in periodically poled lithium niobate channel waveguide *Electron. Lett.* **25** 731
[Lim2010] Lim C G 2010 Characteristics of the ultrafast all-optical cross-phase modulation in InGaAs/AlAs/AlAsSb coupled double-quantum-well optical waveguides *J. Appl. Phys.* **107** 103109
[Lin2007] Lin Q, Zhang J, Piredda G, Boyd R W, Fauchet P M and Agrawal G P 2007 Dispersion of silicon nonlinearities in the near infrared region *Appl. Phys. Lett.* **91** 021111
[Lin2007a] Lin Q, Painter O J and Agrawal G P 2007 Nonlinear optical phenomena in silicon waveguides: modeling and applications *Opt. Express* **15** 16604–44
[Linden2012] Linden S, Niesler F B P, Förstner J, Grynko Y, Meier T and Wegener M 2012 Collective effects in second-harmonic generation from split-ring-resonator arrays *Phys. Rev. Lett.* **109** 15502
[Lis2014] Lis D and Cecchet F 2014 Localized surface plasmon resonances in nanostructures to enhance nonlinear vibrational spectroscopies: towards an astonishing molecular sensitivity *Beilstein J. Nanotechnol.* **5** 2275
[Litchinitser2018] Litchinitser N M 2018 Nonlinear optics in metamaterials *Adv. Phys.* X **3** 702

[Liu2004] Liu A, Rong H, Paniccia M, Cohen O and Hak D 2004 Net optical gain in a low loss silicon-on-insulator waveguide by stimulated Raman scattering *Opt. Express* **12** 4261
[Liu2007] Liu Z, Lin P-T and Wessels B W 2007 Nonlinear photonic crystal waveguide structures based on barium titanite thin films and their optical properties *Appl. Phys. Lett.* **90** 201104
[Liu2010] Liu F, Li Y, Xing Q, Chai L, Hu M, Wang C and Wang C 2010 Three-photon absorption and Kerr nonlinearity in undoped bulk GaP excited by a femtosecond laser at 1040 nm *J. Opt.* **12** 095201
[Liu2011] Liu X, Driscoll J B, Dadap J I, Osgood R M, Assefa S, Vlasov Y A and Green W M J 2011 Self-phase modulation and nonlinear loss in silicon nanophotonic wires near the mid-infrared two-photon absorption edge *Opt. Express* **19** 7778
[Liu2012a] Liu M *et al* 2012 Terahertz-field-induced insulator-to-metal transition in vanadium dioxide metamaterial *Nature* **487** 345
[Liu2012b] Liu X, Kuyken B, Roelkens G, Baets R, Osgood M and Green W M J 2012 Bridging the mid-infrared-to-telecom gap with silicon nanophotonic spectral translation *Nat. Photon.* **6** 667
[Liu2016a] Liu S *et al* 2016 Resonantly enhanced second-harmonic generation using III-V semiconductor all-dielectric metasurfaces *Nano Lett.* **16** 5426
[Liu2016b] Liu X, Pu M, Zhou B, Krückel C J, Fülöp A, Torres-Company V and Bache M 2016 Octave-spanning supercontinuum generation in a silicon-rich nitride waveguide *Opt. Lett.* **41** 2719
[Liu2017] Liu X, Guo Q and Qiu J 2017 Emerging low-dimensional materials for nonlinear optics and ultrafast photonics *Adv. Mater.* **29** 1605886
[Liu2018a] Liu S, Vabishchevich P P, Vaskin A, Reno J L, Keeler G A, Sinclair M B, Staude I and Brener I 2018 An all-dielectric metasurface as a broadband optical frequency mixer *Nat. Commun.* **9** 2507
[Liu2018b] Liu H, Guo C, Vampa G, Zhang J L, Sarmiento T, Xiao M, Bucksbaum P H, Vučković J, Fan S and Reis D A 2018 Enhanced high-harmonic generation from an all-dielectric metasurface *Nat. Phys.* **14** 1006
[Liu2019a] Liu X, Kongsuwan N, Li X, Zhao D, Wu Z, Hess O and Zhang X 2019 Tailoring the third-order nonlinear optical property of a hybrid semiconductor quantum dot metal nanoparticle: from saturable to fano-enhanced absorption *J. Phys. Chem. Lett.* **10** 7594
[Liu2019b] Liu Z, Xu Y, Lin Y, Xiang J, Feng T, Cao Q, Li J, Lan S and Liu J 2019 High-Q quasibound states in the continuum for nonlinear metasurfaces *Phys. Rev. Lett.* **123** 253901
[Liu2020] Liu W, Liu M, Liu X, Wang X, Deng H-X, Lei M, Wei Z and Wei Z 2020 Recent advances of 2D materials in nonlinear photonics and fiber lasers *Adv. Opt. Mater.* **8** 1901631
[Lu2019a] Lu J, Surya J B, Liu X, Xu Y and Tang H X 2019 Octave-spanning supercontinuum generation in nanoscale lithium niobate waveguides *Opt. Lett.* **44** 1492
[Lu2019b] Lu P, Lalam N, Badar M, Liu B, Chorpering B T, Buric M P and Ohodnicki P R 2019 Distributed optical fiber sensing: review and perspective *Appl. Phys. Rev.* **6** 041302
[Lu2021] Lu Y, Zhang Q, Wu Q, Chen Z, Liu X and Xu J 2021 Giant enhancement of THz-frequency optical nonlinearity by phonon polariton in ionic crystals *Nat. Commun.* **12** 3183
[Luk2015] Luk T S, De Ceglia D, Liu S, Keeler G A, Prasankumar R P, Vincenti M A, Scalora M, Sinclair M B and Campione S 2015 Enhanced third harmonic generation from the epsilon-near-zero modes of ultrathin films *Appl. Phys. Lett.* **106** 151103
[Luo2014] Luo L, Chatzakis I, Wang J, Niesler F B P, Wegener M, Koschny T and Soukoulis C M 2014 Broadband terahertz generation from metamaterials *Nat. Commun.* **5** 3055
[Lv2015] Lv R, Robinson J A, Schaak R E, Sun D, Sun Y, Mallouk T E and Terrones M 2015 Transition metal dichalcogenides and beyond: synthesis, properties, and applications of single- and few-layer nanosheets *Acc. Chem. Res.* **48** 56–64
[Ma2016] Ma M and Chen L R 2016 Harnessing mode-selective nonlinear optics for on-chip multi-channel all-optical signal processing *APL Photonics* **1** 086104
[Ma2018] Ma C and Mookherjea S 2018 Simultaneous dual-band entangled photon pair generation using a silicon photonic microring resonator *Quantum Sci. Technol.* **3** 034001
[Maas2008] Maas D J, Rudin B, Bellancourt A-R, Iwaniuk D, Marchese S V, Südmeyer T and Keller U 2008 High precision optical characterization of semiconductor saturable absorber mirrors *Opt. Express* **16** 7571–9
[MacDonald2009] MacDonald K F, Sámson Z L, Stockman M I and Zheludev N I 2009 Ultrafast active plasmonics *Nat. Photon.* **3** 55
[Madden2007] Madden S J, Choi D-Y, Bulla D A, Rode A V, Luther-Davies B, Ta'eed V G, Pelusi M D and Eggleton B J 2007 Long, low loss etched As_2S_3 chalcogenide waveguides for all-optical signal regeneration *Opt. Express* **15** 14414
[Mahmood2014] Mahmood T, Astar W, Cannon B M, Apiratikul P, Porkolab G A, Richardson C J K and Carter G M 2014 Polarization-insensitive wavelength conversion by FWM of 100-GHz-spaced DWDM 4 ± 10 Gb/s RZ-BPSK signals in a birefringent nonlinear AlGaAs waveguide *IEEE J. Quantum. Electron.* **50** 74
[Maier2007] Maier S A 2007 *Plasmonics: Fundamentals and Applications* (Berlin: Springer)
[Mairaj2002] Mairaj A K, Riziotis C, Chardon A M, Smith P G R, Shepherd D P and Hewak D W 2002 Development of channel waveguide lasers in Nd^{3+}-doped chalcogenide (Ga:La:S) glass through photoinduced material modification *Appl. Phys. Lett.* **81** 3708
[Majkić2017] Majkić A, Franke A, Kirste R, Schlesser R, Collazo R, Sitar Z and Zgonik M 2017 Optical nonlinear and electro-optical coefficients in bulk aluminium nitride single crystals *Phys. Status Solidi* b **254** 1700077
[Major2004] Major A, Yoshino F, Nikolakakos I, Aitchison J S and Smith P W E 2004 Dispersion of the nonlinear refractive index of sapphire *Opt. Lett.* **29** 6
[Makarov 2014] Makarov N S *et al* 2014 Two-photon absorption in CdSe colloidal quantum dots compared to organic molecules *ACS Nano* **8** 12572–86
[Maker1964] Maker P D, Savage C M and Terhune R W 1964 Intensity-dependent changes in the refractive index of liquids *Phys. Rev. Lett.* **12** 507
[Makovejs2016] Makovejs S *et al* 2016 Towards superior transmission performance in submarine systems: leveraging ultralow attenuation and large effective area *J. Lightwave Technol.* **34** 114–20
[Malard2013] Malard L M, Alencar T V, Barboza A P M, Mak K F and de Paula A M 2013 Observation of intense second harmonic generation from MoS_2 atomic crystals *Phys. Rev.* B **87** 201401
[Malouin1996] Malouin C, Villeneuve A, Vitrant G and Lessard R A 1996 Degenerate four-wave mixing geometry in thin-film waveguides for nonlinear material characterization *Opt. Lett.* **21** 21
[Malouin1998] Malouin C, Villeneuve A, Vitrant G, Cottin R and Lessard R A 1998 Degenerate four-wave mixing for characterization of thin-film waveguides *J. Opt. Soc. Am.* B **15** 826

[Maradudin2014] Maradudin A A, Sambles J R and Barnes W 2014 *Modern Plasmonics* (Amsterdam: Elsevier)
[Marandi2012] Marandi A, Rudy C W, Plotnichenko V G, Dianov E M, Vodopyanov K L and Byer R L 2012 Mid-infrared supercontinuum generation in tapered chalcogenide fiber for producing octave-spanning frequency comb around 3 μm *Opt. Express* **20** 24218
[Marble2018] Marble C B, Clary J E, Noojin G D, O'connor S P, Nodurft D T, Wharmby A W, Rockwell B A, Scully M O and Yakovlev V V 2018 Z-scan measurements of water from 1150 to 1400 nm *Opt. Lett.* **43** 4196–9
[Marino2019a] Marino G, Gigli C, Rocco D, Lemaître A, Favero I, De Angelis C and Leo G 2019 Zero-order second harmonic generation from AlGaAs-on-insulator metasurfaces *ACS Photonics* **6** 1226
[Marino2019b] Marino G *et al* 2019 Spontaneous photon-pair generation from a dielectric nanoantenna *Optica* **6** 1416
[Markelz1994a] Markelz A G, Asmar N G, Gwinn E G, Sherwin M S, Nguyen C and Kroemer H 1994 Subcubic power dependence of third-harmonic generation for in-plane, far-infrared excitation of lnAs quantum *Semicond. Sci. Technol.* **9** 634
[Markelz1994b] Markelz A G, Gwinn E G, Sherwin M S, Nguyen C and Kroemer H 1994 Giant third-order nonlinear susceptibilities for in-plane far-infrared excitation of single InAs quantum wells *Solid State Electron.* **37** 1243
[Marques1991] Marques M B, Assanto G, Stegeman G I, Möhlmann G R, Erdhuisen E W P and Horsthuis W H G 1991 Large, nonresonant, intensity dependent refractive index of 4-dialkylamino-4'-nitro-diphenyl-polyene side chain polymers in waveguides *Appl. Phys. Lett.* **58** 2613
[Martin2017] Martin A, Sanchez D, Combrié S, de Rossi A and Raineri F 2017 GaInP on oxide nonlinear photonic crystal technology *Opt. Lett.* **42** 599
[Martinez2017] Martinez A, Al Araimi M, Dmitriev A, Lutsyk P, Li S, Mou C, Rozhin A, Sumetsky M and Turitsyn S 2017 Low-loss saturable absorbers based on tapered fibers embedded in carbon nanotube/polymer composites *APL Photonics* **2** 126103
[Matsunaga2013] Matsunaga R, Hamada Y I, Makise K, Uzawa Y, Terai H, Wang Z and Shimano R 2013 Higgs amplitude mode in the BCS superconductors $Nb_{1-x}Ti_xN$ induced by terahertz pulse excitation *Phys. Rev. Lett.* **111** 057002
[Matsusue2011] Matsusue T, Bando H, Fujita S and Takayama Y 2011 Polarization dependence of two-photon absorption coefficient and nonlinear susceptibility tensor in InP *Phys. Status Solidi* c **8** 387
[Mayer and Keilmann 1986a] Mayer A and Keilmann F 1986 Far-infrared nonlinear optics. I. Chi(2) near ionic resonance *Phys. Rev.* B **33** 6954
[Mayer and Keilmann 1986b] Mayer A and Keilmann F 1986 Far-infrared nonlinear optics. II. Chi(3) contributions from the dynamics of free carriers in semiconductors *Phys. Rev.* B **33** 6962
[Mayer2011] Mayer K M and Hafner J H 2011 Localized surface plasmon resonance sensors *Chem. Rev.* **111** 3828
[Mayer2015] Mayer B *et al* 2015 Tunneling breakdown of a strongly correlated insulating state in VO_2 induced by intense multiterahertz excitation *Phys. Rev.* B **91** 235113
[McDonnell2021] McDonnell C, Deng J, Sideris S, Ellenbogen T and Li G 2021 Functional THz emitters based on Pancharatnam-Berry phase nonlinear metasurfaces *Nat. Commun.* **12** 30
[McMorrow1988] McMorrow D, Lotshaw W T and Kenney-Wallace G A 1988 Femtosecond optical kerr studies on the origin of the nonlinear responses in simple liquids *IEEE J. Quantum Electron.* **24** 443–54
[McMorrow1990] McMorrow D and Lotshaw W T 1990 The frequency response of condensed-phase media to femtosecond optical pulses: spectral-filter effects *Chem. Phys. Lett.* **174** 85–94
[McQuillan1970] McQuillan A K, Clements W R L and Stoicheff B P 1970 Stimulated Raman emission in diamond: spectrum, gain, and angular distribution of intensity *Phys. Rev.* A **1** 628–35
[Mei2016] Mei J, Zhong K, Wang M, Liu P, Xu D, Wang Y and Peyghambarian N 2016 High-Repetition-Rate Terahertz Generation in QPM GaAs With a Compact Efficient 2-μm KTP OPO *IEEE Photonics Technol. Lett.* **28** 1501
[Meier2007] Meier J, Mohammed W S, Jugessur A, Qian L, Mojahedi M and Aitchison J S 2007 Group velocity inversion in AlGaAs nanowires *Opt. Express* **15** 12755
[Melentiev2013] Melentiev P N, Afanasiev A E, Kuzin A A, Baturin A S and Balykin V I 2013 Giant optical nonlinearity of a single plasmonic nanostructure *Opt. Express* **21** 13896
[Mesch2016] Mesch M, Metzger B, Hentschel M and Giessen H 2016 Nonlinear plasmonic sensing *Nano Lett.* **16** 3155
[Miao 2015] Miao L, Jiang Y, Lu S, Shi B, Zhao C, Zhang H and Wen S 2015 Broadband ultrafast nonlinear optical response of few-layers graphene: toward the mid-infrared regime *Photon. Res.* **3** 214
[Michaeli2017] Michaeli L, Keren-Zur S, Avayu O, Suchowski H and Ellenbogen T 2017 Nonlinear surface lattice resonance in plasmonic nanoparticle arrays *Phys. Rev. Lett.* **118** 243904
[Mics2015] Mics Z, Tielrooij K-J, Parvez K, Jensen S A, Ivanov I, Feng X, Müllen K, Bonn M and Turchinovich D 2015 Thermodynamic picture of ultrafast charge transport in graphene *Nat. Commun.* **6** 7655
[Midwinter1968] Midwinter J E 1968 Lithium niobate: effects of composition on the refractive indices and optical second-harmonic generation *J. Appl. Phys.* **39** 3033
[Miguez2014] Miguez M L, Barbano E C, Zilio S C and Misoguti L 2014 Accurate measurement of nonlinear ellipse rotation using a phase-sensitive method *Opt. Express* **22** 25530–8
[Miguez2015] Miguez M L, Barbano E C, Coura J A, Zílio S C and Misoguti L 2015 Nonlinear ellipse rotation measurements in optical thick samples *Appl. Phys.* B **120** 653–8
[Miguez2017] Miguez M L, De Souza T G B, Barbano E C, Zilio S C and Misoguti L 2017 Measurement of third-order nonlinearities in selected solvents as a function of the pulse width *Opt. Express* **17** 3553–65
[Milam1976] Milam D and Weber M J 1976 Measurement of nonlinear refractive index coefficients using time resolved interferometry: application to optical materials for high power neodymium lasers *J. Appl. Phys.* **47** 2497–501
[Milam1998] Milam D 1998 Review and assessment of measured values of the nonlinear refractive-index coefficient of fused silica *Appl. Opt.* **37** 546
[Millar1999] Millar P, De La Rue R M, Krauss T F, Aitchison J S, Broderick N G R and Richardson D J 1999 Nonlinear propagation effects in an AlGaAs Bragg grating filter *Opt. Lett.* **24** 685
[Miller1989] Miller D A B, Feuer M D, Chang T Y, Shunk S C, Henry J E, Burrows D J and Chemla D S 1989 Field-effect transistor self-electrooptic effect device: integrated photodiode, quantum well modulator and transistor *IEEE Photonics Technol. Lett.* **1** 62
[Miller2010] Miller D A B 2010 Are optical transistors the logical next step? *Nat. Photon.* **4** 3
[Minovich2015] Minovich A E, Miroshnichenko A E, Bykov A Y, Murzina T V, Neshev D N and Kivshar Y S 2015 Functional and nonlinear optical metasurfaces *Laser Photonics Rev.* **9** 195
[Miró2014] Miró P, Audiffred M and Heine T 2014 An atlas of two-dimensional materials *Chem. Soc. Rev.* **43** 6537–54
[Misawa1995] Misawa K and Kobayashi T 1995 Femtosecond Sagnac interferometer for phase spectroscopy *Opt. Lett.* **20** 1550

[Mizuno2010] Mizuno Y and Nakamura K 2010 Experimental study of Brillouin scattering in perfluorinated polymer optical fiber at telecommunication wavelength *Appl. Phys. Lett.* **97** 021103
[Moille2021] Moille G, Perez E F, Stone J R, Rao A, Lu X, Rahman T S, Chembo Y K and Srinivasan K 2021 Ultra-broadband Kerr microcomb through soliton spectral translation *Nat. Commun.* **12** 7275
[Mollenauer1980] Mollenauer L F, Stolen R H and Gordon J P 1980 Experimental observation of picosecond pulse narrowing and solitons in optical fibers *Phys. Rev. Lett.* **45** 1095
[Møller2015] Møller U, Yu Y, Kubat I, Petersen C R, Gai X, Brilland L and Bang O 2015 Multi-milliwatt mid-infrared supercontinuum generation in a suspended core chalcogenide fiber *Opt. Express* **23** 3282
[Monat2009] Monat C, Corcoran B, Ebnali-Heidari M, Grillet C, Eggleton B J, White T P, O'Faolain L and Krauss T F 2009 Slow light enhancement of nonlinear effects in silicon engineered photonic crystal waveguides *Opt. Express* **17** 2944
[Monat2010] Monat C *et al* 2010 Slow light enhanced nonlinear optics in silicon photonic crystal waveguides *IEEE J. Sel. Top. Quantum Electron.* **16** 344
[Morais2017] Morais N, Roland I, Ravaro M, Hease W, Lemaître A, Gomez C, Wabnitz S, De Rosa M, Favero I and Leo L 2017 Directionally induced quasi-phase matching in homogeneous AlGaAs waveguides *Opt. Lett.* **42** 4287
[Motojima2019] Motojima M, Suzuki T, Shigekawa H, Kainuma Y, An T and Hase M 2019 Giant nonlinear optical effects induced by nitrogen-vacancy centers in diamond crystals *Opt. Express* **27** 32217
[Murata1998] Murata H and Izutsu M 1998 Light-induced index change with a fast response time and nonlinear absorption in the waveguide of a novel organic quinoid dye *J. Opt. Soc. Am.* B **15** 884
[Murray 1993] Murray C B, Norris D J and Bawendi M G 1993 Synthesis and characterization of nearly monodisperse CdE (E = sulfur, selenium, tellurium) semiconductor nanocrystallites *J. Am. Chem. Soc.* **115** 8706–15
[Muto1992] Muto S, Miyagawa K, Ozawa T and Sugiyama S 1992 Hybride-type optical bistability in a thin-film polymer waveguide doped with nonlinear organic dyes *Electron. Commun. Japan* 2 **75** 555
[Myers1997] Myers L E and Bosenberg W R 1997 Periodically poled lithium niobate and quasi-phase-matched optical parametric oscillators *IEEE J. Quantum. Electron.* **33** 1663
[Nahata2003] Nahata A, Linke R A, Ishi T and Ohashi K 2003 Enhanced nonlinear optical conversion from a periodically nanostructured metal film *Opt. Lett.* **28** 423
[Nakatsuhara1998] Nakatsuhara K, Mizumoto T, Munakata R, Kigure Y and Naito Y 1998 All-optical set-reset operation in a distributed feedback GaInAsP waveguide *IEEE Photonics Technol. Lett.* **10** 78
[Nalwa1997] Nalwa H and Miyata S 1997 *Nonlinear Optics of Organic Molecules and Polymers* (London: CRC Press)
[Nappa2006] Nappa J, Russier-Antoine I, Benichou E, Jonin C and Brevet P F 2006 Second harmonic generation from small gold metallic particles: from the dipolar to the quadrupolar response *J. Chem. Phys.* **125** 184712
[Naranjo2007] Naranjo F B, González-Herráez M, Fernández H, Solis J and Monroy E 2007 Third order nonlinear susceptibility of InN at near band-gap wavelengths *Appl. Phys. Lett.* **90** 091903
[Naranjo2009] Naranjo F B, González-Herráez M, Valdueza-Felip S, Fernández H, Solis J, Fernández S and Sánchez-García M A 2009 Non-linear properties of nitride-based nanostructures for optically controlling the speed of light at 1.5 μm *Microelectron. J.* **40** 349
[Neira2015] Neira A D, Olivier N, Nasir M E, Dickson W, Wurtz G A and Zayats A V 2015 Eliminating material constraints for nonlinearity with plasmonic metamaterials *Nat. Commun.* **6** 7757
[Nesterova1996] Nesterova Z V and Alexandrov I V 1996 Nonlinear mode mixing accompanied by effective SRS in capillary liquid-filled fiber *Proc. SPIE* **2853**
[Nevou2006] Nevou L, Tchernycheva M, Julien F, Raybaut M, Godard A, Rosencher E, Guillot F and Monroy E 2006 Intersubband resonant enhancement of second-harmonic generation in GaN/AlN quantum wells *Appl. Phys. Lett.* **89** 151101
[Ngo2014] Ngo C and van de Voorde M H 2014 *Nanotechnology in a nutshell: From simple to complex systems* 1st edn (Paris: Atlantis Press (Zeger Karssen))
[Nielsen2017] Nielsen M P, Shi X, Dichtl P, Maier S A and Oulton R F 2017 Giant nonlinear response at a plasmonic nanofocus drives efficient four-wave mixing *Science* **358** 1179–81
[Nihonyanagi2013] Nihonyanagi S, Mondal J A, Yamaguchi S and Tahara T 2013 Structure and dynamics of interfacial water studied by heterodyne-detected vibrational sum-frequency generation *Annu. Rev. Phys. Chem.* **64** 579
[Niklès1997] Niklès M, Thévenaz L and Robert P A 1997 Brillouin gain spectrum characterization in single-mode optical fibers *J. Lightwave Technol.* **15** 1842–51
[Nikogosyan2005] Nikogosyan D N 2005 *Nonlinear Optical Crystals* (Berlin: Springer)
[Nikolakakos2004] Nikolakakos I P, Major A, Aitchison J S and Smith P W E 2004 Broadband characterization of the nonlinear optical properties of common reference materials *IEEE J. Sel. Top. Quantum Electron.* **10** 5
[Nitiss2022] Nitiss E, Hu J, Stroganov A and Bres C-S 2022 Optically reconfigurable quasi-phase-matching in silicon nitride microresonators *Nat. Photon.* **16** 134–41
[Nizar2021] Nizar S M, Ahamed S R, Priyanka E, Jayasri R and Kesavaraman B 2021 Comparison of different photonic crystal fiber structure: a review *J. Phys.: Conf. Ser.* **1717** 012048
[Noor2020] Noor A, Damodaran A R, Lee I-H, Maier S A, Oh S-H and Ciracì C 2020 Mode-matching enhancement of second-harmonic generation with plasmonic nanopatch antennas *ACS Photonics* **7** 3333
[Normandin1979] Normandin R and Stegeman G I 1979 Nondegenerate four-wave mixing in integrated optics *Opt. Lett.* **4** 58
[Novoselov2004] Novoselov K S, Geim A K, Morozov S V, Jiang D, Zhang Y, Dubonos S V, Grigorieva I V and Firsov A A 2004 Electric field effect in atomically thin carbon films *Science* **306** 666–9
[O'Donnell2019] O'Donnell C F, Chaitanya Kumar S, Schunemann P G and Ebrahim-Zadeh M 2019 Femtosecond optical parametric oscillator continuously tunable across 36–8 μm based on orientation-patterned gallium phosphide *Opt. Lett.* **44** 4570
[Oda2008] Oda H, Inoue K, Yamanaka A, Ikeda N, Sugimoto Y and Asakawa K 2008 Light amplification by stimulated Raman scattering in AlGaAs-based photonic-crystal line-defect waveguides *Appl. Phys. Lett.* **93** 051114
[Ogasawara2000] Ogasawara T, Ashida M, Motoyama N, Eisaki H, Uchida S, Tokura Y, Ghosh H, Shukla A, Mazumdar S and Kuwata-Gonokami M 2000 Ultrafast optical nonlinearity in the quasi-one-dimensional mott insulator Sr_2CuO_3 *Phys. Rev. Lett.* **85** 2204–7
[Ogilvie1972] Ogilvie G J, Esdaile R J and Kidd G P 1972 Transmission loss of tetrachloroethylene-filled liquid-core-fibre light guide *Electron. Lett.* **8** 533–4
[Oguama2005] Oguama F A, Johnson A M and Reed W A 2005 Measurement of the nonlinear coefficient of telecommunication fibers as a function of Er, Al, and Ge doping profiles by using the photorefractive beam-coupling technique *J. Opt. Soc. Am.* B **22** 1600

[Oguama2005a] Oguama F A, Tchouassi A, Johnson A M and Garcia H 2005 Numerical modeling of the induced grating autocorrelation for studying optical fiber nonlinearities in the picosecond regime *Appl. Phys. Lett.* **86** 091101-1–3
[Oguama2005b] Oguama F A, Garcia H and Johnson A M 2005 Simultaneous measurement of the Raman gain coefficient and the nonlinear refractive index of optical fibers: theory and experiment *J. Opt. Soc. Am.* B **22** 426
[Oishi2018a] Oishi M, Shinozaki T, Hara H, Yamamoto K, Matsusue T and Bando H 2018 Measurement of polarization dependence of two-photon absorption coefficient in InP using extended Z-scan technique for thick materials *Jpn. J. Appl. Phys.* **57** 030306
[Oishi2018b] Oishi M, Shinozaki T, Hara H, Yamamoto K, Matsusue T and Bando H 2018 Measurement of third-order nonlinear susceptibility tensor in InP using extended Z-scan technique with elliptical polarization *Jpn. J. Appl. Phys.* **57** 050306
[Okawa1991] Okawa H, Sekiya M, Osawa J, Wada T, Yamada A, Sasabe H and Uryu T 1991 A nonlinear optical waveguide of poly(1,9-decadiyne) *Polym. J.* **23** 147
[Okawachi2020] Okawachi Y, Yu M, Desiatov B, Kim B Y, Hansson T, Loncar M and Gaeta A L 2020 Chip-based self-referencing using integrated lithium niobate waveguides *Optica* **7** 702
[Oliveira2010] Oliveira T R, Fedus K, Manzani D, Falcão-Filho E L, Boudebs G, de Araújo C B and Messaddeq Y 2010 Near-infrared Kerr nonlinearity of $Pb(PO_3)_2$-WO_3 glasses *J. Appl. Phys.* **108** 103523
[Oliveira2014] Oliveira T A, Manzani D, Falcão-Filho E L, Messaddeq Y, Boudebs G, Fedus K and de Araújo C B 2014 Near-infrared nonlinearity of a multicomponent tellurium oxide glass at 800 and 1,064 nm *Appl. Phys.* B **116** 1
[Olshanii1993] Olshanii M, Ovchinnikov Y and Letokhov V S 1993 Laser guiding of atoms in a hollow optical fiber *Opt. Commun.* **98** 77–79
[Olsson1989] Olsson N A 1989 Lightwave systems with optical amplifiers *J. Lightwave Technol.* **7** 1071
[Olszak2010] Olszak P D, Cirloganu C M, Webster S, Padilha L A, Guha S, Gonzalez L P and Van Stryland E W 2010 Spectral and temperature dependence of two-photon and free-carrier absorption in InSb *Phys. Rev.* B **82** 235207
[Ooi2017] Ooi K J A, Ng D K T, Wang T, Chee A K L, Ng S K, Wang Q, Ang L K, Agarwal A M, Kimerling L C and Ta D T H 2017 Pushing the limits of CMOS optical parametric amplifiers with USRN:Si_7N_3 above the two-photon absorption edge *Nat. Commun.* **8** 13878
[Osterhoudt2019] Osterhoudt G B, Diebel L K, Gray M J, Yang X, Stanco J, Huang X and Burch K S 2019 Colossal mid-infrared bulk photovoltaic effect in a type-I Weyl semimetal *Nat. Mater.* **18** 471
[Ostroverkhov2005] Ostroverkhov V, Waychunas G A and Shen Y R 2005 New information on water interfacial structure revealed by phase-sensitive surface spectroscopy *Phys. Rev. Lett.* **94** 046102
[Ota2009] Ota J, Narita W, Ohta I, Matsushita T and Kondo T 2009 Fabrication of periodically-inverted AlGaAs waveguides for quasi-phase-matched wavelength conversion at 1.55 um *Jpn. J. Appl. Phys.* **48** 04C110
[Ottaviano2016] Ottaviano L, Pu M, Semenova E and Yvind K 2016 Low-loss high-confinement waveguides and microring resonators in AlGaAs-on-insulator *Opt. Lett.* **41** 3996
[Owyoung1972] Owyoung A, Hellwarth R W and George N 1972 Intensity-induced changes in optical polarizations in glasses *Phys. Rev.* B **5** 628–33
[Owyoung1973] Owyoung A 1973 Ellipse rotation studies in laser host materials *J. Quantum Electron.* **9** 1164–9
[Ozanam2014] Ozanam C, Savanier M, Lemaître A, Almuneau G, Carras M, Favero I, Ducci S and Leo G 2014 AlGaAs guided-wave second-harmonic generation at 2.23 μm from a quantum cascade laser *Appl. Opt.* **53** 5615
[Padilha2007] Padilha L A, Fu J, Hagan D J, Van Stryland E W, Cesar C L, Barbosa L C, Cruz C H B, Buso D and Martucci A 2007 Frequency degenerate and nondegenerate two-photon absorption spectra of semiconductor quantum dots *Phys. Rev.* B **75** 075325
[Padilha2011] Padilha L A, Nootz G, Olszak P D, Webster S, Hagan D J, Van Stryland E W, Levina L, Sukhovatkin V, Brzozowski L and Sargent E H 2011 Optimization of band structure and quantum-size-effect tuning for two-photon absorption enhancement in quantum dots *Nano Lett.* **11** 1227–31
[Palfrey1985] Palfrey S L and Grischkowsky D 1985 Generation of 16-fsec frequency-tunable pulses by optical pulse compression *Opt. Lett.* **10** 562
[Panoiu2018] Panoiu N C, Sha W E I, Lei D Y and Li G-C 2018 Nonlinear optics in plasmonic nanostructures *J. Opt.* **20** 083001
[Park2011] Park I Y, Kim S, Choi J, Lee D H, Kim Y J, Kling M F, Stockman M I and Kim S W 2011 Plasmonic generation of ultrashort extreme-ultraviolet light pulses *Nat. Photon.* **5** 677
[Park2015] Park K, Lee J, Lee Y T, Choi W, Lee J H and Song Y-W 2015 Black phosphorus saturable absorber for ultrafast mode-locked pulse laser via evanescent field interaction *Ann. Phys.* **527** 770–6
[Passeri2004] Passeri D, Larciprete M C, Belardini A, Paoloni S, Passaseo A, Sibilia C and Michelotti F 2004 Second harmonic generation in AlGaN, GaN and $Al_xGa_{1-x}N$/GaN multiple quantum well structures *Appl. Phys.* B **79** 611–5
[Patankar2018] Patankar S, Wu L, Lu B, Rai M, Tran J D, Morimoto T and Torchinsky D H 2018 Resonance-enhanced optical nonlinearity in the Weyl semimetal TaAs *Phys. Rev.* B **98** 165113
[Patwardhan2021] Patwardhan G N, Ginsberg J S, Chen C Y, Mehdi Jadidi M and Gaeta A L 2021 Nonlinear refractive index of solids in mid-infrared *Opt. Lett.* **46** 1824–7
[Pauzauskie2006] Pauzauskie P J and Yang P 2006 Nanowire photonics *Mater. Today* **9** 36–45
[Payne1972] Payne D N and Gambling W A 1972 New low-loss liquid-core fibre waveguide *Electron. Lett.* **8** 374–6
[Pellemans and Planken1998] Pellemans H P M and Planken P C M 1998 Effect of nonequilibrium LO phonons and hot electrons on far-infrared intraband absorption in n-type GaAs *Phys. Rev.* B **57** R4222
[Pelusi2008] Pelusi M D, Ta'eed V G, Fu L, Magi E, Lamont M R E, Madden S, Choi D-Y, Bulla D A P, Luther-Davies B and Eggleton B J 2008 Applications of highly-nonlinear chalcogenide glass devices tailored for high-speed all-optical signal processing *IEEE J. Sel. Top. Quantum Electron.* **14** 529
[Pelusi2010] Pelusi M D, Luan F, Madden S, Choi D-Y, Bulla D A, Luther-Davies B and Eggleton B J 2010 Wavelength conversion of high-speed phase and intensity modulated signals using a highly nonlinear chalcogenide glass chip *IEEE Photonics Technol. Lett.* **22** 3
[Peschel1999] Peschel U, Morandotti R, Aitchison J S, Eisenberg H S and Silberberg Y 1999 Nonlinearity induced escape from a defect state in waveguide array *Appl. Phys. Lett.* **75** 1348
[Petersen2018] Petersen C R, Prtljaga N, Farries M, Ward J, Napier B, Lloyd G R and Bang O 2018 Mid-infrared multispectral tissue imaging using a chalcogenide fiber supercontinuum source *Opt. Lett.* **43** 999
[Petit2006] Petit L, Carlie N, Villeneuve R, Massera J, Couzi M, Humeau A and Richardson K 2006 Effect of the substitution of S for Se on the structure and non-linear optical properties of the glasses in the system $Ge_{0.18}Ga_{0.05}Sb_{0.07}S_{0.70-x}Se_x$ *J. Non-Cryst. Solids* **352** 5413

[Petit2007] Petit L, Carlie N, Humeau A, Boudebs G, Jain H, Miller A C and Richardson K 2007 Correlation between the nonlinear refractive index and structure of germanium-based chalcogenide glasses *Mater. Res. Bull.* **42** 2107
[Petit2009] Petit L, Carlie N, Chen H, Gaylord S, Massera J, Boudebs G and Richardson K 2009 Compositional dependence of the nonlinear refractive index of new germanium-based chalcogenide glasses *J. Solid State Chem.* **182** 2756
[Planken2001] Planken P C M, Nienhuys H-K, Bakker H J and Wenckebach T 2001 Measurement and calculation of the orientation dependence of terahertz pulse detection in ZnTe *J. Opt. Soc. Am.* B **18** 313
[Polyushkin2011] Polyushkin D K, Hendry E, Stone E K and Barnes W L 2011 THz generation from plasmonic nanoparticle arrays *Nano Lett.* **11** 4718
[Popov1992] Popov V, Shandarov E and Shandarov S 1992 Generation of spatial subharmonic gratings through mode mixing in planar waveguides *J. Opt. Soc. Am.* B **9** 1661
[Porcel2017] Porcel M A G *et al* 2017 Two-octave spanning supercontinuum generation in stoichiometric silicon nitride waveguides pumped at telecom wavelengths *Opt. Express* **25** 1542
[Prasad1987] Prasad P N 1987 Non-linear optical effects in thin organic polymer films *Thin Solid Films* **152** 275
[Prylepa2018] Prylepa A *et al* 2018 Material characterisation with methods of nonlinear optics *J. Phys. D: Appl. Phys.* **51** 043001
[Pu2006] Pu S-C, Yang M-J, Hsu C-C, Lai C-W, Hsieh C-C, Lin S H, Cheng Y-M and Chou P-T 2006 The empirical correlation between size and two-photon absorption cross section of CdSe and CdTe quantum dots *Small* **2** 1308–13
[Pu2010] Pu Y, Grange R, Hsieh C L and Psaltis D 2010 Nonlinear optical properties of core-shell nanocavities for enhanced second-harmonic generation *Phys. Rev. Lett.* **104** 207402
[Pu2016] Pu M, Ottaviano L, Semenova E and Yvind K 2016 Efficient frequency comb generation in AlGaAs-on-insulator *Optica* **3** 823–6
[Pu2018] Pu M, Hu H, Ottaviano L, Semenova E, Vukovic D, Oxenløwe L K and Yvind K 2018 Ultra-efficient and broadband nonlinear algaas-on-insulator chip for low-power optical signal processing *Laser Photonics Rev.* **12** 1800111
[Qu2020] Qu Y *et al* 2020 Enhanced four-wave mixing in silicon nitride waveguides integrated with 2D layered graphene oxide films *Adv. Opt. Mater.* **8** 2001048
[Raab2019] Raab J *et al* 2019 Ultrafast two-dimensional field spectroscopy of terahertz intersubband saturable absorbers *Opt. Express* **27** 2248
[Raab2020] Raab J *et al* 2020 Ultrafast terahertz saturable absorbers using tailored intersubband polaritons *Nat. Commun.* **11** 4290
[Ramelow2019] Ramelow S, Farsi A, Vernon Z, Clemmen S, Ji X, Sipe J E, liscidini M, Lipson M and Gaeta A L 2019 Strong nonlinear coupling in a Si3N4 ring resonator *Phys. Rev. Lett.* **122** 153896
[Ramos1996] Ramos P A and Towe E 1996 Second-harmonic generation of blue light from [112]-oriented III-V antiresonant waveguide heterostructures *Appl. Phys. Lett.* **68** 1754
[Rapaport2003] Rapaport R, Chen G, Mitrofanov O, Gmachl C, Ng H M and Chu S N G 2003 Resonant optical nonlinearities from intersubband transitions in GaN/AlN quantum wells *Appl. Phys. Lett.* **83** 263–5
[Rau2008] Rau I, Kajzar F, Luc J, Sahraoui B and Boudebs G 2008 Comparison of Z-scan and THG derived nonlinear index of refraction in selected organic solvents *J. Opt. Soc. Am.* B **25** 1738–47
[Reichert2014] Reichert M *et al* 2014 Temporal, spectral, and polarization dependence of the nonlinear optical response of carbon disulfide *Optica* **1** 436–45
And see Reichert M *et al* 2014 *Optica* **3** 657–8 (erratum)
[Reimer2014] Reimer C *et al* 2014 Integrated frequency comb source of heralded single photons *Opt. Express* **22** 6535
[Reinisch1983] Reinisch R and Nevière M 1983 Electromagnetic theory of diffraction in nonlinear optics and surface-enhanced nonlinear optical effects *Phys. Rev.* B **28** 1870
[Ren 2016] Ren J, Zheng X, Tian Z, Li D, Wang P and Jia B 2016 Giant third-order nonlinearity from low-loss electrochemical graphene oxide film with a high-power stability *Appl. Phys. Lett.* **109** 221105
[Ren2019] Ren H, Shen L, Runge A F, Hawkins T W, Ballato J, Gibson U and Peacock A C 2019 Low-loss silicon core fibre platform for mid-infrared nonlinear photonics *Light Sci. Appl.* **8** 105
[Renninger2016] Renninger W H, Behunin R O and Rakich P T 2016 Guided-wave Brillouin scattering in air *Optica* **3** 1316–9
[Reshef2019] Reshef O, De Leon I, Alam M Z and Boyd R W 2019 Nonlinear optical effects in epsilon-near-zero media *Nat. Rev. Mater.* **4** 535
[Reshef2019a] Reshef O, Saad-Bin-Alam M, Huttunen M J, Carlow G, Sullivan B T, Ménard J-M, Dolgaleva K and Boyd R W 2019 Multiresonant High–Q Plasmonic Metasurfaces *Nano Lett.* **19** 6429
[Reyna2017] Reyna A S and de Araújo C B 2017 High-order optical nonlinearities in plasmonic nanocomposites—a review *Adv. Opt. Photonics* **9** 720
[Rhee1984] Rhee B K, Bron W E and Kuhl J 1984 Determination of third-order nonlinear susceptibility through measurements in the picosecond time domain *Phys. Rev.* B **30** 7358–61
[Ribeiro-Soares 2015] Ribeiro-Soares J, Janisch C, Liu Z, Elías A L, Dresselhaus M S, Terrones M, Cançado L G and Jorio A 2015 Second Harmonic Generation in WSe_2 *2D Mater.* **2** 045015
[Richardson2010] Richardson D J, Nilsson J and Clarkson A 2010 High power fiber lasers: current status and future perspectives *J. Opt. Soc. Am.* B **27** B63
[Riggs2000] Riggs J E, Walker D B, Carroll D L and Sun Y-P 2000 Optical limiting properties of suspended and solubilized carbon nanotubes *J. Phys. Chem.* B **104** 7071–6
[Robert2016] Robert H M L, Kundrat F, Bermúdez-Ureña E, Rigneault H, Monneret S, Quidant R and Baffou G 2016 Light-assisted solvothermal chemistry using plasmonic nanoparticles *ACS Omega* **1** 2
[Robinson1967] Robinson F N H 1967 Nonlinear optical coefficients *Bell Syst. Tech. J.* **46** 913–56
[Roland2020] Roland I, Ravaro M, Suffit S, Filloux P, Lemaître A, Favero I and Leo G 2020 Second-harmonic generation in suspended AlGaAs waveguides: a comparative study *Micromachines* **11** 229
[Rong2005] Rong H, Liu A, Jones R, Cohen O, Hak D, Nicolaescu R, Fang A and Paniccia M 2005 An all-silicon Raman laser *Nature* **433** 292
[Ros2017] Da Ros F *et al* 2017 Characterization and optimization of a high-efficiency AlGaAs-on-insulator-based wavelength converter for 64- and 256-QAM signals *J. Lightwave Technol.* **35** 3750
[Rosa 2018] Rosa H G, Ho Y W, Verzhbitskiy I, Rodrigues M J F L, Taniguchi T, Watanabe K, Eda G, Pereira V M and Gomes J C V 2018 Characterization of the second- and third-harmonic optical susceptibilities of atomically thin tungsten diselenide *Sci. Rep.* **8** 10035
[Rossi1991] Rossi B, Byrne H J and Blau W 1991 Degenerate four-wave mixing in rhodamine doped epoxy waveguides *Appl. Phys. Lett.* **58** 1712

[Roth2001] Roth T and Laenen R 2001 Absorption of free carriers in diamond determined from the visible to the mid-infrared by femtosecond two-photon absorption spectroscopy *Opt. Commun.* **189** 289
[Russell2014] Russell P S J, Holzer P, Chang W, Abdolvand A and Travers J C 2014 Hollow-core photonic crystal fibres for gas-based nonlinear optics *Nat. Photon.* **8** 278–86
[Rybin2017] Rybin M V, Koshelev K L, Sadrieva Z F, Samusev K B, Bogdanov A A, Limonov M F and Kivshar Y S 2017 High–Q supercavity modes in subwavelength dielectric resonators *Phys. Rev. Lett.* **119** 243901
[Saad-Bin-Alam2021a] Saad-Bin-Alam M *et al* 2021 Ultra-high-Q resonances in plasmonic metasurfaces *Nat. Commun.* **12** 974
[Saad-Bin-Alam2021b] Saad-Bin-Alam M, Baxter J, Awan K M, Kiviniemi A, Mamchur Y, Lesina A C, Tsakmakidis K L, Huttunen M J, Ramunno L and Dolgaleva K 2021 Hyperpolarizability of plasmonic meta-atoms in metasurfaces *Nano Lett.* **21** 51
[Sabella2015] Sabella A, Spence D and Mildren R 2015 Pump-probe measurements of the Raman gain coefficient in crystals using multi-longitudinal-mode beams *IEEE J. Quantum Electron.* **51** 1
[Saeidi2018] Saeidi S, Rasekh P, Awan K M, Tüğen A, Huttunen M J and Dolgaleva K 2018 Demonstration of optical nonlinearity in InGaAsP/InP passive waveguides *Opt. Mater.* **84** 524
[Saha2020] Saha S, Diroll B T, Shank J, Kudyshev Z, Dutta A, Chowdhury S N and Wood M G 2020 Broadband high-speed, and large-amplitude dynamic optical switching with yttrium-doped cadmium oxide *Adv. Funct. Mater.* **30** 1908377
[Sain2019] Sain B, Meier C and Zentgraf T 2019 Nonlinear optics in all-dielectric nanoantennas and metasurfaces: a review *Adv. Photonics* **1** 024002
[Sajadi2015] Sajadi M, Wolf M and Kampfrath T 2015 Terahertz-field-induced optical birefringence in common window and substrate materials *Opt. Express* **23** 28985
[Sajanlal2011] Sajanlal P R, Sreeprasad T S, Samal A K and Pradeep T 2011 Anisotropic nanomaterials: structure, growth, assembly, and functions *Nano Rev.* **2** 5883
[Sanatinia2012] Sanatinia R, Swillo M and Anand S 2012 Surface second-harmonic generation from vertical GaP nanopillars *Nano Lett.* **12** 820–6
[Sanatinia2014] Sanatinia R, Anand S and Swillo M 2014 Modal engineering of second-harmonic generation in single GaP nanopillars *Nano Lett.* **14** 5376–81
[Sanatinia2015] Sanatinia R, Anand S and Swillo M 2015 Experimental quantification of surface optical nonlinearity in GaP nanopillar waveguides *Opt. Express* **23** 756–64
[Sanford2005] Sanford N A, Davydov A V, Tsvetkov D V, Dmitriev A V, Keller S, Mishra U K and Molnar R J 2005 Measurement of second order susceptibilities of GaN and AlGaN *J. Appl. Phys.* **97** 810
[Sanghera2009] Sanghera J S, Shaw B L and Aggarwal I D 2009 Chalcogenide glass-fiber-based Mid-IR sources and applications *IEEE J. Sel. Top. Quantum Electron.* **15** 114
[Santiago-Cruz2021] Santiago-Cruz T, Fedotova A, Sultanov V, Weissflog M A, Arslan D, Younesi M, Pertsch T, Staude I, Setzpfandt F and Chekhova M 2021 Photon pairs from resonant metasurfaces *Nano Lett.* **21** 4423
[Santran2004] Santran S, canioni L, Sarger L, Cardinal T and Fargin E 2004 Precise and absolute measurements of the complex third-order optical susceptibility *J. Opt. Soc. Am.* B **21** 2180–90
[Sarrafi2013] Sarrafi P, Zhu E Y, Dolgaleva K, Holmes B M, Hutchings D C, Aitchison J S and Qian L 2013 Continuous-wave quasi-phase-matched waveguide correlated photon pair source on a III-V chip *Appl. Phys. Lett.* **103** 251115
[Sato2009] Sato H, Abe M, Shoji I, Suda J and Kondo T 2009 Accurate measurements of second-order nonlinear optical coefficients of 6H and 4H silicon carbide *J. Opt. Soc. Am.* B **26** 1892
[Sautter2019] Sautter J D *et al* 2019 Tailoring second-harmonic emission from (111)-GaAs nanoantennas Nano Lett. **19** 3905
[Sauvage2001] Sauvage S, Boucaud P, Brunhes T, Glotin F, Prazeres R, Ortega J-M and Gérard J-M 2001 Second-harmonic generation resonant with s-p transition in InAs/GaAs self-assembled quantum dots *Phys. Rev.* B **63** 113312
[Savanier2011a] Savanier M, Andronico A, Lemaître A, Manquest C, Favero I, Ducci S and Leo G 2011 Nearly-degenerate three-wave mixing at 1.55 μm in oxidized AlGaAs waveguides *Opt. Express* **19** 22582
[Savanier2011b] Savanier M, Andronico A, Lemaître A, Galopin E, Manquest C, Favero I, Ducci S and Leo G 2011 Large second-harmonic generation at 1.55 μm in oxidized AlGaAs waveguides *Opt. Lett.* **36** 2955
[Savanier2013] Savanier M, Ozanam C, Lanco L, Lafosse X, Andronico A, Favero I, Ducci S and Leo G 2013 Near-infrared optical parametric oscillator in a III-V semiconductor waveguide *Appl. Phys. Lett.* **103** 261105
[Savitski2013] Savitski V G, Reilly S and Kemp A J 2013 Steady-state Raman gain in diamond as a function of pump wavelength *IEEE J. Quantum. Electron.* **49** 1
[Säynätjoki2017] Säynätjoki A *et al* 2017 Ultra-strong nonlinear optical processes and trigonal warping in MoS_2 layers *Nat. Commun.* **8** 893
[Sazio2006] Sazio P J *et al* 2006 Microstructured optical fibers as high-pressure microfluidic reactors *Science* **311** 1583
[Scaccabarozzi2006] Scaccabarozzi L, Fejer M M, Huo Y, Fan S, Yu X and Harris J S 2006 Enhanced second-harmonic generation in AlGaAs/AlxOy tightly confining waveguides and resonant cavities *Opt. Lett.* **31** 3626
[Schaar2008] Schaar J E, Vodopyanov K L, Kuo P S, Fejer M M, Yu X, Lin A and Hurlbut W 2008 Terahertz sources based on intracavity parametric down-conversion in quasi-phase-matched gallium arsenide *IEEE J. Sel. Top. Quantum Electron.* **14** 354
[Schaufele1966] Schaufele R F and Weber M J 1966 Raman scattering by lithium niobate *Phys. Rev.* **152** 705
[Schemato2017] Schenato L 2017 A review of distributed fibre optic sensors for geo-hydrological applications *Appl. Sci.* **7** 896
[Schmitt-Rink1989] Schmitt-Rink S, Chemla D S and Miller D A B 1989 Linear and nonlinear optical properties of semiconductor quantum wells *Adv. Phys.* **38** 89
[Schneebeli2013] Schneebeli L, Kieu K, Merzlyak E, Hales J M, DeSimone A, Perry J W, Norwood R A and Peyghambarian N 2013 Measurement of the Raman gain coefficient via inverse Raman scattering *J. Opt. Soc. Am.* B **30** 2930–9
[Schubert2014] Schubert O *et al* 2014 Sub-cycle control of terahertz high-harmonic generation by dynamical Bloch oscillations *Nat. Photon.* **8** 119
[Schuller2007] Schuller J A, Zia R, Taubner T and Brongersma M L 2007 Dielectric metamaterials based on electric and magnetic resonances of silicon carbide particles *Phys. Rev. Lett.* **99** 107401
[Scott2015] Scott R, Achtstein A W, Prudnikau A, Antanovich A, Christodoulou S, Moreels I, Artemyev M and Woggon U 2015 Two photon absorption in II-VI semiconductors: the influence of dimensionality and size *Nano Lett.* **15** 4985–92
[Secondo2020] Secondo R, Khurgin J and Kinsey N 2020 Absorptive loss and band non-parabolicity as a physical origin of large nonlinearity in epsilon-near-zero materials *Opt. Mater. Express* **10** 1545
[Semmlinger2018] Semmlinger M, Tseng M L, Yang J, Zhang M, Zhang C, Tsai W-Y, Tsai D P, Nordlander P and Halas N J 2018 Vacuum ultraviolet light-generating metasurface *Nano Lett.* **18** 5738

[Seo2006] Seo J et al 2006 Third-order optical nonlinearities of singlewall carbon nanotubes for nonlinear transmission limiting application J. Phys.: Conf. Ser. 38 37–40
[Set2004] Set S Y, Yaguchi H, Tanaka Y and Jablonski M 2004 Laser mode locking using a saturable absorber incorporating carbon nanotubes J. Lightwave Technol. 22 51–56
[Shabahang2014] Shabahang S, Tao G, Marquez M P, Hu H, Ensley T R, Delfyett P J and Abouraddy A F 2014 Nonlinear characterization of robust multimaterial chalcogenide nanotapers for infrared supercontinuum generation J. Opt. Soc. Am. B 3 450
[Shalaby and Hauri2015] Shalaby M and Hauri C P 2015 Demonstration of a low-frequency three-dimensional terahertz bullet with extreme brightness Nat. Commun. 6 5976
[Shalaev1998] Shalaev V M and Sarychev A K 1998 Nonlinear optics of random metal-dielectric films Phys. Rev. B 57 13265
[Shalaev2019] Shalaev M I, Walasik W and Litchinitser N M 2019 Optically tunable topological photonic crystal Optica 6 839
[Shaltout2016] Shaltout A M, Clerici M, Kinsey N, Kaipurath R, Kim J, Carnemolla E G and Ferrera M 2016 Doppler-Shift Emulation Using Highly Time-Refracting TCO Layer Conference on Lasers and Electro-Optics p FF2D.6
[Shan2004] Shan , J and Heinz T F 2004 Terahertz Radiation from Semiconductors (Berlin: Springer)
[Sharma2010] Sharma G et al 2010 Time-resolved terahertz spectroscopy of free carrier nonlinear dynamics in semiconductors IEEE Photonics J. 2 578
[Shcherbakov2014] Shcherbakov M R et al 2014 Enhanced third-harmonic generation in silicon nanoparticles driven by magnetic response Nano Lett. 14 6488
[Shcherbakov2017] Shcherbakov M R et al 2017 Ultrafast all-optical tuning of direct-gap semiconductor metasurfaces Nat. Commun. 8 17
[Shcherbakov2019] Shcherbakov M R, Werner K, Fan Z, Talisa N, Chowdhury E and Shvets G 2019 Photon acceleration and tunable broadband harmonics generation in nonlinear time-dependent metasurfaces Nat. Commun. 10 1345
[Sheik-Bahae1989] Sheik-Bahae M, Said A A and Van Stryland E W 1989 High-sensitivity, single-beam n_2 measurements Opt. Lett. 14 955–7
[Sheik-Bahae1990a] Sheik-Bahae M, Hagan D J and Van Stryland E W 1990 Dispersion and band-gap scaling of the electronic kerr effect in solids associated with two-photon absorption Phys. Rev. Lett. 65 96
[Sheik-Bahae1990b] Sheik-Bahae M, Said A A, Wei T-H, Hagan D J and Van Stryland E W 1990 Sensitive measurement of optical nonlinearities using a single beam IEEE J. Quantum. Electron. 26 760–9
[Sheik-Bahae1991] Sheik-Bahae M, Hutchings D C, Hagan D J and Van Stryland E W 1991 Dispersion of bound electronic nonlinear refraction in solids IEEE J. Quantum. Electron. 27 1296
[Sheik-Bahae1997a] Sheik-Bahae M and Ebrahimzadeh M 1997 Measurements of nonlinear refraction in the second-order Chi(2) materials KTiOPO4, KNbO3, β-BaB2O4, and LiB3O5 Opt. Commun. 142 294–8
[Sheik-Bahae1997b] Sheik-Bahae M 1997 Femtosecond Kerr-lens autocorrelation Opt. Lett. 22 6
[Shen1989] Shen Y R 1989 Surface properties probed by second-harmonic and sum-frequency generation Nature 337 519–25
[Shen2002] Shen Y R 2002 The Principles of Nonlinear Optics (Hoboken, NJ: Wiley)
[Shen2020] Shen L, Ren H, Huang M, Wu D and Peacock A C 2020 A review of nonlinear applications in silicon optical fibers from telecom wavelengths into the mid-infrared spectral region Opt. Commun. 463 125437
[Shi2019a] Shi J, Chu H, Li Y, Zhang X, Pan H and Li D 2019 Synthesis and nonlinear optical properties of semiconducting single-walled carbon nanotubes at 1 μm Nanoscale 11 7287–92
[Shi2019b] Shi X, Guo K, Christensen J B, Castaneda M A U, Liu X, Ou H and Rottwitt K 2019 Multichannel photon-pair generation with strong and uniform spectral correlation in a silicon microring resonator Phys. Rev. Appl. 12 034053
[Shi2021] Shi X, Fan W, Lu Y, Hansen A K, Chi M, Yi A, Ou X, Rottwitt K and Ou H 2021 Polarization and sparial mode dependent four-wave mixing in a 4H-silicon carbide microring resonator APL Photonics 6 076106
[Shimano2012] Shimano R, Watanabe S and Matsunaga R 2012 Intense terahertz pulse-induced nonlinear responses in carbon nanotubes J. Infrared Millim. Terahertz Waves 33 861
[Siegman1962] Siegman A E 1962 Nonlinear optical effects: An optical power limiter Appl. Opt. 1 739–44
[Sipe1980] Sipe J E, So V C Y, Fukui M and Stegeman G I 1980 Analysis of second-harmonic generation at metal surfaces Phys. Rev. B 21 4389
[Skauli2002] Skauli T, Vodopyanov K L, Pinguet T J, Schober A, Levi O, Eyres L A and Arisholm G 2002 Measurement of the nonlinear coefficient of orientation-patterned GaAs and demonstration of highly efficient second-harmonic generation Opt. Lett. 27 628
[Smirl1975] Smirl A L 1975 Measurement of Ultrafast Relaxation Times in Semiconductors Using Picosecond Pulses (Tucson, AZ: University of Arizona)
[Smirnova2016] Smirnova D and Kivshar S Y 2016 Multipolar nonlinear nanophotonics Optica 3 1241
[Smith1965] Smith R G, Nassau K and Galvin M F 1965 Efficient continuous optical second-harmonic generation Appl. Phys. Lett. 7 256
[Smith1972] Smith R G 1972 Optical power handling capacity of low loss optical fibers as determined by stimulated Raman and Brillouin scattering Appl. Opt. 11 2489
[Smith1975] Smith W L, Bechtel J H and Bloembergen N 1975 Dielectric-breakdown threshold and nonlinear-refractive-index measurements with picosecond laser pulses Phys. Rev. B 12 706–14
[Smith1999] Smith D D, Yoon Y, Boyd R W, Campbell J K, Baker L A, Crooks R M and George M 1999 Z-scan measurement of the nonlinear absorption of a thin gold film J. Appl. Phys. 86 6200–5
[Smith2011] Smith A and Smith J 2011 Mode instability in high power fiber amplifiers Opt. Express 19 10180
[Smith2018] Smith A V 2018 Crystal Nonlinear Optics 2ndedn (Albequerque: AS-Photonics)
[Smolorz1999] Smolorz S, Wise F and Borrelli N F 1999 Measurement of the nonlinear optical response of optical fiber materials by use of spectrally resolved two-beam coupling Opt. Lett. 24 1103–5
[Smolorz2000] Smolorz S and Wise F 2000 Femtosecond two-beam coupling energy transfer from Raman and electronic nonlinearities J. Opt. Soc. Am. B 17 1636–44
[Smolski2018] Smolski V, Vasilyev S, Moskalev I, Mirov M, Ru Q, Muraviev A and Vodopyanov K 2018 Half-Watt average power femtosecond source spanning 3–8 μm based on subharmonic generation in GaAs Appl. Phys. B 124 101
[Soavi2018] Soavi G et al 2018 Broadband, electrically tunable third-harmonic generation in graphene Nat. Nanotechnol. 13 583–8
[Soileau1983] Soileau M J, Williams W E and Van Stryland E W 1983 Optical power limiter with picosecond response time IEEE J. Quantum. Electron. 19 731–5
[Solís2021] Solís D M and Engheta N 2021 Functional analysis of the polarization response in linear time-varying media: a generalization of the Kramers-Kronig relations Phys. Rev. B 103 144303

[Soon2005] Soon B Y and Haus J W 2005 Third-harmonic generation *Encyclopedia of Modern Optics* ed R D Guenther (Oxford: Elsevier)
[Sorin1984] Sorin W V, Youngquist R C, Cutler C C and Shaw H J 1984 Single-mode-fiber saturable absorber *Opt. Lett.* **9** 315–7
[Sorokin2018] Sorokin E, Marandi A, Schunemann P G, Fejer M M, Byer R L and Sorokina I T 2018 Efficient half-harmonic generation of three-optical-cycle mid-IR frequency comb around 4 μm using OP-GaP *Opt. Express* **26** 9963
[Squier1999] Squier J A and Müller M 1999 Third-harmonic generation imaging of laser-induced breakdown in glass *Appl. Opt.* **38** 5789–94
[Stanton2020] Stanton E J, Chiles J, Nader N, Moody G, Volet N, Chang L, Bowers J E, Nam S W and Mirin R P 2020 Efficient second harmonic generation in nanophotonic GaAs-on-insulator waveguides *Opt. Express* **28** 9521
[Stappaerts1980] Stappaerts E A, Long W H and Komine H 1980 Gain enhancement in Raman amplifiers with broadband pumping *Opt. Lett.* **5** 4–6
[Stassen2019] Stassen E, Kim C, Kong D, Hu H, Galili M, Oxenløwe L K, Yvind K and Pu M 2019 Ultra-low power all-optical wavelength conversion of high-speed data signals in high-confinement AlGaAs-on-insulator microresonators *APL Photonics* **4** 100804
[Stegeman1994] Stegeman G I *et al* 1994 AlGaAs below half bandgap: the silicon of nonlinear optical materials *J. Nonlinear Opt. Phys. Mater.* **3** 347
[Stegeman1996] Stegeman G I, Hagan D J and Torner L 1996 Chi((2)) cascading phenomena and their applications to all-optical signal processing, mode-locking, pulse compression and solitons *Opt. Quantum Electron.* **28** 1691–740
[Stegeman2012] Stegeman G I and Stegeman R A 2012 *Nonlinear Optics: Phenomena, Materials and Devices* (Hoboken, NJ: Wiley)
[Steglich2021] Steglich P *et al* 2021 Silicon-organic hybrid photonics: an overview of recent advances, electro-optical effects and CMOS integration concepts *J. Phys. Photonics* **3** 022009
[Steinberg2018] Steinberg D, Gerosa R M, Pellicer F N, Zapata J D, Domingues S H, Thoroh de Souza E A and Saito L A M 2018 Graphene oxide and reduced graphene oxide as saturable absorbers onto D-shaped fibers for sub 200-fs EDFL mode-locking *Opt. Mater. Express* **8** 144–56
[Stevenson1974] Stevenson J L and Dyott R B 1974 Optical-fibre waveguide with a single-crystal core *Electron. Lett.* **10** 449–50
[Stockman2011] Stockman M I 2011 Nanoplasmonics: past, present, and glimpse into future *Opt. Express* **19** 22029
[Stolen1972] Stolen R H, Ippen E P and Tynes A 1972 Raman oscillation in glass optical waveguide *Appl. Phys. Lett.* **20** 62
[Stolen1974] Stolen R H, Bjorkholm J and Ashkin A 1974 Phase-matched three-wave mixing in silica fiber optical waveguide *Appl. Phys. Lett.* **24** 308
[Stolen1978] Stolen R H and Lin C 1978 Self-phase-modulation in silica optical fibers *Phys. Rev.* A **17** 1448
[Stolen1981] Stolen R H, Bösch M A and Lin C 1981 Phase matching in birefringent fibers *Opt. Lett.* **6** 213–5
[Stolen1992] Stolen R H and Tomlinson W J 1992 Effect of the Raman part of the nonlinear refractive index on propagation of ultrashort optical pulses in fibers *J. Opt. Soc. Am.* B **9** 565–73
[Stolen2008] Stolen R H 2008 The early years of fiber nonlinear optics *J. Lightwave Technol.* **26** 1021
[Stolt2021] Stolt T *et al* 2021 Backward phase-matched second-harmonic generation from stacked metasurfaces *Phys. Rev. Lett.* **126** 33901
[Stone1972] Stone J 1972 Optical transmission in liquid-core quartz fibers *Appl. Phys. Lett.* **20** 239–40
[Street1997a] Street M W, Whitbread N D, Hamilton C J, Vogele B, Stanley C R, Hutchings D C, Marsh J H, Aitchison J S, Kennedy G T and Sibbett W 1997 Modification of the second-order optical nonlinearities in AlGaAs asymmetric multiple quantum well waveguides by quantum well intermixing *Appl. Phys. Lett.* **70** 2804
[Street1997b] Street M W, Whitbread D N, Hutchings D C, Arnold J M, Marsh J H, Aitchison J S, Kennedy G T and Sibbett W 1997 Quantum-well intermixing for the control of second-order nonlinear effects in AlGaAs multiple-quantum-well waveguides *Opt. Lett.* **22** 1600
[Sugita1999] Sugita T, Mizuuchi K, Kitaoka Y and Yamamoto K 1999 31%-efficient blue second-harmonic generation in a periodically poled MgO:$LiNbO_3$ waveguide by frequency doubling of an AlGaAs laser diode *Opt. Lett.* **24** 1590
[Sun1994] Sun C-K, Vallée F, Acioli L H, Ippen E P and Fujimoto J G 1994 Femtosecond-tunable measurement of electron thermalization in gold *Phys. Rev.* B **50** 15337
[Sun2000] Sun C-K, Chu S-W, Tai S-P, Keller S, Mishra U K and DenBaars S P 2000 Scanning second-harmonic/third-harmonic generation microscopy of gallium nitride *Appl. Phys. Lett.* **77** 2331
[Sundaram2018] Sundaram R S 2018 2D materials devices: challenges in device fabrication Device & Materials Engineering Community - Nature (available at: https://engineeringcommunity.nature.com/posts/40483-2d-materials-devices-challenges-in-device-fabrication)
[Sundheimer1993] Sundheimer M L, Bosshard C, Van Stryland E W, Stegeman G I and Bierlein J D 1993 Large nonlinear phase modulation in quasi-phase-matched KTP waveguides as a result of cascaded second-order processes *Opt. Lett.* **18** 1397
[Suresh2021] Suresh S, Reshef O, Alam M Z, Upham J, Karimi M and Boyd R W 2021 Enhanced nonlinear optical responses of layered epsilon-near-zero metamaterials at visible frequencies *ACS Photonics* **8** 125
[Sutherland1996] Sutherland R L 1996 *Handbook of Nonlinear Optics* (New York: Marcel Dekker)
[Sutherland2003] Sutherland R L 2003 *Handbook of nonlinear optics* 2nd edn (Boca Raton, FL: CRC Press)
[Sylvestre2021] Sylvestre T *et al* 2021 Recent advances in supercontinuum generation in specialty optical fibers *J. Opt. Soc. Am.* B **38** F90–F103
[Ta'eed2005] Ta'eed V G, Shokooh-Saremi M, Fu L, Moss D J, Rochette M, Littler I C M and Luther-Davies B 2005 Integrated all-optical pulse regenerator in chalcogenide waveguides *Opt. Lett.* **30** 2900
[Taheri1996] Taheri B, Liu B J, Appling D, Powell R C and Song J J 1996 Intensity scan and two photon absorption and nonlinear refraction of C60in toluene *Appl. Phys. Lett.* **68** 1317
[Tal2020] Tal M, Keren-Zur S and Ellenbogen T 2020 Nonlinear plasmonic metasurface terahertz emitters for compact terahertz spectroscopy systems *ACS Photonics* **7** 3286
[Tani2012] Tani S, Blanchard F and Tanaka K 2012 Ultrafast carrier dynamics in graphene under a high electric field *Phys. Rev. Lett.* **109** 166603
[Teng2020] Teng D, Wang K and Li Z 2020 Graphene-Coated Nanowire Waveguides and Their Applications *Nanomaterials* **10** 229
[Ter-Mikirtychev2014] Ter-Mikirtychev V 2014 *Fundamentals of Fiber Lasers and Fiber Amplifiers* (Berlin: Springer)
[Thakur2019] Thakur S, Semnani B, Safavi-Naeini S and Majedi A H 2019 Experimental characterization of the ultrafast, tunable and broadband optical Kerr nonlinearity in graphene *Sci. Rep.* **9** 10540
[Thoen2000] Thoen E R, Donnelly J P, Groves S H, Hall K L and Ippen E P 2000 Proton bombardment for enhanced four-wave mixing in InGaAsP-InP waveguides *IEEE Photonics Technol. Lett.* **12** 311

[Thompson1976] Thompson D E, McMullen J D and Anderson D B 1976 Second-harmonic generation in GaAs stack of plates using high-power CO_2 laser radiation *Appl. Phys. Lett.* **29** 113
[Tiedje2007] Tiedje H F, Haugen H K and Preston J S 2007 Measurement of nonlinear absorption coefficients in GaAs, InP and Si by an optical pump THz probe technique *Opt. Commun.* **274** 187
[Tien2010] Tien M C, Bauters J F, Heck M J R, Blumenthal D J and Bowers J E 2010 Ultra-low loss Si_3N_4 waveguides with low nonlinearity and high power handling capability *Opt. Express* **18** 23562
[Timofeeva 2016] Timofeeva M, Bouravleuv A, Cirlin G, Shtrom I, Soshnikov I, Reig Escalé M, Sergeyev A and Grange R 2016 Polar second-harmonic imaging to resolve pure and mixed crystal phases along GaAs nanowires *Nano Lett.* **16** 6290–7
[Tishchenko2022] Tishchenko A, Geernaert T, Vermeulen N, Berghmans F and Baghdasaryan T 2022 Simultaneous modal phase and group velocity matching in microstructured optical fibers for second harmonic generation with ultrashort pulses *Opt. Express* **30** 1206
[Tokunaga1995] Tokunaga E, Terasaki A and Kobayashi T 1995 Femtosecond phase spectroscopy by use of frequency-domain interference *J. Opt. Soc. Am.* B **12** 753
[Tollefson2021] Tollefson J 2021 US achieves laser-fusion record: what it means for nuclear-weapons research *Nature* **597** 163
[Tonouchi2007] Tonouchi M 2007 Cutting-edge terahertz technology *Nat. Photon.* **1** 97
[Torruellas1995] Torruellas W E, Wang Z, Hagan D J, Van Stryland E W, Stegeman G I, Torner L and Menyuk C 1995 Observation of two-dimensional spatial solitary waves in a quadratic medium *Phys. Rev. Lett.* **74** 5036–9
[Toruellas1991] Toruellas W E, Weller-Brophy L A, Zanoni R, Stegeman G I, Osborne Z and Zelinski B J J 1991 Third-harmonic generation measurement of nonlinearities in SiO2-TiO_2 sol-gel films *Appl. Phys. Lett.* **58** 1128
[Trojánek2010] Trojánek F, Žídek K, Dzurňák B, Kozák M and Malý P 2010 Nonlinear optical properties of nanocrystalline diamond *Opt. Express* **18** 1349
[Tsai2009] Tsai T R, Wu T H, Liao J C, Wei T H, Chiang H P, Hwang J S and Chen Y F 2009 Characterization of nonlinear absorption of InN epitaxial films with femtosecond pulsed transmission Z-scan measurements *J. Appl. Phys.* **105** 066101
[Tsang1991] Tsang H K, penty R V, White I H, Grant R S, Sibbett W, Soole J B D, LeBlanc H P, Andreadakis N C, Bhat R and Koza M A 1991 Two-photon absorption and self-phase modulation in InGaAsP/InP multi-quantum-well waveguides *J. Appl. Phys.* **70** 3992
[Tsang2002] Tsang H K, Wong C S, Liang T K, Day I E, Roberts S W, Harpin A, Drake J and Asghari M 2002 Optical dispersion, two-photon absorption and self-phase modulation in silicon waveguides at 1.5 μm wavelength *Appl. Phys. Lett.* **80** 416
[Tsuchida2007] Tsuchida H, Simoyama T, Ishikawa H, Mozume T, Nagase M and Kasai J-I 2007 Cross-phase-modulation-based wavelength conversion using intersubband transition in InGaAs/AlAs/AlAsSb coupled quantum wells *Opt. Lett.* **32** 751
[Tuggle2017] Tuggle M A, Kucera C, Hawkins T W, Sligh D, Runge A F, Peacock A C, Dragic P D and Ballato J 2017 Highly nonlinear yttrium-aluminosilicate optical fiber with a high intrinsic stimulated Brillouin scattering threshold *Opt. Lett.* **42** 4849
[Tuniz2008] Tuniz A, Brawley G, Moss D J and Eggleton B J 2008 Two-photon absorption effects on Raman gain in single mode As_2Se_3 chalcogenide glass fiber *Opt. Express* **16** 18524
[Tuniz2021] Tuniz A 2021 Nanoscale nonlinear plasmonics in photonic waveguides and circuits *Riv. Nuovo Cim.* **44** 193–249
[Tuovinen2002] Tuovinen H, Kauranen M, Jefimovs K, Vahimaa P, Vallius T, Turunen J, Tkachenko N V and Lemmetyinen H 2002 Linear and second-order nonlinear optical properties of arrays of noncentrosymmetric gold nanoparticles *J. Nonlinear Opt. Phys. Mater.* **11** 421
[Turchinovich2012] Turchinovich D, Hvam J M and Hoffmann M C 2012 Self-phase modulation of a single-cycle terahertz pulse by nonlinear free-carrier response in a semiconductor *Phys. Rev.* B **85** 201304
[Turner-Foster2010] Turner-Foster A C, Foster M A, Salem R, Gaeta A L and Lipson M 2010 Frequency conversion over two-thirds of an octave in silicon nanowaveguides *Opt. Express* **18** 1904
[Ulbricht2011] Ulbricht R, Hendry E, Shan J, Heinz T and Bonn M 2011 Carrier dynamics in semiconductors studied with time-resolved terahertz spectroscopy *Rev. Mod. Phys.* **83** 543
[Urquhart2011] Urquhart P 2011 *Advances in Optical Amplifiers* (Rijeka: InTech)
[Vabishchevich2018] Vabishchevich P P, Liu S, Sinclair M B, Keeler G A, Peake G M and Brener I 2018 Enhanced second-harmonic generation using broken symmetry III-V semiconductor fano metasurfaces *ACS Photonics* **5** 1685
[Valdueza-Felip2008] Valdueza-Felip S, Naranjo F B, Gonzalez-Herraez M, Fernandez H, Solis J, Guillot F, Monroy E, Nevou L, Tchernycheva M and Julien F H 2008 Characterization of the resonant third-order nonlinear susceptibility of Si-doped GaN–AlN quantum wells and quantum dots at 1.5 μm *Integrated Photonics and Nanophotonics Research and Applications* (Optica Publishing Group) p ITuB7
[Valdueza-Felip2012] Valdueza-Felip S, Monteagudo-Lerma L, Mangeney J, Gonzalez-Herraez M, Julien F H and Naranjo F B 2012 Nonlinear absorption at optical telecommunication wavelengths of InN films deposited by RF sputtering *IEEE Photonics Technol. Lett.* **24** 1998
[Van Dantzig and Planken1999] Van Dantzig N A and Planken P C M 1999 Time-resolved far-infrared reflectance of n-type GaAs *Phys. Rev.* B **59** 1586
[van Dijk2007] van Dijk M A, Lippitz M, Stolwijk D and Orrit M 2007 A common-path interferometer for time-resolved and shot-noise-limited detection of single nanoparticles *Opt. Express* **15** 2273
[Van Stryland1985] Van Stryland E, Woodall M A, Vanherzeele H and Soileau M J 1985 Energy band-gap dependence of two-photon absorption *Opt. Lett.* **10** 490–2
[Van Stryland1994] Van Stryland E and Chase L 1994 Two photon absorption: inorganic materials *Handbook of Laser Science and Technology* ed M Weber (Boca Raton, FL: CRC Press) pp 299–328 (supplement 2, section 8)
[Van Stryland2009a] Van Stryland E and Hagan D 2009 Measuring nonlinear refraction and its dispersion via propagation *Self-focusing: Past and Present (Springer Topics of Applied Physics Series* vol 114) ed R Boyd, S Lukishova and R Shen (New York: Springer) pp 573–91
[Van Stryland2009b] Van Stryland E, Hagan D, Webster S and Padilha L 2009 Nonlinear spectroscopy: absorption and refraction *Proc. SPIE* **7504** 750415
[Vance1998] Vance F W, Lemon B I and Hupp J T 1998 Enormous hyper-Rayleigh scattering from nanocrystalline gold particle suspensions *J. Phys. Chem.* B **102** 10091
[VanDerZiel1974] Van der Ziel J P, Miller R C, Logan R A, Nordland W A and Mikulyak R M 1974 Phase-matched second-harmonic generation in GaAs optical waveguides by focused laser beams *Appl. Phys. Lett.* **25** 238
[VanDerZiel1976] Van der Ziel J P, Ilegems M, Foy P W and Mikulyak R M 1976 Phase-matched second harmonic generation in a periodic GaAs waveguide *Appl. Phys. Lett.* **29** 775

[VanLaer2015] Van Laer R, Kuyken B, Van Thourhout D and Baets R 2015 Interaction between light and highly confined hypersound in a silicon photonic nanowire *Nat. Photon.* **9** 199
[Vermeulen2016a] Vermeulen N, Castelló-Lurbe D, Cheng J L, Pasternak I, Krajewska A, Ciuk T, Strupinski W, Thienpont H and Van Erps J 2016 Negative Kerr nonlinearity of graphene as seen via chirped-pulse-pumped self-phase modulation *Phys. Rev. Appl.* **6** 044006
[Vermeulen2016b] Vermeulen N, Cheng J L, Sipe J E and Thienpont H 2016 Opportunities for wideband wavelength conversion in foundry-compatible silicon waveguides covered with graphene *IEEE J. Sel. Top. Quantum Electron.* **22** 8100113
[Vermeulen2018] Vermeulen N, Castelló-Lurbe D, Khoder M, Pasternak I, Krajewska A, Ciuk T, Strupinski W, Cheng J L, Thienpont H and Van Erps J 2018 Graphene's nonlinear-optical physics revealed through exponentially growing self-phase modulation *Nat. Commun.* **9** 2675
[Vermeulen2022] Vermeulen N 2022 Perspectives on nonlinear optics of graphene: opportunities and challenges *APL Photonics* **7** 020901
[Vieweg2010] Vieweg M, Gissibl T, Pricking S, Kuhlmey B T, Wu D C, Eggleton B J and Giessen H 2010 Ultrafast nonlinear optofluidics in selectively liquid-filled photonic crystal fibers *Opt. Express* **18** 25232–40
[Vignaud2004] Vignaud D, Lampin J F and Mollot F 2004 Two-photon absorption in InP substrates in the 1.55 μm range *Appl. Phys. Lett.* **85** 239
[Villeneuve1995a] Villeneuve A, Mamyshev P, Kang J U, Stegeman G I, Aitchison J S and Ironside C N 1995 Time-domain all-optical demultiplexing with a semiconductor directional coupler *Appl. Phys. Lett.* **66** 1668
[Villeneuve1995b] Villeneuve A, Kang J U, Aitchison J S and Stegeman G I 1995 Unity ratio of cross- to self-phase modulation in bulk AlGaAs and AlGaAs/GaAs multiple quantum well waveguides at half the band gap *Appl. Phys. Lett.* **67** 760
[Villeneuve1995c] Villeneuve A, Mamyshev P, Kang J U, Stegeman G I, Aitchison J S and Ironside C N 1995 Efficient time-domain demultiplexing with separate signal and control wavelengths in an AlGaAs nonlinear directional coupler *IEEE J. Quantum. Electron.* **31** 2165
[Vincenti2011] Vincenti M A, De Ceglia D, Ciattoni A and Scalora M 2011 Singularity-driven second- and third-harmonic generation at ε-near-zero crossing points *Phys. Rev.* A **84** 63826
[Viswanath2001] Viswanath A K 2001 Surface and interfacial recombination in semiconductors *Handbook of Surfaces and Interfaces of Materials* ed H Nalwa (New York: Academic) ch 3, pp 217–84
[Vodopyanov2006] Vodopyanov K L, Fejer M M, Yu X, Harris J S, Lee Y S, Hurlbut W C and Lynch C 2006 Terahertz-wave generation in quasi-phase-matched GaAs *Appl. Phys. Lett.* **89** 141119
[Vodopyanov2014] Vodopyanov K L, Makasyuk I and Schunemann P G 2014 Grating tunable 4–14 μm GaAs optical parametric oscillator pumped at 3 μm *Opt. Express* **22** 4131
[Waclawek2019] Waclawek J P, Kristament C, Moser H and Lendl B 2019 Balanced-detection interferometric cavity-assisted photothermal spectroscopy *Opt. Express* **27** 12183
[Wada1996] Wada A, Okude S, Sakai T and Yamauchi R 1996 GeO_2 concentration dependence of nonlinear refractive index coefficients of silica-based optical fibers *Electron. Commun. Japan* 1 **79** 811–7 (Translated from Denshi Joho Tsushin Gakkai Ronbunshi 1995 78-B-1 811–7)
[Wagner1995] Wagner H P, Wittmann S, Schmitzer H and Stanzl H 1995 Phase matched second harmonic generation using thin film ZnTe optical waveguides *J. Appl. Phys.* **77** 3637
[Wagner1997] Wagner H P, Kuhnelt M, Wein G, Hahn B, Gebhardt W, Eisert D, Bacher G and Forchel A 1997 Phase matched second harmonic generation using a $\chi^{\wedge}((2)$)modulated ZnTe/ZnSe optical waveguide *J. Lumin.* **72–74** 87
[Wagner2007] Wagner S J, Meier J, Helmy A S, Aitchison J S, Sorel M and Hutchings D C 2007 Polarization-dependent nonlinear refraction and two-photon absorption in GaAs/AlAs superlattice waveguides below the half-bandgap *J. Opt. Soc. Am.* B **24** 1557
[Wagner2009] Wagner S J, Holmes B M, Younis U, Helmy A S, Aitchison J S and Hutchings D C 2009 Continuous wave second-harmonic generation using domain-disordered quasi-phase matching waveguides *Appl. Phys. Lett.* **94** 151107
[Wagner2011] Wagner S J, Holmes B M, Younis U, Sigal I, Helmy A S, Aitchison J S and Hutchings D C 2011 Difference frequency generation by quasi-phase matching in periodically intermixed semiconductor superlattice waveguides *IEEE J. Quantum. Electron.* **47** 834
[Waldermann2008] Waldermann F *et al* 2008 Measuring phonon dephasing with ultrafast pulses using Raman spectral interference *Phys. Rev.* B **78** 1–6
[Wang1999] Wang S, Pasiskevicius V, Hellström J, Laurell F and Karlsson H 1999 First-order type II quasi-phase-matched UV generation in periodically poled KTP *Opt. Lett.* **24** 978
[Wang2009] Wang F X, Rodríguez F J, Albers W M, Ahorinta R, Sipe J E and Kauranen M 2009 Surface and bulk contributions to the second-order nonlinear optical response of a gold film *Phys. Rev.* B **80** 233402
[Wang2012] Wang C, Zhang T and Lin W 2012 Rational synthesis of noncentrosymmetric metal–organic frameworks for second-order nonlinear optics *Chem. Rev.* **112** 1084
[Wang2012a] Wang K-Y and Foster A C 2012 Ultralow power continuous-wave frequency conversion in hydrogenated amorphous silicon waveguides *Opt. Lett.* **37** 1331
[Wang2012b] Wang K-Y, Petrillo K G, Foster M A and Foster A C 2012 Ultralow-power all-optical processing of high-speed data signals in deposited silicon waveguides *Opt. Express* **20** 24600
[Wang2013] Wang T, Venkatram N, Gosciniak J, Cui Y, Qian G, Ji W and Tan D T H 2013 Multi-photon absorption and third-order nonlinearity in silicon at mid-infrared wavelengths *Opt. Express* **21** 32192
[Wang2014a] Wang K, Feng Y, Chang C, Zhan J, Wang C, Zhao Q, Coleman J N, Zhang L, Blau W J and Wang J 2014 Broadband ultrafast nonlinear absorption and nonlinear refraction of layered molybdenum dichalcogenide semiconductors *Nanoscale* **6** 10530–5
[Wang2014b] Wang T, Gai X, Wei W, Wang R, Yang Z, Shen X and Luther-Davies B 2014 Systematic z-scan measurements of the third order nonlinearity of chalcogenide glasses *Opt. Mater. Express* **4** 1011
[Wang2015] Wang T, Ng T D K, Ng S-K, Toh Y-T, Chee A K L, Chen G F R, Wang Q and Tan D T H 2015 Supercontinuum generation in bandgap engineered, back-end CMOS compatible silicon rich nitride waveguides *Laser Photonics Rev.* **9** 498
[Wang2017] Wang J, Bisson P J, Marmolejos J M and Shultz M J 2017 Nonlinear interferometer: design, implementation, and phase-sensitive sum frequency measurement *J. Chem. Phys.* **147** 064201
[Wang2018] Wang J, Jiang Z, Chen H, Li J, Yin J, Wang J, He T, Yan P and Ruan R 2018 High energy soliton pulse generation by a magnetron-sputtering-deposition-grown $MoTe_2$ saturable absorber *Photon. Res.* **6** 535–41
[Wang2018a] Wang L, Xie W, Van Thourhout D, Zhang Y, Yu H and Wang S 2018 Nonlinear silicon nitride waveguides based on a PECVD deposition platform *Opt. Express* **26** 9645

[Wang2018b] Wang C, Langrock C, Marandi A, Jankowski M, Zhang M, Desiatov B, Fejer M M and Lončar M 2018 Ultrahigh-efficiency wavelength conversion in nanophotonic periodically poled lithium niobate waveguides *Optica* **5** 1438
[Wang2019] Wang H, Ciret C, Cassagne C and Boudebs G 2019 Measurement of the third order optical nonlinearities of graphene quantum dots in water at 355 nm, 532 nm and 1064 nm *Opt. Mater. Express* **9** 339
[Wang2020] Wang Z, Hu T, Liang R and Wei M 2020 Application of zero-dimensional nanomaterials in biosensing *Front. Chem.* **8** 320
[Wang2020a] Wang J, Clementi M, Minkov M, Barone A, Carlin J-F, Grandjean N, Gerace D, Fan S, Galli M and Houdré R 2020 Doubly resonant second-harmonic generation of a vortex beam from a bound state in the continuum *Optica* **7** 1126
[Wang2021] Wang K, Seidel M, Nagarajan K, Chervy T, Genet C and Ebbesen T 2021 Large optical nonlinearity enhancement under electronic strong coupling *Nat. Commun.* **12** 1486
[Wang2020b] Wang X, Huang S-C, Hu S, Yan S and Ren B 2020 Fundamental understanding and applications of plasmon-enhanced Raman spectroscopy *Nat. Rev. Phys.* **2** 253
[Ward1969] Ward J F and New G H C 1969 Optical third harmonic generation in gases by a focused laser beam *Phys. Rev.* **185** 57
[Wathen2014] Wathen J J, Apiratikul P, Richardson C J K, Porkolab G A, Carter G M and Murphy T E 2014 Efficient continuous-wave four-wave mixing in bandgap-engineered AlGaAs waveguides *Opt. Lett.* **39** 3161
[Weber1978] Weber M J, Milam D and Smith W L 1978 Nonlinear refractive index of glasses and crystals *Opt. Eng.* **17** 463–9
[Wei2019] Wei Z and Zhuiykov S 2019 Challenges and recent advancements of functionalization of two-dimensional nanostructured molybdenum trioxide and dichalcogenides *Nanoscale* **11** 15709–38
[Wei2017] Wei J, Chaitanya Kumar S, Ye H, Devi K, Schunemann P G and Ebrahim-Zadeh M 2017 Nanosecond difference-frequency generation in orientation-patterned gallium phosphide *Opt. Lett.* **42** 2193
[Wei2018] Wei J, Kumar S C, Ye H, Schunemann P G and Ebrahim-Zadeh M 2018 Performance characterization of mid-infrared difference-frequency-generation in orientation-patterned gallium phosphide *Opt. Mater. Express* **8** 555
[Wen2018] Wen X, Li G, Gu C, Zhao J, Wang S, Jiang C, Palomba S, De Sterke C M and Xiong Q 2018 Doubly enhanced second harmonic generation through structural and epsilon-near-zero resonances in TiN nanostructures *ACS Photonics* **5** 2087
[Wherrett1984] Wherrett B S 1984 Scaling rules for multiphoton interband absorption in semiconductors *J. Opt. Soc. Am.* B **1** 67
[Willner2014] Willner A E, Khaleghi S, Chitgarha M R and Yilmaz O F 2014 All-optical signal processing *J. Lightwave Technol.* **32** 660
[Willner2019] Willner A E 2019 *Optical Fiber Communications* 7th edn (Amsterdam: Elsevier)
[Wilson2020] Wilson D J, Schneider K, Hönl S, Anderson M, Baumgartner Y, Czornomaz L, Kippenberg T J and Seidler P 2020 Integrated gallium phosphide nonlinear photonics *Nat. Photon.* **14** 57
[Winnerl2000] Winner L S *et al* 2000 Frequency doubling and tripling of terahertz radiation in a GaAs/AlAs superlattice due to frequency modulation of Bloch oscillations *Appl. Phys. Lett.* **77** 1259
[Winzer2018] Winzer P J, Neilson D T and Chraplyvy A R 2018 Fiber-optic transmission and networking: the previous 20 and the next 20 years *Opt. Express* **26** 24190
[Woerner2013] Woerner M, Kuehn W, Bowlan P, Reimann K and Elsaesser T 2013 Ultrafast two-dimensional terahertz spectroscopy of elementary excitations in solids *New J. Phys.* **15** 025039
[Wokaun1981] Wokaun A, Bergman J G, Heritage J P, Glass A M, Liao P F and Olson D H 1981 Surface second-harmonic generation from metal island films and microlithographic structures *Phys. Rev.* B **24** 849
[Wolf2015] Wolf O *et al* 2015 Phased-array sources based on nonlinear metamaterial nanocavities *Nat. Commun.* **6** 7667
[Woodward2016] Woodward R I *et al* 2016 Characterization of the second- and third-order nonlinear optical susceptibilities of monolayer MoS_2 using multiphoton microscopy *2D Mater.* **4** 011006
[Wronski1981] Wronski C R and Daniel R E 1981 Photoconductivity, trapping, and recombination in discharge-produced, hydrogenated amorphous silicon *Phys. Rev.* B **23** 794
[Wu2009] Wu J, Gupta A K, Gutierrez H R and Eklund P C 2009 Cavity-enhanced stimulated Raman scattering from short GaP nanowires *Nano Lett.* **9** 3252–7
[Wu2015] Wu C-L, Chiu Y-J, Chen C-L, Lin Y-Y, Chu A-K and Lee C-K 2015 Four-wave-mixing in the loss low submicrometer Ta_2O_5 channel waveguide *Opt. Lett.* **40** 4528
[Wu2017] Wu L, Patankar S, Morimoto T, Nair N L, Thewalt E, Little A and Orenstein J 2017 Giant anisotropic nonlinear optical response in transition metal monopnictide Weyl semimetals *Nat. Phys.* **13** 350
[Wu2021] Wu Z, Zhang Y, Zeng S, Li J, Xie Y, Chen Y and Yu S 2021 Low-noise Kerr frequency comb generation with low temperature deuterated silicon nitride waveguides *Opt. Express* **29** 29557
[Wurtz2008] Wurtz G A and Zayats A V 2008 Nonlinear surface plasmon polaritonic crystals *Laser Photonics Rev.* **2** 125
[Xing2019] Xing P, Ma D, Ooi K J A, Choi J W, Agarwal A M and Tan D 2019 CMOS-compatible PECVD silicon carbide platform for linear and nonlinear optics *ACS Photonics* **6** 1162
[Xiong2011] Xiong C, Pernice W, Ryu K K, Schuck C, Fong K Y, Palacios T and Tang H X 2011 Integrated GaN photonic circuits on silicon (100) for second harmonic generation *Opt. Express* **19** 10462
[Xu1997] Xu C Q, Takemasa K, Nakamura K, Shinozaki K, Okayama H and Kamijoh T 1997 Device length dependence of optical secondharmonic generation in AlGaAs quasiphase matched waveguides *Appl. Phys. Lett.* **70** 1554
[Xu1998] Xu C-Q, Takemasa K, Nakamura K, Okayama H and Kamihoh T 1998 AlGaAs semiconductor quasi-phase-matched wavelength converters *Jpn. J. Appl. Phys.* **37** 823
[Xu2013] Xu B, Omura M, Takiguchi M, Martinez A, Ishigure T, Yamashita S and Kuga T 2013 Carbon nanotube/polymer composite coated tapered fiber for four wave mixing based wavelength conversion *Opt. Express* **21** 3651–7
[Xu2017] Xu F, Wu Z-X and Lu Y-Q 2017 Nonlinear optics in optical-fiber nanowires and their applications *Prog. Quantum Electron.* **55** 35–51
[Xu2017a] Xu X, Zheng X, He F, Wang Z, Subbaraman H, Wang Y, Jia B and Chen R T 2017 Observation of third-order nonlinearities in graphene oxide film at telecommunication wavelengths *Sci. Rep.* **7** 9646
[Xu2017b] Xu Y, Jiang X-F, Ge Y, Guo Z, Zeng Z, Xu Q-H, Zhang H, Yu X-F and Fan D 2017 Size-dependent nonlinear optical properties of black phosphorus nanosheets and their applications in ultrafast photonics *J. Mater. Chem.* C **5** 3007–13
[Xu2019] Xu L *et al* 2019 Dynamic nonlinear image tuning through magnetic dipole quasi-BIC ultrathin resonators *Adv. Sci.* **6** 1802119
[Xu2020] Xu L *et al* 2020 Forward and backward switching of nonlinear unidirectional emission from GaAs nanoantennas *ACS Nano* **14** 1379
[Xue2016] Xue X, Xuan Y, Wang C, Wang P-H, Liu Y, Niu B, Leaird D E, Qi M and Weiner A M 2016 Thermal tuning of Kerr frequency combs in silicon nitride microring resonators *Opt. Express* **24** 687
[Yamashita2019] Yamashita S 2019 Nonlinear optics in carbon nanotube, graphene, and related 2D materials *APL Photonics* **4** 034301

[Yan2012a] Yan X-Q, Liu Z-B, Chen Y-S and Tian J-G 2012 Polarization characteristics of nonlinear refraction and nonlinear scattering in several solvents *J. Opt. Soc. Am.* B **29** 2721–8
[Yan2012b] Yan L, Willner A E, Wu X, Yi A, Bogoni A, Chen Z-Y and Jiang H-Y 2012 All-optical signal processing for ultrahigh speed optical systems and networks *J. Lightwave Technol.* **30** 3760
[Yan2016] Yan K, Vu K, Wang R and Madden S 2016 Greater than 50% inversion in erbium doped chalcogenide waveguides *Opt. Express* **24** 23304
[Yan2017] Yan B and Felser C 2017 Topological materials: Weyl semimetals *Annu. Rev. Condens. Matter Phys.* **8** 337
[Yan2020] Yan J, Liu X, Ma C, Huang Y and Yang G 2020 All-dielectric materials and related nanophotonic applications *Mater. Sci. Eng.* R **141** 100563
[Yang2015] Yang Y, Wang W, Boulesbaa A, Kravchenko I I, Briggs D P, Puretzky A, Geohegan D and Valentine J 2015 Nonlinear fano-resonant dielectric metasurfaces *Nano Lett.* **15** 7388
[Yang2018a] Yang Y, Zenin V A and Bozhevolnyi S I 2018 Anapole-assisted strong field enhancement in individual all-dielectric nanostructures *ACS Photonics* **5** 1960
[Yang2018b] Yang Y, Wu J, Xu X, Liang Y, Chu S T, Little B E, Morandotti R, Jia B and Moss D J 2018 Enhanced four-wave mixing in waveguides integrated with graphene oxide *APL Photonics* **3** 120803
[Yang2019] Yang Y *et al* 2019 High-harmonic generation from an epsilon-near-zero material *Nat. Phys.* **15** 1022
[Yang2020] Yang F, Gyger F and Thévenaz L 2020 Intense Brillouin amplification in gas using hollow-core waveguides *Nat. Photon.* **14** 700–8
[Yao2018] Yao B *et al* 2018 Broadband gate-tunable terahertz plasmons in graphene heterostructures *Nat. Photon.* **12** 22–28
[Yeh2007] Yeh K L, Hoffmann M C, Hebling J and Nelson K A 2007 Generation of 10 μJ ultrashort terahertz pulses by optical rectification *Appl. Phys. Lett.* **90** 171121
[Yesodha2004] Yesodha S K, Sadashiva Pillai C K and Tsutsumi N 2004 Stable polymeric materials for nonlinear optics: a review based on azobenzene systems *Prog. Polym. Sci.* **29** 45
[Yin2008] Yin S S, Kim J, Zhan C, An J, Lee J, Ruffin P, Edwards E, Brantley C and Luo C 2008 Supercontinuum generation in single crystal sapphire fibers *Opt. Commun.* **281** 1113
[Yin2014] Yin X, Ye Z, Chenet D A, Y. Y, O'Brien K, Hone J C and Zhang X 2014 Edge nonlinear optics on a MoS_2 atomic monolayer *Science* **344** 488–90
[Yoo1995] Yoo S J B, Bhat R, Caneau C and Koza M A 1995 Quasi-phase-matched second-harmonic generation in AlGaAs waveguides with periodic domain inversion achieved by wafer-bonding *Appl. Phys. Lett.* **66** 3410
[Yoo1996] Yoo S J B, Caneau C, Bhat R, Koza M A, Rajhel A and Antoniades N 1996 Wavelength conversion by difference frequency generation in AlGaAs waveguides with periodic domain inversion achieved by wafer bonding *Appl. Phys. Lett.* **68** 2609
[You2018] You J W, Bongu S R, Bao Q and Panoiu N C 2018 Nonlinear optical properties and applications of 2D materials: theoretical and experimental aspects *Nanophotonics* **8** 63–97
[Yu2005] Yu X, Scaccabarozzi L, Harris J S Jr, Kuo P S and Fejer M M 2005 Efficient continuous wave second harmonic generation pumped at 1.55 μm in quasi-phase-matched AlGaAs waveguides *Opt. Express* **13** 10742
[Yu2007] Yu X, Scaccabarozzi L, Lin A C, Fejer M M and Harris J S 2007 Growth of GaAs with orientation-patterned structures for nonlinear optics *J. Cryst. Growth* **301–302** 163
[Yu2013] Yu Y, Gai X, Wang T, Ma P, Wang R, Yang Z and Luther-Davies B 2013 Mid-infrared supercontinuum generation in chalcogenides *Opt. Mater. Express* **3** 1075
[Yu2014] Yu Y, Gai X, Ma P, Choi D-Y, Yang Z, Wang R and Luther-Davies B 2014 A broadband, quasi-continuous, mid-infrared supercontinuum generated in a chalcogenide glass waveguide *Laser Photonics Rev.* **8** 792
[Yu2019] Yu M, Desiatov B, Okawachi Y, Gaeta A L and Lončar M 2019 Coherent two-octave-spanning supercontinuum generation in lithium-niobate waveguides *Opt. Lett.* **44** 1222
[Zahedpour2015] Zahedpour S, Wahlstrand J K and Milchberg H M 2015 Measurement of the nonlinear refractive index of air constituents at mid-infrared wavelengths *Opt. Lett.* **40** 5794–7
[Zaks2012] Zaks B, Liu R B and Sherwin M S 2012 Experimental observation of electron–hole recollisions *Nature* **483** 580
[Zervas2014] Zervas M N and Codemard C 2014 High power fiber lasers: a review *IEEE J. Sel. Top. Quantum Electron.* **20** 219
[Zervas2019] Zervas M N 2019 Transverse mode instability, thermal lensing and power scaling in Yb^{3+}-doped high-power fiber amplifiers *Opt. Express* **27** 19019
[Zhang1994] Zhang X, Ebskamp F and Pedersen R 1994 Input power limits and maximum capacity in long-haul WDM lightwave systems due to stimulated Raman scattering *Opt. Commun.* **107** 358
[Zhang1996] Zhang H Y, He Z H, Shih Y H, Schurman M, Feng Z C and Stall R A 1996 Study of nonlinear optical effects in GaN:Mg epitaxial film *Appl. Phys. Lett.* **69** 2953
[Zhang2011] Zhang Y, Grady N K, Ayala-Orozco C and Halas N J 2011 Three-dimensional nanostructures as highly efficient generators of second harmonic light *Nano Lett.* **11** 5519
[Zhang2015a] Zhang H 2015 Ultrathin two-dimensional nanomaterials *ACS Nano* **9** 9451–69
[Zhang2015b] Zhang S *et al* 2015 Direct observation of degenerate two-photon absorption and its saturation in WS_2 and MoS_2 monolayer and few-layer films *ACS Nano* **9** 7142–50
[Zhang2016] Zhang Y, Husko C, Lefrancois S, Rey I H, Krauss T F, Schroder J and Eggleton B J 2016 Cross-phase modulation-induced spectral broadening in silicon waveguides *Opt. Express* **24** 443–51
[Zhang2017a] Zhang Y-X and Wang Y-H 2017 Nonlinear optical properties of metal nanoparticles: a review *RSC Adv.* **7** 45129–44
[Zhang2017b] Zhang B, Liu S, Wu X, Yi T, Fang Y, Zhang J and Song Y 2017 Ultrafast dynamics of carriers and nonlinear refractive index in bulk polycrystalline diamond *Optik* **130** 1073
[Zhang2019a] Zhang Y *et al* 2019 Doping-induced second-harmonic generation in centrosymmetric graphene from quadrupole response *Phys. Rev. Lett.* **122** 047401
[Zhang2019b] Zhang M, Buscaino B, Wang C, Shams-Anasari A, Reimer C, Zhu R, Kahn J M and Lončar M 2019 Broadband electro-optic frequency comb generation in a lithium niobate microring resonator *Nature* **568** 373
[Zhang2020a] Zhang W *et al* 2020 Ultrafast terahertz magnetometry *Nat. Commun.* **11** 4247
[Zhang2020b] Zhang Y, Zhong K and Tsang H K 2021 Raman lasing in multimode silicon racetrack resonators *Laser Photonics Rev.* **15** 2000336
[Zhang2020c] Zhang Y, Tao L, Yi D, Xu J-B and Tsang H K 2020 Enhanced four-wave mixing with MoS_2 on a silicon waveguide *J. Opt.* **22** 025503

[Zhang2021] Zhang D, Cui H, Zhu C, Lv K, Zhang H, Liu X and Qiu J 2021 Nanoscale engineering of optical nonlinearity based on a metal nitride/oxide heterostructure *ACS Appl. Mater. Interfaces* **13** 1253–60
[Zhang and Turchinovich2021] Zhang W and Turchinovich D 2021 Rigorous signal reconstruction in terahertz emission spectroscopy *Opt. Express* **29** 24411
[Zhao2009] Zhao Q, Zhou J, Zhang F and Lippens D 2009 Mie resonance-based dielectric metamaterials *Mater. Today* **12** 60
[Zhao2015] Zhao H *et al* 2015 Visible-to-near-infrared octave spanning supercontinuum generation in a silicon nitride waveguide *Opt. Lett.* **40** 2177
[Zhao2018] Zhao P, Reichert M, Benis S, Hagan D J and Van Stryland E W 2018 Temporal and polarization dependence of the nonlinear optical response of solvents *Optica* **5** 583–94
[Zheng2014] Zheng X, Jia B, Chen X and Gu M 2014 *In situ* third-order non-linear responses during laser reduction of graphene oxide thin films towards on-chip non-linear photonic devices *Adv. Mater.* **26** 2699–703
[Zheng2015a] Zheng X, Chen R, Shi G, Zhang J, Xu Z, Cheng X and Jiang T 2015 Characterization of nonlinear properties of black phosphorus nanoplatelets with femtosecond pulsed Z-scan measurements *Opt. Lett.* **40** 3480–3
[Zheng2015b] Zheng X, Zhang Y, Chen R, Cheng X, Xu Z and Jiang T 2015 Z-scan measurement of the nonlinear refractive index of monolayer WS_2 *Opt. Express* **23** 15616–23
[Zheng2019a] Zheng Y, Pu M, Sahoo H K, Semenova E and Yvind K 2019 High-quality-factor AlGaAs-on-sapphire microring resonators *J. Lightwave Technol.* **37** 868
[Zheng2019b] Zheng Y, Pu M, AYi A, Ou X and Ou H 2019 4H-SiC microring resonators for nonlinear integrated photonics *Opt. Lett.* **44** 5784
[Zheng2021] Zheng Y and Chen X 2021 Nonlinear wave mixing in lithium niobate thin film *Adv. Phys.* X **6** 1889402
[Zhou2020a] Zhou L, Fu H, Lv T, Wang C, Gao H, Li D, Deng L and Xiong W 2020 Nonlinear optical characterization of 2D materials *Nanomaterials* **10** 2263
[Zhou2020b] Zhou Y, Alam M Z, Karimi M, Upham J, Reshef O, Liu C and Boyd R W 2020 Broadband frequency translation through time refraction in an epsilon-near-zero material *Nat. Commun.* **11** 2180
[Zhu2006] Zhu Z-H, Ye W-M, Ji J-R, Y X-D and Zen C 2006 High-contrast light-by-light switching and AND gate based on nonlinear photonic crystals *Opt. Express* **14** 1783
[Zlatanovic2010] Zlatanovi S, Park J S, Moro S, Boggio C J M, Divliansky I B, Alic N, Mookherjea S and Radic S 2010 Mid-infrared wavelength conversion in silicon waveguides using ultracompact telecom-band-derived pump source *Nat. Photon.* **4** 561
[Zubyuk2019] Zubyuk V V *et al* 2019 Low-power absorption saturation in semiconductor metasurfaces *ACS Photonics* **6** 2797
[Zverev1999] Zverev P G, Basiev T T and Prokhorov A M 1999 Stimulated Raman scattering of laser radiation in Raman crystals *Opt. Mater.* **11** 335–52